University of New Mexico
UNM Digital Repository

Physics & Astronomy ETDs | Electronic Theses and Dissertations

6-25-2015

The Arecibo L-Band Feed Array Zone of Avoidance Survey

Travis McIntyre

Follow this and additional works at: https://digitalrepository.unm.edu/phyc_etds

Recommended Citation
McIntyre, Travis. "The Arecibo L-Band Feed Array Zone of Avoidance Survey." (2015). https://digitalrepository.unm.edu/phyc_etds/42

This Dissertation is brought to you for free and open access by the Electronic Theses and Dissertations at UNM Digital Repository. It has been accepted for inclusion in Physics & Astronomy ETDs by an authorized administrator of UNM Digital Repository. For more information, please contact disc@unm.edu.

Travis Patrick McIntyre

Candidate

Physics and Astronomy

Department

This dissertation is approved, and it is acceptable in quality and form for publication:

Approved by the Dissertation Committee:

Dr. Patricia Henning , Chairperson

Dr. Richard Rand

Dr. Ylva Pihlstrom

Dr. Dave Westpfahl

Dr. Robert Minchin

The Arecibo L-Band Feed Array Zone of Avoidance

by

Travis Patrick McIntyre

B.S., Physics, Clemson University, 2006

DISSERTATION

Submitted in Partial Fulfillment of the
Requirements for the Degree of

Doctor of Philosophy
Physics

The University of New Mexico

Albuquerque, New Mexico

May, 2015

DEDICATION

Dedicated to my parents.

"The small man builds cages for everyone he knows
While the sage, who must duck her head when the moon is low,
Keeps dropping keys all night long
For all the beautiful, rowdy prisoners."

-Hafiz

"No one is an island entire of itself; every one
is a piece of the continent, a part of the main;
if a clod be washed away by the sea, Europe
is the less, as well as if a promontory were, as
well as any manner of thy friends or of thine
own were; any one's death diminishes me,
because I am involved in humanity.
And therefore never send to know for whom
the bell tolls; it tolls for thee."

-John Donne

ACKNOWLEDGMENTS

First, I would like to thank my adviser, Trish Henning. Her attention to detail and commitment to excellent work have helped make me an immeasurably better scientist and a more thoughtful, independent, and confident person both professionally and personally. I would like to thank the insightful, hard working, and capable Emmanuel Momjian, who is the best collaborator you could ask for. I would also like to thank my collaborators and fellow cube searchers, Zhon Butcher, Steve Schneider, Lister Staveley-Smith, Wim van Driel, and Jessica Rosenberg. I would like to thank my graduate adviser, Ylva Pihlstrom, for guiding me through the first years of grad school and teaching assistantships. I would like to thank Ivan Deutsch for his support and encouragement in the department. I would like to thank Gyula Jozsa for his assistance and friendship at Westerbork. I would like to thank Chris Salter, Tapasi Ghosh, Arun Venkataraman, Angel Vasquez, David Loiselle, Lucy Lopez, and most of all Patrick Taylor, whose assistance and friendship at Arecibo were priceless to me, capisce? I would like to thank Jonas Anderson, Alex Tacla, Frank Schinzel, Eric Miller, Stephan Wenger, Chris Fierre, Fonda Day, and Bill Miller, whose assistance and friendship in Albuquerque were priceless to me. I would like to thank my very dear friend Helen Davis, who is the most delightful person that I know, for our dissertation writing club, but mostly for endless laughter and friendship. I would like to thank my undergraduate adviser, Dieter Hartmann, whose boundless encouragement and enthusiasm launched my research career, as well as Stuart Bishop, Terry Tritt, Dave Moyle, Don Clayton, Autumn Homewood, and Kirin Garimella. I would like to thank Mark Leising for all the great advice and old driver. I would like to thank the ultimate community in Albuquerque for all the good memories. I would like to thank Katie Richardson, whose unwavering belief in me taught me to believe in myself. I would like to thank all the staff of the Arecibo Observatory and the island of Puerto Rico, where my heart often wanders.

Finally, the two reasons without whom this dissertation would not exist. First, my family. My sister Katie who always admired me, my brother Jesse who always looked after me, my sister Gretchen who always understood me, and Sequoia and Irish, who I never forget. Most of all my mom and dad. Their encouragement, support, and unconditional love have been the most wonderful and steadfast things in my life. My parents are the two most amazing people in the world. They are the kindest, most loving, and most selfless people that I know. They are the parents that anybody would dream of. Lastly, and most important of all, I would like to thank and truly acknowledge Robert Minchin, a person of the highest quality. Without Robert's kindness, guidance, and friendship I would not be defending today. The world would be a wonderful place if it was made up of Robert Minchins; competent, productive, open-minded, funny, considerate, thoughtful, caring, and calm.

The Arecibo L-Band Feed Array Zone of Avoidance

by

Travis Patrick McIntyre

B.S., Physics, Clemson University, 2006

Ph.D., Physics, University of New Mexico, 2015

Abstract

The Arecibo L-Band Feed Array Zone of Avoidance (ALFA ZOA) Survey detects galaxies behind the Milky Way from 21cm emission by neutral hydrogen gas (H I). ALFA ZOA is conducted in two phases: shallow and deep. Observations for the Shallow survey are finished and 45% of the survey has an adjudicated catalog with 280 detections at a sensitivity of 5.4 mJy at 9 km s^{-1} channel resolution. An additional 173 bright detections are found so far outside the adjudicated area. The survey is complete above integrated flux, $F_{HI} = 2.2$ Jy km s^{-1} and has a positional accuracy of 26″. The estimated H I mass function has values $\Phi_* = 4.8 \pm 1.1 \times 10^{-3}$, $\log M_* = 9.87 \pm 0.11$, and $\alpha = 1.34 \pm 0.11$, and the H I critical density is $\Omega_{HI} = 4.3 \pm 1.1 \times 10^{-4}$. The survey finds 3 out of 7 named large scale structures to have been misplaced in density reconstruction maps from the literature. Three galaxy groups are discovered within 20 Mpc and one may have the mass and distance to recover the mass density dipole vector. First results from the Deep survey find 61 galaxies within a 15 square degree area. The Deep survey reaches its expected sensitivity of rms = 1 mJy at 9 km s^{-1} channel resolution, and is shown to be complete above integrated flux, F_{HI} = 0.5 Jy km s^{-1}, detecting galaxies out to a recessional velocity of nearly 19,000 km s^{-1}. ALFA ZOA increases the number of galaxies cataloged in the area by 100%, and the number with known redshift by over 800%.

Contents

List of Figures

List of Figures

Chapter 1

Introduction

1.1 Introduction

The Arecibo L-Band Feed Array Zone of Avoidance (ALFA ZOA) Survey searches for galaxies behind the Milky Way, a region of sky with very few extragalactic detections because of stars, dust, and gas in the Galaxy that interfere with light emitted by objects on the other side. ALFA ZOA detects 21cm emission from neutral hydrogen gas (H I), which is not affected by extinction and is only confused with Milky Way sources at velocities less than $|100|$ km s^{-1}. H I observations can detect galaxies with neutral hydrogen gas, which are predominantly late-type galaxies, spirals, dwarfs, and irregulars. This chapter explains why the Zone of Avoidance should be surveyed for galaxies, how this can be done, and provides an overview of what the ALFA ZOA survey is doing. Section 1.2 provides a background for ZOA science, Section 1.3 explains the science goals of ZOA research, Section 1.4 explains neutral hydrogen observations, Section 1.5 presents an overview of the ALFA ZOA survey, Section 1.6 outlines the chapters of the dissertation.

1.2 Background

1.2.1 Zone of Avoidance

The Zone of Avoidance has its name from being the part of the sky "avoided" by galaxies. It is an area of sky mostly centered on the plane of the Milky Way where the stars, dust, and gas in the Galaxy make it difficult to observe emission from sources on the other side because of extinction and confusion. Extinction is caused by the scattering and absorption of incoming radiation on dust particles, effectively reducing the amount of radiation that reaches the observer. Extinction around the plane of the Milky Way reduces incoming emission by more than $A_B = 1$ mag for about 15% of the universe centered on the Galactic plane (Kraan-Korteweg 2000). Confusion is caused by not being able to differentiate between two sources of emission. A distribution of all known galaxies in the universe as of 2003 is shown in Figure 1.1. The effect of the ZOA on galaxy detections around the Milky Way can clearly be seen.

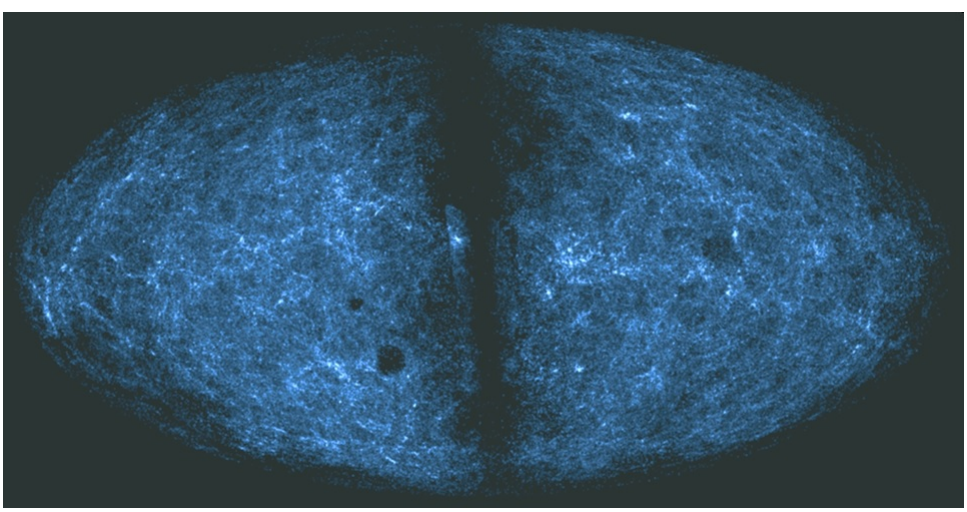

Figure 1.1 Distribution of about one million galaxies in supergalactic coordinates (Paturel et al. 2003).

Extinction decreases as the wavelength of the observation increases. Near-, mid-, and far-infrared observations have a significantly smaller Zone of Avoidance than visual wavelengths, though confusion remains an issue for any photometric observing technique. Neutral hydrogen is not affected by extinction and it is largely optically thin, so it does not experience confusion with the Milky Way for extragalactic sources redshifted beyond the Galaxy's H I distribution ($\sim |100|$ km s^{-1}).

1.2.2 Observing the Zone of Avoidance

The Zone of Avoidance covers about 25% of the sky for the distribution of optically visible galaxies (Kraan-Korteweg 2000). Even the most modern optical redshift surveys avoid searching for galaxies in the ZOA. Figure 1.2 shows the distribution of galaxy detection for the 6dF Galaxy Survey (6DFGS; Jones et al. 2004; Jones et al. 2009). The survey has a Zone of Avoidance below Galactic latitudes, $b < |10°|$.

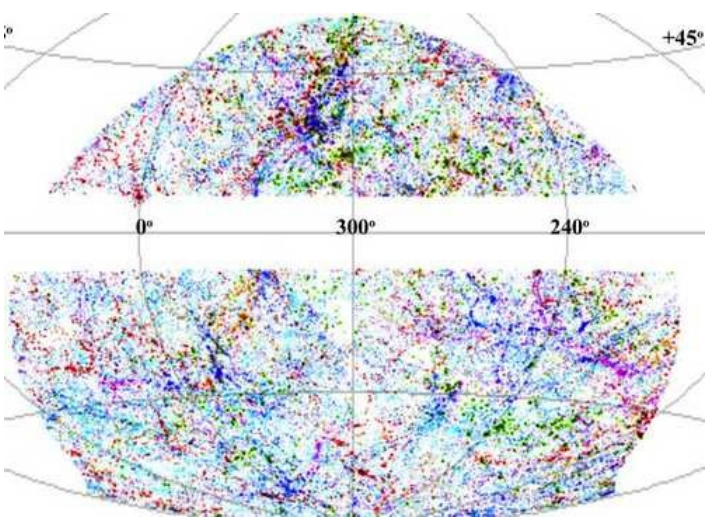

Figure 1.2 Distribution of Final Release 6DFGS galaxies in Galactic coordinates taken from the 6DFGS official image gallery (www.6dfgs.net).

In the near-infrared (NIR), the effect of extinction is reduced by several orders of

magnitude, reducing the Zone of Avoidance. Ten magnitudes of extinction at B-band is equal to one magnitude at NIR wavelengths. Figure 1.3 shows the distribution of galaxies for the 2 Micron All Sky Survey (2MASS; Skrutskie et al. 2006), the most modern NIR survey completed. The ZOA appears to cover about 4% of the sky (Kraan-Korteweg & Jarrett 2005), clearly a much smaller ZOA than for visual observations. While NIR observations are affected little by Galactic extinction, they still suffer from confusion with sources in the Milky Way. This is particularly true for the 2MASS Redshift Survey (2MRS; Huchra et al. 2012), which can only obtain redshift measurements at other wavelengths. The ZOA for 2MRS is shown in Figure 1.3 and covers Galactic latitudes $b < |5°|$ ($< |8°|$ near Galactic center). The ZOA is much larger for the redshift survey because redshifts are obtained at various wavelengths.

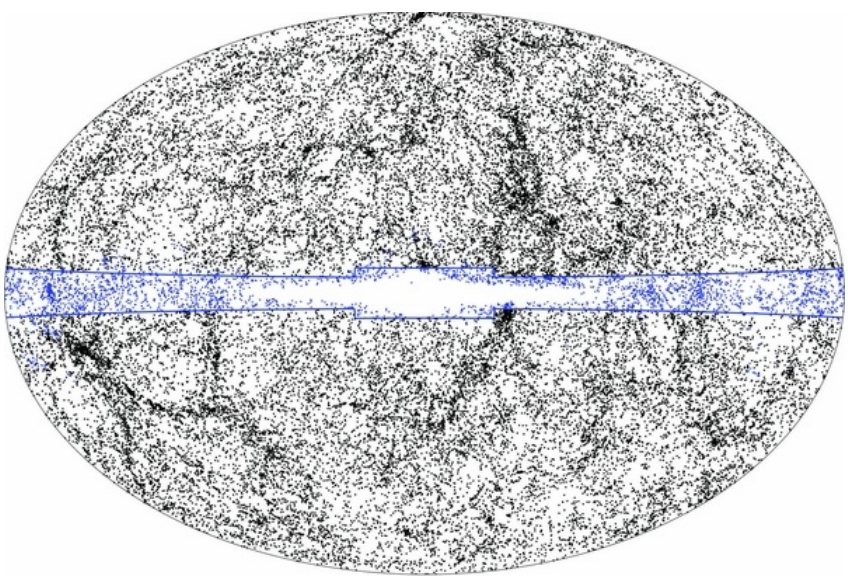

Figure 1.3 Distribution of 2MASS galaxies in Galactic coordinates (Huchra et al. 2012). The Zone of Avoidance for the 2MASS redshift catalog is shown in blue. The apparent flare at the edges is a projection effect.

Far infrared (FIR) observations are affected negligibly by extinction though confusion with Galactic sources does persists. Figure 1.4 shows the distribution of In-

frared Astronomical Satellite (IRAS) galaxies (Saunders et al. 2000). The dark gray mask shows the ZOA for the IRAS Behind the Plane catalog, which was a concerted effort to reduce the IRAS ZOA. The ZOA covers 8% of the sky and is about the same size for FIR as it is for NIR observations. FIR is sensitive to normal spiral and starburst galaxies, but is biased against galaxies without active star formation, like most dwarfs and ellipticals.

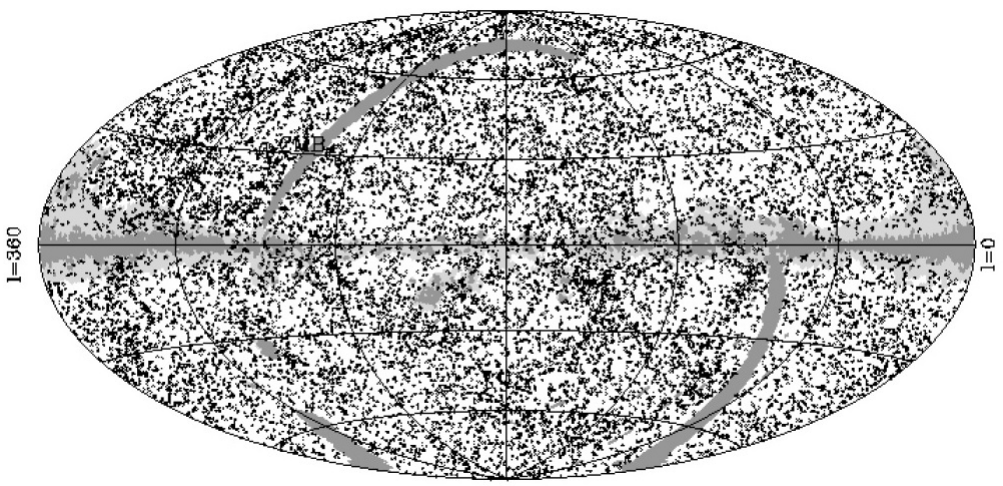

Figure 1.4 Distribution of IRAS galaxies in Galactic coordinates, centered on the Galactic anticenter (Saunders et al. 2000). The ZOA is shown in dark gray, along with the regions not surveyed by IRAS.

H I observations have virtually no Zone of Avoidance (Kerr & Henning 1987). Two large, blind H I surveys of the Zone of Avoidance have been completed: The Dwingeloo Obscured Galaxies Survey (DOGS) and the HI Parkes Zone of Avoidance Survey (HIZOA). DOGS detected 43 galaxies in the northern hemisphere within $\pm 5^\circ$ of the Galactic plane and out to 4000 km s^{-1} redshift velocity (Henning et al. 1998). HIZOA detected about 1000 galaxies in the southern hemisphere up to a declination of $+25^\circ$ and out to 12,700 km s^{-1} redshift velocity (Donley et al. 2005; Henning et al. 2000, 2005, Shafi 2008). A distribution of HIZOA galaxies is shown in two areas around the ALFA ZOA precursor survey in Figure 1.5. All known galaxies in

the same redshift range are shown for comparison, extracted from the Lyon-Meudon Extragalactic Database (LEDA). The traditional Zone of Avoidance is clearly "filled in" by HIZOA.

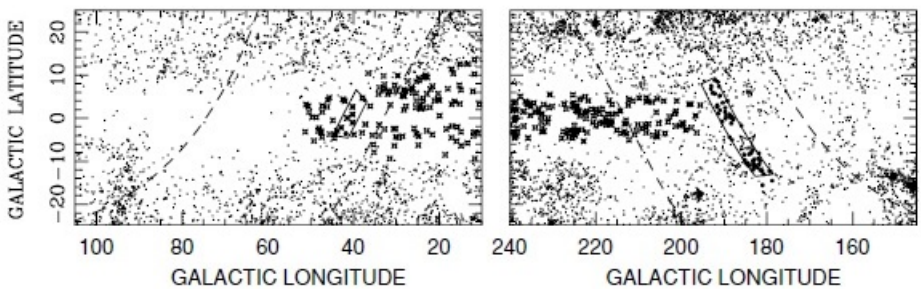

Figure 1.5 Distribution of cataloged LEDA objects within 12,000 km s^{-1} (small dots) and H I detections (crosses) from Parkes HIZOA galaxies in areas of sky near the ALFA ZOA precursor survey (Henning et al. 2010). The ALFA ZOA precursor survey areas (roughly rectangular boxes) are shown.

1.3 Why Study the ZOA

1.3.1 Cosmic Microwave Background Dipole

There is a dipole anisotropy in the cosmic microwave background (CMB) that is explained as the effect of the peculiar motion of the Local Group (LG) relative to the CMB (Kogut et al. 1993). Figure 1.6 shows an all-sky distribution of the CMB anisotropy, in topocentric reference frame, from observations with the Cosmic Background Explorer (COBE) satellite. The peculiar motion of the Local Group is a function of the gravitational force on the LG from the distribution of mass in the local Universe. Determining the peculiar motion vector separately from CMB observations, by measuring the distribution of local mass density directly, puts constraints on cosmological parameters (Kraan-Korteweg 2000). The amplitude of the mass density dipole is in good agreement with the CMB dipole, but the direction of

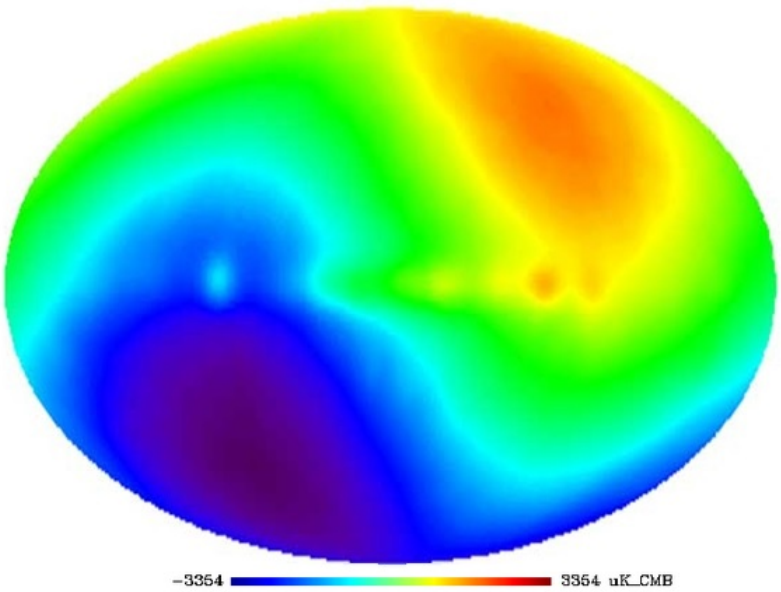

Figure 1.6 The anisotropy dipole in the CMB in Galactic coordinates. Image taken from the Cosmic Background Explorer (COBE) official image gallery.

the vector is in disagreement on the order of $\leq 30°$ (Loeb and Narayan 2008), even for the most modern homogeneous all sky surveys (15° IRAS PSCz; Schmoldt et al. 1999, 13° 2MRS; Erdogdu et al. 2006). An obvious reason for the discrepancy could be that there are currently no true all sky extragalactic surveys because of the ZOA. The ZOA is one of the main contributors to the uncertainty in the mass density dipole estimates (Rowan-Robinson et al. 2000). It has been suggested (Loeb and Narayan 2008) that undiscovered mass behind the Milky Way ($\sim 10^{12} M_{\odot}$ at 1Mpc or $\sim 10^{15} M_{\odot}$ at 20Mpc) may explain the discrepancy between the cosmic microwave background dipole and what is expected from the gravitational acceleration imparted on the Local Group by matter in the local universe (Erdogdu et al. 2006). Surveying the ZOA may solve this discrepancy.

While shallow H I surveys have uncovered a large, spiral galaxy at ~ 3 Mpc (Dwingeloo, Kraan-Korteweg et al. 1994), and more sensitive surveys have discovered

nearby dwarf galaxies (McIntyre et al. 2011, Massey et al. 2003, Begum et al. 2005), H I ZOA surveys have shown that there are no hidden galaxies within 1 Mpc with neutral hydrogen mass, M_{HI}, greater than $M_{HI} \sim 10^6$ $M_\odot$ in the southern sky (Henning et al. 2000) and $M_{HI} \sim 10^7$ $M_\odot$ in the northern sky (Henning et al. 1998). A nearby massive spiral (total mass $\sim 10^{12} M_\odot$) behind the Milky Way can now largely be ruled out as a way to recover the mass dipole vector. An unknown galaxy cluster (total mass $\sim 10^{15} M_\odot$) at 20 Mpc could still affect the mass dipole vector, however, because most of the northern sky is only starting to be surveyed deeply enough to detect a cluster at 20 Mpc (EBHIS; Kerp et al. 2011), and analysis of the full HIZOA survey in the southern sky is ongoing.

1.3.2 Large Scale Structure

The large scale structure (LSS) of the Universe is predominantly comprised of thin overdense filaments of galaxies surrounding large volumes of underdense voids. The size and scale of these features puts cosmological constraints on the early formation of structure in the Universe, and thus on how the Universe was formed (Kraan-Korteweg 2000). There have been many efforts made to map out large scale structure from redshift surveys at multiple wavelengths (e.g. CfA Redshift Survey; Huchra et al. 1983, 2dF Galaxy Redshift Survey; Colless et al. 2001, Sloan Digital Sky Survey; Abazajian, K., et al., 2003, 2MASS Redshift Survey; Huchra et al. 2012), but the Zone of Avoidance still obscures structure in a large part of the sky, limiting knowledge of the extent and distribution of structure across the plane of the Milky Way. Most efforts have resorted to predicting LSS in the ZOA by extrapolating from structure above and below the plane (e.g. Kolatt et al. 1995, Erdogdu et al. 2006). These density reconstruction maps may have incorrect assumptions about the distribution in the ZOA, creating nonexisting structure or misplacing predicted structure. Mapping galaxies in the ZOA with actual detections in redshift space is necessary to

minimize uncertainty in the distribution of LSS. An H I survey will provide a useful check on the validity of density reconstruction maps. Further, understanding the specific geometry of voids is a useful tool for constraining cosmological parameters (Lavaux 2010a). The shapes of voids behind the Milky Way must be recovered with ZOA observations in order to apply these constraints.

1.4 Neutral Hydrogen Observations

Hydrogen is the most abundant element in the universe. Neutral hydrogen spontaneously emits radiation at 21cm wavelength from the hyperfine transition between the electron spin up and spin down states. The difference in energy between these states is equivalent to the 21cm photon. This radiation is very rare, occuring 2.9×10^{-15} s^{-1}. Though the spontaneous emission of 21cm is very rare, hydrogen is so abundant that a galaxy like the Milky Way, which has $8\times10^{9}M_{\odot}$ of neutral hydrogen (Kalberla & Kerp 2009), will emit

$$\frac{(8\times10^{9}M_{\odot})(2\times10^{30}\mathrm{kg}/M_{\odot})}{1.6\times10^{-27}\mathrm{kg/H}}\ 2.9\times10^{-15}\mathrm{s}^{-1} = 3\times10^{52}\mathrm{21cmphotonspersecond.} \quad (1.1)$$

Using neutral hydrogen observations to survey the sky requires understanding what types of objects are being detected. H I gas is not abundant in every galaxy type. Figure 1.8 shows a distribution of parameters across the Hubble sequence of galaxy types (Roberts & Haynes 1994). H I is most abundant in late-type galaxies and nearly nonexistent in elliptical galaxies. H I mass is ten times more common in Sb- and Sc-type galaxies than in lenticulars and irregulars, but the log fraction of H I mass to total mass increases linearly from early to late-type galaxies. The H I mass to B-band luminosity ratio goes down significantly for dwarf and irregular galaxies. Dwarfs and irregulars have the same average H I content as lenticulars, but lenticulars are 10 times more luminous in B-band.

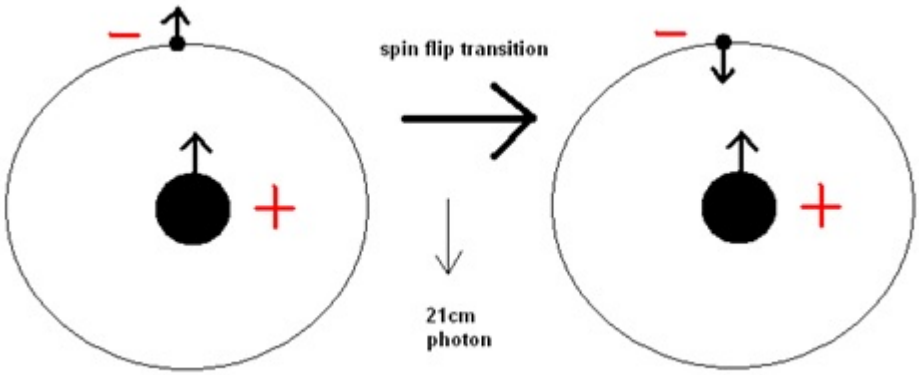

Figure 1.7 Illustration of the spontaneous radiation that causes hydrogen to emit at 21cm wavelength.

The spectral line profile of H I detections depends on the morphological type and orientation of the galaxy detected. Neutral hydrogen in spiral galaxies is located mostly in the galaxy's disk (Bosma 1978). Edge-on spiral galaxies will exhibit a distinctive double-horn profile shape in spectral line data, each horn corresponding with gas from the advancing or receding edge of the spiral disk. Most of the gas is rotating at the same velocity because of the flat rotation curve of a typical spiral galaxy. Observing the radial motion of this distribution from Earth produces the double-horn profile. Figure 1.9 shows an example of an edge-on spiral galaxy from the ALFA ZOA precursor survey.

A face-on spiral or a galaxy without disk-like structure (dwarfs, spheroidals) will produce a single peak with a generally Gaussian distribution in their spectral line profiles. The plurality of their H I is located at the systemic velocity of the galaxy and the profile is broadened by the velocity dispersion of the distribution. Galaxies with single peak profiles are easier to detect than double-horn profiles of the same integrated flux because they are concentrated over fewer channels, increasing the peak flux density.

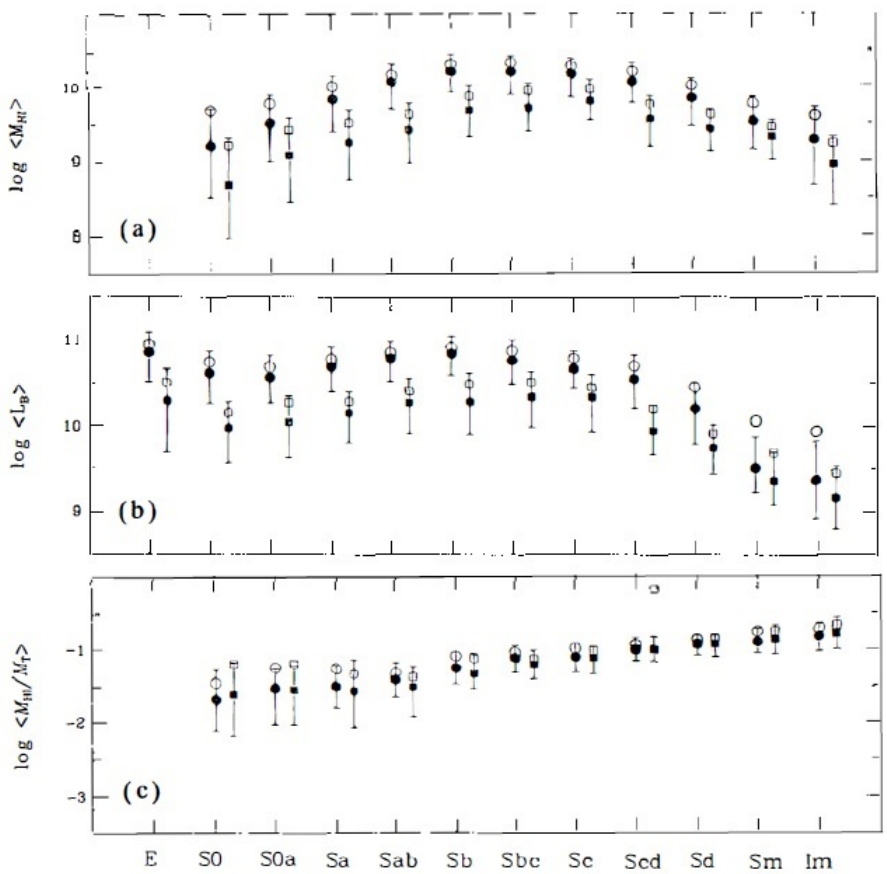

Figure 1.8 Global galaxy parameters per Hubble type. Filled symbols are medians; open ones are mean values. The lower bar is the 25th percentile; the upper the 75th percentile. (a) H I mass, (b)B-band luminosity, (c)H I mass fraction. All units are in $M_{\odot}$. Figure taken from Roberts & Haynes (1994).

1.5 The ALFA ZOA Survey

1.5.1 Telescope

The Arecibo Radio Telescope is a 305-meter (1000 ft) spherical fixed dish reflector with an altitude-azimuth receiver that is steerable within 20° of zenith ($\delta = +18°$). The telescope uses a modified Gregorian design, with both secondary and tertiary reflectors, to center the receiver room in the focal line above the dish. The sub-

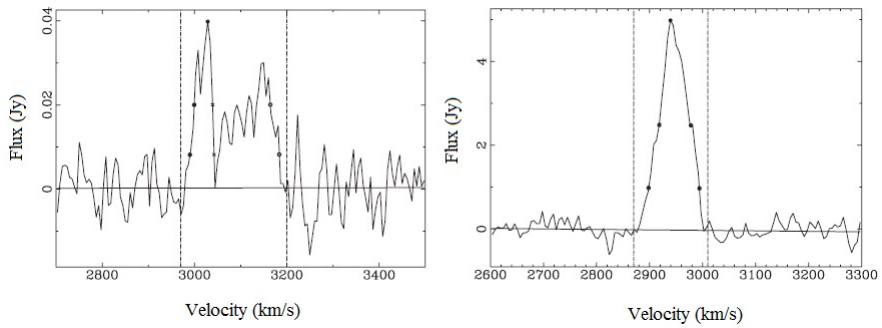

Figure 1.9 Examples of H I profiles from the ALFA ZOA Precursor survey (Henning et al. 2010). Left Panel. H I profile for an edge-on spiral galaxy. Right Panel. H I profile for a face-on spiral or galaxy without disk structure.

reflectors are specially shaped in order to correct for spherical aberration and so that the receiver can be positioned in the focal plane. The receiver room and sub-reflectors are situated on a platform that is suspended 150m over the telescope by 18 cables attached to three separate towers. The main dish is comprised of nearly 40,000 (1m $\times$ 2m) panels with an aggregate surface error $<$ 3mm (Goldsmith 2002), sensitive to frequencies up to 10 GHz. The dish is situated in a valley where the panels are supported several meters above the ground. A screen around the perimeter shields the receiver room from thermal emission and reflections from the surrounding mountains.

The telescope is steered by driving the receiver along an altitude arm that can rotate in azimuth. The receiver does not illuminate the entire area of the dish at once, rather it illuminates different areas across the dish as it is driven which changes the normal vector of the focal plane due to the optical nature of a spherical reflector. Changing the normal vector of the focal plane thus changes the direction of the telescope beam on the sky. Figure 1.10 shows a diagram of the telescope design.

Arecibo can observe sources with declinations $-2^\circ < \delta < +38^\circ$. The Milky Way crosses this declination range in two places, between Galactic longitudes $l = 30^\circ - 75^\circ$

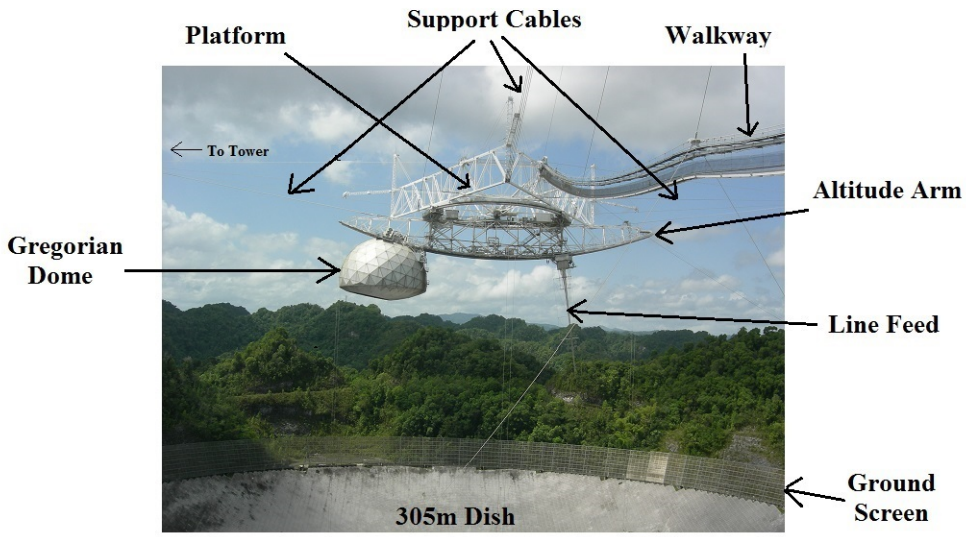

Figure 1.10 Diagram of the Arecibo Radio Telescope. The three support towers are located outside the picture. The line feed is a 430 MHz receiver and the Gregorian Dome contains all other receivers and the corrective reflectors. There are tie-downs not visible here that stabilize the platform. The structure can be accessed by the walkway or a lift not shown in the diagram.

in the inner Galaxy and $l = 170° - 215°$ in the outer Galaxy, as illustrated in Figure 1.11. Galactic longitude is defined to be $l = 0°$ towards the center of the Milky Way as viewed from Earth and $l = 180°$ towards the anticenter. Galactic latitude is defined to be $b = 0°$ along the plane of the Milky Way and $b = \pm 90°$ at the poles. The inner Galaxy region is looking towards the center of the Milky Way and the outer Galaxy region is looking away from the center.

1.5.2 Receiver

The ALFA receiver consists of seven independent beams with two orthogonal linear polarizations each, allowing the survey to cover area seven times faster than a single beam receiver. The center beam is surrounded by six outer beams in a hexagonal

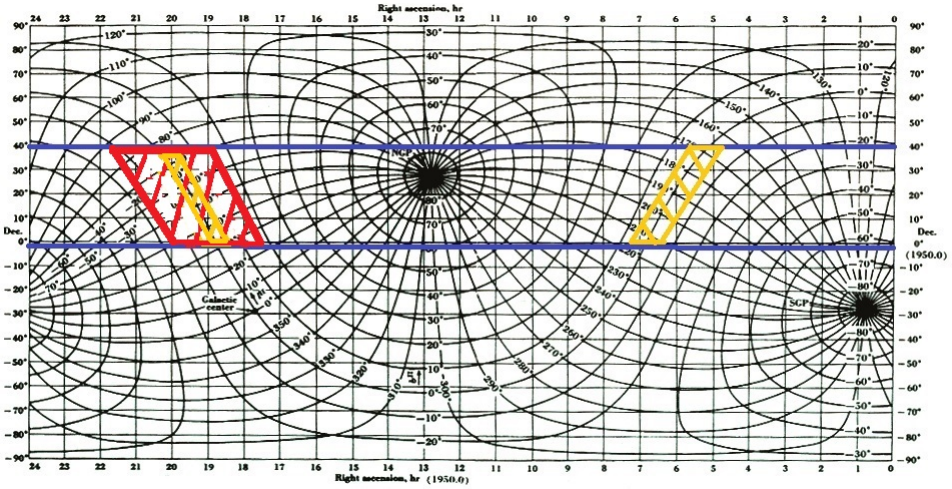

Figure 1.11 Coordinate map of the sky overlaying Galactic coordinates on top of the Equatorial coordinate system. Blue lines indicate the observable sky visible with Arecibo. The red box shows the Shallow Survey area and the orange boxes shows the Deep Survey area. Image modified from Kraus (1966).

pattern. The receiver covers frequencies 1 - 2 GHz and the FWHM at 1.4 GHz is approximately 3.4′ per beam. The gain of the seven ALFA beams ranges between 8.5 and 11 K Jy^{-1}, and the system temperatures range between 26 and 30 K. The footprint of the ALFA FWHM on the sky is illustrated in Figure 1.12.

1.5.3 Survey Overview

The ALFA ZOA survey is conducted in two phases: a shallow and a deep phase. The shallow phase (rms = 5 - 7 mJy at 9 - 20.6 km s^{-1} velocity resolution) covers about 1350 square degrees in the inner Galaxy ($30° < l < 75°$, $|b| < 15°$, $v < 11,000$ km s^{-1}). Within the Shallow Survey, there are two different observing schemes that correspond with significantly different sensitivities. The deep survey, five times more sensitive (rms = 1 at 9 km s^{-1} velocity resolution), will cover about 300 square degrees in both the inner ($30° \leq l \leq 75°; b \leq |2°|$) and outer ($175° \leq l \leq 207°; -2° \leq$

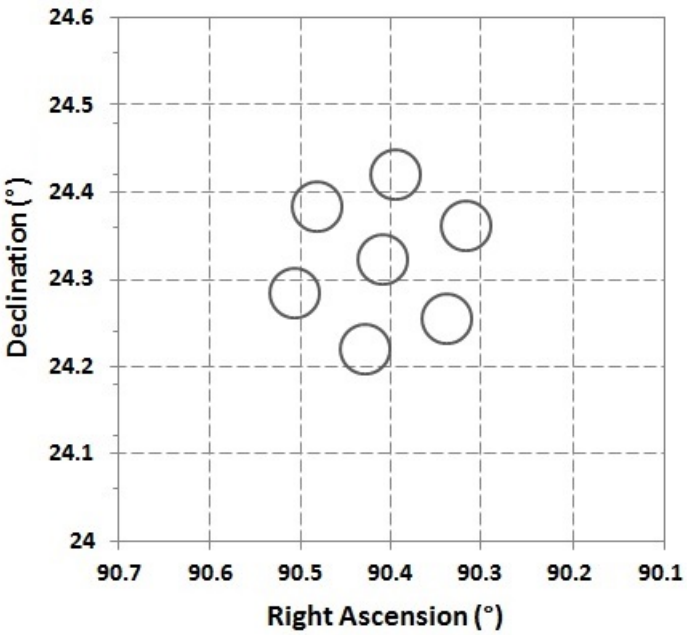

Figure 1.12 Footprint of the seven ALFA beams in equatorial coordinates. The receiver can be rotated. It is shown here rotated 19° on the sky.

$b \leq +1°$) Galaxy, out to 20,000 km s^{-1} redshift velocity. The survey is not centered on $b = |0°|$ in the outer Galaxy because it is centered on the Galactic plane, which is warped in that area. Figure 1.13 shows the areas covered by ALFA ZOA in comparison to the two previous large blind neutral hydrogen ZOA surveys. The Shallow Survey covers about the same total area as HIZOA and DOGS, though at fewer longitudes and larger latitudes. The deep survey covers about 25% as much area as the shallow survey.

The ALFA ZOA survey observes large scale structure across many areas and distances. In the inner Galaxy, the ALFA ZOA survey area intersects the Pegasus Cluster, C7, and Cξ overdensitites, using the naming scheme from the most comprehensive density reconstruction map (Erdogdu et al. 2006). It also probes the Aquarius, Corona Borealis, Delphinus, and Cygnus voids. In the outer Galaxy, the survey intersects known overdensities: the Orion Cluster, Abell 539, Abell 634, and

CIZA J0603.8+2939 as well as C1, C5, C10, C21, and C31. It also probes the Orion, Canis Major, and Lepus Voids. ALFA ZOA also discovers new structures if they are present.

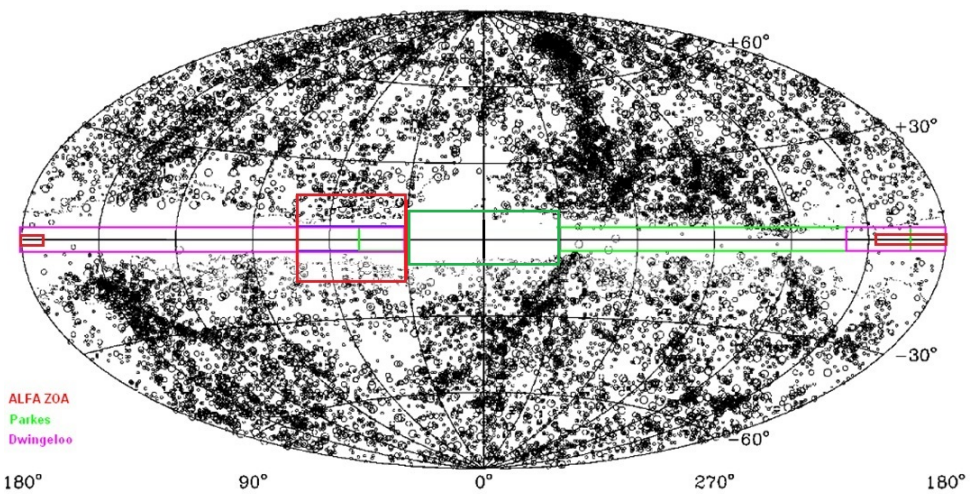

Figure 1.13 Survey areas in Galactic coordinates for the three largest 21cm ZOA surveys: ALFA ZOA (red), HIZOA (green), DOGS (pink), overlayed on a plot of optical galaxy detections with diameters greater than 1.3′. Image modified from Kraan-Korteweg & Lahav (2000).

1.6 Dissertation Outline

This dissertation is comprised of five chapters and an appendix. This chapter has been the introduction. Chapter 2 presents the first results of the ALFA ZOA Deep survey, including survey design, data reduction, source detection method, and survey performance. Chapter 3 presents the ALFA ZOA Shallow Survey, which has been searched to 90% and cataloged to 45%. The survey design, data reduction process, search method, selection function, H I mass function, and large scale structure results are discussed. Chapter 4 presents nearby galaxies discovered by the ALFA ZOA Shallow Survey and discusses their impact on the mass density dipole. Chapter

5 summary the ALFA ZOA survey and suggests useful future work. As of this defense, part of Chapter 4 has been published and Chapter 2 has been submitted for publication. The appendices list catalog tables, H I profiles, and data reduction code.

1.7 Acknowledgments

We acknowledge the usage of the HyperLeda database (leda.univ-lyon1.fr). This publication makes use of data products from the Wide-field Infrared Survey Explorer, which is a joint project of the University of California, Los Angeles, and the Jet Propulsion Laboratory/California Institute of Technology, funded by the National Aeronautics and Space Administration. This research has made use of the NASA/ IPAC Infrared Science Archive, which is operated by the Jet Propulsion Laboratory, California Institute of Technology, under contract with the National Aeronautics and Space Administration. We acknowledge the use of the Legacy Archive for Microwave Background Data Analysis (LAMBDA), part of the High Energy Astrophysics Science Archive Center (HEASARC). HEASARC/LAMBDA is a service of the Astrophysics Science Division at the NASA Goddard Space Flight Center. The authors would like to thank former UNM graduate student G. Vaive-Barron for contributing to source detection efforts. The Arecibo Observatory is operated by SRI International under a cooperative agreement with the National Science Foundation (AST-1100968), and in alliance with Ana G. Mendez-Universidad Metropolitana, and the Universities Space Research Association. This work was supported in part by the Cornell NAIC Predoctoral Fellowship and the NASA New Mexico Space Grant program. The National Radio Astronomy Observatory is a facility of the National Science Foundation operated under cooperative agreement by Associated Universities, Inc. This research has made use of the NASA/IPAC Extragalactic Database

(NED) which is operated by the Jet Propulsion Laboratory, California Institute of Technology, under contract with the National Aeronautics and Space Administration.

Chapter 2

ALFA ZOA Deep Survey: First Results

2.1 Introduction

The Arecibo L-Band Feed Array Zone of Avoidance (ALFA ZOA) Deep Survey is a blind neutral hydrogen (H I) survey for galaxies in the ZOA out to distances of 200 h^{-1} Mpc. The full survey will cover nearly 300 square degrees behind both the inner and outer Galaxy regions visible with the Arecibo Telescope, with a sensitivity of 1 mJy per beam (at 9 km s^{-1} velocity resolution). The sensitivity and depth of ALFA ZOA will probe large scale structure out to 200 h^{-1} Mpc in an area of sky that intersects with known overdensities: the Orion Cluster, Abell 539, Abell 634, and CIZA J0603.8+2939 as well as C1, C5, C10, C21, and C31 (Erdogdu et al. 2006). It will also probe the Orion, Canis Major, and Lepus Voids. The survey will detect H I to greater depth than recent, large H I surveys (ALFALFA $v < 20,000$ 9 km s^{-1}; Haynes et al. 2011, HIPASS; Zwaan et al. 2005), allowing ALFA ZOA to probe environments at farther distances. The low mass end of the H I mass function

(HIMF) has been shown by some studies to have a significantly steeper slope when measured at high sensitivity at distances outside the local Universe (Arecibo Galaxy Environment Survey "AGES" $v < 20,000$ 9 km s^{-1}; Davies et al. 2011, Arecibo Ultra Deep Survey "AUDS" $v < 50,000$ 9 km s^{-1}; Freudling et al. 2011). If confirmed, this could have a major impact on the amount of hydrogen gas available for ongoing star formation and galaxy evolution. ALFA ZOA Deep is similar in sensitivity to AGES and surveys 10^3 times more area than AUDS, putting it in a unique position to check the latest HIMF results as an unbiased, blind survey.

Recent results have shown that our knowledge of the bulk flow of peculiar velocities within 60 h^{-1} Mpc ($h = \mathrm{H}_0/100$, H_0 is the Hubble constant in km s^{-1} Mpc^{-1}) is complete enough to be constrained by cosmic variance and so no new galaxy discoveries within this distance will result in a significant correction to the dipole vector (Watkins et al. 2009). Asymmetry in large scale structure beyond 100 h^{-1} Mpc remains as a likely explanation (Lavaux et al. 2010), though even the most modern all sky redshift surveys retain a Zone of Avoidance at these distances (Huchra et al. 2012), forcing bulk motion studies to "fill in" the ZOA by cloning galaxies above and below the Plane (Lavaux & Hudson 2011). The ALFA ZOA Deep survey can detect large scale structure out to 200 h^{-1} Mpc, detecting galaxies at the volumes that may be contributing to the discrepancy between the cosmic microwave background dipole and the mass density dipole (Erdogdu et al. 2006), which drives the peculiar velocity of the Local Group.

This chapter describes the observation, data reduction, source detection, and parameterization techniques for the ALFA ZOA Deep Survey. It presents a catalog of the first results of the survey, coming from a 15 square degree region, and uses these results to analyze survey performance. Section 2.2 describes the observation technique of the survey. Section 2.3 discusses the data reduction process. Section 2.4 describes the survey search method and source parameterization. Section 2.5

presents the first results catalog. Section 2.6 discusses survey accuracy, sensitivity, and effectiveness. Section 2.7 discusses large scale structure uncovered by the survey. Section 2.8 is the conclusion.

2.2 Survey Design

2.2.1 Backend

The telescope and receiver used by the ALFA ZOA Deep survey are described in Chapter 1. Observations are recorded in one-second integrations using the Mock Spectrometer, which performs an "on the fly" Fast Fourier Transform each time the voltage is sampled. The digital spectrometer covers 300 MHz from 1225 MHz to 1525 MHz using two overlapping 172 MHz sub-bands centered on 1300 MHz and 1450 MHz. The sub-bands overlap between 1364 MHz and 1386 MHz so that there is no loss of sensitivity due to roll off at the edges of the bandpass. Each sub-band is divided into 8192 channels, producing a spectral resolution of 21 kHz. This equates to a velocity resolution of ~ 4.5 km s^{-1} for neutral hydrogen emission.

2.2.2 Observations

The ALFA ZOA Deep survey covers nearly 300 square degrees through both the inner ($30^\circ \leq l \leq 75^\circ; b \leq |2^\circ|$) and outer ($175^\circ \leq l \leq 207^\circ; -2^\circ \leq b \leq +1^\circ$) Galaxy. ALFA ZOA takes data simultaneously with a survey for pulsars in the Milky Way (PALFA; e.g. Cordes et al. 2006) and a Galactic radio recombination line survey (SIGGMA; Liu et al. 2013), as well as several SETI groups that receive data from the ALFA receiver (Astropulse; Von Korff et al. 2013, SETI@home; Anderson et al. 2002, Serendip V.v; Cobb et al. 2000). In particular, the first fast radio burst

detected with an instrument other than the 13-beam receiver of the Parkes Radio Telescope (Spitler et al. 2014) was discovered by PALFA using the same data taken by ALFA ZOA for this paper.

Observations in the outer Galaxy are controlled by ALFA ZOA, and the inner Galaxy is controlled by PALFA. The setup of observations is slightly different between the inner and outer regions and this is discussed in the next section. The first results presented in this paper come from a completely surveyed, 15 square degree area in the outer Galaxy centered on $l = 192°$ and $b = -2°$. The area was chosen to intersect large scale structure predicted from known structure above and below the Galactic Plane. The dimensions are $330' \times 164'$, ranging across right ascensions 05:55:30 to 06:18:20 and declinations +14:30:00 to +17:12:00. The first results area extends below $b = -2°$ because it was observed before the full survey area was constrained to be within $2° \leq b \leq +1°$. Observations were conducted from December 2010 to March 2012. Figure 2.1 shows a map of the survey area in the outer Galaxy including pointings that have been observed so far.

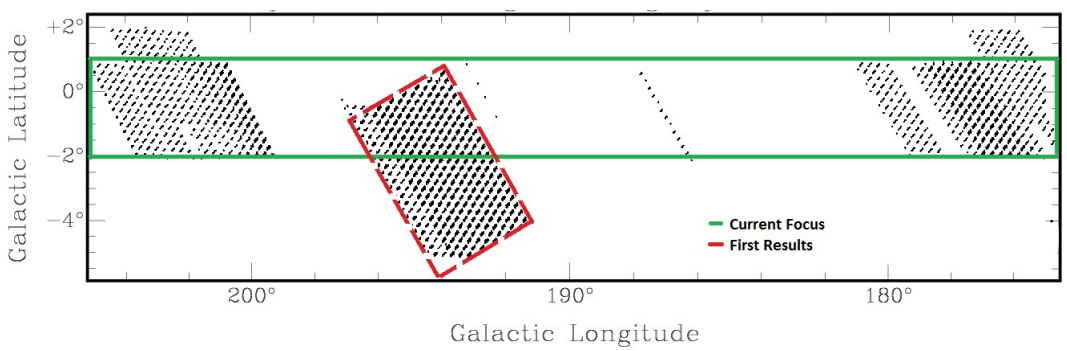

Figure 2.1 Sky coverage of the survey in the Outer Galaxy in Galactic coordinates. Each black dot is a central beam pointing. The area inside the dashed, red box is the focus of the First Results Catalog. The area inside the solid, green box is the focus for the full survey.

2.2.3 Tiling Pattern

Commensal observations are an incredibly efficient use of telescope time (e.g. five other projects listed above take data simultaneously with ALFA ZOA) but require compromises between commensal partners. While drift scans have been shown to produce superior baselines for spectral line surveys (Briggs et al. 1997), the ALFA ZOA Deep Survey is constrained to tracking single pointings due to commensal obligations. One method to bandpass correct a single pointing is self-subtraction of a bandpass by its median filter, though this was shown to be inadequate for use as a data reduction procedure in a blind H I galaxy survey (McIntyre 2013a). As such, the survey uses the position switching method for bandpass correction, a non-standard observing mode for extragalactic ALFA surveys, requiring ALFA ZOA Deep to observe position switched pairs and develop unique software for data reduction. Position switching uses a total power on-off technique to remove the bandpass from a source (ON) by subtracting the bandpass from a position off-source (OFF). For a blind survey, ON and OFF observations are interchangeable, explained in further detail in Section 2.3. ALFA ZOA uses the geometry of the ALFA pattern to generate a list of pointings that most efficiently covers the survey area and is designed so that several different pointings can be tracked over the same path of alt-az coordinates in order to produce flat baselines.

The survey tiling pattern is made from clusters of three beam patterns, the centers of which are separated by one FWHM along an axis tilted 19° from north-south, as shown in Figure 2.2. Clusters fully cover their area and fit into surrounding clusters in order to fill in the survey area without Nyquist sampling. The axis of the ALFA receiver is rotated counter-clockwise, 19° from north-south, so that adjacent clusters to the east and west are centered on the same declination roughly 60 seconds of right ascension apart. This allows the survey to integrate one pointing for 270 seconds, for instance, and have time to slew to another pointing 300 seconds of right ascension

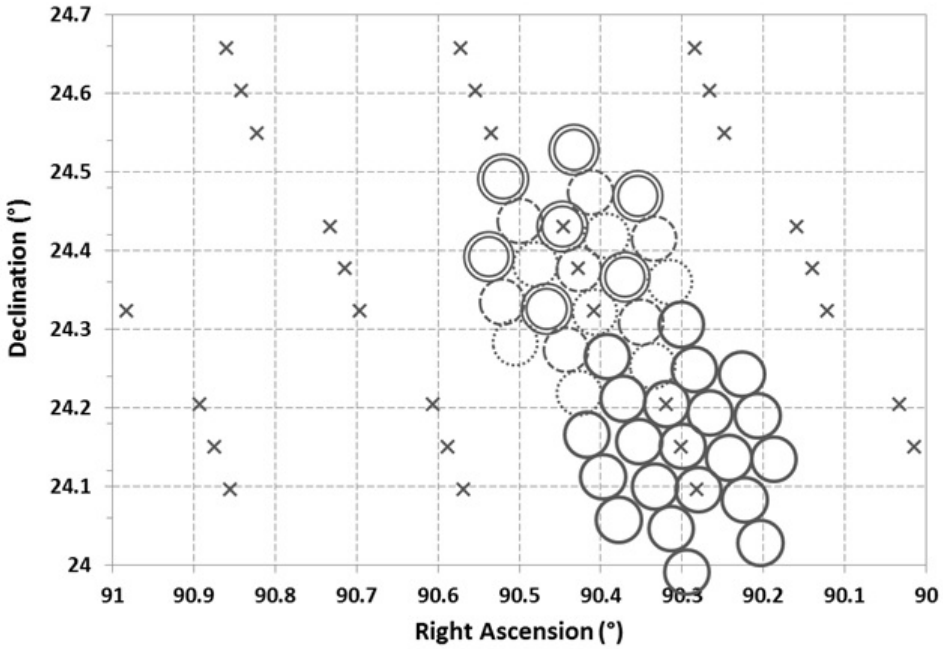

Figure 2.2 Tiling pattern used by the ALFA ZOA Deep Survey shown for a small region of sky. Clusters of three pointings fully cover their area and fit into surrounding clusters. The seven beams of the ALFA pattern are included for two of the clusters to demonstrate how the geometry of the ALFA beams is used to cover the survey area. One cluster shows the beams coded separately for the three different pointings.

away so that it can then track over the same alt-az path (i.e. create an ON-OFF pair). Every two observations must be observed in pairs in this way in order to apply bandpass correction, and the full survey area is filled out by leapfrogging through this tiling pattern.

The observing setup is slightly different between the inner and outer Galaxy regions because of commensal obligations. In the inner Galaxy, each pointing is integrated for 270 seconds on sky and then 6 seconds on the ALFA high flux noise diode for calibration. A single ALFA beam pattern covers a 60 square arcminute area, and about 10 pointings can be observed in an hour. At this rate, the survey covers approximately 10 square degrees per 60 hours of telescope time, though the

area is not covered at the Nyquist sampling rate, so it is covered exactly like the tiling pattern shown in Figure 2.2. A lack of Nyquist sampling results in a greater positional error and H I mass values not fully recovered.

Outer Galaxy observations are taken for 180 second integrations and 6 seconds on the high flux noise diode. Each pointing has two Nyquist counterparts, each 1/2 FWHM away on either side, perpendicular to the axis of the three pointing cluster. That is, the outer galaxy area is covered with three times as many pointings shown in the tiling pattern in Figure 2.2. The effective integration time for each spatial position is the same as in the inner Galaxy. However, the survey coverage rate is slower by a factor of two because three 180 second integrations are taken in the outer Galaxy for every one 270 second integration taken in the inner Galaxy. Surveying an area that is Nyquist sampled allows the integrated flux of a detection to be fully recovered.

2.3 Data Reduction

2.3.1 Process

The ALFA ZOA Deep Survey developed unique software for data reduction in the IDL programming language because of the total power on-off observing technique. Data reduction code is displayed in Appendix A. Data is taken in one-second integrations in order to reduce data size and limit the effect of beam smearing. Each one-second integration of a telescope pointing needs to be identified with its off-source counterpart, within a small angular separation, $\delta\theta$, where,

$$\delta\theta^2 = \Delta\phi^2 + \Delta\theta^2, \tag{2.1}$$

$$\delta\theta = \sqrt{[\phi_{ON}\ cos(\theta_{ON}) - \phi_{OFF}\ cos(\theta_{OFF})]^2 + (\theta_{ON} - \theta_{OFF})^2}, \tag{2.2}$$

where ϕ and θ are the azimuth and altitude coordinates in radians, respectively, of the integrations on-source (ON) and off-source (OFF). Though ALFA ZOA does not know a priori which pointings will detect a source, it must treat each pointing as a possible ON. The smallest $\delta\theta$ for each ON integration is used to create a reduced bandpass by,

$$REDUCED(j) = (ON(j) - OFF(j))/(OFF(j)/MEDOFF), \tag{2.3}$$

where j is channel number and MEDOFF is the median value of the OFF spectrum over all channels. The subtracted bandpass is divided by the normalized value, OFF(j)/MEDOFF, to correct for bandpass response per frequency.

In an effort to define an upper limit for $\delta\theta$, several observations were taken during June 2010 to test the effect of ON-OFF alt-az positional difference on the quality of spectral baselines. The results from this test show that the upper limit is $\delta\theta_{lim} = 1.7'$ (McIntyre 2013b), or 1/2 FWHM. If a one-second integration does not have an off-source integration within $\delta\theta_{lim}$, then it is rejected. For an ON that has at least one OFF within $\delta\theta_{lim}$, then the OFF with the smallest $\delta\theta$ for each ON integration is used to create a reduced bandpass, (ON-OFF)/OFF. This is divided by the median of the OFF bandpass for normalization. All the reduced spectra from one pointing (maximum 270 in the inner Galaxy, 180 in the outer) are median-combined to reject spurious RFI and recover the total integration time of the pointing. Most ON-OFF pairs have integrations rejected due to separation larger than $\delta\theta_{lim}$, though it is very rare to have more than 20 integrations rejected. The noise diode from the OFF is used to calibrate from receiver units into temperature, and the gain, G(beam, ZA, polarization), converts temperature into janskys. The frequency is resampled with a linear interpolation from topocentric to barycentric and converted relativistically into heliocentric velocity using the optical velocity convention. The two polarizations are averaged and the spectrum is Hanning smoothed, which mitigates ringing effects and lowers noise by a factor of $\sqrt{2}$, but worsens spectral resolution by a factor of

two.

The final, reduced spectrum for a 270 second integration has a noise level of 1 mJy per channel at a velocity resolution of 9 km s^{-1}. The velocity range of the high frequency sub-band is cut to heliocentric velocities, v_{hel} = -2,000 km s^{-1} to 12,000 km s^{-1} and a third order polynomial baseline is auto-fitted and subtracted over this spectrum to remove continuum emission and large bandwidth features. The low frequency sub-band is cut to a velocity range of v_{hel} = 10,000 km s^{-1} to 21,000 km s^{-1} and also fit by a third order polynomial. The bandpass at velocities beyond 21,000 km s^{-1} contains a significant amount of RFI and has not been incorporated into the survey at this point. The reduced spectra are then made into data cubes of right ascension, declination, and velocity by the program Gridzilla (Barnes et al. 2001).

Gridzilla is part of the AIPS++ software package, and is used to create a data cube by spatially gridding spectra. For ALFA ZOA Deep, Gridzilla is set to clip spectra between -50 mJy and 500 mJy, and make a cube containing $1' \times 1'$ pixels. Each input spectrum is assigned to all pixels within a $4'$ diameter of the spectrum's coordinates using a Top-Hat kernel. In pixels where multiple spectra contribute they are median-combined, weighted by the angular distance of the pixel from each spectrum's original coordinates using a beam power pattern with FWHM = $3.4'$. The end result is a 3-dimensional data structure with axes of right ascension, declination, and heliocentric velocity. Position-velocity planes can be iteratively viewed to search for galaxy detections.

2.4 Search Method and Source Parameterization

The data cube is searched for detections by visually inspecting over the usable velocity range using the visualization tool, Karma KVIS (Gooch 1996). This is done by

examining image planes in position-velocity slices and using a greyscale to represent flux intensity. The data cube is examined by three independent searchers (two authors and a UNM graduate student in the case of this First Results paper), who look for profile shapes consistent with known galaxies, e.g. Gaussian, double-horn, etc. Lists of galaxy candidates are prepared independently by each searcher. These lists are compared with the astronomical coordinate comparison tool, Starlink TOPCAT (Tool for OPerations on Catalogues and Tables) version 3.9 (Taylor 2005), in order to match sources with RA, Dec, and velocity coordinates within tolerances of $5'$, $5'$, and 300 km s^{-1}, respectively. The matched lists are adjudicated by a separate author who re-examines the position of each candidate source and either accepts it into the catalog or rejects it as a false detection. These adjudicated sources are adopted into a working catalog and each source is parameterized using MBSPECT in the software package, MIRIAD (Sault et al. 1995).

For unresolved sources, a spectral profile is created from the weighted emission inside a $5'$ x $5'$ box surrounding the position of the source. The emission is weighted by spatially fitting a Gaussian to a moment 0 map integrated over a user-defined range of velocities, and a profile is created as shown in Figure 2.3. In an iterative process, the profile shape is visually inspected and a new velocity range is chosen for the profile (shown as the vertical dotted lines in Figure 2.3). The profile window is also used to create a mask for autofitting a polynomial to the baseline within 2000 km s^{-1} of the profile, usually to first order but up to fourth order in rare cases. This fit is used to remove any features in the baseline around the source. The integrated flux, F_{HI}, is computed by subtracting the polynomial fit and integrating the flux inside the profile window. The open circles on the outer edges of the profile in Figure 2.3 represent the velocity widths, W_{50} and W_{20}, at 50% and 20% peak flux, respectively. The closed circle at the top is the location of the peak flux. The central heliocentric velocity, v_{hel}, is taken as the midpoint of the W_{50} value.

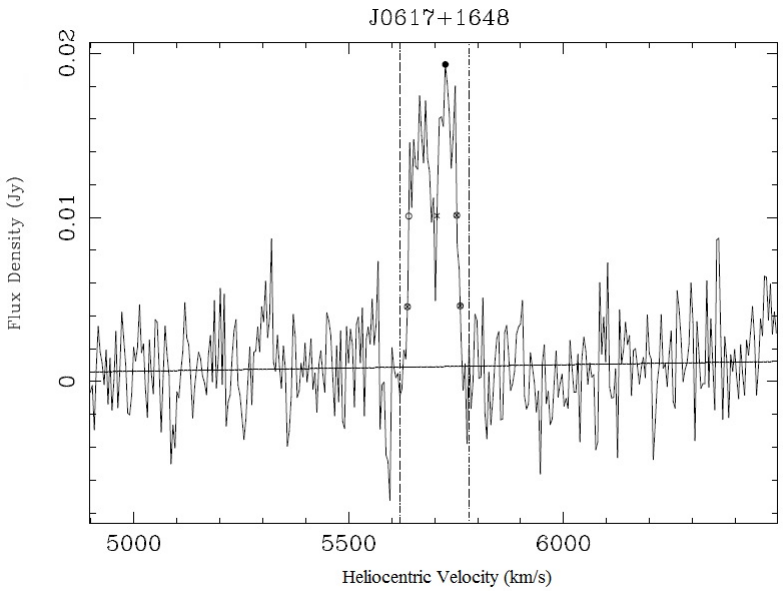

Figure 2.3 H I profile of ALFA ZOA J0617+1648, created from MIRIAD output. The vertical dotted lines are user defined and create a profile window that source parameters are extracted from. The open circles on the outer edges of the detection represent the W_{20} and W_{50} velocity widths, and the closed circle at the top is the location of the peak flux.

All sources go through the MIRIAD parameterization process as unresolved, but then are re-examined to determine the existence of sources with extended emission. A first list of potentially extended sources is constructed from the size of the Gaussian fit for each source as output by MBSPECT. All sources with major axes greater than $3.4'$ make a candidate list of extended sources. Moment 0 maps are then created for each candidate using the MIRIAD task, MOMENT. These maps are inspected visually using Karma KPVSLICE (Gooch 1996) and a spatial profile for each source is created by integrating flux across a user-defined major axis. These spatial profiles are saved as an array and fed into the IDL program GAUSSFIT, which computes a non-linear least-squares Gaussian fit. From this fit, the FWHM of the source is determined.

Every source with FWHM $> 3.4'$ makes it into a shorter candidate list and all of

these are re-examined again using KPVSLICE in order to determine an individual aperture size to use for each galaxy. KPVSLICE shows the velocity spectrum from the data cube that corresponds with each spatial pixel in the moment map. The user counts how many single spatial pixels contain a clear detection in the velocity spectrum, and decides on a corresponding aperture box height and width. These new box sizes are then used to re-determine source parameterization using MIRIAD, where spectral profiles are created by summing flux over all channels and pixels inside the aperture and within the profile window and then beam corrected. The position of the source is determined from the center pixel of the aperture, as opposed to the center of a Gaussian fit, but all other source parameterization techniques are the same as for unresolved sources. The rms of resolved sources is higher than for unresolved sources because of the greater number of pixels summed over. For example, a moment map for resolved source, ALFA ZOA J0602+1452, is shown in Figure 2.4. The box size of the aperture used is $23' \times 23'$ (RA x Dec).

2.5 The ALFA ZOA Deep Survey: First Results Catalog

The ALFA ZOA Deep Survey: First Results catalog contains 61 galaxies. Profiles are shown in Figure 2.5. Several parameters for the sources in the catalog can be seen in Table C1 in Appendix C as the table is too wide to be placed here. Table C1 presents the following information on the catalog:

Column (1). ALFA ZOA source name. Sources with extended emission are labeled with the 'e' superscript.

Column (2). Right Ascension of the fitted position in hours, minutes, seconds, J2000 epoch.

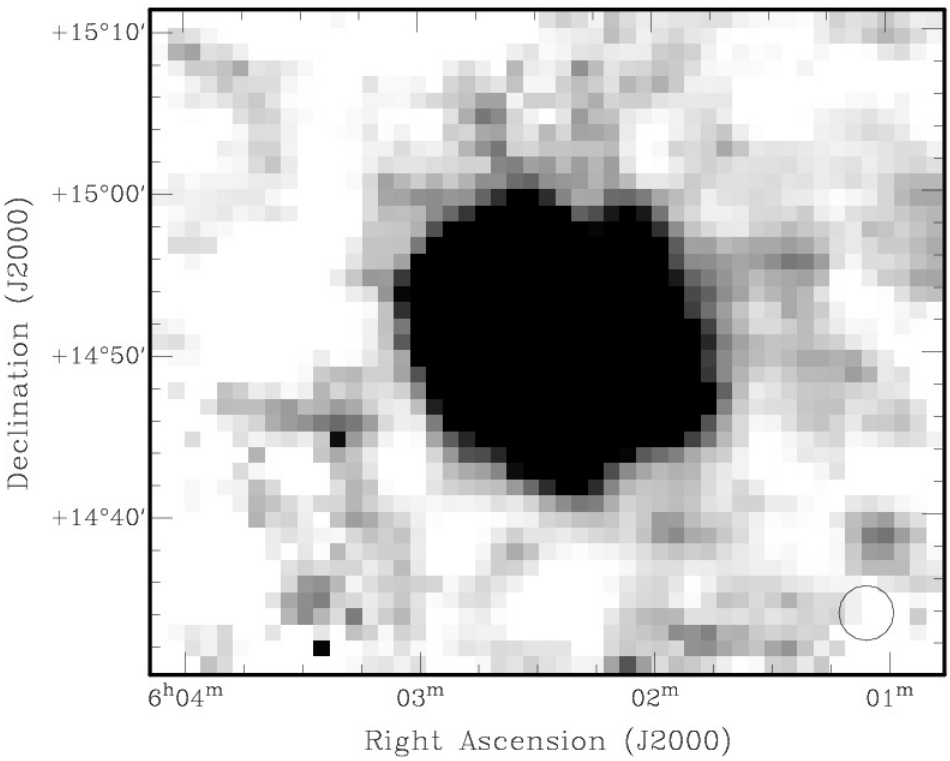

Figure 2.4 Moment map of ALFA ZOA J0602+1452. Beam size (FWHM = 3.4′) is shown in bottom right corner. A clear extension beyond $5' \times 5'$ can be seen on this resolved source.

Column (3). Declination of the fitted position in degrees, arcminutes, arcseconds, J2000 epoch.

Columns (4) and (5). l and b, Galactic longitude and latitude in degrees, respectively, of the fitted position in degrees.

Column (6). F_{HI}, integrated flux in Jy km s^{-1}.

Column (7). v_{hel}, heliocentric velocity in km s^{-1}.

Columns (8) and (9). W_{50} and W_{20}, velocity width in km s^{-1} of the profile at 50% and 20% of the peak flux level, respectively.

Column (10). D_{LG}, distance to the galaxy in Mpc in the Local Group refer-

ence frame (Courteau & van den Bergh 1999), using Hubble's Law for cosmological redshift distance and taking $H_0 = 70$ km s^{-1} Mpc^{-1}.

Column (11). Log M_{HI}, logarithm of the total H I mass in $M_\odot$ calculated from,

$$M_{HI} = 2.36 \times 10^5 \, D_{LG}^2 \, F_{HI}, \tag{2.4}$$

where D_{LG} is the distance to the galaxy and F_{HI} is the integrated flux as described above.

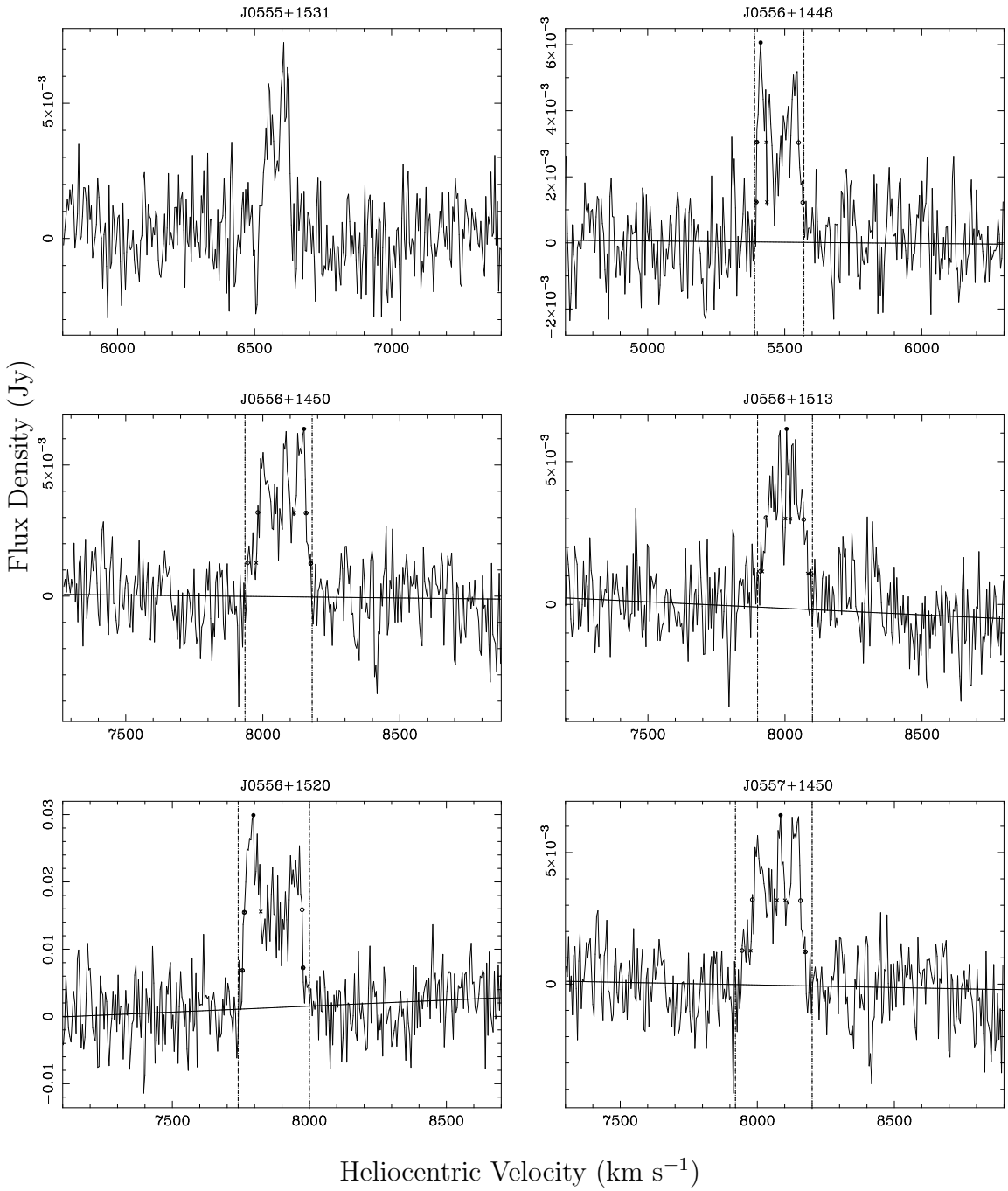

Figure 2.5 H I profiles of ALFA ZOA detections. The description of the profiles is the same as in Figure 2.3.

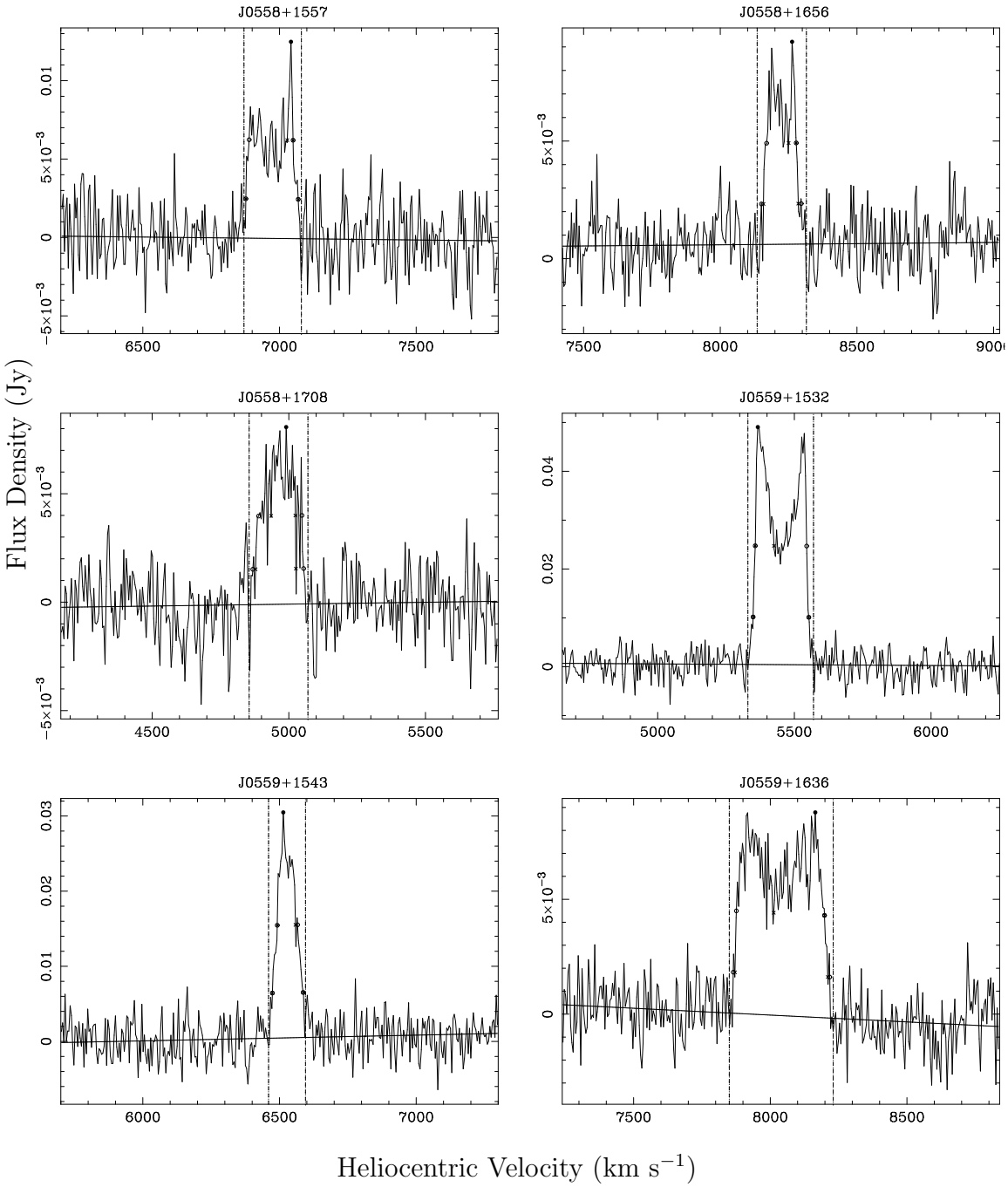

Figure 2.5 (continued)

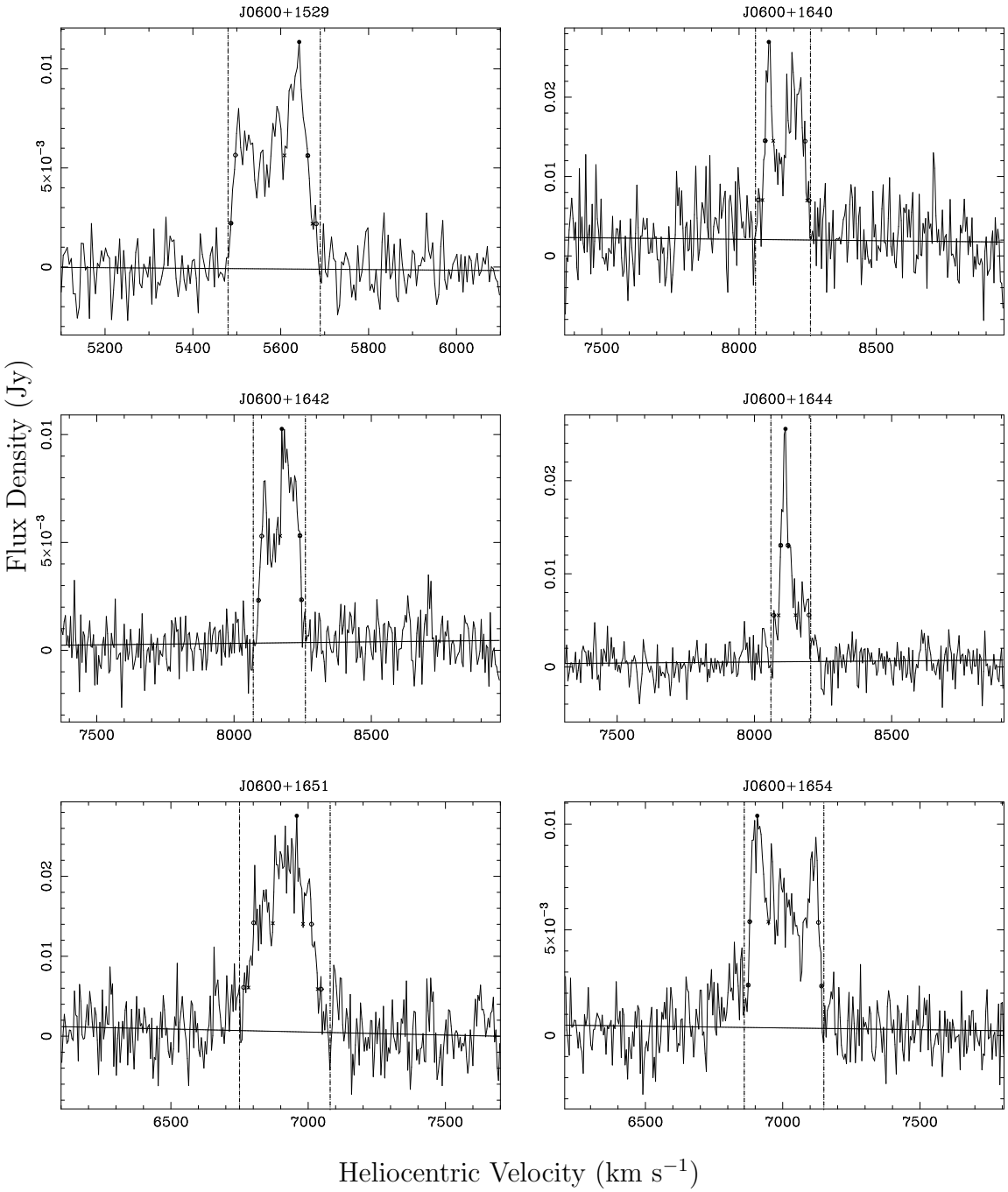

Figure 2.5 (continued)

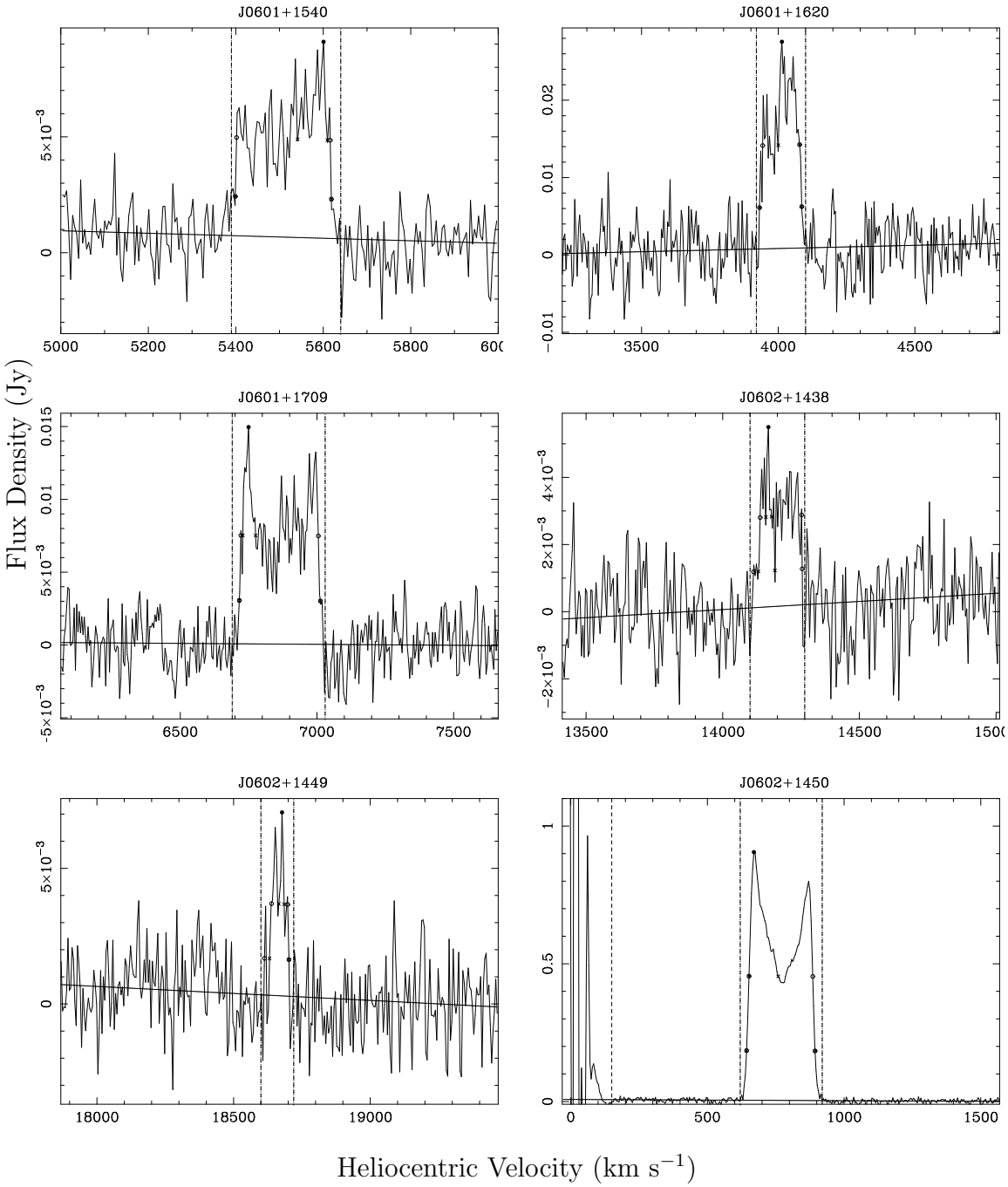

Figure 2.5 (continued)

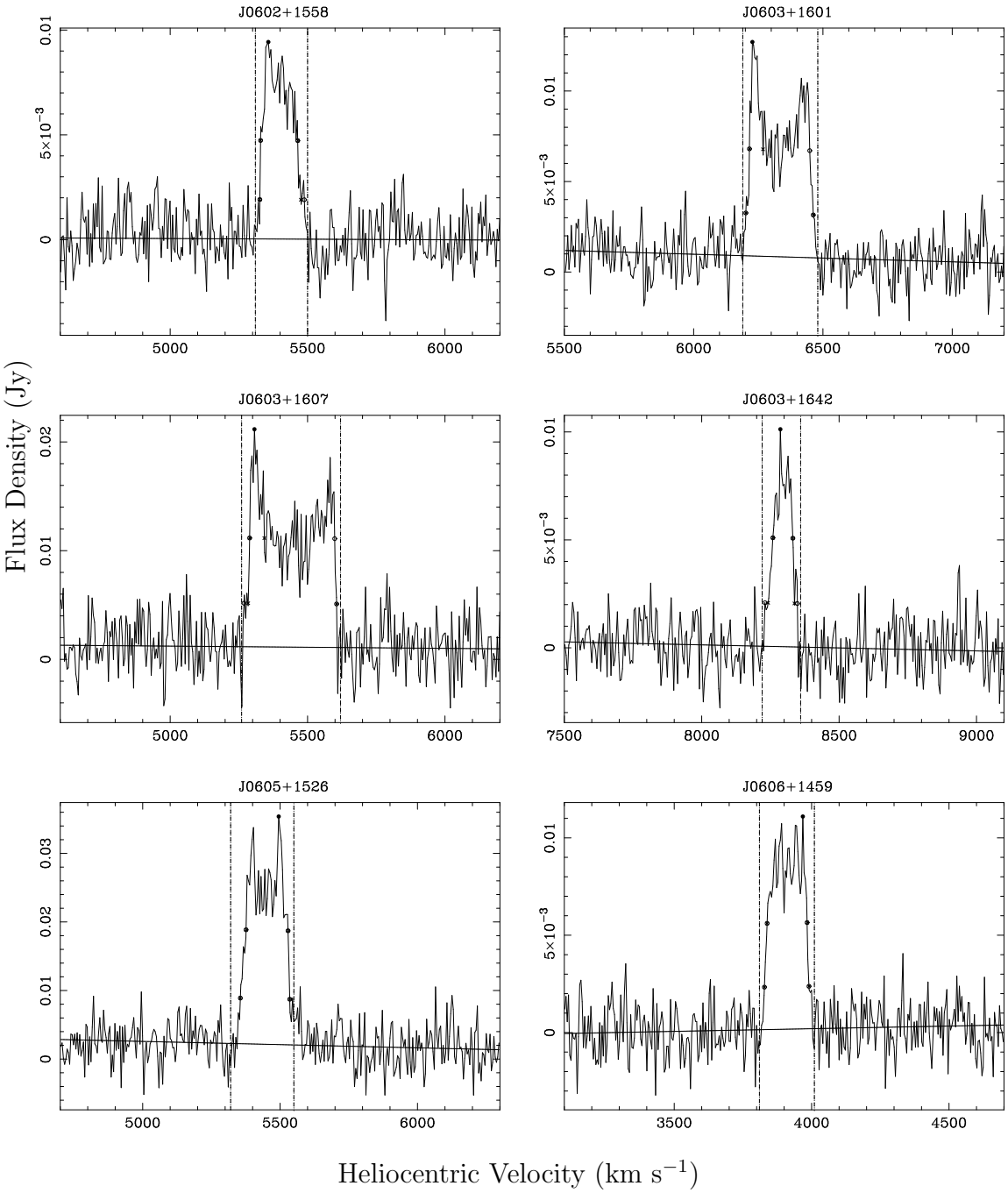

Figure 2.5 (continued)

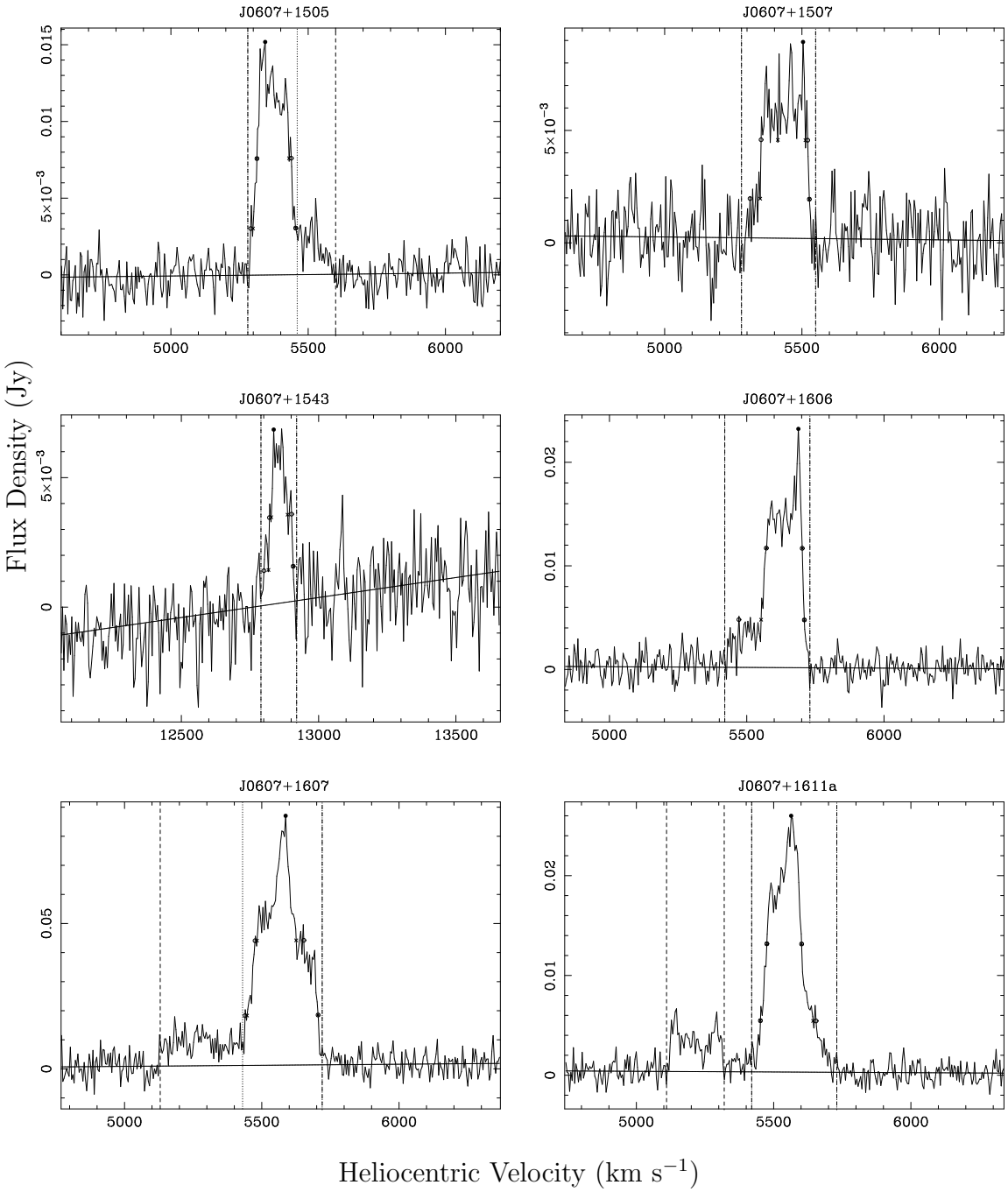

Figure 2.5 (continued)

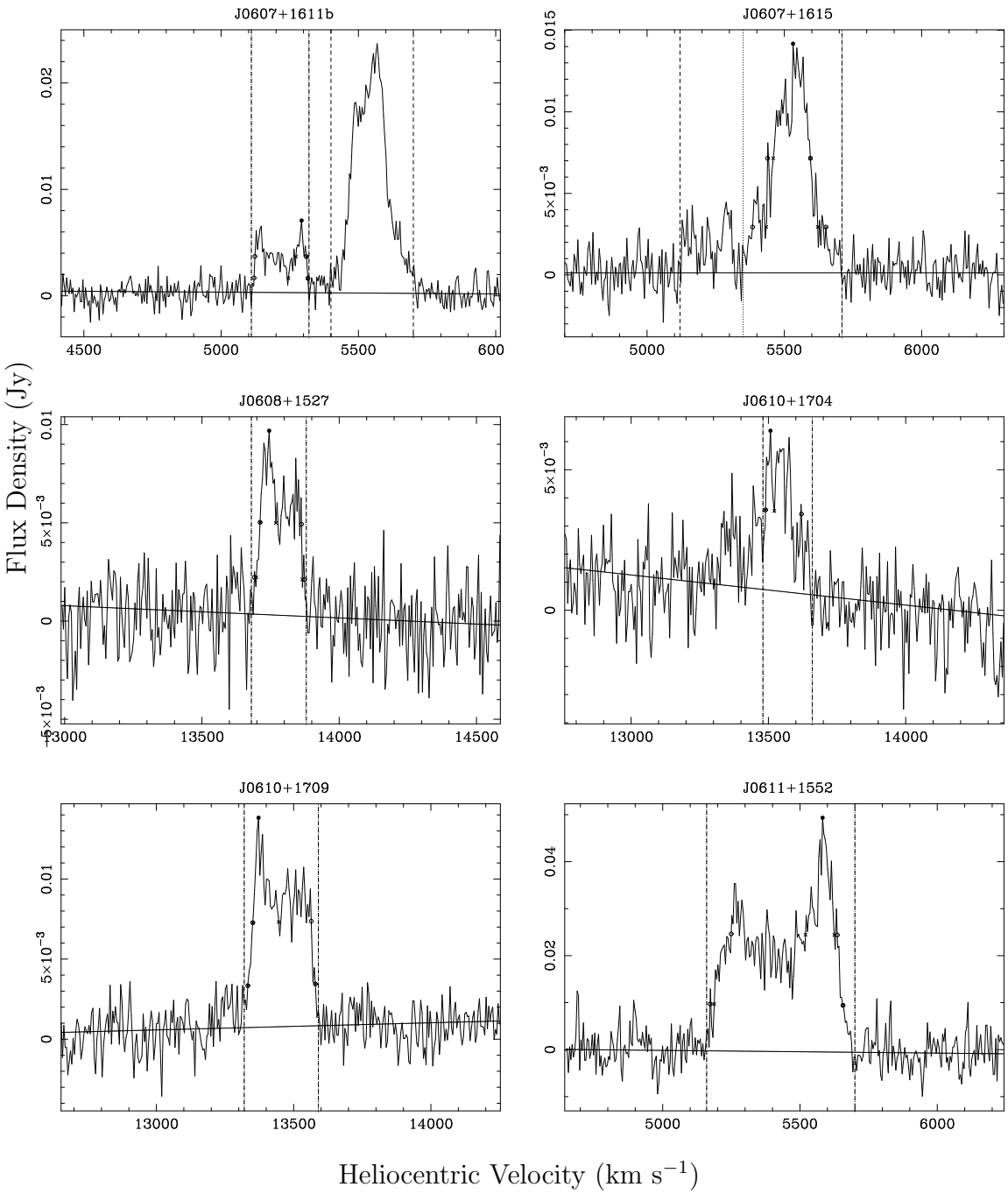

Figure 2.5 (continued)

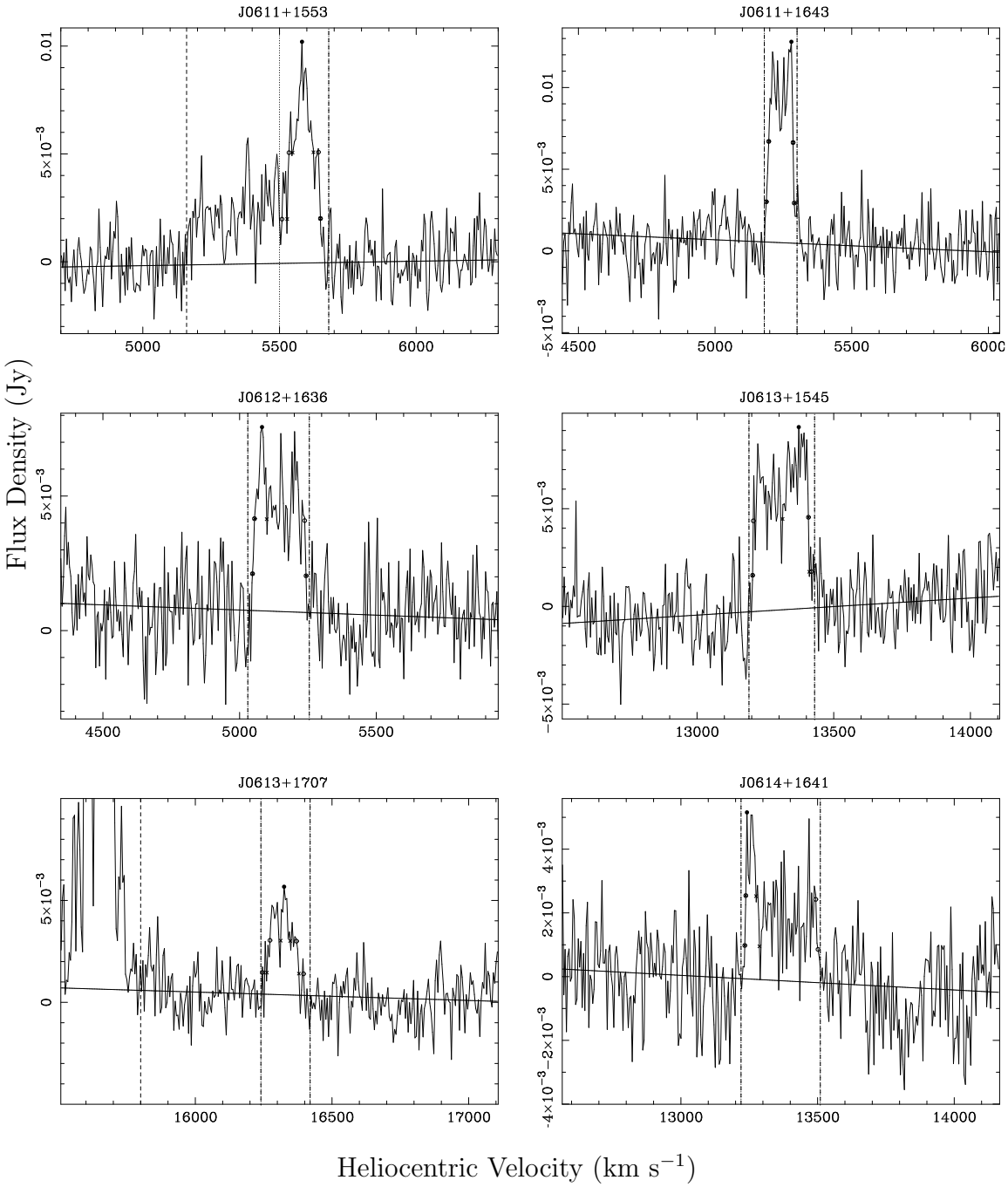

Figure 2.5 (continued)

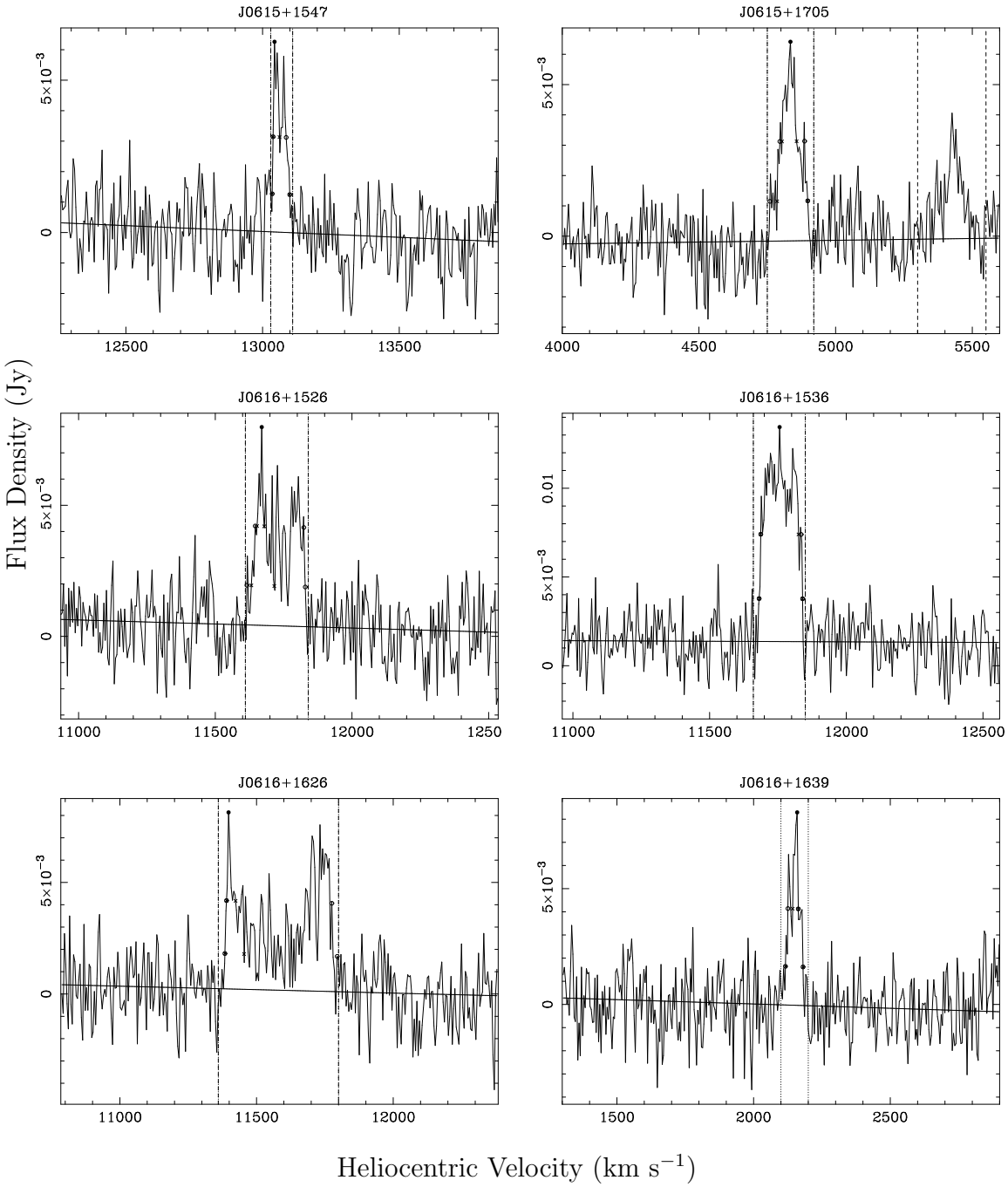

Figure 2.5 (continued)

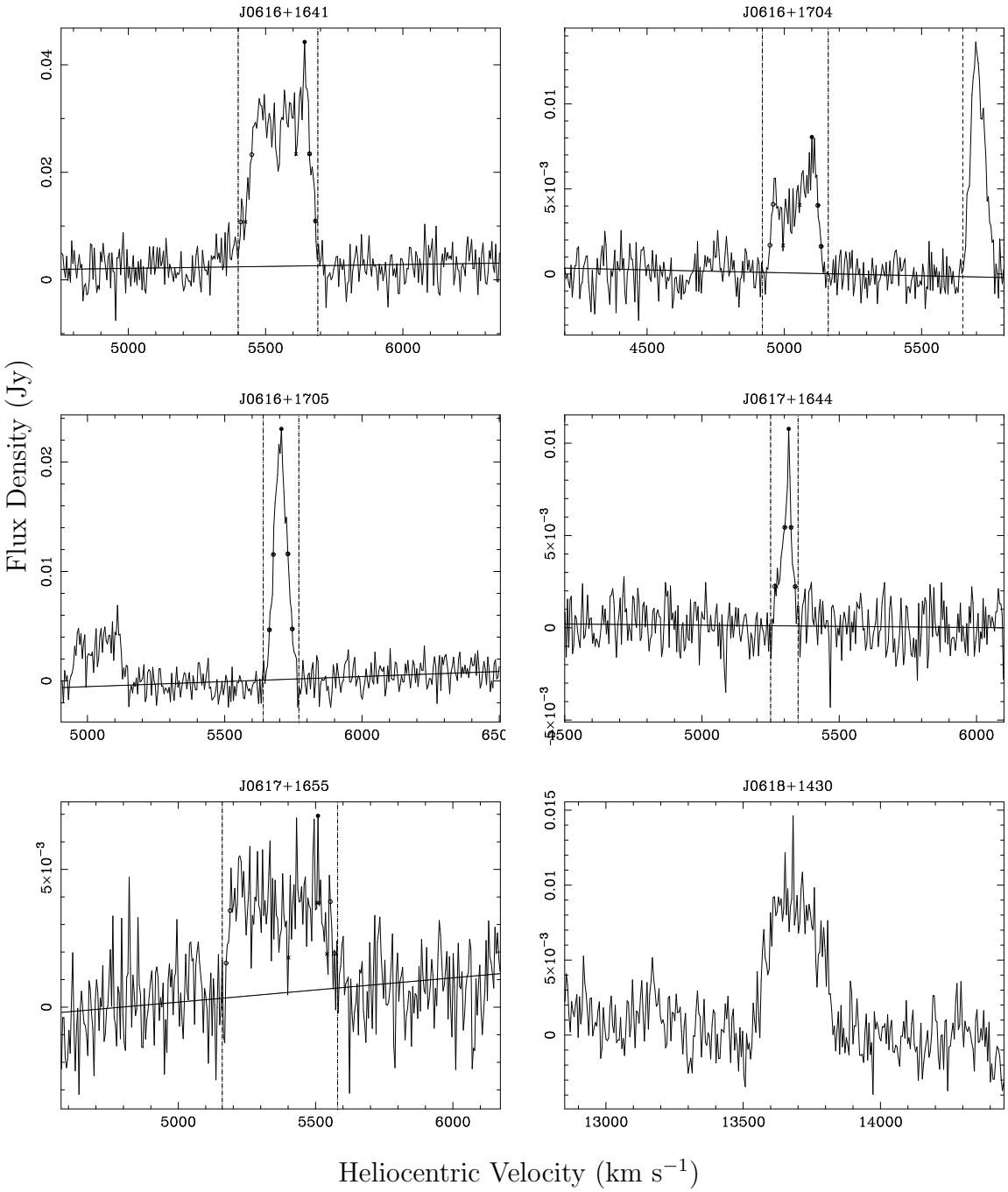

Figure 2.5 (continued)

The uncertainties on F_{HI}, v_{hel}, W_{50}, and W_{20} were calculated in the same way as Koribalski et al. (2004). The uncertainty of integrated flux is

$$\sigma(F_{HI}) = 4(S/N)^{-1} \, (Sp \, F_{HI} \, \delta v)^{1/2}, \tag{2.5}$$

where Sp is the peak flux, S/N is the signal-to-noise ratio Sp to $\sigma(Sp)$, F_{HI} is the integrated flux, and δv is the velocity resolution of the data, 9 km s^{-1}. The integrated flux uncertainty is modified from calculating the error under the curve of a Gaussian function as demonstrated by Fouque et al. (1990). $\sigma(Sp)$ is the error in the peak flux

$$\sigma(Sp)^2 = rms^2 + (0.05 \, Sp)^2. \tag{2.6}$$

$\sigma(Sp)$ increases with peak flux density, estimated by Koribalski et al. (2004) to be 5%. The uncertainty in the heliocentric velocity is

$$\sigma(v_{hel}) = 4 \, (S/N)^{-1} \, (P \, \delta v)^{1/2}, \tag{2.7}$$

where

$$P = 0.5 \, (W_{20} - W_{50}) \tag{2.8}$$

is a measure of the steepness of the profile edges. The uncertainties in the velocity widths are given by

$$\sigma(W_{20}) = 3 \, \sigma(v_{hel}), \tag{2.9}$$

$$\sigma(W_{50}) = 2 \, \sigma(v_{hel}). \tag{2.10}$$

The uncertainties on D_{LG} and M_{HI} are not calculated as those values rely heavily on cosmological assumptions as opposed to measurement uncertainty.

Two sources are located on the edge of the cube, J0555+1531 and J0618+1430, and so their flux could not be completely recovered. Their positions are listed in the

catalog followed by a semi-colon in order to indicate that they were not measured through the parameterization process described in the previous section. None of their other parameters are derived and so are indicated with ellipses.

Histograms of parameters from the survey are shown in Figure 2.6. The distribution of heliocentric velocity shows detections out to nearly 19,000 km s^{-1}. The velocity widths show detections of dwarf galaxies with $W_{50} \sim 30$ km s^{-1} as well as large spirals with $W_{50} \sim 400$ km s^{-1}. The distribution of integrated flux ranges from 0.2 Jy km s^{-1} to 150 Jy km s^{-1}. The distribution of mass ranges from M_{HI}= $10^{7.8}$ to $10^{10.4} M_{\odot}$.

2.5.1 Counterparts

The NASA/IPAC Extragalactic Database (NED) was searched for extragalactic sources within a radius of 2′ at each galaxy's position in order to find potential counterparts in the literature. NED was also searched for H I extragalactic counterparts within 8′ and 100 km s^{-1}. The counterparts are listed in Table C2 in Appendix C, which presents the following information:

Column (1). ALFA ZOA source name.

Column (2). Galactic longitude, l, in degrees.

Column (3). Galactic latitude, b, in degrees.

Column (4). Foreground extinction, A_B, as estimated by Schlafly & Finkbeiner (2011).

Column (5). Primary name of the counterpart as given by NED.

Column (6). Separation in arcminutes between ALFA ZOA detection and counterpart.

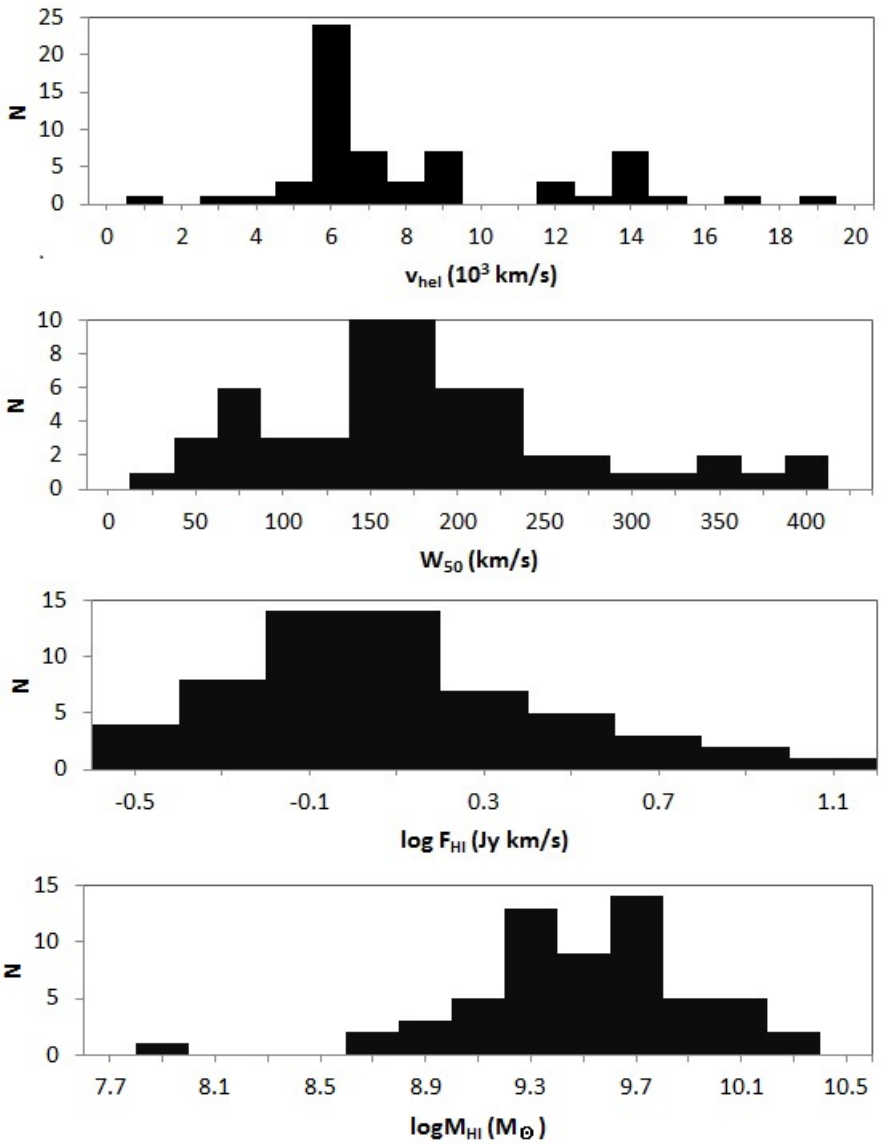

Figure 2.6 Histograms of H I parameters from the ALFA ZOA Deep Survey. From top to bottom: heliocentric velocity, velocity width at 50% peak flux, integrated flux, logarithm of H I mass.

Column (7). Difference in v_{hel} between ALFA ZOA detection and counterpart in km s^{-1}.

Figure 2.7 shows the distribution of ALFA ZOA and 2 Micron All Sky Survey

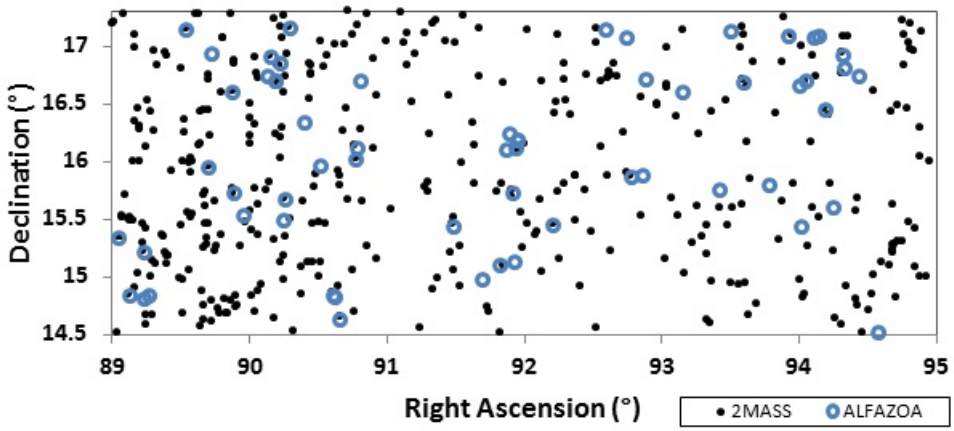

Figure 2.7 Distribution of ALFA ZOA (open blue circles) and 2MASS (black dots) detections within the survey area.

(2MASS; Skrutskie et al. 2006) detections within the data cube. There are 26 detections (43% of all sources) that have at least one counterpart within 2′. Two of these have known redshifts. Some positions have more than one counterpart within 2′, and so there are 30 possible counterparts listed in the table. No attempt is made to distinguish between multiple counterparts for the same position unless the counterpart has a known v_{hel} within 100 km s^{-1} of the ALFA ZOA detection. Every H I source with a counterpart has at least one 2MASS galaxy associated with it. Figure 2.8 shows the histogram of ALFA ZOA heliocentric velocities. Detections that have a possible counterpart are coded with a diagonal stripe. The percent of detections with a counterpart beyond 10,000 km s^{-1} drops by 20%.

Galaxy Classification

There is no clear bimodal color distribution for galaxies in NIR like there is in optical (Jarrett 2000) and so 2MASS colors do not reliably allow for the classification of an individual galaxy's morphological type. However, there are parameters other than

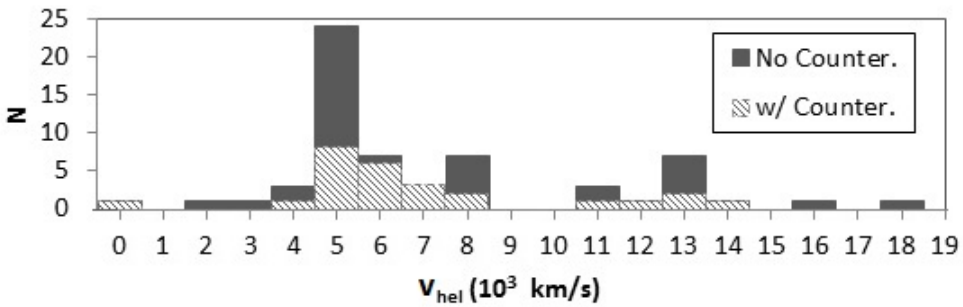

Figure 2.8 Histogram of heliocentric velocities for galaxies with no counterpart (solid) and with a counterpart (diagonal).

color indices that indicate morphological type, such as mass and size.

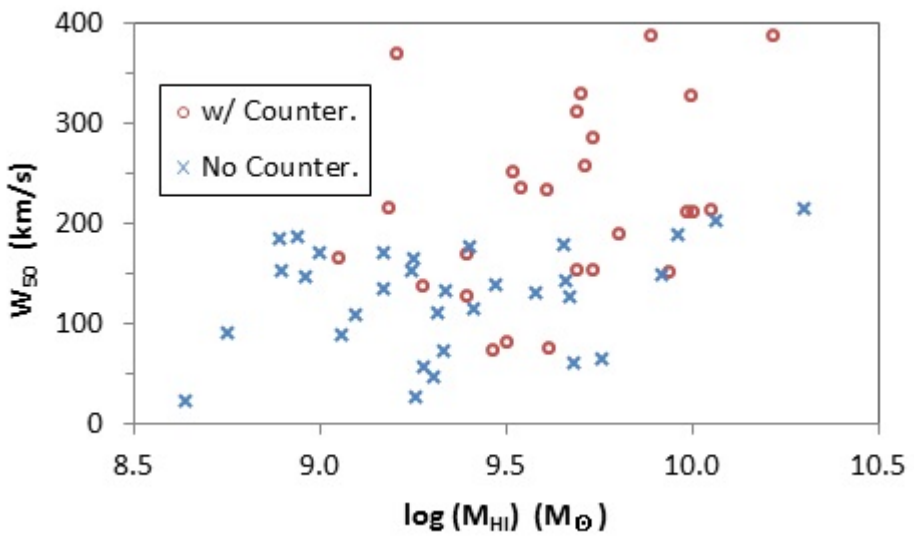

Figure 2.9 W_{50} versus M_{HI} for ALFA ZOA detections, showing both objects with counterparts (red, open circles) and without counterparts (blue, x's).

Figure 2.9 shows velocity width, W_{50}, versus H I mass, M_{HI}, for ALFA ZOA detections, marking objects that have a counterpart and those without a counterpart separately. The existence of a counterpart has a strong dependence on velocity width and H I mass. There are no counterparts with a velocity width below $W_{50} = 70$

km s^{-1}, and every detection with a velocity width above W_{50} = 215 km s^{-1} has a counterpart. The mean velocity width is W_{50} = 218, 125 km s^{-1} for counterparts and no counterparts, respectively. The mean H I mass is log $< M_{HI} >$ = 9.65 $M_{\odot}$ for detections with a counterpart versus log $< M_{HI} >$ = 9.31 $M_{\odot}$ for detections without counterparts, over two times more massive on average. The two subsamples are statistically different in velocity width and H I mass at 4.6σ- and 3.5σ-confidence levels, respectively. Nearly every large spiral galaxy (i.e. W_{50} > 200km s^{-1}, log M_{HI} > 9.5 $M_{\odot}$) detected by ALFA ZOA was also detected by 2MASS. The vast majority of smaller spirals and dwarf galaxies (i.e. W_{50} < 200 km s^{-1}, log M_{HI} < 9.5 $M_{\odot}$) were not detected by 2MASS.

A strong indicator of morphological type is the H I mass fraction (Roberts & Haynes 1994), or the percentage of the total mass of the galaxy that is made of neutral hydrogen. The total mass of a galaxy, M_{tot}, can be estimated from the Virial theorem assuming a gravitationally bound system as (Rolfs & Wilson 1996),

$$M_{tot} = 250\ v_{1/2}^2\ R, \tag{2.11}$$

where $v_{1/2}$ is the inclination-corrected velocity width, in km s^{-1}, of the galaxy at 50% peak flux, and R is the radius inside which M_{tot} is estimated, in parsecs. Total mass cannot be estimated for ALFA ZOA detections without knowing the galaxy's angular size in order to calculate R, and the inclination in order to calculate $v_{1/2}$, where $v_{1/2} = W_{50}/sin(i)$. For galaxies without counterparts, this is not possible to determine directly because the majority of detections are unresolved and so their angular size and inclination are unknown. However, the linear diameter of neutral hydrogen in a galaxy can be estimated from its M_{HI} (Meyer et al. 2004),

$$log(M_{HI}) = 1.96\ log(D_{HI}) + 6.52, \tag{2.12}$$

where D_{HI} is the H I diameter in kiloparsecs, defined at a surface density of 1

$M_\odot\ pc^{-2}$. A galaxy's H I mass fraction within D_{HI} is then,

$$\frac{M_{HI}}{M_{tot}} = \frac{M_{HI}}{250\ (W_{50}\ csc(i))^2\ M_{HI}^{0.51}\ 10^{-0.63}} = \frac{10^{-1.77}\ M_{HI}^{0.49}}{(W_{50}\ csc(i))^2}, \tag{2.13}$$

where i is the galaxy's inclination with respect to us. If it is assumed that inclination is not preferentially different for galaxies with a counterpart and those without, then the H I mass fraction between these two subsets can be compared.

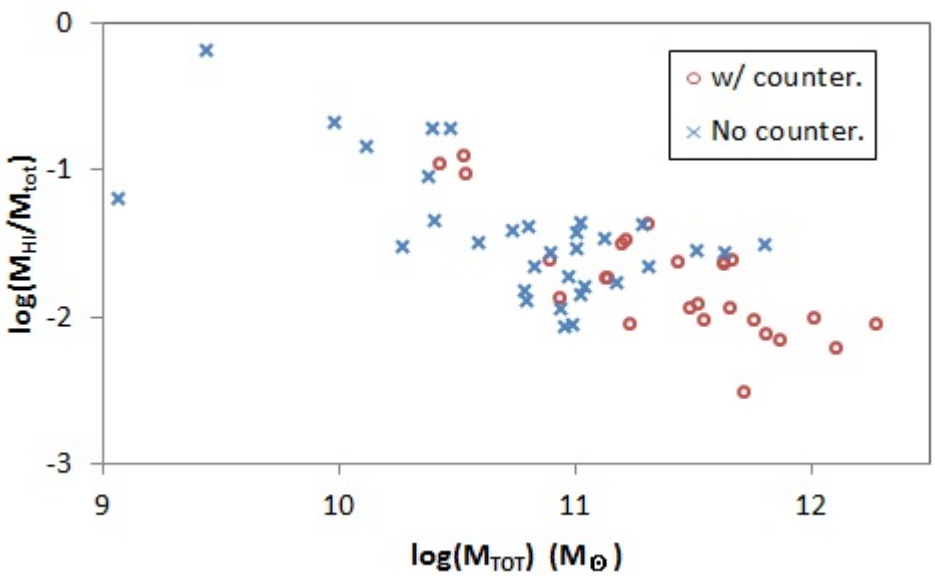

Figure 2.10 H I mass fraction versus total mass for ALFA ZOA detections, showing both objects with counterparts (red, open circles) and without counterparts (blue, x's).

Figure 2.10 shows a plot of H I mass fraction versus total mass for ALFA ZOA detections, marking objects that have a counterpart and those without a counterpart separately. For the sake of the comparison, the most common inclination for a randomly oriented sample of disks, $i = 60°$ (Garcia-Gomez & Athanassoula 1991), is used. With different assumptions for i, the scale of Figure 2.10 slides up and down, but the relative distribution does not change, so that, regardless of i, the average difference in H I mass fraction between the two samples is $log < (\Delta M_{HI}/M_{tot}) > = 0.47$, about the difference between Sa-type spirals and Sm-type irregulars. This

demonstrates that 2MASS is more sensitive to the early-type galaxy subsample of ALFA ZOA detections and less sensitive to the late-type subsample, as expected. The subsamples of H I mass fraction are statistically different from each other at the 4.2σ-confidence level. In reference to the Roberts and Haynes (1994) plots of galaxy parameters by morphological type, the red tail at the bottom right of the plot is consistent with large Sa-type spirals. The blue group of galaxies on the left half is consistent with mostly Sd-type and later. There is clear overlap between galaxies with and without counterparts in the middle of the plot, corresponding with morphologies between Sa- and Sm-type galaxies.

2.6 Survey Performance

2.6.1 Positional Accuracy

The positional accuracy of ALFA ZOA should be well within the FWHM of the telescope (FWHM = $3.4'$) because the survey is Nyquist sampled. Figure 2.11 shows the positional separation between ALFA ZOA Deep detections and their counterparts. The counterpart with the smallest separation is chosen for this plot when there are multiple possible counterparts for the same source. All of the nearest counterparts are 2MASS galaxies. The positional accuracy of 2MASS is $0.5''$ (Skrutskie et al. 2006), over two orders of magnitude finer than the FWHM of ALFA ZOA, meaning that the distribution of separations should be almost entirely due to the positional uncertainty of the ALFA ZOA Survey. There can be intrinsic offset between a galaxy's neutral hydrogen and stellar structure, though an offset of a kiloparsec only subtends $3''$ at 4000 km s^{-1} (beyond which 25 of 26 counterparts are located).

Assuming that counterparts are real and the separations in Figure 2.11 are due to uncertainty in ALFA ZOA positions, then their standard deviation is an estimate

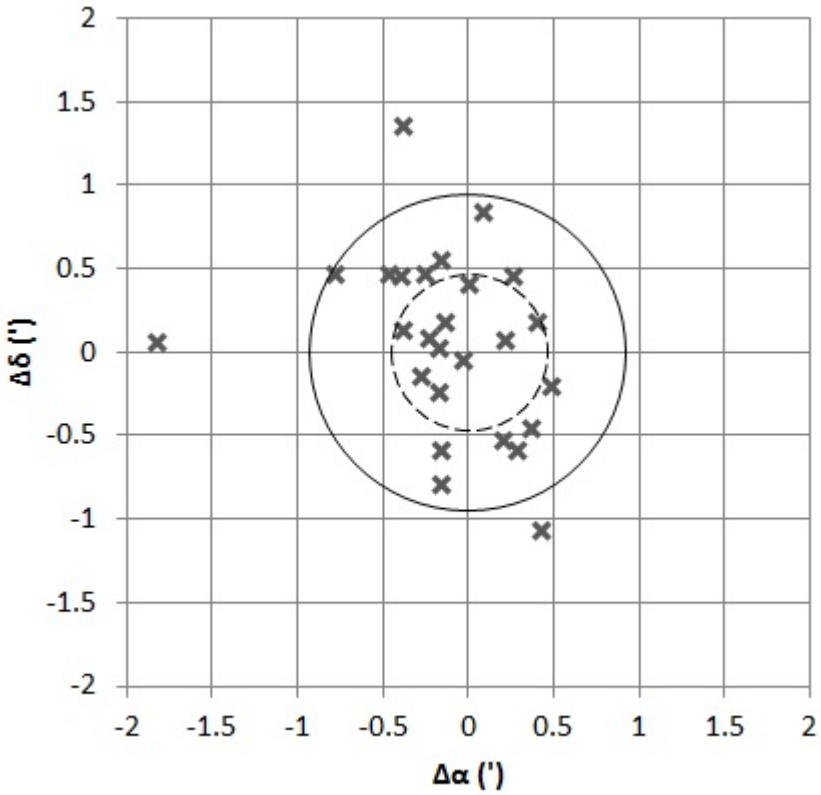

Figure 2.11 Separations (ALFA ZOA minus literature) in right ascension ($\Delta\alpha$) and declination ($\Delta\delta$) between ALFA ZOA Deep and NED counterparts, in arcminutes. The one (dashed circle) and two (solid circle) standard deviations of the separations are shown.

of the positional accuracy of the survey. The standard deviation of separations is $\sigma = 0.47'$, and this value is adopted as the survey's positional accuracy. The one (dashed circle) and two (solid circle) σ boundaries are overplotted in Figure 2.11. The distribution of positions shows an average offset in right ascension of $< \Delta\alpha >= 0.12'$ to the east. This offset is not considered to be statistically significant as it is found to be at only a 1.3σ-confidence level. There is no indication that positions are systematically offset in declination.

2.6.2 Sensitivity

Noise

The noise level of the ALFA ZOA Deep data cube reached its expected rms value of 1 mJy (at 9 km s^{-1} velocity resolution). Figure 2.12 shows the cube's rms as a function of heliocentric velocity. The rms was averaged over an inner quarter of the image plane, chosen in an area with a relatively low detection rate in order not to pollute the rms map with source flux. The mean noise is rms = 1 mJy for the high frequency sub-band (i.e. v_{hel} < 11,500 km s^{-1}), but it increases to rms = 1.2 mJy for the low frequency sub-band (i.e. v_{hel} > 10,000 km s^{-1}). The overlap between the two sub-bands can be seen between 10,000 km s^{-1} and 11,500 km s^{-1}. It is clear that the radio frequency interference (RFI) prevalent outside of the protected frequencies (i.e. 1400 - 1427 MHz) raises the average system temperature non-negligibly inside the low frequency sub-band.

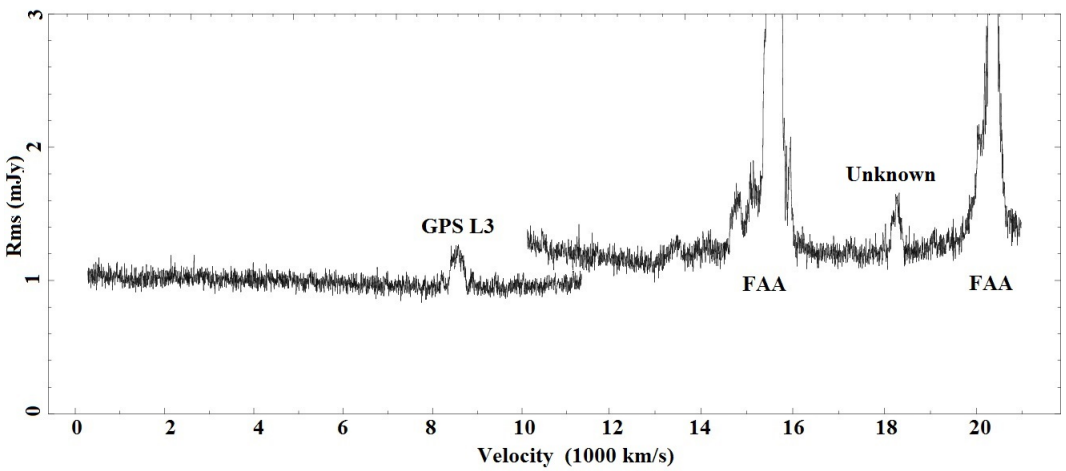

Figure 2.12 Noise in mJy per heliocentric velocity averaged over the inner quarter of the image plane for both the high- and low-frequency sub-bands. Major RFI is labeled.

Known RFI is labeled in Figure 2.12 using information provided by Arecibo

Observatory. The GPS L3 satellite produces RFI at 1381 MHz that spans velocities from 8400 - 8800 km s^{-1}. FAA radar from the airport at Punta Borinquen near Aguadilla and east of San Juan at Pico del Este produces RFI at 1350 MHz and 1330 MHz, covering velocities ranging from 14,600 - 16,000 km s^{-1} and 19,700 - 20,700 km s^{-1}, respectively. There is also RFI at 1339 MHz, spanning velocities from 18,100 - 18,400 km s^{-1}. There is no RFI source currently known to the Observatory at 1339 MHz.

H I Detection Limit

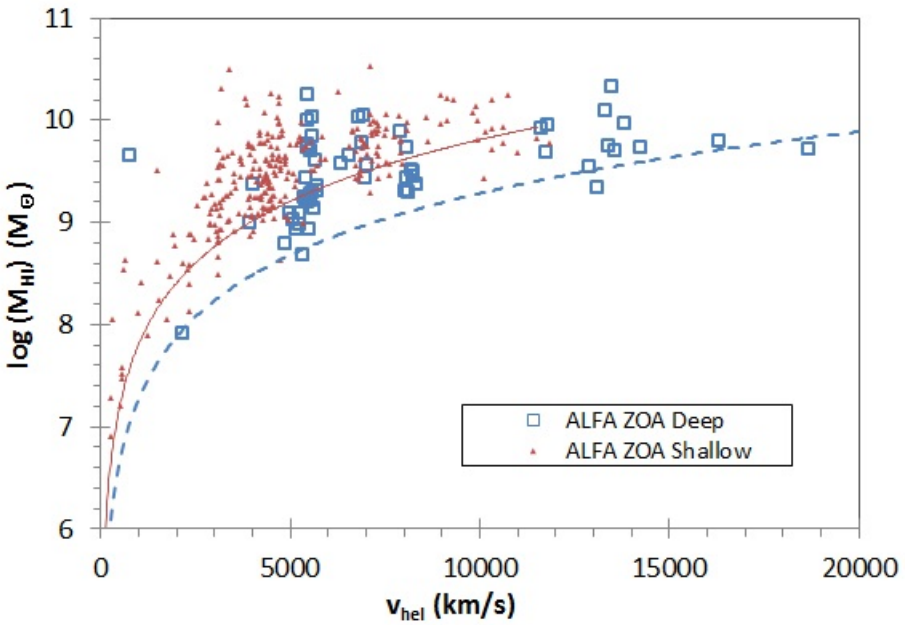

Figure 2.13 H I mass as a function of heliocentric velocity for both the ALFA ZOA Deep (open blue boxes) and Shallow (closed red triangles) Survey detections. Predicted H I mass detection limit is shown for the Deep (dashed blue line) and Shallow (solid red line) Surveys.

Figure 2.13 shows a plot of H I mass as a function of velocity for both the Deep (open boxes) and Shallow (closed triangles; rms = 5.4 mJy; Henning et al. 2010;

McIntyre et al. in prep.) Surveys. The sensitivity and depth of the Deep Survey can clearly be seen. Gaps in detections at specific redshifts are due to the RFI discussed above as well as large scale structure, which will be discussed in the next section.

The detection limit of the survey is defined as the farthest distance that a specific H I mass can be detected above a signal-to-noise ratio, S/N = 6.5. A fit of the detection limit of each survey is shown in Figure 2.13 using criteria devised by Giovanelli et al. (2007) for a bivariate signal-to-noise ratio,

$$S/N = \frac{F_{HI}}{rms\ (2\ \delta v\ W_{50})^{1/2}}, \tag{2.14}$$

where F_{HI} is the integrated flux in Jy km s^{-1}, W_{50} is the half peak velocity width in km s^{-1}, rms is the noise in Jy, and δv = 9 km s^{-1} is the velocity resolution of the survey. Though sources can be detected below the detection limit as seen in Figure 2.13, Giovanelli et al. showed empirically that sources above S/N = 6.5 have a 95% reliability rate, and this estimate is adopted for this paper. Solving for F_{HI} and plugging into equation (2.4) gives an expression for the H I mass detection limit of the survey,

$$M_{HI} = 2.36 \times 10^5\ r^2\ S/N\ rms\ (2\ \delta v\ W_{50})^{1/2}, \tag{2.15}$$

where r is the distance to a detection in Mpc, a value of W_{50} = 200 km s^{-1} is chosen for the plot in Figure 2.13, and the distance is converted from Mpc to heliocentric velocity using H_0 = 70 km s^{-1}. The typical noise of the survey is rms = 5.4 mJy, 1 mJy for the shallow, deep survey respectively. The superiority of the deep survey at detecting lower mass sources out to heliocentric velocities of 20,000 km s^{-1} can clearly be seen.

2.6.3 Completeness

The completeness limit of the survey is the lowest integrated flux, $F_{HI\,lim}$, above which every galaxy can be detected. One technique for measuring completeness is

by fitting a power law with a slope of -3/2 to the histogram of flux. The completeness limit is reached where the histogram begins to deviate from the slope. However, this method only works if galaxies are homogeneous and isotropic, which is not the case for the small area surveyed in our First Results Catalog. An alternative method for determining the survey's completeness is the Test for Completeness, T_c, a statistical test derived by Rauzy (2001) for a magnitude-redshift sample, independent of large scale structure. The method takes a sample of galaxies within a given volume and brighter than a given flux and compares the number of galaxies that are fainter and brighter than every galaxy in the sample. T_c is calculated for H I as in Zwaan et al. (2004).

T_c should follow a Gaussian distribution with an average value of 0 and unit variance for galaxy samples that are above the completeness limit, and move systematically to negative values for samples that are not complete. A plot of T_c as a function of integrated flux can be seen in Figure 2.14. T_c begins to fall below -1 at $F_{HI\,lim} < 0.7$ Jy km s^{-1}. It hovers near -1 until $F_{HI\,lim} < 0.4$ Jy km s^{-1}, where it systematically drops below -2. For a Gaussian distribution, the certainty level for the significance of a one-sided event is 84%, 98%, 99% for values associated with -1σ, -2σ, -3σ respectively. This indicates that the survey is not complete below 0.4 Jy km s^{-1} with about a 98% confidence level. The completeness limit adopted for the ALFA ZOA Deep Survey is $F_{HI\,lim} = 0.5$ Jy km s^{-1}, where T_c = -1.25.

The bottom panel of Figure 2.14 shows an attempt to measure the completeness from where the flux histogram deviates from a -3/2 power law. The value for completeness using this method is $F_{HI\,lim} = 1$ Jy km s^{-1}, significantly higher than the T_c method. As mentioned above, the power law technique should fail if the distribution of galaxies in the survey area is not homogeneous, which is the case for our small First Results area dominated by large-scale structure. Further, a completeness limit of $F_{HI\,lim} = 0.5$ Jy km s^{-1} makes sense compared to recent H I surveys, given

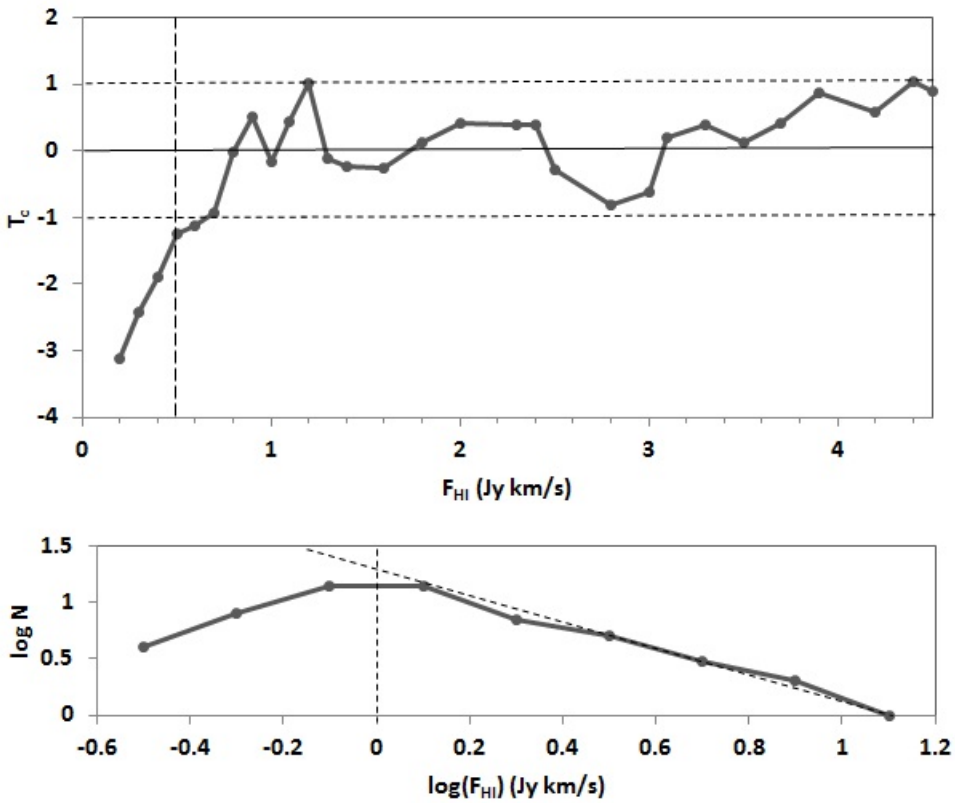

Figure 2.14 Top Panel. Test of completeness for ALFA ZOA. Horizontal dashed lines indicate unit variance. The vertical dashed line shows the adopted completeness limit. Bottom Panel. Log-log histogram of integrated flux. The -3/2 slope (diagonal dashed line) falls off from the fit somewhere between -0.1 and 0.1, indicating that the completeness is reached somewhere around 1 Jy km s^{-1} (vertical dashed line).

differing rms sensitivities, as illustrated in Figure 2.15.

For normalized comparison, the noise for ALFALFA (Saintonge 2007) and HIPASS (Zwaan et al. 2004) is scaled to a velocity resolution of 9 km s^{-1}. Figure 2.15 shows a remarkably well fit, linear relationship between H I survey noise and integrated flux completeness limit, indicating that the T_c method is giving an expected value compared to how other surveys are performing. It should be noted that ALFALFA (Haynes et al. 2011) published bivariate completeness as a function of integrated

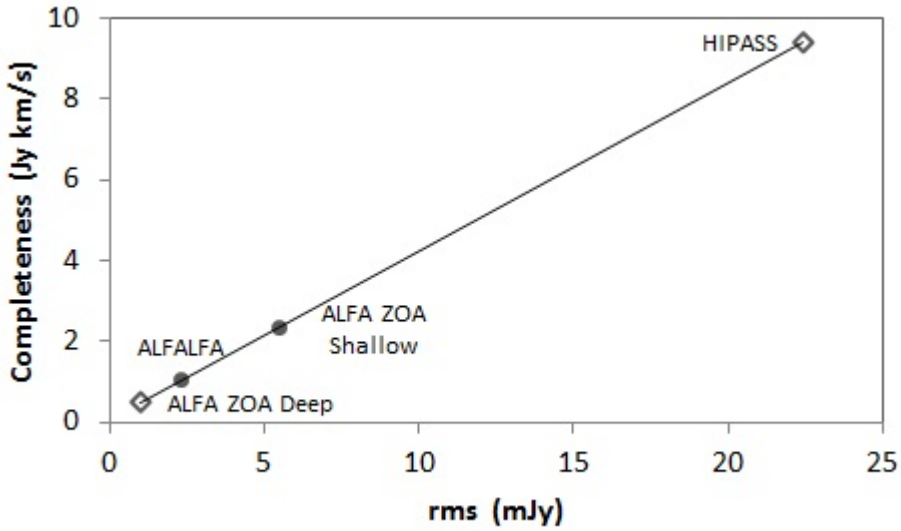

Figure 2.15 Integrated flux completeness limit versus rms for major surveys. The open diamonds indicate surveys that used the T_c method and the closed circles are for surveys that fit a -3/2 power law for calculating completeness limit.

flux, F_{HI}, and galaxy velocity width, W_{50}, and so the completeness limit for their average W_{50} is used for Figure 2.15.

Figure 2.16 shows a log-log plot of integrated flux, F_{HI}, versus velocity width, W_{50} for ALFA ZOA. Similar to the bivariate signal-to-noise ratio used to estimate the detection limit of the survey, discussed in Section 2.6.2, the relationship between F_{HI} and W_{50} can be used to estimate the bivariate completeness limit, $F_{HI}(W_{50})_{\,lim}$, above which every galaxy can be detected. $F_{HI}(W_{50})_{\,lim}$ is estimated by scaling equation (2.11) so that $F_{HI\,lim} = 0.5$ Jy km s^{-1} at the mean W_{50}. The mean velocity width is $W_{50} = 167$ km s^{-1}, so the bivariate completeness limit can be estimated as,

$$log[F_{HI}(W_{50})_{\,lim}] = 0.5\ log(W_{50\,lim}) - 1.4. \tag{2.16}$$

Both the bivariate detection limit (dashed line) and bivariate completeness limit (solid line) are shown in Figure 2.16. It should be noted that, while three ALFA ZOA Deep detections are located below the detection limit line in Figure 2.13 and

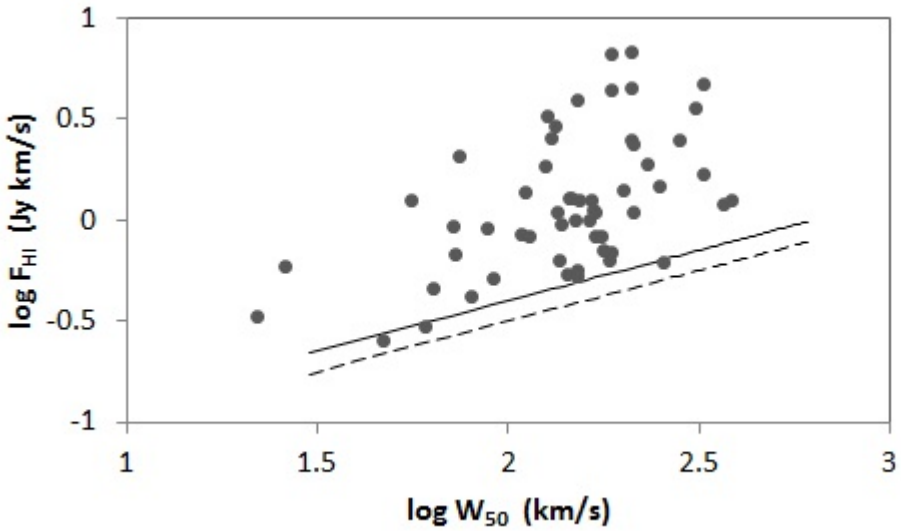

Figure 2.16 Log-log plot of integrated flux versus velocity width. The detection limit of the survey (dashed line) and the bivariate completeness limit (solid line) are shown.

none are below the line here, that is because an estimate of $W_{50} = 200$ km s^{-1} was assumed to make the plot in Figure 2.13.

2.6.4 Zone of Avoidance

Figure 2.17 shows a plot of integrated flux, F_{HI}, as a function of foreground extinction, A_B. Extinction estimates were taken at the position of each ALFA ZOA detection using NED as described in Section 2.5.1. It should be noted that estimates of extinction at $|b| < 5°$ are particularly uncertain (Schlegel, Finkbeiner & Davis 1998). This plot does not show a relationship between F_{HI} and extinction, indicating that our survey does not have a Zone of Avoidance, as expected.

Sources with higher F_{HI} are more likely to have a counterpart, and counterparts are less likely at higher A_B. This is expected, as the purpose of ALFA ZOA is to detect galaxies in areas with high extinction, where surveys at higher frequencies

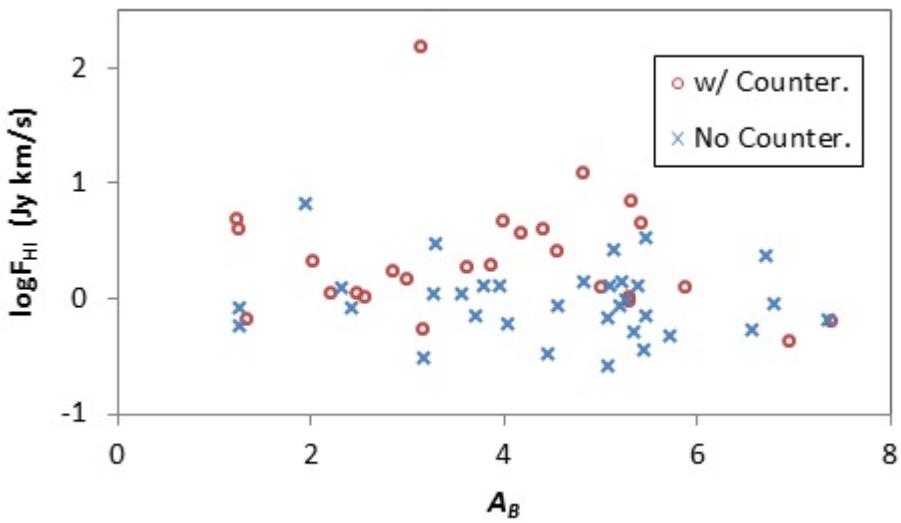

Figure 2.17 Integrated flux as a function of extinction, A_B. Detections with a counterpart (open red circles) and with no counterpart (blue x's) are shown.

cannot. 55% of detections have a counterpart below $A_B = 3.5$ magnitudes while only 37% have counterparts above $A_B = 3.5$ mag.

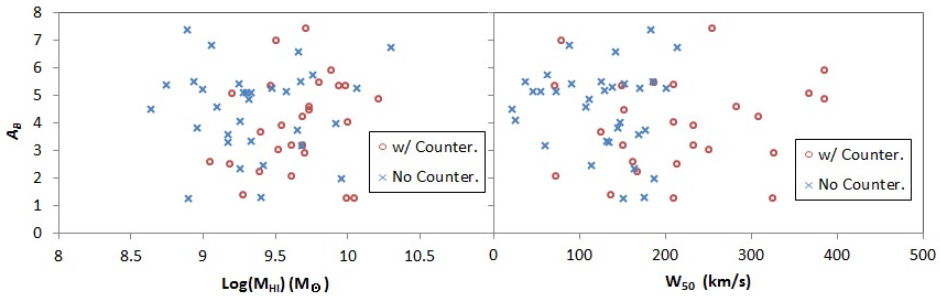

Figure 2.18 Left panel. Extinction versus logM_{HI}, color coded for those with counterparts (open red circles) and those without (blue x's). Right panel. Extinction versus velocity width, W_{50}, same color scheme as left panel.

Because the number of detections is not very high, it is possible that the detections at high extinction happen to come from intrinsically low mass or low velocity width galaxies that are less sensitive to NIR observations. Figure 2.18 shows a plot

of extinction, A_B, as a function of M_{HI} and W_{50}, color coded for those with a counterpart (open red circles) and those without (blue x's). There is a near uniform distribution of M_{HI} and W_{50} at all extinctions, indicating there is nothing intrinsic about the galaxies being detected that causes a lack of counterparts at high extinction. The even distribution of W_{50} and M_{HI} across extinction is another indicator of the efficacy of ALFA ZOA at penetrating the Zone of Avoidance. For instance, ALFA ZOA J0610+1709 has the highest M_{HI}, and 15th highest F_{HI} in the catalog, with a large velocity width $W_{50} = 215$ km s^{-1}, but it has no counterpart in the literature, even though it is a bright spiral that should be easily detected by a deep NIR survey. The most likely reason why it has gone undiscovered is because it is located in an area of high extinction, $A_B = 6.7$ ($A_J = 1.3$) or high stellar crowding, both of which affect low-latitude optical and NIR surveys but are of no concern to 21-cm surveys.

2.7 Large Scale Structure

While it is not quite a "pencil beam" survey the first results area is narrow enough that it does not fairly probe large scale structure (LSS) in angular dimensions. Therefore, examining a histogram of redshifts is a useful way to explore large scale structure in redshift space. Figure 2.19 shows detections per velocity above the completeness limit (thick line) along with the expected number of detections per velocity (thin line). The expected number of detections is calculated by integrating the HIMF at the completeness limit using values from Martin et al. (2010). As we are expecting to detect every galaxy above the completeness limit, the difference between the two lines is a measure of the over- and underdensity of the large scale structure cut across by the survey. Redshifts where significant RFI occurs are labeled. RFI can limit the sensitivity of the survey over the volume affected by its bandwidth. A more robust

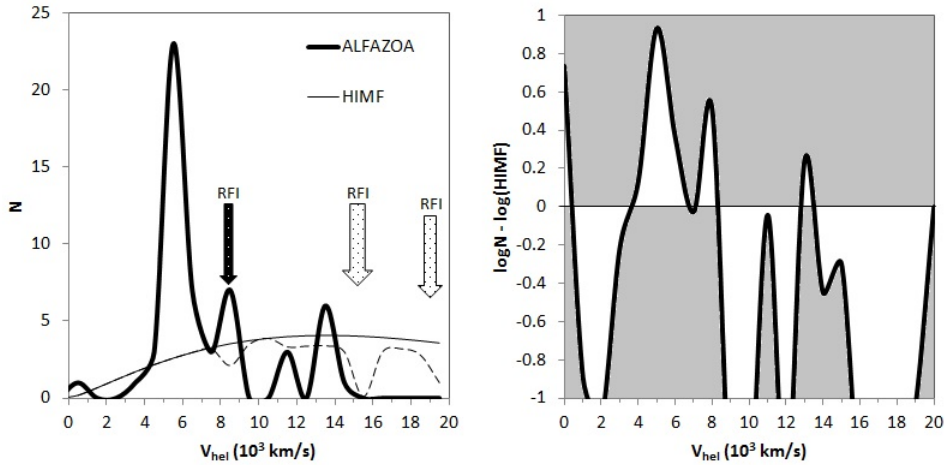

Figure 2.19 Left panel. Distribution of ALFA ZOA detections (thick solid line) that are above the completeness limit, as a function of redshift. The expected distribution (thin solid line) from integrating the HIMF (Martin et al. 2010) is shown along with a more robust expectation (dashed line) from taking into account RFI and rms = 1.2 mJy for the low sub-band. Velocities with significant RFI are labeled; the arrow with white polkadots indicates the redshift and bandwidth of the GPS L3 Satellite, black polkadots are for FAA radar. Right panel. The log difference between ALFA ZOA and the robust expected distribution. Observed large scale structure is shaded white.

estimate of the expected distribution of detections for ALFA ZOA is shown (dashed line) by taking into account the effect of RFI on survey volume as well as the increase in noise in the low sub-band (i.e rms = 1.2 mJy for $v_{hel} > 11{,}500$ km s^{-1}).

2.7.1 Comparison to Predicted Large Scale Structure

Erdogdu et al. (2006) created density reconstruction maps out to 16,000 km s^{-1} from the Two Micron Redshift Survey (2MRS; Huchra et al. 2012). The Zone of Avoidance for 2MRS is $|b| < 5°$ in the outer Galaxy, and so Erdogdu et al. were forced to predict the extent of large scale structure across the ZOA. Comparing ALFA ZOA detections with the Erdogdu density maps is a good check for the effectiveness of predicting LSS in the ZOA. Figure 2.20 shows a wedge plot of ALFA ZOA detections (open circles)

alongside 2MRS detections (black dots) and indicates major overdensities from the density reconstructions of Erdogdu et al. inside the red ovals. ALFA ZOA confirms the continuation across the ZOA of much of the structure predicted by Erdogdu et al., and contradicts some of the predictions as well.

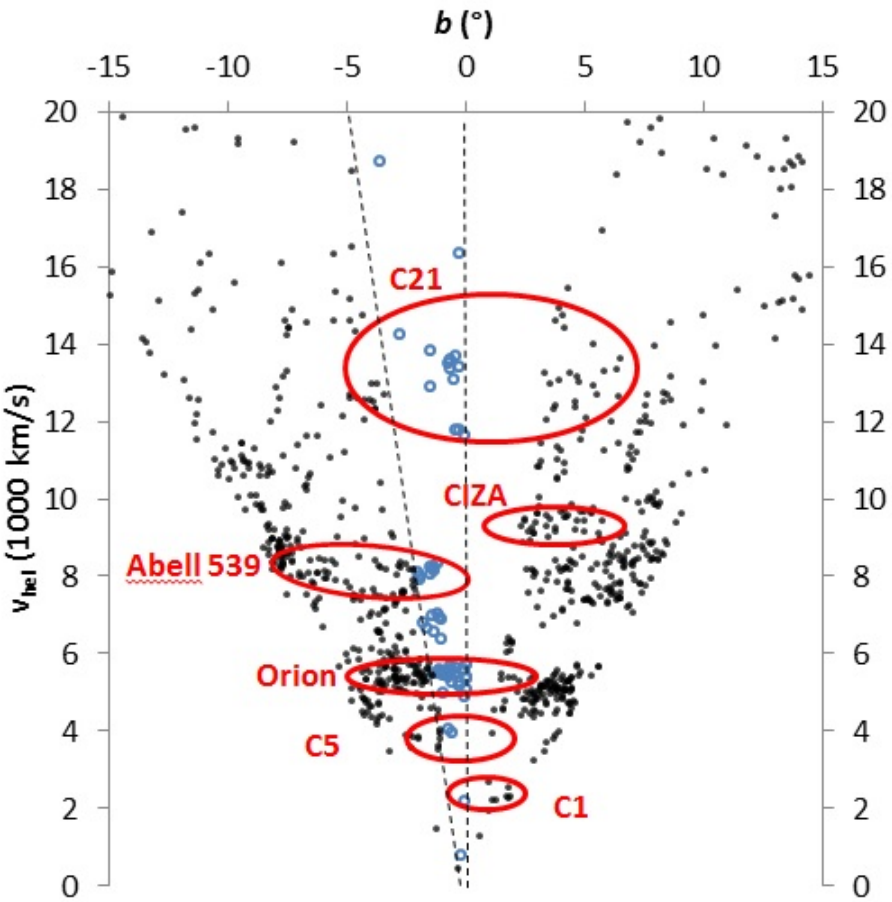

Figure 2.20 2MRS galaxies (black dots) and ALFA ZOA detections (blue open circles) plotted in polar coordinates. Overdensities predicted from 2MRS (Erdogdu et al. 2006) are circled in red and the Erdogdu et al. naming convention is preserved. The field of view of the first results survey is shown (dotted line). In the plot, CIZA is shorthand for CIZA J0603.8+2939.

Referring to Figures 2.19 and 2.20, the prediction of the overdensity C1 and its extension through C5 from 2000 km s^{-1} to 4000 km s^{-1} is not confirmed, though

galaxies at the location of C1 and C5 are detected. The Orion overdensity at 6000 km s^{-1} is clearly confirmed to extend into the ZOA, as is Abell 539 at 8000 km s^{-1}. Abell 539 is most likely an even greater overdensity than detected here because of RFI from the GPS L3 satellite affecting velocities 8400 km s^{-1} - 8800 km s^{-1}. Galaxies between Orion and Abell 539 can be seen around $v_{hel} \sim 7000$ km s^{-1}, though whether there is a connection between Orion and Abell 539 in redshift space cannot be confirmed. CIZA J0603.8+2939 is confirmed not to extend below $b = 0°$. A significant underdensity is confirmed between 9000 and 12,000 km s^{-1}, though this underdensity appears to be greater and extend farther in redshift than predicted. Large scale structure from C21 is confirmed as an overdensity starting at 13,500 km s^{-1} but its extent through 16,000 km s^{-1} cannot be confirmed because of FAA radar interference. The very strong RFI presence due to FAA radar from 14,600 to 16,000 km s^{-1} most likely contributes to a lack of detections of C21 galaxies in that velocity range. ALFA ZOA detects a significant underdensity from 16,000 to 20,000 km s^{-1}, at velocities beyond the range of 2MRS and the Erdogdu density reconstruction maps. There are no detections above the completeness limit in that velocity range though an average universe would contain 10 galaxies above the completeness limit in that region. There is narrow RFI around 18,500 km s^{-1} that affects sensitivity at that velocity and the FAA radar starting at 20,000 km s^{-1} reduces sensitivity to zero at the edge of the cube's velocity cutoff. Figure 2.21 shows sky distribution plots of ALFA ZOA and 2MRS detections for the three volumes where ALFA ZOA detects an overdensity. While near infrared maintains a clear Zone of Avoidance, ALFA ZOA easily traces large scale structure through the lowest Galactic latitudes.

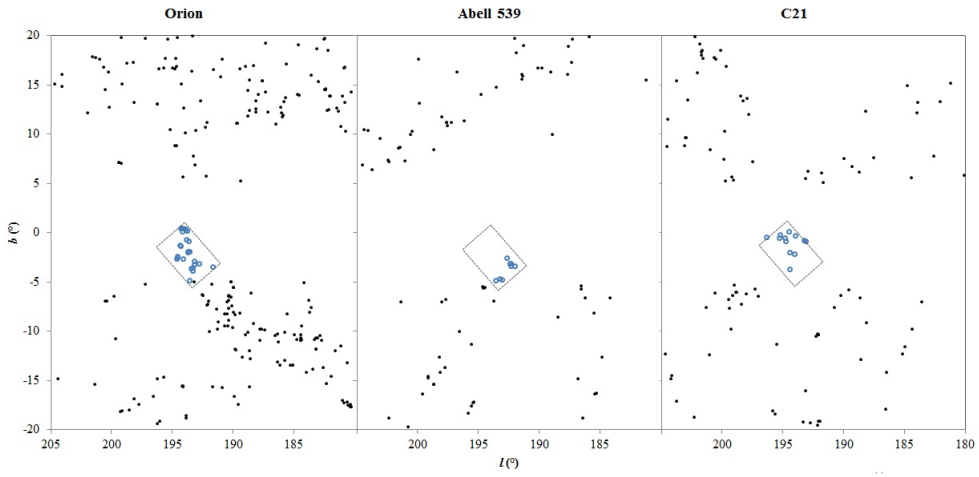

Figure 2.21 Sky distribution plots showing 2MRS (black dots) and ALFA ZOA (open blue circles) detections for the three major overdensities detected by ALFA ZOA. The overdensities are labeled above each plot and the field of view of the first results survey is shown (dotted line). Orion covers the velocity range 5000 to 6000 km s^{-1}. Abell 549 ranges from 7500 to 8500 km s^{-1}. C21 ranges from 12,000 to 15,000 km s^{-1}.

2.8 Conclusion

The ALFA ZOA Deep Survey has achieved its expected noise level of 1 mJy (at 9 km s^{-1} resolution) and it is complete above $F_{HI} = 0.5$ Jy km s^{-1}. First results display the ability to detect galaxies out to nearly $v_{hel} = 19{,}000$ km s^{-1} and at extinctions that surveys at other wavelengths struggle to penetrate. ALFA ZOA Deep has completed 15 square degrees in the outer Galaxy and is continuing to take data, intending to cover about 300 square degrees in both the inner ($30° \leq l \leq 75°; b \leq |2°|$) and outer ($175° \leq l \leq 207°; -2° \leq b \leq +1°$) Galaxy, over the next several years.

Chapter 3

ALFA ZOA Shallow Survey

3.1 Introduction

The ALFA ZOA Shallow Survey searches for 21-cm line emission from neutral hydrogen (H I) in galaxies behind the disk of the Milky Way out to 11,500 km s^{-1}. As a spectral line survey, ALFA ZOA generally only has confusion with Galactic H I within approximately $\pm$100 km s^{-1} and can detect H I sources at velocities redshifted beyond Galactic emission. The survey covers 1350 square degrees through the inner Galaxy at longitudes $30° < l < 75°$ and latitudes $|b| < 15°$. There are three main science goals for the ALFA ZOA Shallow Survey; determine if nearby galaxies behind the Milky Way affect the mass dipole vector of the Local Group, uncover large scale structure across the Galactic plane, estimate the neutral hydrogen mass function. This chapter will address the latter two (the next chapter addresses nearby galaxy detections).

A derth of galaxy detections in the ZOA forces all sky density reconstructions to predict LSS in the ZOA by extrapolating from structure above and below the plane (Kraan-Korteweg 2000). Mapping galaxies in the ZOA with actual detections from

an H I survey will provide a useful check on the validity of density reconstruction maps. In the inner Galaxy, the Shallow ALFA ZOA survey area intersects the Pegasus Cluster, C7, and Cξ overdensitites, using the naming scheme from the most comprehensive density reconstruction map (Erdogdu et al. 2006). It also probes the Aquarius, Corona Borealis, Delphinus, and Cygnus voids.

This chapter presents the method and results of the ALFA ZOA Shallow Survey and analyzes the mass function and the large scale structure uncovered by the survey. Section 2 describes the design of the survey. Section 3 presents data reduction methods. Section 3.4 describes source detection and presents the survey catalog. Section 3.5.1 presents results from a literature search for counterparts and uses the results to categorize the types of objects detected by the survey. Section 3.6 compares the detection parameters against literature values. Section 3.7 develops a selection function for the adjudicated ALFA ZOA catalog and this is used in Section 3.8 to estimate a neutral hydrogen mass function. Section 3.9 discusses large scale structure uncovered by the survey and compares this to predictions from density reconstruction maps. The final section summarizes the results of the survey and discusses future work.

3.2 Survey Design

3.2.1 Observations

The telescope and receiver used by the ALFA ZOA Deep survey are described in Chapter 1. The ALFA ZOA Shallow Survey covers about 1360 square degrees between $b < |15°|$ and $l = 30° - 75°$. Observations began May 2008 and finished in August 2009, taking 322 hours of total observing time. The survey area is comprised of five separate fields called A, B, C, D, and Z, illustrated in Figure 3.1. Fields A,

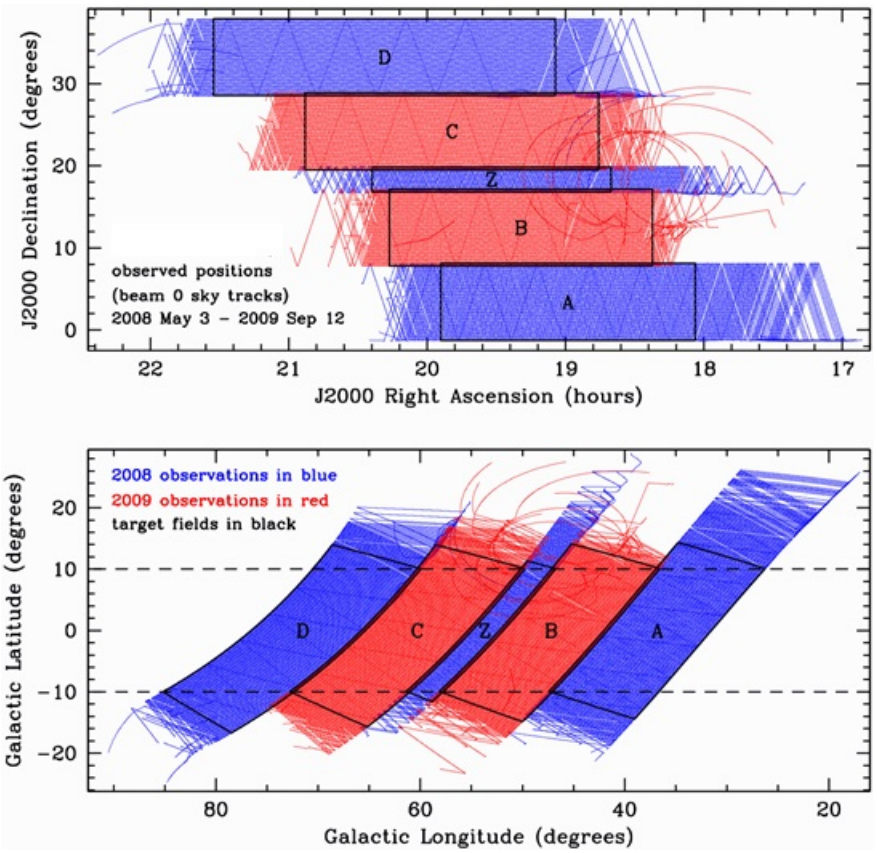

Figure 3.1 Scan pattern from every observation in the ALFA ZOA survey in Equatorial coordinates (top) and Galactic coordinates (bottom). Fields A, D, and Z were observed in 2008 with the WAPP spectrometer and fields B and C were observed in 2009 with the Mock spectrometer (Image courtesy of I-GALFA).

B, C, and D were observed in meridian nodding mode: The telescope drives north and south on the meridian along the altitude arm of the telescope at a constant rate of 1.53° per sidereal minute, constantly taking data while the sky rotates past in Right Ascension, creating observing scans in W-shaped patterns on the sky, called "lambdas". Adjacent lambdas overlap so that each position is crossed twice, from one lambda in each direction (northward and southward). The ALFA receiver is rotated such that each beam follows a path that is equally spaced, 1.83′ apart, from the other 6 beams on the sky as seen in Figure 3.2.

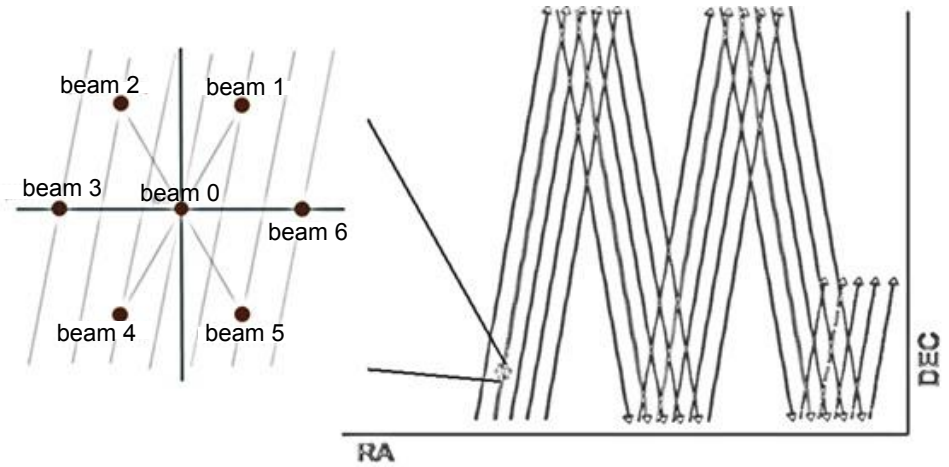

Figure 3.2 Illustration of the meridian nodding mode observing technique. Observations are taken in scans that track W shaped patterns, called lambdas, across the sky. One lambda produces seven equally spaced beam scans that are separated by 1.83′.

Z field consists of declinations that cross the zenith and so was not observed in meridian nodding mode as an alt-az telescope cannot cross the zenith because of the discontinuity in azimuth at the crossing. Z field was observed by positioning the telescope at an angle off the meridian and nodding in azimuth angle, again with beams spaced 1.83′ apart. Beam paths are separated by 1.83′, about 1/2 FWHM, to allow the survey to be Nyquist sampled. Nyquist sampling allows reconstruction all of the flux from a point source as illustrated in Figure 3.3.

Nodding mode was chosen as the observing technique as part of the commensal partnership with I-GALFA (Park et al. 2013) and GALFACTS (Taylor & Salter 2010). Nodding is a more efficient survey method than pointed observations because the telescope is constantly taking data as it drives (i.e. there is no down time while the telescope is slewing between sources). Driving the telescope also allows area to be covered more quickly (though at a lower sensitivity of course) than holding the telescope in a fixed position while the sky drifts past like in a drift scan observing mode. Having each pointing crossed twice also allows independent measurements of

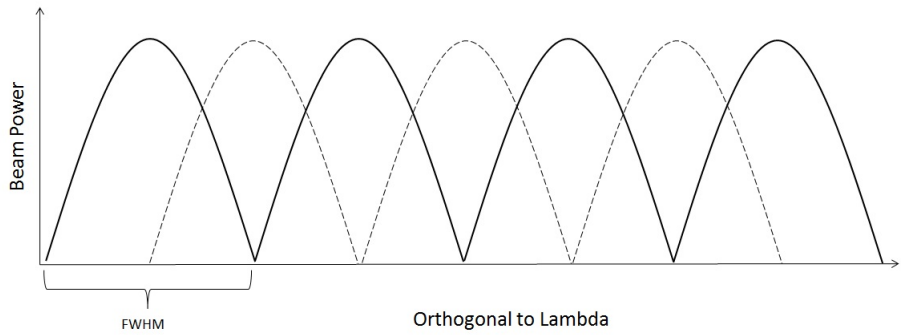

Figure 3.3 Illustration of survey beam spacings in one dimension, where each shape represents the power pattern above a beam's FWHM. The flux of any point source in a blind survey cannot be reconstructed by sampling at a rate of only one beam per FWHM, like the solid line beams alone, as it is unknown where in the power pattern the source falls. By adding the dashed line beams, the survey is now Nyquist sampled and the flux of any point source can be reconstructed.

gain needed for the continuum observations taken for GALFACTS.

3.2.2 Backend

The shallow ALFA ZOA survey used two different spectrometer backends at different times over the course of the observations; the Wideband Arecibo Pulsar Processor (WAPP) and the Mock spectrometer. Radiation is measured as a change in voltage at the receiver and this data is converted from voltage per time into a power spectrum of receiver units per frequency using an auto-correlator for the WAPP and an "on the fly" Fast Fourier Transform (FFT) for the Mock. An auto-correlator spectrometer samples the voltage at different time lags and performs the auto-correlation function over every lag. If the receiver detects some voltage V_0 at time t=0, and some voltage V(t) at time t, then the auto-correlation function, a(t), gives

$$a(t) =< V_0 V(t) >, \tag{3.1}$$

where the brackets represent the mean value of the product. The auto-correlations are then converted into a power spectrum by taking their Fourier transform,

$$S(\nu) = \int_0^\tau a(t) e^{-i2\pi t\nu}\, dt \tag{3.2}$$

where $S(\nu)$ is the power spectrum in receiver units per frequency, ν, and τ is the total number of samples to integrate over. Conversely, an "on the fly" FFT spectrometer performs a Fourier transform on each voltage sample,

$$F(\nu) = \int_0^\tau V(t) e^{-i2\pi t\nu}\, dt \tag{3.3}$$

and then converts into a power spectrum,

$$S(\nu) = |F(\nu)|^2. \tag{3.4}$$

The end result is the same between an auto-correlator and an FFT backend, but an auto-correlator is more hardware intensive while an FFT backend is more software intensive. The diagram in Figure 3.4 summarizes the methods used by the different backends.

V(t) (Voltage)	⇔ FT	*F(v)* (FFT)
⇓		⇓
<V_0V(t)> (Auto-correlation)	⇔ FT	S(v) (Power spectrum)

Figure 3.4 Two different methods used to convert voltage per time into a power spectrum. An auto-correlator operates on voltage before applying a Fourier Transform, an FFT performs a Fourier Transform first.

Observations in 2008 covered fields A, D, and Z (hereafter A+D) using the WAPP spectrometer with 2048 channels covering 100 MHz of bandwidth from $\nu = 1330$ MHz to 1430 MHz. This gives a channel spacing of 48.8 kHz or a velocity resolution, δv,

at 1420 MHz of,

$$\frac{\nu_e - \nu_o}{\nu_o} = z \sim \frac{v}{c} \text{ at small v,} \tag{3.5}$$

$$\delta v = \frac{48.8}{\nu_o} c = 10.3 \text{ km s}^{-1}, \tag{3.6}$$

where z is redshift, ν_e is the rest frequency of emitted radiation, ν_o is the observed frequency, and c is the speed of light. Considering the rolloff in sensitivity at the edge of the bandpass, the usable velocity range for searching at 21cm in this bandwidth is v_{hel} = -1000 km s^{-1} to 10,500 km s^{-1}. The WAPP recorded integrations every 200ms. It also utilized a low flux noise diode that fired for 100ms every integration because of calibration requirements for commensal partners.

Observations in 2009 covered fields B and C (hereafter B+C) using the Mock spectrometer, which covers 300 MHz from 1225 MHz to 1525 MHz using two overlapping 172 MHz sub-bands centered on 1300 MHz and 1450 MHz. The sub-bands overlap between 1364 MHz and 1386 MHz so that there is no loss of sensitivity due to roll off at the edges of the bandpass. Each sub-band is divided into 8192 channels, producing a spectral resolution of 21 kHz or a velocity resolution of δv = 4.5 km s^{-1} at 1420 MHz. The searchable velocity range for the high frequency sub-board is -1000 km s^{-1} to 11,500 km s^{-1}. The low frequency sub-board has not yet been searched for the shallow ALFA ZOA survey as the expected number of detections in the sub-board is less than 10% of the survey's total detections as calculated by integrating the HIMF (Martin et al. 2010), though it is planned to be searched in the future. The Mock spectrometer recorded data in 1s integrations. The low flux noise diode was fired during the observations of B+C fields, but it was not injected into the Mock data set. Both WAPP and Mock spectrometers sampled a high flux noise diode for 3s integrations at the top and bottom of the nodding lambdas.

3.3 Data Reduction

The data for B+C fields is bandpass calibrated in total power on-off mode using LiveData (Barnes et al. 2001). Each 1s integration is operated on using (ON-OFF)/OFF in order to take the bandpass shape out of the spectrum, where ON is a given integration and OFF is a median combination of all integrations in the same lambda scan between $4'$ and $60'$ away. Total power on-off calibration produces flat baselines and normalizes receiver response per channel as illustrated in Figure 3.5. Flat baselines are necessary for avoiding signal confusion and reducing noise in a spectrum. Ideally, the spectrum for an OFF observation would be taken soon after an ON and would drive over the same alt-az coordinates because bandpass shape is a function of time and telescope position but it is not possible to drive over the same alt-az coordinates in meridian nodding mode.

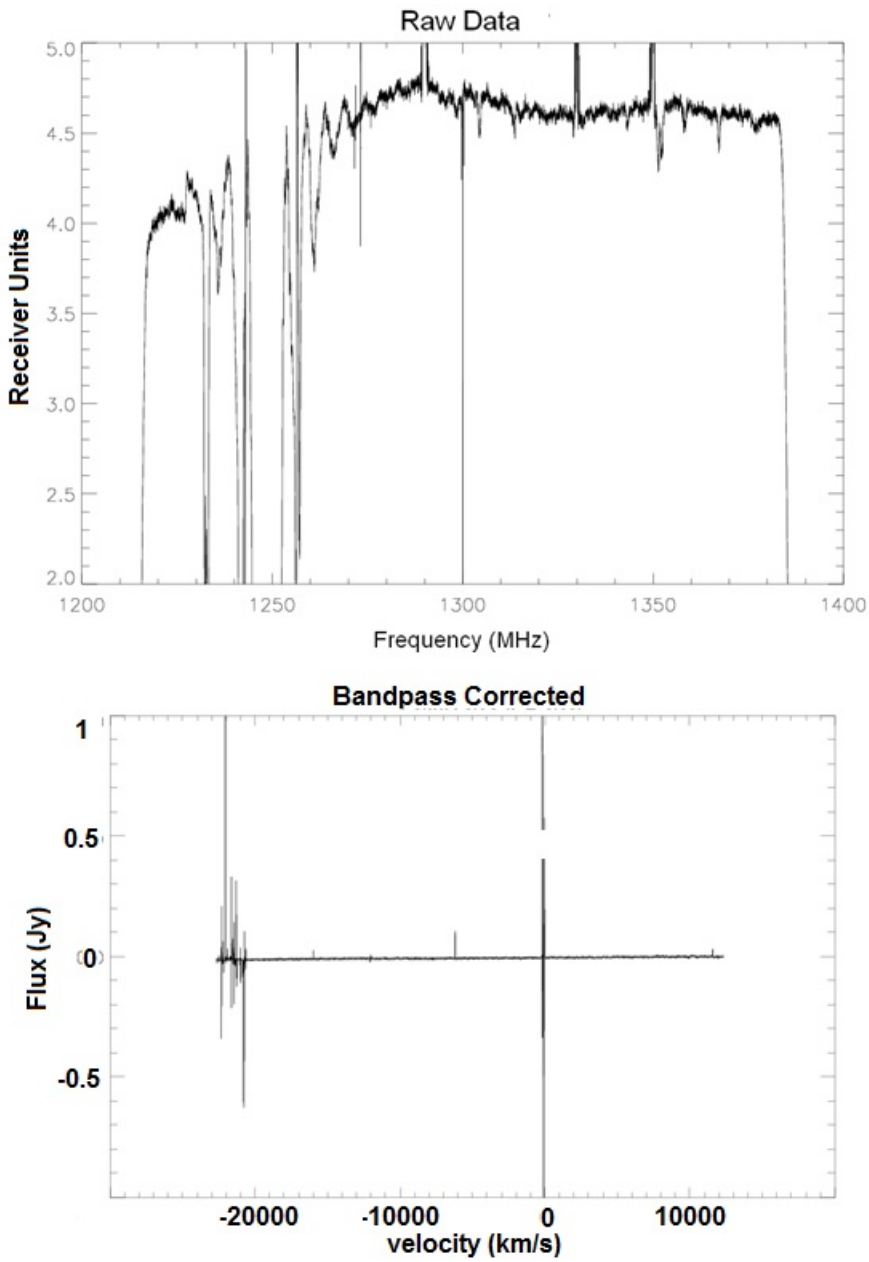

Figure 3.5 Top Panel. Raw data from the telescope in receiver units versus topocentric frequency. Bottom Panel. Data after applying (ON-OFF)/OFF bandpass correction, in flux density versus heliocentric velocity.

Even though the low flux diode was not injected into the Mock data, the firing of the calibrator was recorded in the FITS header. As such, LiveData was not able to distinguish between the winking low flux diode and the high flux noise diode that fired at the top and bottom of every lambda. Therefore, the high flux diode was not able to be used to calibrate the data. Because of this, a telescope average of system temperature was used to convert from receiver units into temperature. This injects about a 10% error into the flux values because the real system temperature ranges from 26K to 30K, according to data kept by the observatory.

The frequency, ν, is resampled relativistically in LiveData with a linear interpolation from topocentric to barycentric using,

$$\nu_{bary} = \frac{1 - v/c}{\sqrt{1 - v/c^2}} \nu_{topo} \tag{3.7}$$

where v is the velocity of the telescope relative to the Earth-Sun barycenter, stored in the observations file, and c is the speed of light. The frequency is then converted into redshifted heliocentric velocity, v_{hel}, using,

$$v_{hel} = \frac{(z+1)^2 - 1}{(z+1)^2 + 1} c, \tag{3.8}$$

where c is the speed of light and z is redshift. v_{hel} is calculated using the optical velocity convention meaning that redshift is linear with wavelength,

$$z = \frac{\lambda_o - \lambda_e}{\lambda_e}, \tag{3.9}$$

where $\lambda_o = c/\nu_{bary}$ is the observed spectral line wavelength and $\lambda_e = 21.1$cm is the wavelength of emission. The baseline of this spectrum is fit for continuum emission to first order and the result is subtracted in order to produce a baseline centered on 0K. The gain, G(beam, ZA, polarization), taken from a table of values provided by the observatory, is applied to convert units into janksys and the final reduced spectrum is Hanning smoothed. Hanning smoothing applies a filter function to the spectrum in the form,

$$w(n) = \frac{1}{2}[1 - cos(\frac{2\pi n}{N-1})], \tag{3.10}$$

where N = 5 is the width of the filter in channels and n is the channel number in the filter so that w = [0, 0.25, 0.5, 0.25, 0]. Every channel has this smoothing kernel applied in a running average across the spectrum. Hanning smoothing significantly reduces the effect of Gibbs ringing, an artifact of the partial sums in a Fourier series (Gibbs 1898). Gibbs ringing produces unstable baselines near strong spectral line sources. Hanning smoothing reduces noise by a factor of $\sqrt{2}$, but worsens velocity resolution by a factor of two (to 9 km s^{-1} for B+C, 20.6 km s^{-1} for A+D).

Data are written out by LiveData into SDFITS file format in order to process into data cubes using Gridzilla (Barnes et al. 2001). Gridzilla is part of the AIPS++ software package, and is used to create data cubes by spatially gridding spectra. Gridzilla is set to clip spectra between -50 mJy and 500 mJy, and make cubes roughly 20 square degrees made up of $1' \times 1'$ pixels. Each input spectrum is assigned to all pixels within a $3.4'$ diameter of the spectrum's coordinates using a Top-Hat kernel. In pixels where spectra overlap, they are median-combined, weighted by the angular distance of the pixel from each spectrum's original coordinates using a beam power pattern with FWHM = $3.4'$. The end result is a 3-dimensional data structure with axes of right ascension, declination, and heliocentric velocity. An RA-Velocity slice of the data cube is shown in Figure 3.6.

Each ALFA ZOA field has a different number of cubes and cube sizes that cover the entire area of the field. Multiple cubes per field are produced in order to create manageable sizes for optimizing computer processing time and search technique. Adjacent cubes overlap by a minimum of $15'$ in order to fully recover flux from sources on the cube edge. Cubes are split into two declination ranges for each field and several right ascension ranges, as displayed in Table 3.1. Field Z is not shown as central cube coordinates will depend on examining the reduced data. As a consequence of cubes overlapping, several sources are located in more than one cube and so multiple records of the same source must be carefully filtered out of the final

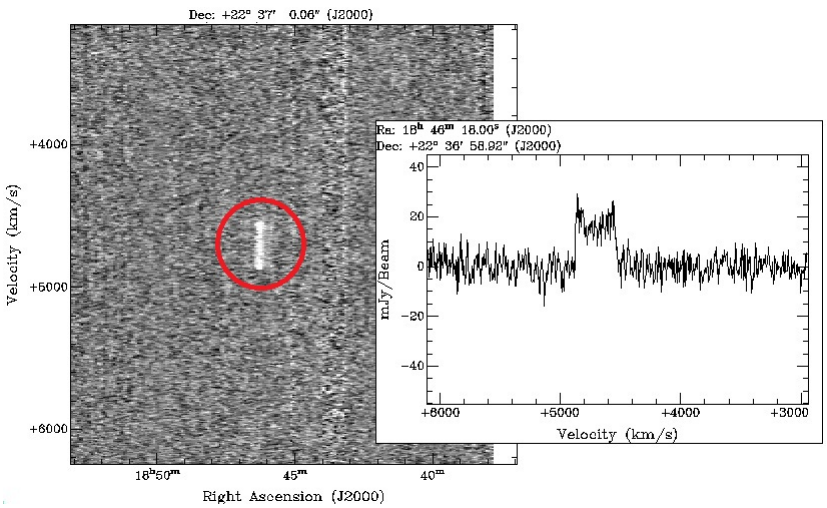

Figure 3.6 A slice of data cube in the RA-Velocity plane. All spectra for a given declination are laid down vertically in velocity space and displayed next to each other spanning the Right Ascension range of the cube. The insert on the right shows the spectrum centered on the detection circled in red.

Table 3.1 Summary of cubes produced for each ALFA ZOA survey field.

Field	Cubes	Cube Size ($' \times '$)	Central RA (hh:mm, hh:mm, ..., hh:mm)	Central Dec (dd:mm, dd:mm)
Field A	22	236 × 286	20:02.5, 19:47.5, ..., 17:32.5	05:37, 01:08
Field B	18	270 × 300	20:22.5, 20:07.5, ..., 18:22.5	14:50, 10:10
Field C	20	225 × 290	21:00, 20:45, ..., 18:45	26:25, 21:55
Field D	22	236 × 286	21:30, 21:15, ..., 19:00	35:27, 30:58

catalog.

Data for A+D fields are sent through a separate data reduction process developed in IDL by ALFA ZOA. Data reduction scripts are presented in Appendix A. A+D field data was saved as a binary file rather than in the standard FITS format. As such, the data cannot be fed directly into LiveData for bandpass calibration. The raw files are read into a data structure using IDL and corrections are applied in order to recover the correct beam positions, Julian date, integration times, and topo- to barycentric velocity conversions. Every 200 ms record contains 100 ms where the low flux

noise diode was on, LOWCALONN, and 100 ms where it was off, LOWCALOFF. These instances are recorded separately for each record. The low flux noise diode is extracted from the bandpass by first identifying the 100 ms where it is on and off for every record, j, and subtracting the two, LOWCAL[j] = (LOWCALON[j]-LOWCALOFF[j])/LOWCALOFF[j]. A median of all occurrences within a lambda is used to create a LOWCAL bandpass that is subtracted from every instance where the low flux noise diode was fired. LOWCAL-removed instances are then combined with instances where the low flux diode was off, into corrected 200 ms records.

The data is then bandpass corrected in IDL in the same way as described for LiveData: total power on-off, (ON-OFF)/OFF, by creating an OFF from a median of all records between $4'$ and $60'$ away from an ON. Records are binned into 1 second integrations using a median combine before bandpass calibration in order to significantly reduce processing time. After bandpass calibration, spectra are resampled from topo- to barycentric frequency and a third order baseline is auto-fitted and subtracted over this spectrum. The high flux noise diode (hical) is then applied to calibrate from reciever units into system temperature. The records that contain the hical are not known a priori and so must be identified by automatic detection and extraction. An IDL script looks for the power, steepness, and the time in the data near where the hical was fired (i.e for 3 seconds near the top and bottom of the lambda). The hical was checked empirically for variation across the observation session, but any variation was not found to be statistically significant and so the records where the hical is fired are median combined across all the locations it was fired for one lambda in order to create a shape for the hical bandpass. The known hical bandpass in kelvin, provided by Arecibo Observatory, is divided by the bandpass measured from observations and every record is multiplied by this calibration per channel in order to convert from power into temperature. This is then multiplied by the gain per beam per altitude per polarization by calling a table of gain values accessible in Arecibo IDL. The files are written out into an SDFITS file with the proper keywords

for gridding with Gridzilla. Data reduction scripts are presented in Appendix A.

3.4 ALFA ZOA Shallow Survey Catalog

3.4.1 Search Method and Source Parameterization

Search method and source parameterization for the ALFA ZOA Shallow Survey follow the same techniques described in Chapter 2. An example of an H I profile from B+C fields is shown in Figure 3.7.

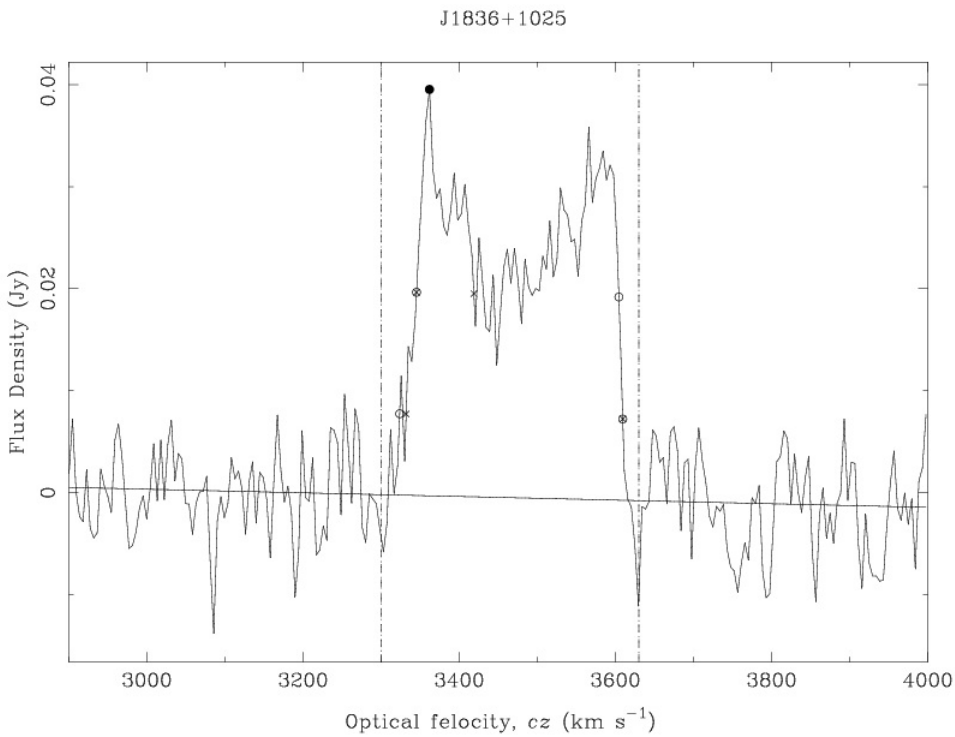

Figure 3.7 H I profile of ALFA ZOA J1836+1025, created from MIRIAD output. Notations are the same as described in Chapter 2.

Though source detection and parameterization is currently done manually for

ALFA ZOA, the automated detection program, *Duchamp* Source Finder (Whiting 2012), was tried on B+C field data. *Duchamp* is a software program that attempts to automatically identify astronomical sources in data cubes with two spatial axes and one frequency axis. *Duchamp* identifies sources by locating groups of contiguous voxels that lie above some user-input detection threshold. *Duchamp* does not look for detections of a certain shape (e.g. double-horn profile) or fit sources with any shape. *Duchamp* outputs the locations and basic parameters of the sources that it finds.

In an attempt to utilize *Duchamp* for ALFA ZOA, a data cube was first searched manually and adjudicated for detections. Then *Duchamp* was run over the same data cube using a variety of input parameters and the results were compared. The basic input parameters for *Duchamp* are snrCut, minPix, and minChannels, where snrCut is the detection threshold for a voxel in multiples of σ above the noise, minPix is the minimum number of contiguous pixels above snrCut, and minChannels is the minimum number of contiguous channels above snrCut. The lowest sensible choice for minChannels is 3, as almost every galaxy has a velocity width greater than 27 km s^{-1}. An ALFA ZOA point source is well fit by a Gaussian inside a $5' \times 5'$ box, so minPix should be 25. Starting with snrCut = 3, the output from *Duchamp* produces too many sources. Increasing snrCut decreased the sources found, but when increased to where *Duchamp* finds the same number of sources as are found manually, the *Duchamp* sources are mostly centered on bright continuum emission and not real. Many different iterations of values for the three main input parameters can be run, but the same problem always results. There are too many fake sources found or too many real sources missed. Ultimately, *Duchamp* was abandoned as a source finder for the ALFA ZOA data set. The cause of the failure is most likely due to the large amount of continuum emission present in the cubes.

3.4.2 ALFA ZOA Survey B+C Catalog

The ALFA ZOA Shallow Survey B+C catalog contains 280 galaxies. Profiles are shown in Appendix B. Table C.3 in Appendix C presents the following information on the catalog:

Column (1). ALFA ZOA source name. Sources with extended emission are labeled with the 'e' superscript.

Column (2). Right Ascension of the fitted position in hours, minutes, seconds, J2000 epoch.

Column (3). Declination of the fitted position in degrees, arcminutes, arcseconds, J2000 epoch.

Columns (4) and (5). l and b, Galactic longitude and latitude in degrees, respectively, of the fitted position in degrees.

Column (6). F_{HI}, integrated flux in Jy km s^{-1}.

Column (7). v_{hel}, heliocentric velocity in km s^{-1}.

Columns (8) and (9). W_{50} and W_{20}, velocity width in km s^{-1} of the profile at 50% and 20% of the peak flux level, respectively.

Column (10). D_{LG}, distance to the galaxy in Mpc in the Local Group reference frame (Courteau & van den Bergh 1999), using Hubble's Law for cosmological redshift distance and taking $H_0 = 70$ km s^{-1}/Mpc.

Column (11). Log M_{HI}, logarithm of the total H I mass in $M_\odot$ calculated from Roberts (1962),

$$M_{HI} = 2.36 \times 10^5 \; D_{LG}^2 \; F_{HI} \tag{3.11}$$

The uncertainties on F_{HI}, v_{hel}, W_{50}, and W_{20} were calculated in the same way as

described in Chapter 2: ALFA ZOA Deep. Several sources are located on the edge of the field and so their flux could not be completely recovered. Their positions are listed in the catalog followed by a semi-colon in order to indicate that they were not measured through the parameterization process described in the previous section. None of their other parameters are derived and so are indicated with ellipses.

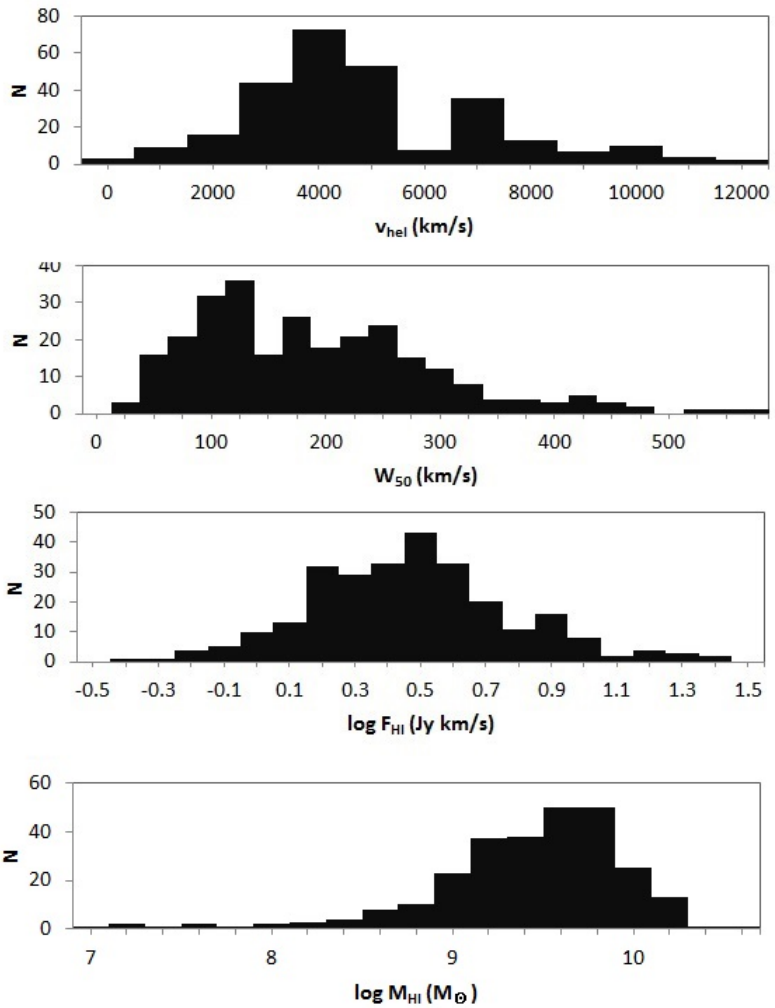

Figure 3.8 Histograms of H I parameters for B+C fields. From top to bottom: heliocentric velocity, velocity width at 50% peak flux, integrated flux, logarithm of H I mass.

Several histograms of parameters from the survey are shown in Figure 3.8. The

histogram of heliocentric velocity shows a distribution of galaxies throughout the detectable velocity range of the survey. The velocity widths show detections of dwarf galaxies with W_{50} as low as 20 km s^{-1} as well as massive spirals with $W_{50} >$ 600 km s^{-1}. The distribution of integrated flux ranges from under 1 Jy km s^{-1} to over 50 Jy km s^{-1}. The distribution of mass ranges from M_{HI}= $10^{6.9}$ to $10^{10.5} M_{\odot}$.

3.4.3 ALFA ZOA A+D Bright Source Catalog

There are 173 detections in the A+D catalog. The A+D catalog is shown in Table C.4 in Appendix C. Histograms of A+D parameters are shown in Figure 3.9. A+D cubes have not been searched by multiple collaborators and the catalog has not been adjudicated yet. This is planned for the near future and an adjudicated list will be prepared for publication. The A+D catalog presented here includes bright sources as decided on by T. McIntyre. A+D field detections are not used for much of the following discussion because the catalog does not have a selection function yet associated with it. A+D field detections are used in this Chapter to discuss large scale structure later on but, by default, most sections will only be using B+C fields for analysis unless otherwise stated.

3.5 Counterparts

3.5.1 Counterparts Catalog

The NASA Extragalactic Database (NED) was searched for extragalactic sources within a radius of 2′ at each B+C field galaxy's position in order to find potential counterparts in the literature. NED was also searched out to larger radii for H I extragalactic counterparts though with velocity constraints (8′ and within 200 km

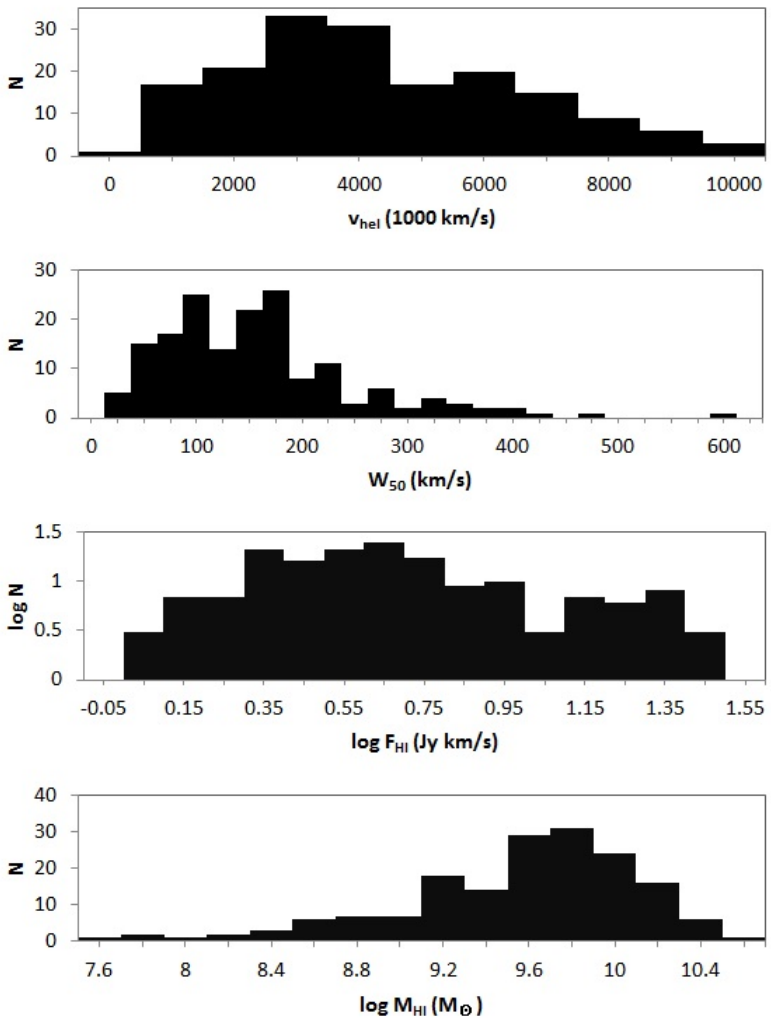

Figure 3.9 Histograms of H I parameters for A+D fields.

s^{-1}). The counterparts are listed in Table C.5 in Appendix C, which presents the following information:

Column (1). ALFA ZOA name.

Column (2). Galactic latitude, b, in degrees.

Column (3). Foreground extinction, A_B, as estimated by Schlafly & Finkbeiner

(2011).

Column (4). Primary name of the counterpart as given by NED.

Column (5). Electromagnetic bands with a cataloged counterpart in the literature labeled for visual (V), near infrared (NIR), far infrared (FIR), and neutral Hydrogen (HI). Detections without a counterpart in the literature that have a counterpart in images from the Wide-Field Infrared Survey Explorer (WISE) are listed at the end.

Column (6). Separation in arcminutes between ALFA ZOA detection and counterpart.

Column (7). Difference in v_{hel} between ALFA ZOA detection and counterpart in km s^{-1}.

A sky distribution of ALFA ZOA detections and galaxies from LEDA (Paturel et al. 2003) within 0 km s^{-1} and 11,500 km s^{-1} is shown in Figure 3.10. There are 152 detections (55% of all sources) that have at least one counterpart. Some positions have more than one counterpart within 2′, and so there are 161 possible counterparts listed in the table. No attempt is made to distinguish between multiple counterparts for the same position unless the counterpart has a known v_{hel} within 200 km s^{-1} of the ALFA ZOA detection. Counterparts for ALFA ZOA detections come from a range of observed bands, including neutral hydrogen. The H I counterparts are denoted with a red dot and come from the The H I Parkes Zone of Avoidance Survey (HIZOA; Donley et al. 2005). Figure 3.11 shows the number of counterparts that come from different parts of the spectrum. The majority of counterparts were detected in the optical and near infrared. Near infrared (NIR) counterparts come from the 2 Micron All Sky Survey (2MASS; Skrutskie et al. 2006) while optical counterparts come from a wide range of observations and surveys. Far infrared (FIR) come from the Infrared Astronomical Satellite (IRAS; Neugebauer et al. 1984). H I counterparts come from a range of surveys.

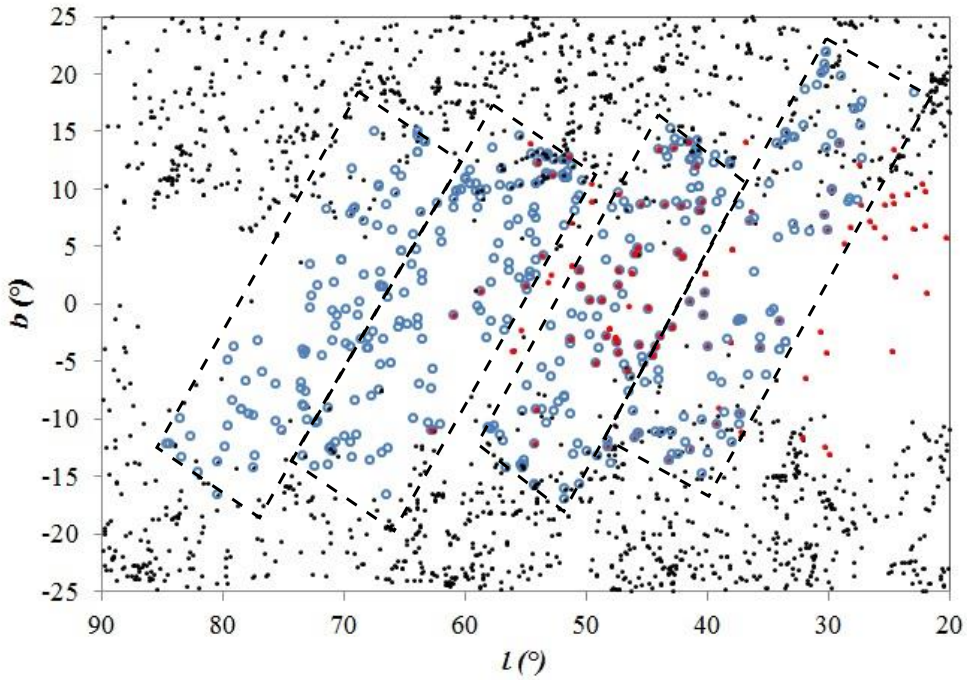

Figure 3.10 Distribution of ALFA ZOA (open blue circles) and LEDA (black dots) detections within the survey area for all velocities between 0 km s^{-1} and 11,500 km s^{-1}. Both B+C and A+D field detections are shown. Small red dots show the location of HIZOA detections(Donley et al. 2005). The ALFA ZOA survey area is outlined (dashed boxes).

Figure 3.12 shows a histogram of ALFA ZOA heliocentric velocities. Detections that have a possible counterpart are coded with a diagonal stripe. The percent of detections with a counterpart is shown in the bottom panel of the figure. While there are fewer counterparts at low and high velocities on average, the decrease is not statistically significant.

3.5.2 Zone of Avoidance

Figure 3.13 shows a histogram of detections per Galactic latitude. There is an increase in detections at high latitude due to large scale structure (Section 3.9).

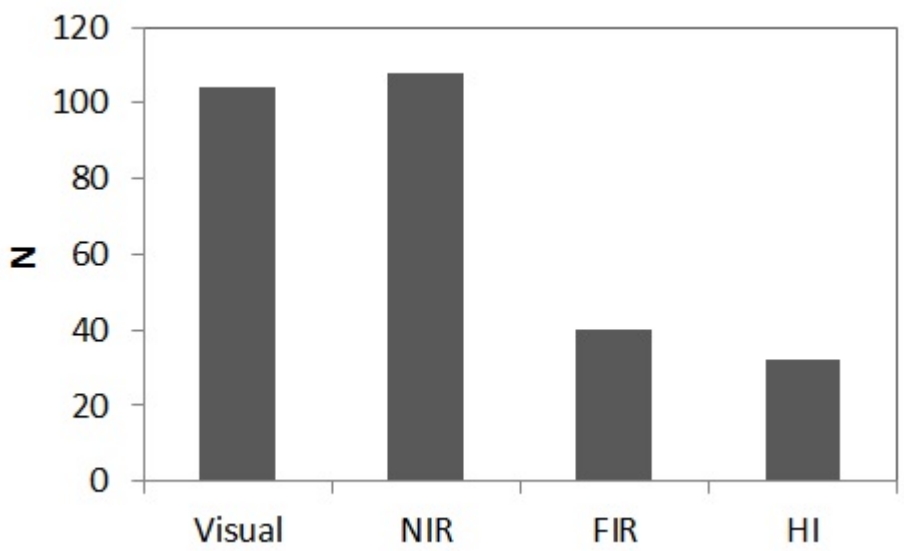

Figure 3.11 Number of counterparts at different bands across the electromagnetic spectrum for B+C fields. Counterparts come from optical, near infrared, far infrared, and 21cm observations (HI).

However, the distribution of detections per latitude with respect to the standard deviation shows that there is no statistically significant change in detections within $|b| < 10^\circ$ across the Galactic plane. That is, there is no Zone of Avoidance. As a comparison, Figure 3.14 shows the number of ALFA ZOA galaxies with a counterpart in the literature as a function of latitude. The percent of ALFA ZOA detections with a counterpart is shown in the right panel and H I counterparts are denoted with diaganol lines. There are no counterparts within a 5° range across the Galactic Plane at a wavelength outside of 21cm. 21% of galaxies have a counterpart within $|b| < 5^\circ$, 57% have a counterpart from $|b| = 5^\circ$ to 10°, and 80% have a counterpart from $|b| = 10^\circ$ to 15°. On average, a one degree bin has 5 percentage points fewer counterparts towards lower Galactic latitude.

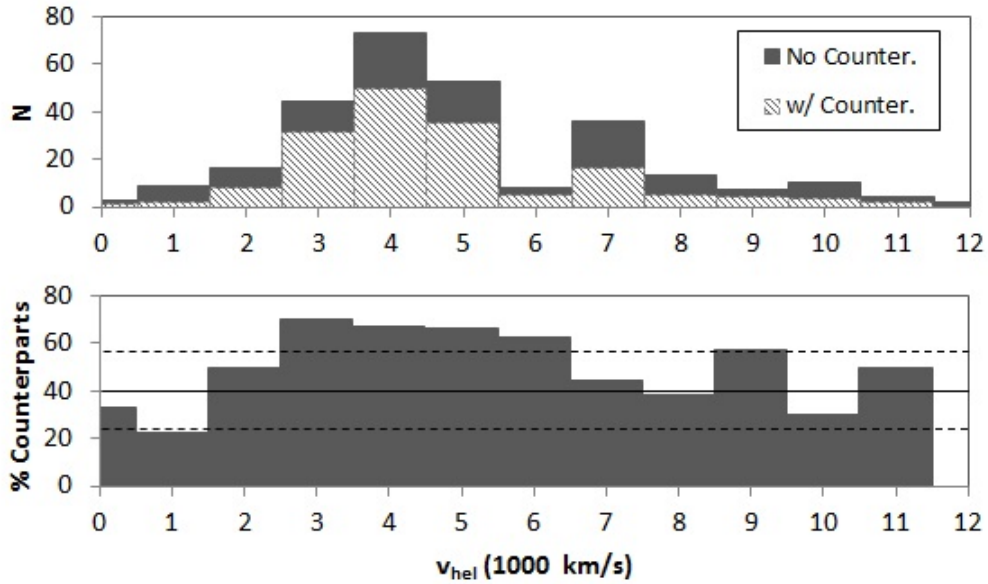

Figure 3.12 Top Panel. Histogram of heliocentric velocities for galaxies with no counterpart (solid) and with a counterpart (diagonal) for B+C fields. Bottom Panel. Percent of detections with a counterpart. The median percent (solid line) and one standard deviation of percents (dashed lines) are shown.

3.5.3 WISE Counterparts

In addition to the search for counterparts within NED, images from the Wide-Field Infrared Survey Explorer (WISE) were also searched in 2′ radii centered on ALFA ZOA detections with no counterpart in NED. WISE mapped the entire sky at mid-infrared wavelengths 3.4μm, 4.6μm, 12μm, and 22μm (Jarrett et al. 2013). The two shortest wavelengths, slightly longer than 2MASS bands, predominantly trace stellar structure. The 12μm band is most sensitive to polycyclic aromatic hydrocarbon emission coming from regions located at the boundaries of H II regions and molecular clouds, and the 22μm band is most sensitive to warm dust from hot H II regions.

There is no WISE galaxy catalog currently published (Jarrett et al. 2013), and so there are no WISE names or fitted positions to use for columns 4 and 6 in Table

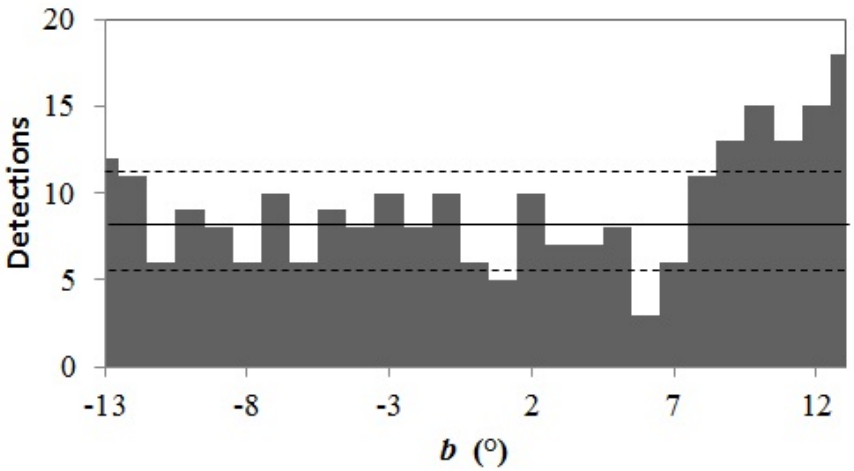

Figure 3.13 Histogram of detections per Galactic latitude. The median of detections per latitude (solid line) and one standard deviation (dashed lines) are shown.

C.5. For this paper, WISE images were searched by one or two authors who determined the existence of a WISE galaxy detection manually using very simple aperture photometry tools available on the NASA/IPAC Infrared Science Archive. Positions with bright 2MASS counterparts were first searched in order to see what galaxies typically look like in the WISE data. These bright galaxies were always identified in the 3.4μm and 4.6μm bands and sometimes were also found in the 12μm and 22μm bands. Therefore, when searching positions without a literature counterpart, WISE counterparts were identified primarily by their extended emission in the 3.4μm and 4.6μm bands. Counterparts were rejected if they were seen in the 12μm and 22μm bands without being identifiable in the 3.4μm and 4.6μm bands because stellar thermal emission is exponentially less bright at longer micron wavelengths, and so only Galactic emission will be seen at the longer wavelengths with no component at 3.4μm or 4.6μm. That is, emission from a galaxy's H II regions will not dominate its stellar emission. There are 21 instances where a possible WISE detection is the only counterpart for an ALFA ZOA source within 2′. A list of these detections is given at the bottom of Table 4. Figure 3.15 shows the percent of ALFA ZOA detections per

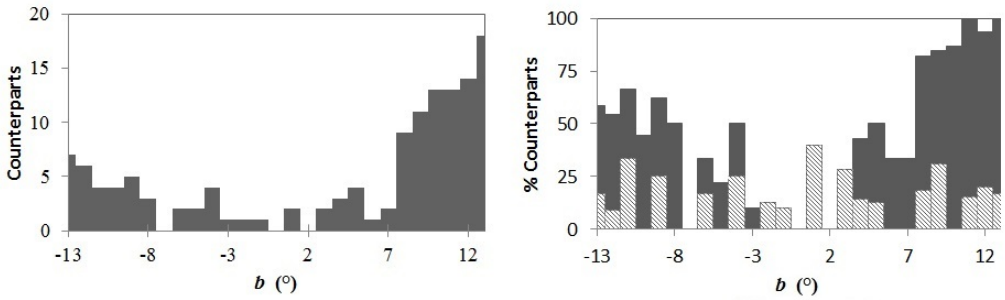

Figure 3.14 Left Panel. Histogram of counterparts per Galactic latitude. Right Panel. Percent of ALFA ZOA counterparts per Galactic latitude. Counterparts from other H I blind surveys are denoted with diagonal lines.

Galactic latitude that have a counterpart when WISE data is included. The percent of counterparts per latitude is significantly increased at low latitude when WISE counterparts are included compared to Figure 3.14. The right panel of the figure shows the fractional increase in counterparts per latitude when WISE is included. It is clear that WISE is more proficient at detecting galaxies to lower Galactic latitudes than what already exists in the literature.

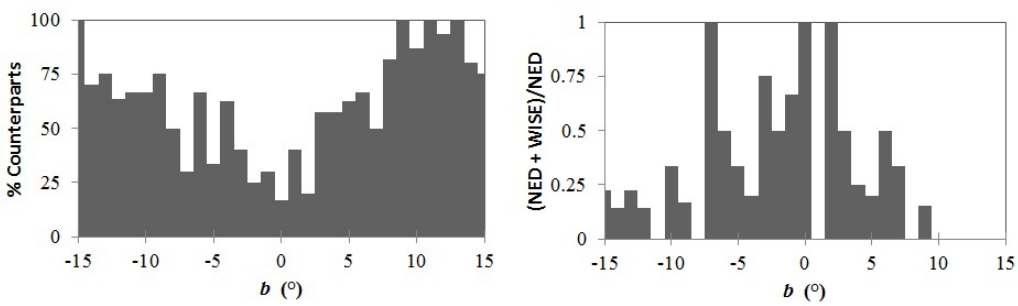

Figure 3.15 Left Panel. Percent of ALFA ZOA detections with a counterpart per Galactic latitude including both NED and WISE. Right Panel. Fraction increase in counterparts per latitude from the inclusion of WISE data.

3.5.4 Galaxy Classification

21cm observations are sensitive to low mass, late-type galaxies that have an abundance of neutral hydrogen and little stellar luminosity (Roberts & Haynes 1994). Galaxies with more abundant reserves of gas will typically have more ongoing star formation and will be bluer in color. By contrast, NIR observations are more sensitive to red stars than blue stars, corresponding with sensitivity to gas-poor systems (Jarrett et al. 2000a). Optical observations in general are the most sensitive to the bulk of stellar colors but are the most hindered by extinction. One would therefore expect a distribution of ALFA ZOA galaxies to have few counterparts in the literature at very low H I masses, as the lowest H I mass sources have the highest fraction of gas to stellar mass (Roberts & Haynes 1994). High H I mass sources and galaxies with broad velocity widths typically have more stars, and so should be more likely to have a counterpart in the literature.

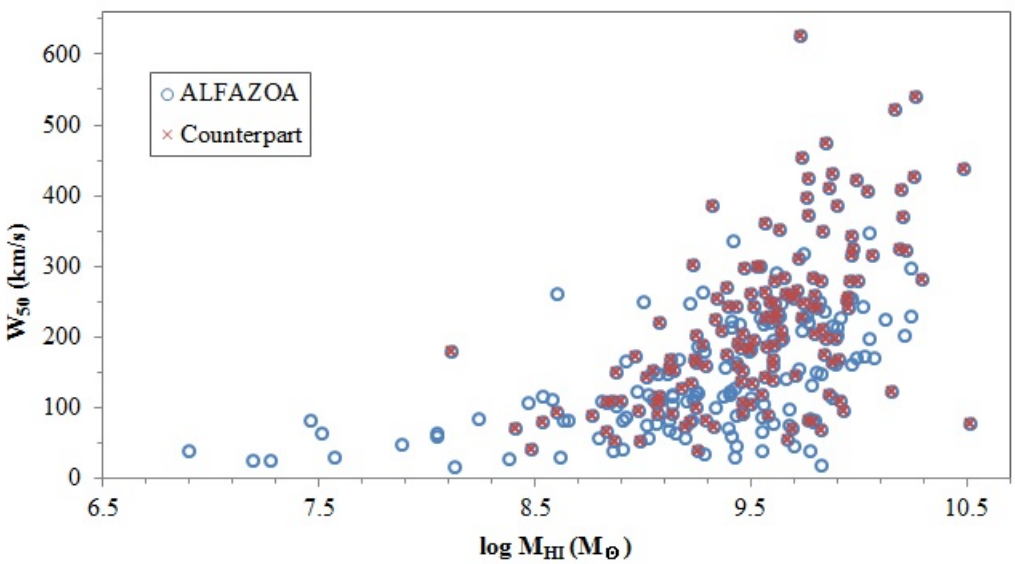

Figure 3.16 W_{50} versus M_{HI} for ALFA ZOA B+C field detections (blue, open circles). A detection is marked with a red x if it has a counterpart in NED.

Figure 3.16 shows velocity width, W_{50}, versus H I mass, M_{HI}, for ALFA ZOA detections, color coded for detections that have a counterpart in NED. The existence of a counterpart may have some dependence on velocity width and H I mass. There are very few galaxies with a counterpart below $W_{50} = 70$ km s^{-1}, and every detection with a velocity width above $W_{50} = 350$ km s^{-1} has a counterpart. The mean velocity width is $< W_{50} > = 215$ km s^{-1} for detections with counterparts versus $< W_{50} > = 179$ km s^{-1} for all detections, though the averages are within one standard deviation of each other. The mean H I mass is $\log < M_{HI} > = 9.54\ M_{\odot}$ for detections with a counterpart versus $\log < M_{HI} > = 9.42\ M_{\odot}$ for all detections, about 30% more massive on average, though the averages are within one standard deviation of each other. At the very lowest H I masses, only one galaxy out of 13 with $M_{HI} < 8.4\ M_{\odot}$ has a counterpart.

3.6 Validity of Parameters

3.6.1 Comparison to the Literature

Figure 3.17 shows the F_{HI} values from the literature versus ALFA ZOA values. Most literature values are from the Parkes survey. A fit to the data gives a slope of 1.05. The standard deviation of literature F_{HI} divided by ALFA ZOA values is $\sigma = 0.38$, and this is shown by the dashed lines in the right panel of the figure. The fit to the slope is not statistically different from 1, and so it is concluded that literature values are not different from ALFA ZOA values, meaning that the data is calibrated correctly.

Figure 3.18 shows a histogram of the difference, Δv, in heliocentric velocity between ALFA ZOA and the literature. The distribution has an average velocity difference of $< \Delta v > =$ -5 km s^{-1} with a standard deviation of $\sigma = 41$ km s^{-1}, indicating

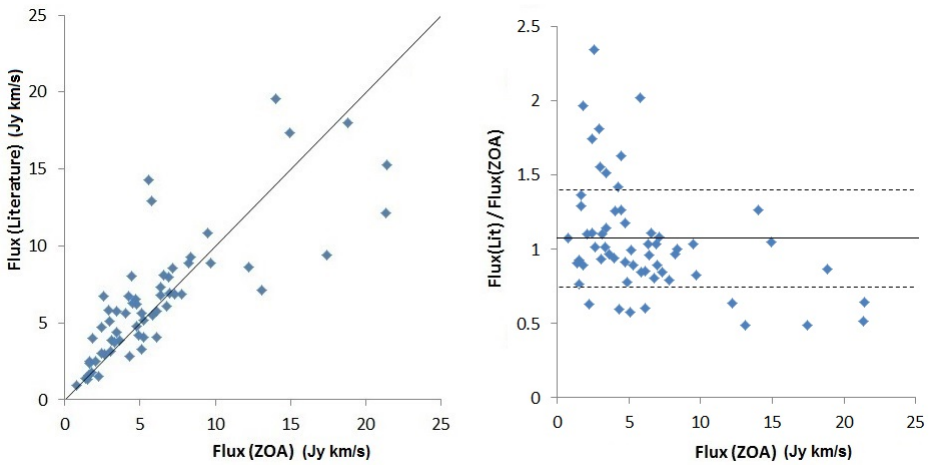

Figure 3.17 Left panel. F_{HI} values from the literature versus ALFA ZOA B+C fields. The black line is a slope of 1. Right panel. Literature F_{HI} divided by ALFA ZOA values. The black line is a fit with a slope of 0 and the dashed lines are one standard deviation.

that there is no systematic offset in ALFA ZOA velocities. While velocities derived from H I observations should have errors on the order of a few km s^{-1}, many velocities in the literature come from optical observations with errors several times higher, hence the broad distribution of the histogram. In fact, the distribution is best fit by a superposition of two Gaussians with standard deviations $\sigma = 50, 18$ km s^{-1}, corresponding with the optical counterpart distribution and H I counterpart distribution, respectively.

3.6.2 Positional Accuracy

The positional accuracy of ALFA ZOA should be well within the FWHM of the telescope (FWHM = 3.4′) because the survey is Nyquist sampled. Figure 3.19 shows the offset in separations, ALFA ZOA minus literature, between ALFA ZOA Shallow detections and their counterparts. The counterpart with the smallest separation is chosen for this plot when there are multiple possible counterparts for the same

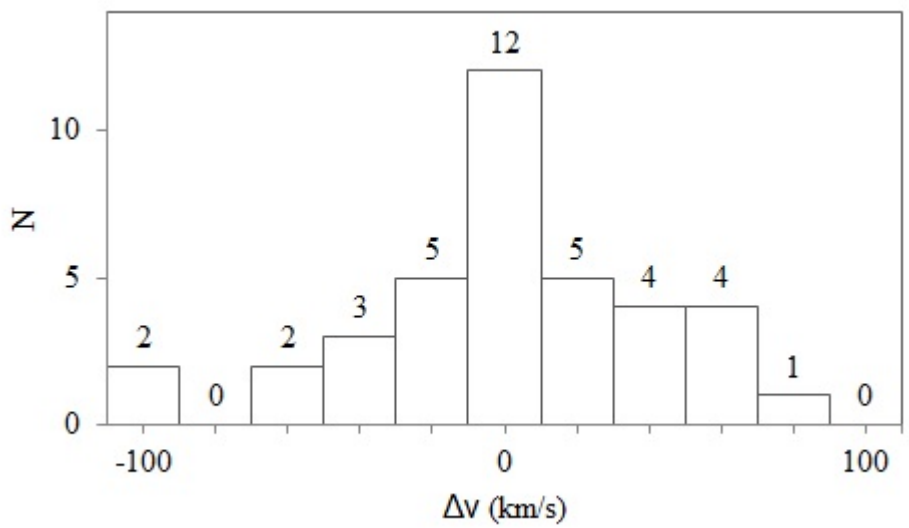

Figure 3.18 Histogram of the difference in heliocentric velocity between ALFA ZOA B+C fields and the literature.

source. Over 93% of counterparts come from optical or infrared observations whose positional accuracies are orders of magnitude finer than the FWHM of ALFA ZOA, meaning that the distribution of separations should be almost entirely due to the positional uncertainty of the ALFA ZOA Survey. There can be intrinsic offset between a galaxy's neutral hydrogen and stellar structure, though offset of a kiloparsec only subtends $6''$ at 2000 km s^{-1}, beyond which over 90% of counterparts are located.

Assuming that the separations in Figure 3.19 are due to uncertainty in ALFA ZOA positions, then their standard deviation is an estimate of the positional accuracy of the survey. The standard deviation of separations is $\sigma = 0.48'$. The true positional accuracy is most likely finer as it is possible that not every counterpart within $2'$ truly corresponds with a detection, but rather happens to fall in the line of sight. Counterparts with known v_{hel} corresponding with an ALFA ZOA detection are most certainly true counterparts. There are 38 optical or infrared counterparts with an associated v_{hel} in the counterparts catalog. Their positional distribution is shown in

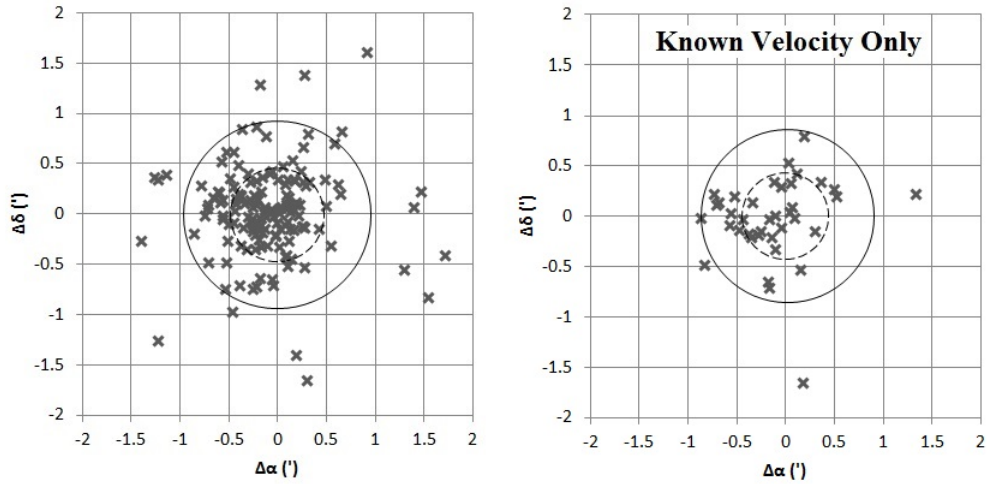

Figure 3.19 Left Panel. Separations (ALFA ZOA minus literature) in right ascension ($\Delta\alpha$) and declination ($\Delta\delta$) between ALFA ZOA B+C fields and NED counterparts, in arcminutes. Right Panel. Same as left panel but only for counterparts with a known heliocentric velocity. The one (dashed circle) and two (solid circle) standard deviations of the separations are shown for each panel.

the right panel of Figure 3.19. The standard deviation of their separations is $\sigma = 0.43'$, which is adopted as the survey's positional accuracy.

There is a median offset in positions in right ascension of $\widetilde{\Delta\alpha} = 0.125'$ to the east. Calculating a Student's t-test, σ_t, for $\widetilde{\Delta\alpha}$ gives,

$$\sigma_t = \frac{\widetilde{\Delta\alpha}}{\sigma/\sqrt{N}} = 3.2, \tag{3.12}$$

where $\sigma = 0.48'$ is the standard deviation of separations and N=152 is the total number of separations. The offset is statistically significant at over 99.8% confidence level, meaning that there is a clear systematic effect causing an offset in source positions. This is likely caused by the meridian nodding observation mode. Sources drift across the telescope beam in right ascension over the 1 s integration time, so that the positions recorded at the start of the integration are offset 0.5 s to the west of their true positions. This causes true positions to be systematically located 7.5″, or 0.125′, to the east of where they are recorded, exactly the same as the median

offset found between ALFA ZOA sources and the literature. Positions reported for the catalog are corrected for the 7.5″ offset. There is no indication that positions are systematically offset in declination.

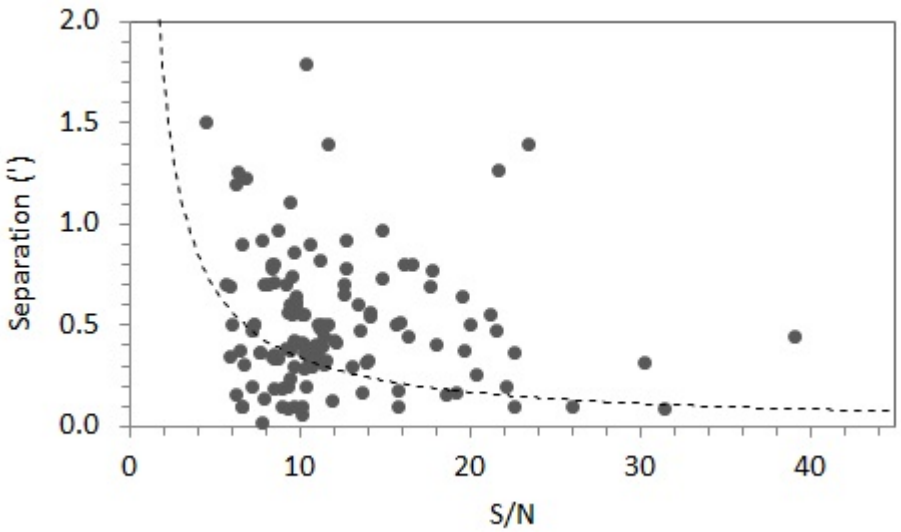

Figure 3.20 Distribution of separations between ALFA ZOA and counterpart positions as a function of signal-to-noise ratio for B+C fields. The dashed curve is FWHM divided by S/N as suggested by Koribalski et al. (2004).

It has been estimated that the positional accuracy for a galaxy is the beam size divided by the signal to noise ratio (S/N) of the detection (Koribalski et al. 2004). It has been shown that signal-to-noise is a function of both integrated flux and velocity width (Giovanelli et al. 2007),

$$S/N = \frac{F_{HI}}{rms\ (2\ \delta v\ W_{50})^{1/2}}, \tag{3.13}$$

where rms is the noise of the survey in Jy, and $\delta v = 9$ km s^{-1} is the velocity resolution of the survey. This estimate for signal-to-noise is adopted for the ALFA ZOA survey. The bivariate dependency of S/N on both flux and velocity width is discussed in more detail in Section 3.7.3. Figure 3.20 shows the distribution of separations between ALFA ZOA and counterpart positions as a function of signal-to-noise ratio. A plot

(dashed curve) of the suggested positional accuracy dependence is shown,

$$Positional\ Accuracy = \frac{FWHM}{S/N}, \tag{3.14}$$

where FWHM = 3.4′. A fit to the data is not presented as no clear fit is identified.

3.7 ALFA ZOA Selection Function

3.7.1 Sensitivity

The noise level of the ALFA ZOA Shallow Survey reached rms = 5.4 mJy (at 9 km s^{-1} velocity resolution) for B+C fields. Figure 3.21 shows a typical cube's rms as a function of heliocentric velocity. The rms was averaged over an inner quarter of the image plane, chosen in an area with a relatively low detection rate in order not to pollute the rms map with brightness temperature from H I detections. Known RFI is labeled using information provided by Arecibo Observatory. H I emission from the Milky Way obscures detections in heliocentric velocities from -100 to +100 km s^{-1}. The increase in noise from 4500 - 5500 km s^{-1} is caused by an intermodulation product (intermod) at 1396 MHz that is on 50% of the time, effectively reducing the number of detections by 50% in that velocity range. An intermod is caused by the introduction of signals at integer sums of frequencies from two or more unwanted signals. The GPS L3 satellite produces RFI at 1381 MHz that spans velocities from 8400 - 8800 km s^{-1}. The sensitivity in this velocity range is reduced to zero. Rolloff from the edge of the bandpass limits the searchable velocities to within 11,500 km s^{-1}.

The sensitivity worsens considerably for A+D fields. The noise is rms = 7.0 mJy (at 20.6 km s^{-1} velocity resolution) for the majority of the bandpass, but increases exponentially beyond 7000 km s^{-1}, as seen in Figure 3.22. The significant decrease

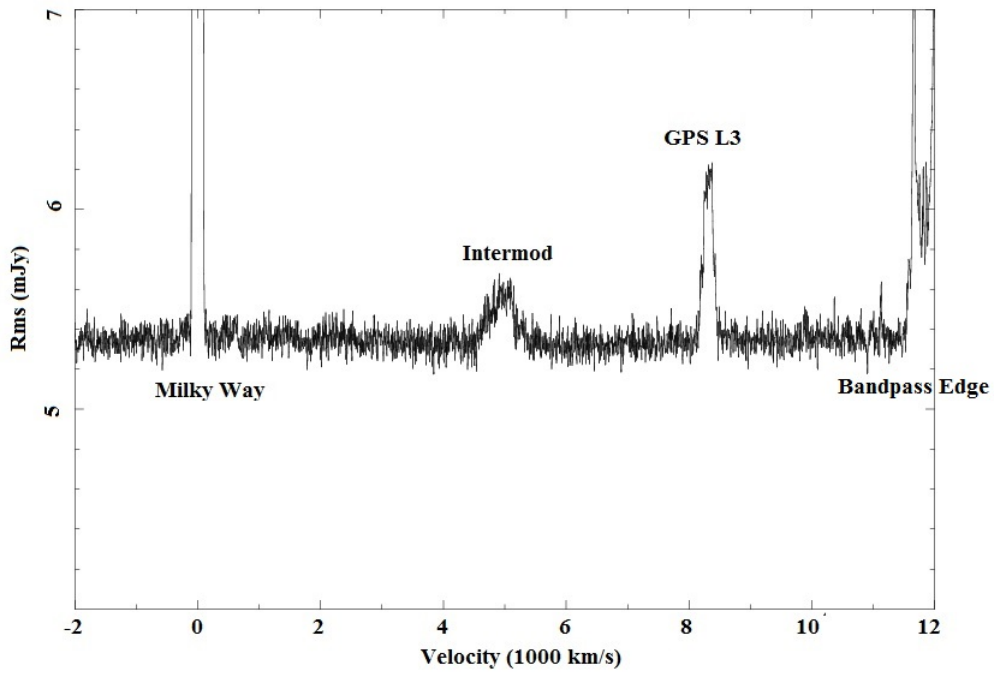

Figure 3.21 Noise in mJy per heliocentric velocity for B+C fields averaged over the inner quarter of the image plane of a typical data cube. Major RFI is labeled.

in sensitivity at velocities beyond 7000 km s^{-1} is due to a low frequency filter used to damp RFI prevalent outside of the protected 1420 MHz band for commensal partners. The intermod at 5000 km s^{-1} is not seen in the data for A+D fields, though RFI from the GPS L3 satellite can been in the figure. Rolloff at the edge of the bandpass reduces the searchable velocities to within 10,500 km s^{-1}.

The sensitivity of the survey is also dependent on the zenith angle (ZA) of the telescope. Figure 3.23 shows the noise of the survey as a function of declination across all fields. The zenith at Arecibo is 18.3°, so ZA = $|18.3° - Declination|$ for data taken in meridian nodding mode. The dependence of sensitivity on zenith angle can clearly be seen, decreasing with increasing ZA across the majority of angles. The

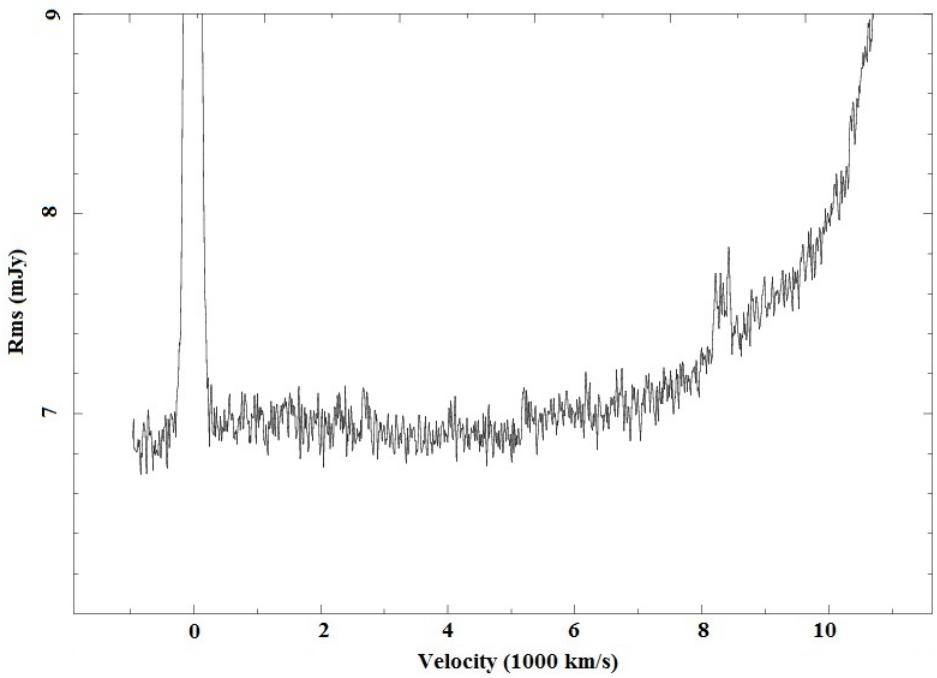

Figure 3.22 Noise in mJy per heliocentric velocity for A+D fields averaged over the inner quarter of the image plane of a typical data cube.

difference in sensitivity between A+D fields and B+C fields can also be seen in this figure.

3.7.2 Reliability

The reliability, $R(S/N)$ of the survey is defined as the chance that a detection is real. To determine the reliability of ALFA ZOA detections, follow-up observations to confirm detections of 13 sources were taken on May 23rd, 2013 and 14 more were taken on November 29th, 2013. Sources were chosen by signal-to-noise ratio, ranging from S/N = 4.2 to 8.4, in order to determine the reliability of the survey as a function of signal-to-noise ratio. This range of S/N values was chosen because blind H I surveys have shown the greatest change in reliability over this range (Cf. Zwaan

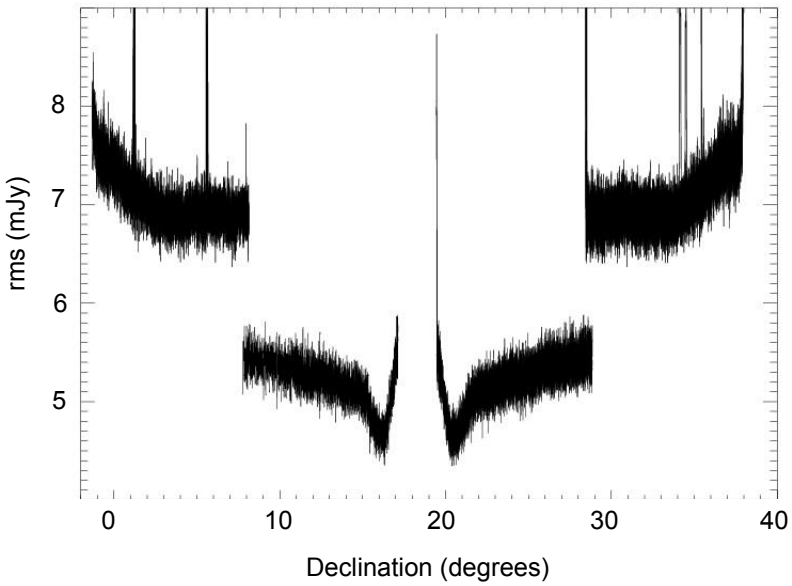

Figure 3.23 Noise in mJy per declination (which equates to zenith angle from the center outward) for A-, B-, C-, D-field from left to right, respectively.

et al. 2004). Follow-up observations were taken with the L-band Wide receiver on the Arecibo telescope for 180 seconds of integration time using a total power on-off observing mode. Data were taken with the WAPP spectrometer with 4096 channels across a bandwidth of 25 MHz giving a velocity resolution of 1.3 $\mathrm{km\,s^{-1}}$ and rms = 2.5 mJy. The data were reduced and parametrized with the standard package of IDL programs provided by the Observatory.

Figure 3.24 shows the results of the follow-up observations as the fraction of detections that were confirmed in bins of signal-to-noise ratio. The errors shown are from Poisson statistics. Most of the bins are made from at least four follow-up observations except for the two smallest S/N bins, made up of two. The reliability of the survey is derived from the fit of this data. The dashed line is the best fit logistic

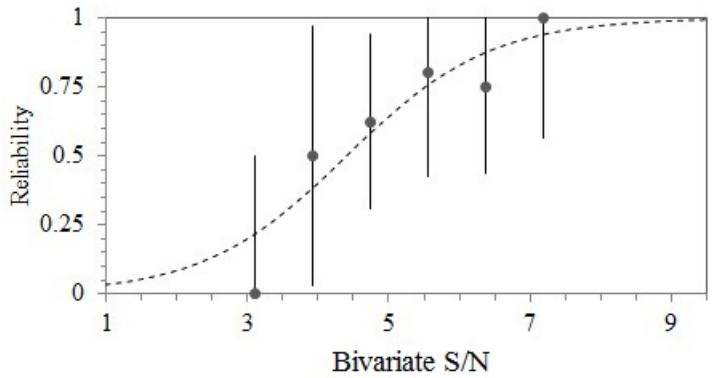

Figure 3.24 The fraction of follow-up observations that are confirmed real as a function of bivariate signal-to-noise. Errors shown are from Poisson statistics. The dashed line is the best fit function.

function (Verhulst 1845),

$$R(S/N) = \frac{1}{1 - e^{-\beta(S/N-\gamma)}} \tag{3.15}$$

where $\beta = 0.99$ determines the steepness of the curve and $\gamma = 4.4$ determines the S/N where the reliability is 50%. As anticipated, the reliability changes considerably over the range of S/N that was reobserved. There are no confirmed sources below S/N = 4 and the survey becomes 90% reliable at S/N = 6.6 with every follow-up observation above S/N = 7 confirming a detection. Figure 3.24 shows the reliability estimate of the original working catalog, though of course the unconfirmed sources are removed from the catalog presented in Table 2. One might expect a source with S/N = 5 to be far greater than 50% reliable, however this should only be the case for finding detections in completely Gaussian noise. The survey baselines are not comprised of only Gaussian noise, but also RFI, continuum emission, and bandpass shapes due to telescope reflections. The overall reliability of the survey, R_{tot} can be calculated as,

$$R_{tot} = \frac{\sum R(S/N)}{N}, \tag{3.16}$$

where N=261 is the total number of parameterized detections. The total reliability of the survey is 97.7% when sources that were confirmed in follow-up observations are assigned an individual reliability of R(S/N)=1. On average, there are likely to be six sources out of 261 in the final parameterized catalog that are not real galaxies. No reliability is associated with the 19 galaxies located overlapping the edge of the data cube that could not be parameterized with Miriad.

3.7.3 Detection Limit

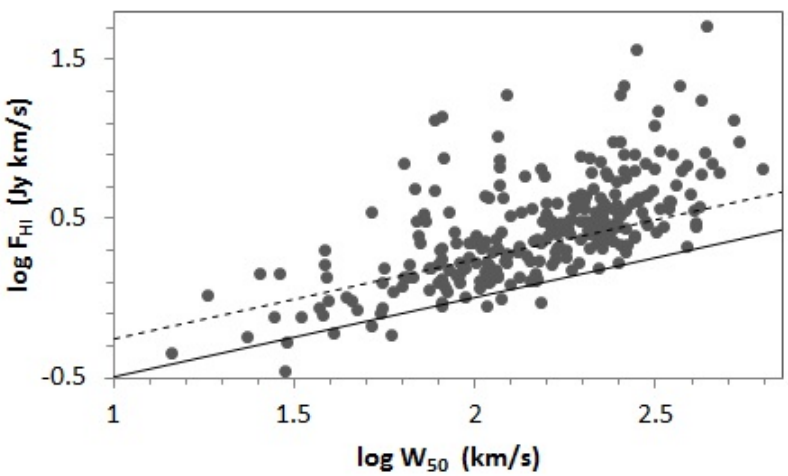

Figure 3.25 Log-log plot of integrated flux versus velocity width for B+C fields. The solid line is the detection limit and the dashed line is the bivariate completeness limit explained in Section 3.7.4.

The detection limit of the survey is defined by ALFA ZOA to be the level at which a detection is 50% likely to be real, R(S/N) = 0.5, occuring at S/N = 4.4. Figure 3.25 shows a log-log plot of integrated flux, F_{HI}, versus velocity width, W_{50}. A relationship between F_{HI} and W_{50} can clearly be seen. A plot of the detection limit using S/N = 4.4 for Equation (3.13) is shown as the solid line. It appears that there could be a change in the slope of the detection limit at $W_{50} > 200$ km s^{-1}, as

is estimated by ALFALFA (Haynes et al. 2011). There is a strong standing wave in the ALFA ZOA bandpass with a velocity width of 200 km s^{-1}, indicating that a drop off in sensitivity at those velocity widths is possible. For the ALFA ZOA data, however, fitting a break in detection limit at $W_{50} > 200$ km s^{-1} (log[200] = 2.3) is not statistically significantly different from using Equation (3.13).

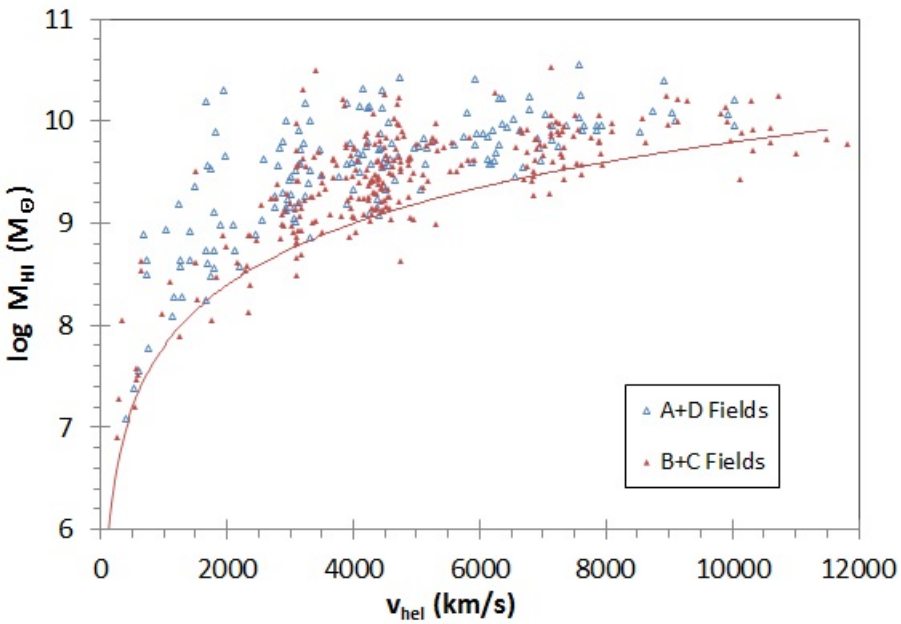

Figure 3.26 H I mass as a function of heliocentric velocity for both the A+D (open blue triangles) and B+C (closed red triangles) fields. H I mass detection limit for S/N = 4.4 is shown for B+C (solid red line) fields.

Figure 3.26 shows a plot of H I mass as a function of velocity for both the A+D (open blue triangles) and B+C (closed red triangles) fields. The difference in sensitivity between the two fields can be seen. The effect on sensitivity from the intermod at 5000 km s^{-1} can clearly be seen for the B+C fields. A lack of detections around 8500 km s^{-1} can also be seen for both fields due to the GPS L3 satellite. The detection limit is shown for B+C fields (solid line). A+D fields do not have a well defined detection limit determined yet. To plot the detection limit in the figure, it

is assumed that W_{50} = 163 km s^{-1}, the mean velocity width of the catalog. For a homogeneous distribution of sources and a flux-limited survey, the distribution of detections in the figure should be most populous near the detection limit. This can be seen for B+C field except in areas of major RFI. There are several more galaxies below the detection limit in Figure 3.26 than in Figure 3.25 because a velocity width must be assumed in order to plot the detection limit in Figure 3.26.

3.7.4 Completeness

For a homogeneous distribution of galaxies in some volume of the universe, the distribution of detections in a flux-limited sample versus integrated flux should follow a -3/2 power law (i.e. as volume increases radially, there are "cubed more" galaxies to detect per inverse square law of flux). A flux-limited sample, like ALFA ZOA, will deviate from this power law below where the sample is not complete. That is, the completeness limit of the sample is the lowest integrated flux, $F_{HI\,lim}$, above which every galaxy can be detected. $F_{HI\,lim}$ can be estimated, then, by fitting a -3/2 slope to a log-log plot of a histogram of flux and identifying the bin where the histogram begins to deviate from the fit.

To estimate the completeness limit, a histogram of log flux is created, and a parameter, ξ^*, is defined as,

$$\xi^* = log(F_{HI}^{3/2}\ \frac{dN}{d\ logF_{HI}}) \tag{3.17}$$

where $dN/d\ logF_{HI}$ is the number of detections in each bin of log flux, similar to the method used by Haynes et al. (2011). Plotting ξ^* per log F_{HI} gives a flat distribution for integrated fluxes above the completeness limit as seen in Figure 3.27. The data is fit from the highest flux to increasingly lower flux bins with a slope of zero, and the completeness limit is determined where the χ^2 of the fit begins to systematically increase. This begins to happen at $logF_{HI}$ = 0.35 Jy km s^{-1}, where the value of ξ^*

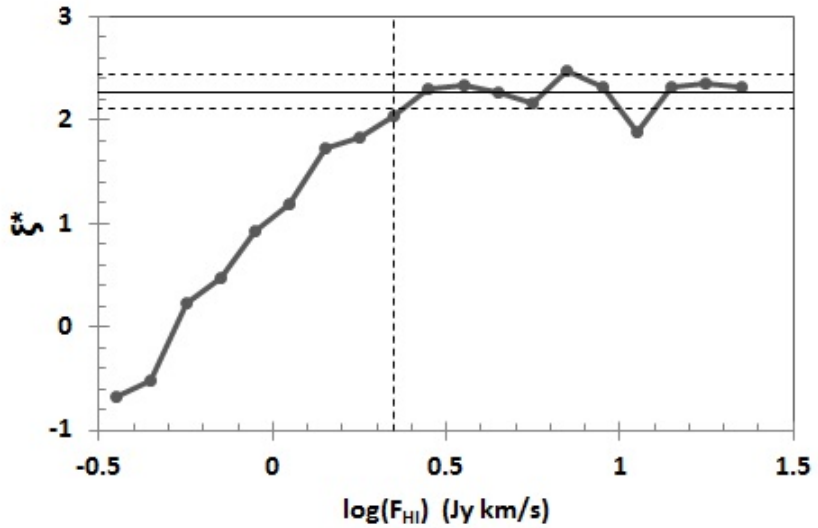

Figure 3.27 Distribution of ξ^* for B+C fields. The horizontal, solid line is the best linear fit with slope = 0. The dashed vertical line is the bin where the data begins to systematically deviate from the fit.

is 1.4σ below the fit. A 1.4σ event occurs 15% of the time in a random distribution, and so the completeness limit, $F_{HI\,lim}$, is concluded to be $F_{HI\,lim} = 2.2$ Jy km s^{-1}. The bivariate completeness limit, $F_{HI}(W_{50})_{\,lim}$ for ALFA ZOA, a function of both integrated flux and galaxy velocity width, is estimated by scaling Equation (3.13) so that $F_{HI\,lim} = 2.3$ Jy km s^{-1} at the median W_{50}. The median velocity width is W_{50} = 163 km s^{-1}, so the bivariate completeness limit can be estimated as,

$$log[F_{HI}(W_{50})_{\,lim}] = 0.5\ log(W_{50\,lim}) - 0.76, \tag{3.18}$$

Figure 3.25 shows the bivariate completeness limit as the dashed line. Because of the relationship between F_{HI} and W_{50}, the distribution of the completeness limit and the detection limit drop off in the same way and so there is a constant offset between the two in log-space. The completeness limit is not yet determined for A+D fields.

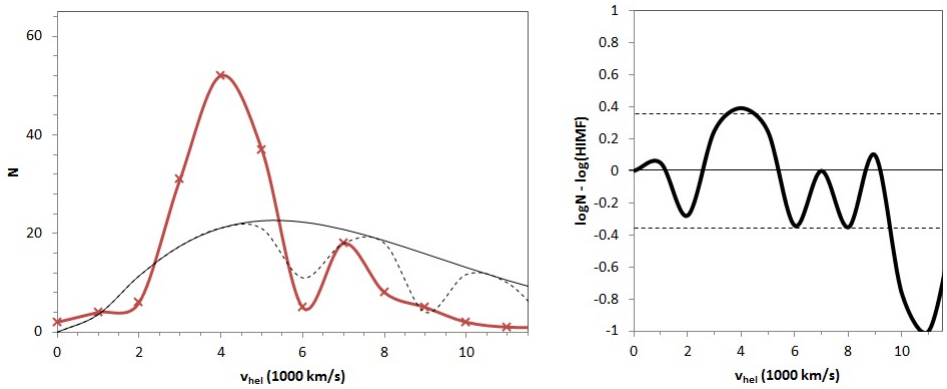

Figure 3.28 Left panel. Distribution of ALFA ZOA detections for B+C fields (thick solid line) that are above the completeness limit, as a function of heliocentric velocity. The expected distribution (thin solid line) from integrating the HIMF (Martin et al. 2010) is shown along with a more robust expectation (dashed line) from taking into account the effect of RFI on the searchable velocity space. Right panel. The log difference between ALFA ZOA and the robust expected distribution. The dashed lines show the 1σ level for a Gaussian distribution.

Homogeneity

The -3/2 power law technique assumes a homogeneous distribution of galaxies. Figure 3.28 shows detections per velocity that are above the completeness limit (thick line) along with the expected number of detections per velocity (thin line). The expected number of detections is calculated by integrating the HIMF at the completeness limit using values from the ALFALFA survey (Martin et al. 2010). As we are expecting to detect every galaxy above the completeness limit, the difference between the two lines is a measure of the homogeneity in the universe above the survey. The variation around mean density should be Gaussian for a homogeneous distribution. There does appear to be a statistically significant drop off in detections at velocities beyond $v_{hel} = 8000$ km s^{-1}, however, RFI limits the sensitivity of the survey over the volume affected by its bandwidth, and so a more robust estimate of the expected distribution of detections is shown (dashed line) by taking into account

the effect of RFI on survey volume. The log difference between ALFA ZOA and the robust expected distribution is shown in the right panel of Figure 3.28. One standard deviation is also shown (dashed line).

When taking into account the effect of RFI, there is only a significant drop off in detections at velocities beyond v_{hel} = 10,000 km s^{-1}. The number of expected detections for $v_{hel} \geq$ 10,000 km s^{-1} is 23.7 while only 4 detections are found over the same range. This is a statistically significant difference from a Gaussian distribution, meaning that the survey volume does not contain a homogeneous distribution of galaxies at velocities beyond v_{hel} = 10,000 km s^{-1}. The completeness limit as a function of survey sensitivity for recent blind H I surveys is given in Chapter 2: ALFA ZOA Deep. $F_{HI\,lim}$ = 2.2 Jy km s^{-1} for B+C fields fits very well with the linear relationship between H I survey noise and integrated flux completeness limit, indicating that any inhomogeneities in the ALFA ZOA galaxy sample are not affecting the determination of the survey's completeness limit.

3.8 The H I Mass Function

3.8.1 Methodology

The HIMF for the ALFA ZOA Shallow Survey Catalog is estimated using the $1/V_{max}$ method (Schmidt 1968). Each H I source is weighted by the total volume, V_{max}, that it could be detected over and the value of the HIMF for a particular H I mass is determined by summing up all of the weights in that H I mass bin. V_{max} is calculated separately for each source by carefully implementing the survey's selection function. The selection function, in terms of estimating the HIMF, is a combination of the survey's bivariate completeness limit (Equation 3.18) and searchable spectral bandpass (Cf. Section 3.7.1) contained within the maximum detectable Local Group centric

velocity-distance, d_{max}. For a given source, d_{max} is determined by the bivariate completeness limit, so that,

$$d_{max} = \sqrt{\frac{M_{HI}}{2.36 \times 10^5 \ [F_{HI}(W_{50})_{\,lim}]}} = \sqrt{\frac{M_{HI}}{2.36 \times 10^{3.73-0.73\ log(W_{50})}}} \tag{3.19}$$

The total volume that a source can be detected within is then,

$$V_{max} = 4/3\ \pi\ (d^3_{max} - \Delta d_{RFI})\ f_{sky} \tag{3.20}$$

where $f_{sky} = 0.011$ is the fraction of the total area of sky searched and

$$\Delta d_{RFI} = \begin{cases} 1 & : d_{max} < 45 \\ (0.5(d^3_{max} - 45^3) + 1) & : 45 < d_{max} < 55 \\ (0.5(55^3 - 45^3) + 1) & : 55 < d_{max} < 84 \\ (d^3_{max} - 84^3 + 0.5(55^3 + 45^3) + 1) & : 84 < d_{max} < 88 \\ (88^3 - 84^3 + 0.5(55^3 + 45^3) + 1) & : 88 < d_{max} < 115 \\ (d^3_{max} - 115^3 + (88^3 - 84^3) + 0.5(55^3 + 45^3) + 1 & : d_{max} > 115 \end{cases}$$

is a correction for the effect of sensitivity limitations on the searchable volume, and all units are in h^{-1}_{100} Mpc. There are four discrete slices of volume where RFI effects the sensitivity of the survey: within heliocentric velocities less than 100 km s^{-1} due to the Milky way, between 4500 and 5500 km s^{-1} due to the intermod, from 8400 - 8800 km s^{-1} due to the GPS L3 satellite, and beyond 11,500 km s^{-1} due to rolloff at the edge of the bandpass. A more detailed explanation of sensitivity in the bandpass and its effect on the searchable volume is described in Section 3.7.1.

The $1/V_{max}$ method works on the assumption of a homogeneous distribution of galaxies. As explained in Section 3.7.4, inhomogeneity in the survey area is shown not to be statistically significant. Another method to check for a homogeneous distribution of galaxies is $< V/V_{max} >$ (Schmidt 1968). That is, the ratios of the volume galaxies are detected within to their maximum detectable volume should be evenly distributed between 0 and 1 with a mean of 0.5 for a homogeneous distribution of

galaxies. $< V/V_{max} >$=0.57 for ALFA ZOA. This is consistent with $< V/V_{max} >$ values for other blind H I surveys that have shown that inhomogeneous distributions on this scale do not significantly impact their HIMF (HIZOA $< V/V_{max} > = 0.54$; Donley et al. 2005, Arecibo Dual Beam Survey (ADBS) $< V/V_{max} > = 0.60$; Rosenberg & Schneider 2002).

3.8.2 ALFA ZOA HIMF

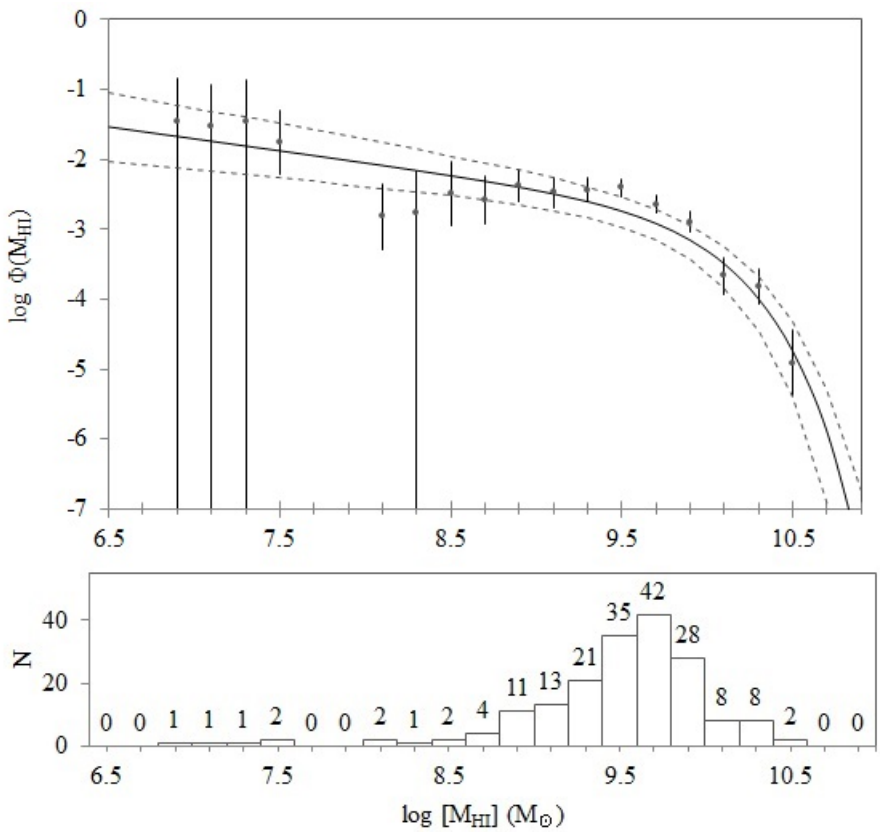

Figure 3.29 ALFA ZOA HIMF for B+C fields. The black curve is a best-fit Schechter function. The dashed lines represent the 1σ errors on the fit. A histogram of M_{HI} for sources used to make the HIMF is shown below the plot.

Estimating an HIMF now simply becomes summing $1/V_{max}$ for each bin of log

M_{HI}. Figure 3.29 shows the ALFA ZOA HIMF for B+C fields for a bin size of 0.2 dex. The HIMF is fit with a Schechter function (Schechter 1976),

$$\Phi(M_{HI}) = \frac{dn}{d\ logM} = \Phi_*\ ln10\ (\frac{M_{HI}}{M_*})^{\alpha+1}\ e^{(-\frac{M_{HI}}{M_*})} \tag{3.21}$$

where $\Phi(M_{HI})$ is the number of H I sources per cubic Megaparsec per dex of H I mass, Φ_* is a normalization factor, M_* is the H I mass in solar masses where the function turns over between high and low mass, and α controls the slope of the low mass end. The error bars on the detections come from Poisson statistics for the number of H I sources in each bin. The number of H I sources in each bin is presented in a histogram below the HIMF. The values for the fit are $\Phi_* = 4.8 \pm 1.1 \times 10^{-3}$, $\log M_* = 9.87 \pm 0.11$, and $\alpha = 1.34 \pm 0.11$. These values are remarkably similar to the most comprehensive HIMF to date (ALFALFA $\Phi_* = 4.8 \pm 0.3 \times 10^{-3}$, $\log M_* = 9.87 \pm 0.02$, and $\alpha = 1.34 \pm 0.02$; Martin et al. 2010), though with errors 3 to 6 times larger. The 1σ errors of the fit are shown as the dashed lines in Figure 3.29. The variance in the fit is likely due to large scale structure influencing the HIMF in discrete bins of H I mass, especially at the low mass end, which is derived from the smallest volume of space. Galaxies with $M_{HI} = 10^{8.5} M_\odot$ must come from within $v_{hel} < 2100$ km s^{-1}. Though it has been shown (Sections 3.7.4 and 3.8.1) that the universe is satisfactorily homogeneous for the sample of ALFA ZOA detections, the large variance on the fit of the HIMF indicates that the sample is not homogeneous for discrete bins of H I mass. Again though, the entirety of the fit is in very good agreement with the most comprehensive HIMF to date. The values for Φ_* and α are almost exactly the same as Martin et al. and M_* is within the error of the fit. Because of this, it is concluded again that the homogeneity of the sample is adequate for determining the HIMF for the global sample even though it may deviate locally.

Summing over all bins gives $\Omega_{HI} = 4.3 \pm 1.1 \times\ 10^{-4}$. Remarkably again, this is the same value found by ALFALFA ($\Omega_{HI} = 4.3 \pm 0.3 \times\ 10^{-4}$), though with an error 4 times larger. Martin et al. determined that the Ω_{HI} derived by ALFALFA

indicates 15% more H I mass in the universe than previously thought. The same is derived by the ALFA ZOA HIMF, though not at a statistically significant level. The HIMF is not estimated for A+D fields yet.

3.9 Large Scale Structure

Figure 3.30 shows a series of sky distribution plots for all ALFA ZOA detections (B+C and A+D fields) alongside the distribution of galaxies from the 2MASS Redshift Survey (2MRS; Huchra et al. 2012) for a variety of velocity ranges. The ability to detect large scale structure across the Galactic Plane can clearly be seen.

Figure 3.31 shows the distribution of ALFA ZOA and 2MRS detections out into velocity-space in a series of wedge plots centered on each of the four ALFA ZOA fields. The central longitude of each field is labeled in the bottom left corner of each plot for reference. Again, the continuation of large scale structure across the Plane can be seen. Named large scale structure is labeled from the density reconstruction maps in the ZOA predicted from 2MRS detections above and below the Plane by Erdogdu et al. (2006). The large scale structure naming convention of Erdogdu et al. is adopted for this paper. Large scale structure uncovered by ALFA ZOA is a useful tool for analyzing the effectiveness of predicting density in the ZOA from detections above and below the Plane. Figure 3.32 shows ALFA ZOA detections overplotted on the density reconstruction maps from Erdogdu et al. The effectiveness of their maps can be examined by referring to Figures 3.30, 3.31, and 3.32.

The Delphinus void is the largest underdensity in the sky at 2500 km s^{-1}. ALFA ZOA only covers a tiny corner of Delphinus, though it discovers a small overdensity inside the edge of the void (l, b, v = 40°, -10°, 1500 km s^{-1}). There appears to be an overdensity at 1500 km s^{-1} that persists as a significant overdensity, spanning velocities 1500 km s^{-1} to 4500 km s^{-1} at (l, b = 30°, +13°), eventually drifting west

towards l = 42° at 4500 km s^{-1} where it connects with the C7 overdensity. This newly discovered structure extends well into the Corona Borealis void out to (l, b, v = 40°, +10°, 4000 km s^{-1}), though the void is confirmed at lower longitudes and latitudes. The C7 overdensity is confirmed from 3000 km s^{-1} to 5000 km s^{-1} at (l, b = 55°, +10°), though it does not appear to extend into the ZOA out to 6000 km s^{-1} over as wide an area as predicted. The predicted connection through the Galactic Plane between C7 and Cξ is confirmed. The biggest discovery in this velocity range is the large scale structure completely bisecting the Cygnus void through the Galactic Plane to connect C7 with the Pegasus overdensity at 4000 - 4500 km s^{-1}. There is clearly a filament between the two overdensities from l = 55° to 85°, contradicting the prediction that the two overdensities were separated by the Cygnus void. ALFA ZOA only intersects Pegasus in a small area, though Pegasus is confirmed as an overdensity from 4000 to 5000 km s^{-1} at (l, b = 80°, -15°).

The Aquarius void is confirmed at l = 80° from b = 0° to -15° and v = 5000 to 7000 km s^{-1}. The unnamed void at l = 60° is confirmed over the same region. The Cξ overdensity is detected from 4500 km s^{-1} to 7500 km s^{-1} at (l, b = 50°, -15°) and it does appear to expand into the ZOA as predicted. A small overdensity is predicted at (l, b, v = 55°, +12°, 7500 km s^{-1}). This is confirmed, but located at a lower latitude, b = +5°. This unnamed overdensity is not detected anywhere above b = +10° and appears to extend significantly more towards b = 0° than expected. Another unnamed overdensity in this velocity range is detected where predicted at (l, b, v = 45°, -15°, 7500 km s^{-1}) and there is some structure connecting these two overdensities across the Plane, where a void is predicted.

3.9.1 Overview of Large Scale Structure Predictions

There are seven named density reconstructions in the Erdogu et al. maps that intersect with the ALFA ZOA survey area. Of the seven, C7, Cξ, Pegasus, and Aquarius

are confirmed to be where predicted. Two voids, Corona Borealis and Delphinus, are not totally contradicted but both have overdensities inside their borders. Corona Borealis is intersected by an unpredicted overdensity that may be a filament of C7. Delphinus contains an unpredicted overdensity just inside its border, though the extent of it is not known as it is on the edge of the survey area. The seventh named density, the Cygnus void, is completely bisected by an unpredicted overdensity that connects Pegasus to C7. Tautologically, the named density reconstructions are confirmed 4 out of 7 times, questionable 2 out of 7 times, and disconfirmed 1 out of 7 times when examined by large scale structure detected in the ALFA ZOA survey. For future work, developing a mass density model for ALFA ZOA data could quantify the accuracy of the 2MRS density reconstructions.

3.10 Conclusion

3.10.1 Summary

The ALFA ZOA Shallow Survey has so far detected 454 galaxies over 1100 square degrees behind the Milky Way. The survey reached its expected sensitivity of rms = 5.4 mJy at 9 km s^{-1} channel resolution in 45% of the area (B+C fields), but the sensitivity worsens to rms = 7 mJy at 20.3 km s^{-1} channel resolution for the rest of the area (A+D fields). The positional accuracy of the survey is 26″ and the survey is shown to have no Zone of Avoidance. 152 B+C field detections (55% of sources) have a possible counterpart in the literature, though this is reduced to 21% within $|b| < 5°$. A fully adjudicated source catalog shows the survey to be complete above integrated flux, $F_{HI} = 2.2$ Jy km s^{-1} for B+C fields. An HIMF is estimated using the survey's selection function and the values of the best-fit parameters are very similar to ALFALFA. The values for the ALFA ZOA fit are $\Phi_* = 4.8 \pm 1.1 \times 10^{-3}$,

$\log M_* = 9.87 \pm 0.11$, and $\alpha = 1.34 \pm 0.11$. The estimate for the H I critical density is $\Omega_{HI} = 4.3 \pm 1.1 \times\ 10^{-4}$.

The survey confirms the extent of the C7, Cξ, and Pegasus overdensities, as well as the Aquarius void behind the Milky Way. The Corona Borealis, Delphinus, and Cygnus voids are not where predicted. Three out of seven large scale structures from density reconstruction maps are not found in ALFA ZOA where predicted. Additionally, an unpredicted overdensity, starting at (l, b, v = 30°, +13°, 1500 km s^{-1}) and connecting with the C7 overdensity at (l, b, v = 42°, +13°, 4500 km s^{-1}) is also discovered.

3.10.2 Future Work

ALFA ZOA A+D fields have not yet been searched by multiple group members, and so this is planned for the near future. Why these fields have a much lower sensitivity than B+C is not currently known. A+D should not be at a lower sensitivity because they were observed in the same way. It would be ideal to solve this problem though ideas by current group members have been exhausted. Z field has not gone through the data reduction process yet and so this is also planned. Once A+D+Z fields are searched and adjudicated, their selection function can be determined and used to estimate an HIMF.

Automated source detection software was not successful for finding detections effectively in the ALFA ZOA data set. Developing a program to automate source detection is something that should be worked on for future H I ZOA surveys as the increased sensitivity of future telescopes makes the number of sources unmanageable for manual detection. In the era of square kilometer area radio astronomy, various search algorithms are being developed for source detection (e.g. Whiting & Humphreys 2012) that could prove useful for H I ZOA surveys going forward.

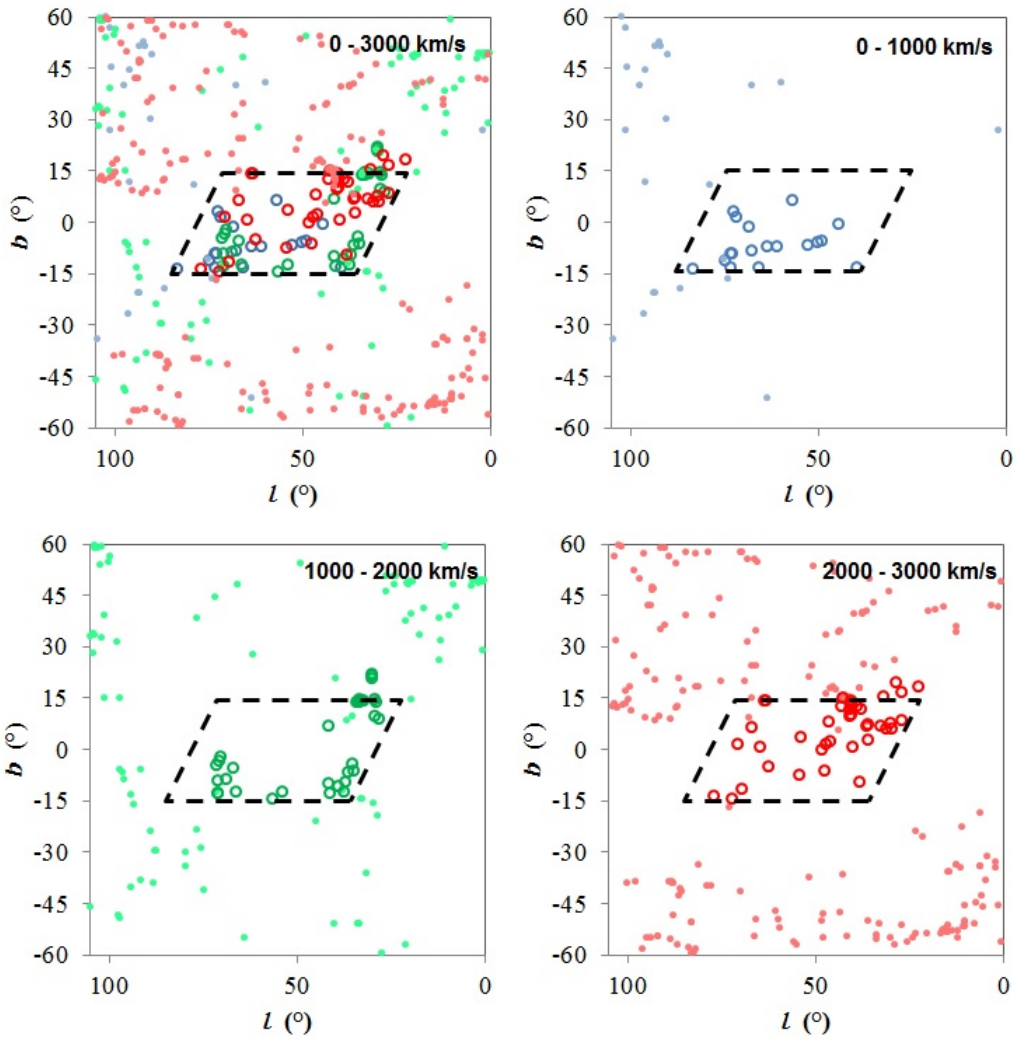

Figure 3.30 Distribution of ALFA ZOA (open circles) and 2MRS (closed circles) detections in 3000 km s^{-1} slices. The top left plot is color coded in 1000 km s^{-1} sub-slices from near (blue) to far (red). The next three plots show only the 1000 km s^{-1} sub-slices. The range of heliocentric velocities covered by each plot is labeled at the top. The dashed box indicates the approximate survey area.

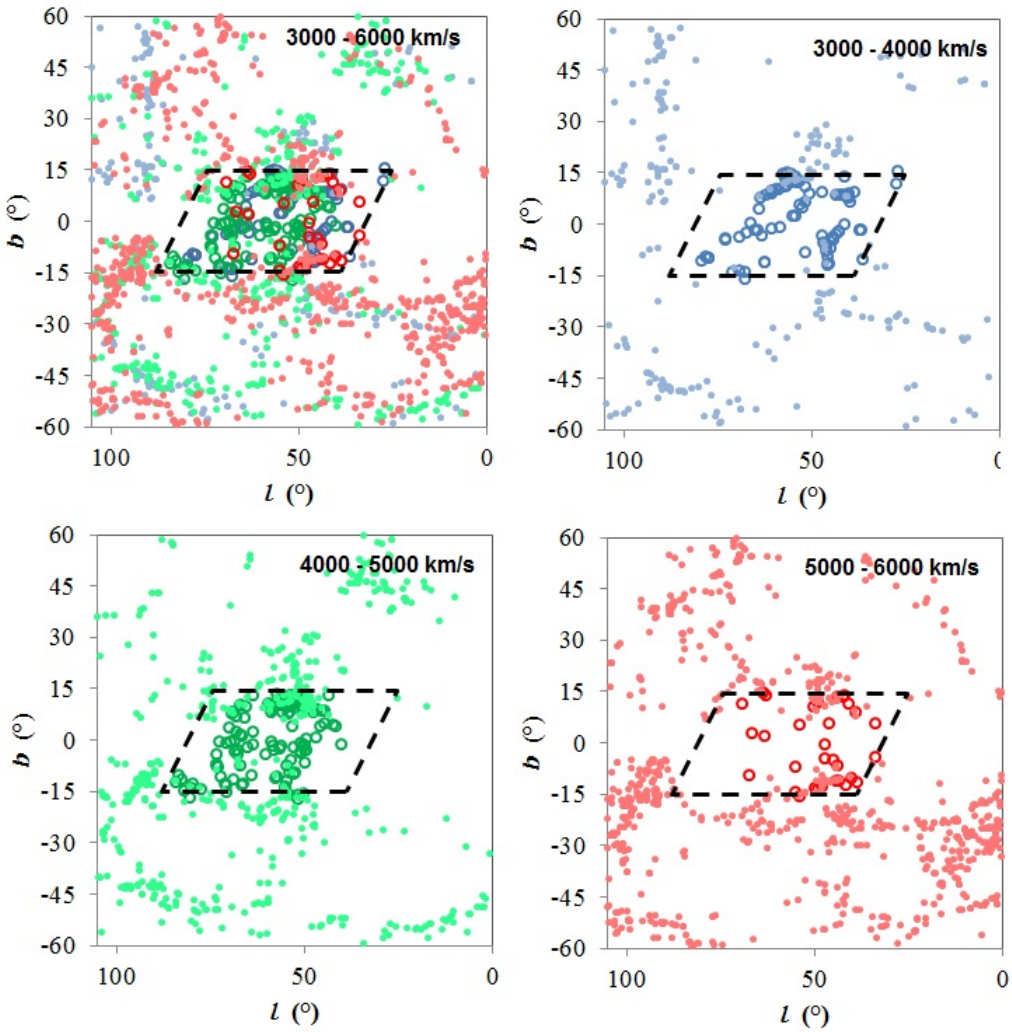

Figure 3.30 (continued)

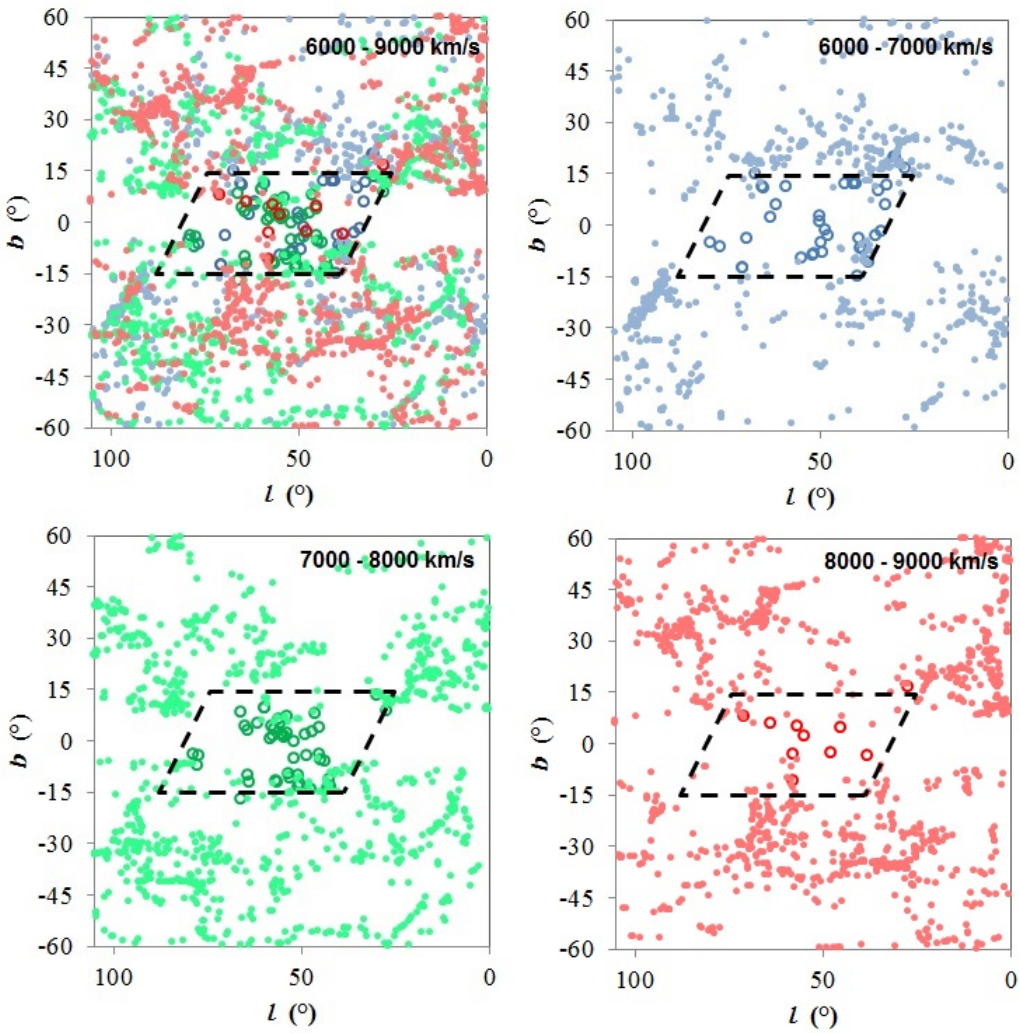

Figure 3.30 (continued)

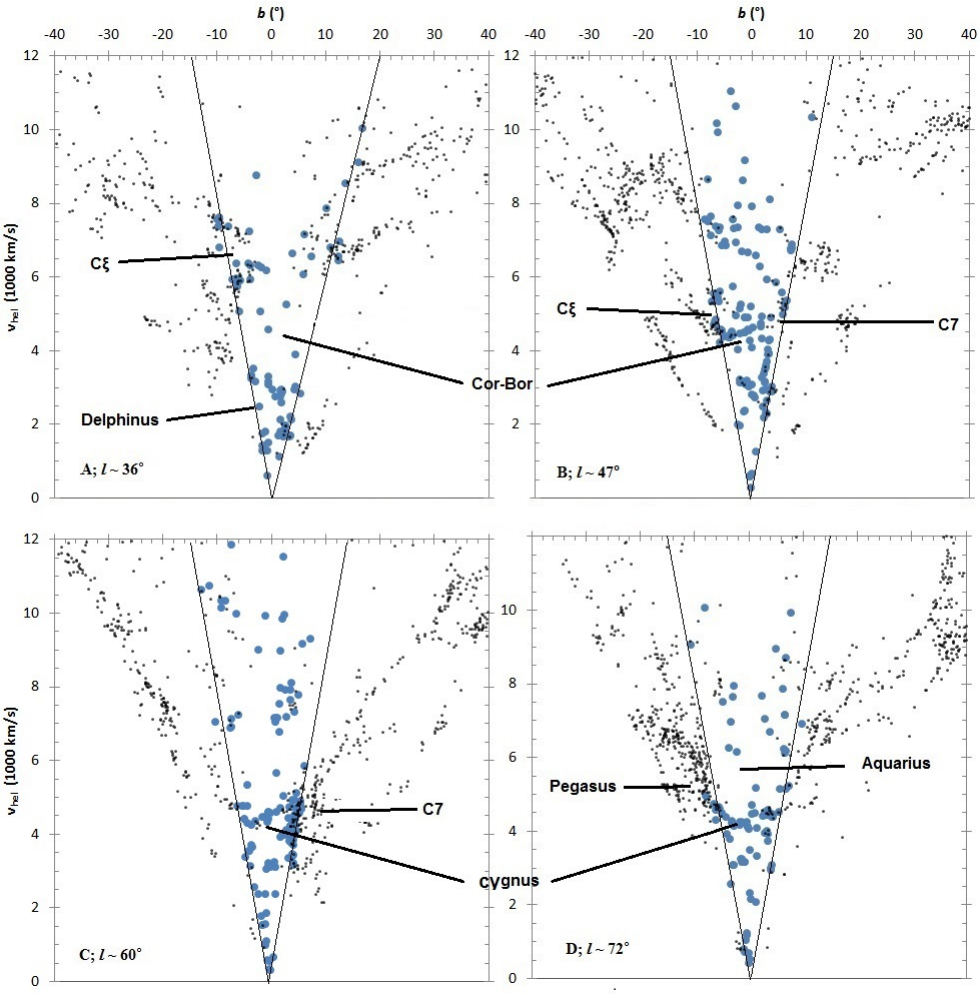

Figure 3.31 ALFA ZOA (large blue circles) and 2MRS (small black dots) detections in polar coordinates. The distribution of galaxies is shown across Galactic latitude in segments of longitude that correspond with the four ALFA ZOA fields. The fields and their central longitude are labeled in each plot. The survey area of each field is shown by the thin diagonal lines. Named large scale structure is labeled: C7, Cξ and Pegasus overdensities, Aquarius, Corona Borealis, Delphinus, and Cygnus voids.

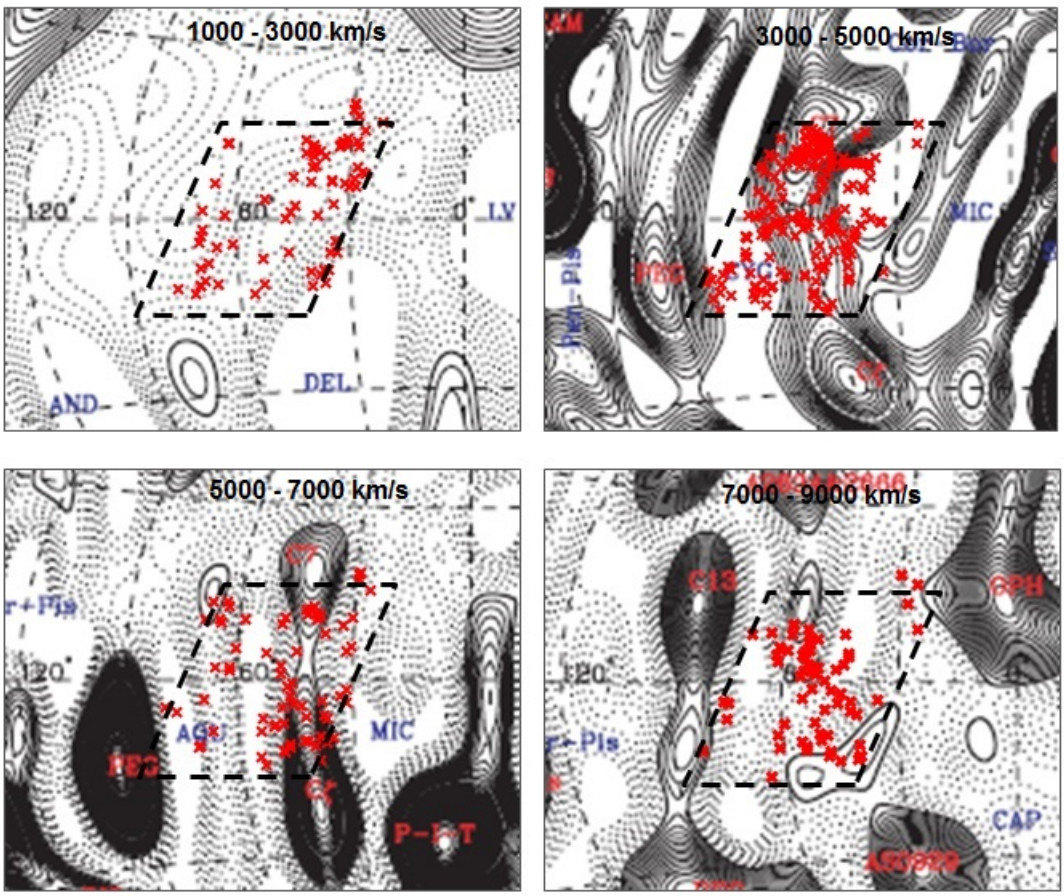

Figure 3.32 Density reconstruction maps from 2MRS data (Erdogdu et al. 2006) overlayed with ALFA ZOA detections (red x's) for several velocity ranges, labeled at the top of each plot. The approximate ALFA ZOA survey area is shown (dashed box).

Chapter 4

Nearby Galaxies in the Zone of Avoidance

4.1 Introduction

It has been suggested (Loeb and Narayan 2008) that undiscovered mass behind the Milky Way ($\sim 10^{12} M_{\odot}$ at 1Mpc or $\sim 10^{15} M_{\odot}$ at 20Mpc) may explain the discrepancy between the cosmic microwave background dipole and what is expected from the gravitational acceleration imparted on the Local Group by matter in the local universe (Erdogdu et al. 2006). As seen in previous chapters, ALFA ZOA can successfully discover galaxies behind the Milky Way. This chapter analyzes nearby galaxies discovered by ALFA ZOA that may contribute to the mass density dipole.

While shallow H I surveys have uncovered a large, spiral galaxy at $\sim$ 3 Mpc (Kraan-Korteweg et al. 1994), and more sensitive surveys have discovered nearby dwarf galaxies (McIntyre et al. 2011, Massey et al. 2003, Begum et al. 2005), H I ZOA surveys have shown that there are no hidden Local Group galaxies with neutral hydrogen mass, M_{HI}, greater than $M_{HI} \sim 10^6$ M$_{\odot}$ in the southern sky (Henning et

al. 2000) and $M_{HI} \sim 10^7$ $M_\odot$ in the northern sky (Henning et al. 1998). A nearby massive spiral ($10^{12} M_\odot$) behind the Milky Way can now largely be ruled out as a way to recover the mass dipole vector. A galaxy cluster ($10^{15} M_\odot$) at 20 Mpc could still affect the mass dipole vector, however, because most of the northern sky is only starting to be surveyed deeply enough to detect a cluster at 20 Mpc with the Effelsberg-Bonn HI survey (ENHIS; Kerp et al. 2011). Results from HIZOA in the southern sky are forthcoming.

This chapter discusses nearby galaxies (i.e within 20 Mpc) detected by the ALFA ZOA survey in order to determine if their mass contributes to the mass density dipole. There are too few galaxies for analysis in the ALFA ZOA deep survey, so this section will examine nearby galaxies from the shallow survey only. Section 4.2 presents the nearby galaxies discovered by ALFA ZOA. Section 4.3 outlines the selection algorithm for galaxy group membership. Sections 4.4-7 analyze ALFA ZOA galaxy groups discovered in an effort to characterize group members and determine overall group dynamical mass. Section 4.8 discusses the range of estimates that are feasible for the dynamical mass of the galaxy groups. Section 4.9 summarizes results and makes suggestions for future work on determining group masses.

4.2 Nearby Galaxies

Nearby galaxies are defined to be galaxies within 20 Mpc, as determined by their Local Group-centered recessional velocity, v_{LG}, and assuming a Hubble constant, H_0 = 70 km s^{-1} Mpc^{-1}. The velocity cutoff for nearby galaxies is v_{LG} = 1400 km s^{-1}. Table 4.1 lists an abridged set of parameters for the 26 galaxies from the ALFA ZOA survey meeting this criterion, sorted by Local Group centered distance, D_{LG}; Column 1 is the source name; Columns 2 and 3 are Galactic longitude and latitude in degrees, respectively; Column 4 is the integrated flux, F_{HI}, in Jy km s^{-1}; Column

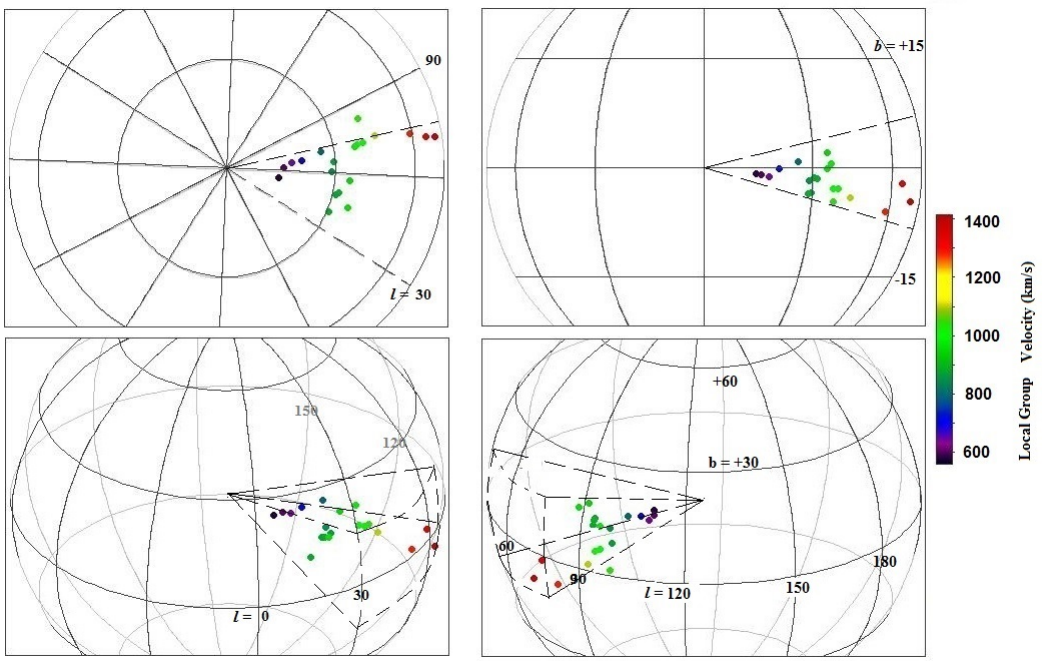

Figure 4.1 Distribution in a spherical coordinate system of ALFA ZOA galaxies within 20 Mpc in Galactic coordinates. Every gridline is 30° apart. Longitude and latitude gridlines are in degrees and labeled around the distribution where appropriate. Detections are color-coded by v_{LG} in km s^{-1}. The dashed lines sketch out the edge of the survey volume. The top left panel is looking down from above the Galactic North Pole. Top right panel is looking across the Galactic center towards low longitudes. The bottom panels are looking down from various high latitude angles.

5 is the heliocentric velocity, v_{hel}, in km s^{-1}; Column 6 is the velocity width at half peak flux, W_{50}, in km s^{-1}; Column 7 is the Local Group centered distance, D_{LG}, in Mpc, Column 8 is the H I mass in $M_{\odot}$. Errors associated with the parameters can be seen in the full catalog table. Figure 4.1 shows the spatial and velocity distribution of these galaxies from several angles. Only ALFA ZOA detections are shown because only ALFA ZOA detections are used to determine galaxy groups by utilizing the survey's selection function (described in Section 3).

Table 4.1 Abridged Parameters of Nearby Galaxies in ALFA ZOA

ALFA ZOA Name	l (°)	b (°)	F_{HI} (Jy km s^{-1})	v_{hel} (km s^{-1})	W_{50} (km s^{-1})	D_{LG} Mpc	M_{HI} ($M_\odot$)
J1952+1429	52.83	-6.41	0.8	274	38	7	6.9
J2018+2319	63.73	-7.07	1.4	299	26	7	7.3
J2032+2559	67.72	-8.12	7.0	339	64	8	8.0
J2008+3052	68.80	-1.02	1.5	410	61	9	7.5
J1950+0008	39.93	-13.06	2.0	606	102	11	7.7
J1940+1154	49.21	-5.25	1.4	580	29	11	7.6
J2012+2114	61.14	-6.93	0.6	543	24	11	7.2
J1944+1238	50.27	-5.71	1.2	592	63	11	7.5
J2000+3632	72.79	3.27	1.8	531	75	11	7.7
J1914+1017	44.76	-0.47	14.0	655	81	11	8.6
J2046+2144	66.14	-13.17	0.9	568	81	11	7.5
J1911+2419	56.90	6.70	10.4	642	116	12	8.5
J2006+3504	72.13	1.57	34.1	686	117	13	9.2
J2050+2946	73.19	-9.03	17.4	716	60	14	8.9
J2050+2959	73.31	-8.82	12.2	731	66	14	8.8
J2137+3410	83.40	-13.44	2.2	750	107	15	8.1
J2103+2953	75.13:	-11.14:	···	795:	···	15	···
J1753+0344	29.58	14.71	2.0	1124	97	17	8.1
J2105+2708	73.31	-13.25	1.8	984	178	18	8.1
J2029+3120	71.75	-4.55	16.3	1041	136	19	9.1
J2045+2811	71.27	-9.19	3.0	1098	69	19	8.4
J1841+1102	41.71	7.12	0.8	1264	47	20	7.9
J1920+0016	36.51	-6.34	4.8	1270	143	20	8.7
J1951+0130	41.34	-12.72	5.6	1266	89	20	8.7
J1940+0040	39.21	-10.56	2.4	1286	70	20	8.4
J2022+3123	70.93	-3.28	2.9	1165	98	20	8.4

4.2.1 Distance Uncertainty

While the error on topocentric velocity is within a few km s^{-1} and the conversion to heliocentric velocity, v_{hel}, is known to very high accuracy, the Local Group centered reference frame is more model dependent and therefore carries a higher error associated with it ($\pm$18 km s^{-1}; Courteau & van den Bergh 1999). The correction factor depends on Galactic longitude and latitude of the source and so is applied differently for every galaxy. Figure 4.2 shows the distribution of corrections applied for converting to Local Group reference frame for the nearby ALFA ZOA detections.

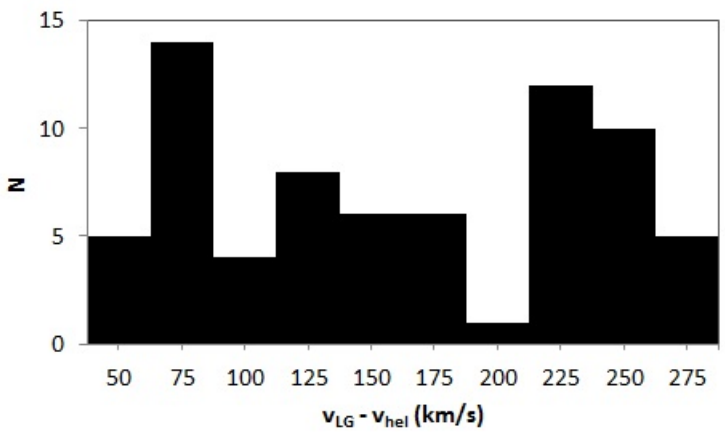

Figure 4.2 The distribution of corrections made for conversion from heliocentric to Local Group-centric velocity for nearby ALFA ZOA galaxies.

While converting to Local Group centered velocities contributes some error to distance estimate, a significantly higher contribution to distance uncertainty comes from the application of Hubble's law. Hubble's law describes the distance between two comoving coordinates, but doesn't automatically take into account the peculiar velocity of galaxies. Galaxies have a dispersion of peculiar velocities in the local universe of $\sigma = 298 \pm 34$ km s^{-1} (Masters 2008). This corresponds with distance error of $\pm$4 Mpc for an individual galaxy from using Hubble's law if the peculiar velocity is completely in the radial direction. Chapter 2 discussed the average statistical

distribution of galaxy inclinations (<i> = 60°), and this same distribution should apply to random peculiar velocities. On average then, cos <i> = 1/2 of a random peculiar velocity will be in the radial direction, so the expected standard deviation on Hubble's law distances is ±2 Mpc.

4.2.2 Local Group Detections

There are probably no Local Group galaxies in the catalog. Detecting galaxies in the Local Group is particularly difficult for ALFA ZOA because Local Group reference frame corrections are all positive in the survey area meaning that a Local Group galaxy in ALFA ZOA must be found at a negative heliocentric velocity, assuming no error on Hubble's law distances. Figure 4.2 indicates that any galaxy with $v_{LG} \sim 0$ must be located at heliocentric velocities ranging from -50 to -275 km s^{-1}. Galaxies at +100 to -100 km s^{-1} will be nearly impossible to detect because of Milky Way emission and galaxies with $v_{hel} < -100$km s^{-1} will be confused with High Velocity Clouds (HVCs). The left panel of Figure 4.3 shows the distribution of HVCs in the Milky Way as a function of Galactic longitude. The ALFA ZOA survey is in an area where HVCs heavily populate the negative velocities. The right panel of the Figure shows the distribution of v_{hel} where Local Group galaxies can be found in the ALFA ZOA survey area. It can be seen that any Local Group galaxy in the survey will be located at the same spatial and velocity coordinates as HVCs. HVCs have a profile shape very similar to dwarf galaxies (or galaxies without clear rotation curves), so there is no way to distinguish between the two objects in a blind neutral hydrogen survey. Any galaxy with a flat-top or double-horn profile can be distinguished from an HVC, though none of these were found in ALFA ZOA. One thing to note is that Figure 4.3 gives strong evidence that none of the nearby ALFA ZOA detections listed in Table 4.1 have been confused for HVCs.

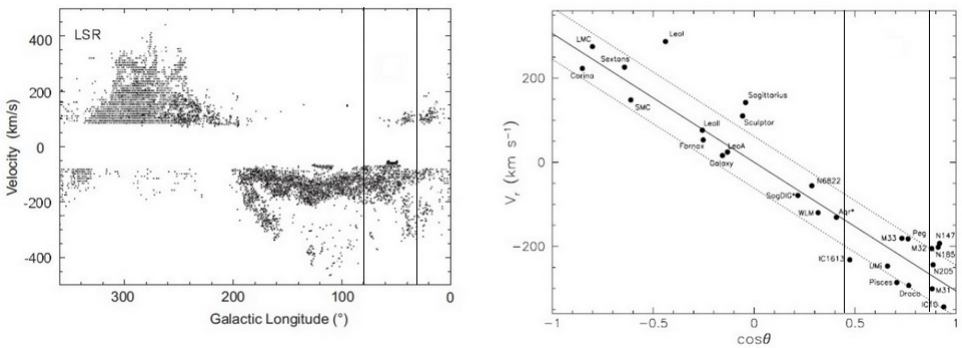

Figure 4.3 The thin vertical lines are the areas within which ALFA ZOA detections will be located. Left Panel. Galactic longitude versus heliocentric velocity distribution of High Velocity Clouds (Morras et al. 2000). Right Panel. Heliocentric velocity versus the cosine of the angular distance from the solar apex. The black dots are Local Group galaxies. The solar motion solution (solid line) of Courteau and van den Bergh ($v = 306$ km s^{-1}, $l = 99°$, $b = -3°$) and the Local Group radial velocity dispersion (dashed lines), $\sigma_r = 61$ km s^{-1} are shown.

4.3 Group Membership

There are several methods for identifying galaxy groups (Bahcall 1988). For this chapter, galaxy groups are identified using simple criteria for a flux-limited redshift catalog modified from Huchra & Geller (1982). A group identity algorithm is defined for galaxies within spatial and velocity constraints of each other, based on the ALFA ZOA selection function. Each galaxy, i, from the catalog is searched for a group companion, j, within a linear separation,

$$D_{ij} = 2sin(\theta/2)\ V/H_0 \leq D_{MHI}(V, M_{HI,i}, M_{HI,j}) \tag{4.1}$$

where

$$V = (v_i + v_j)/2, \tag{4.2}$$

and a velocity difference,

$$V_{ij} = |v_i - v_j| \leq V_{MHI}(V, M_{HI,i}, M_{HI,j}), \tag{4.3}$$

where v_i and v_j are the Local-Group centered velocities of the detections in km s^{-1}, $M_{HI,i}$ and $M_{HI,j}$ are their H I masses, θ is their angular separation, and D_{MHI} and V_{MHI} are weighted distance and velocity that adjust the search volume according to the survey's selection function as described below. If there is no companion found within the constraints of the search algorithm, then a galaxy is not considered a member of a group. Any companions found are added to the list of group membership and subsequently searched as described above for further members, and so on. That is, any galaxy added to a group list is then searched for more group members with the volume associated with its selection function. This process is repeated until no more groups are found. A group consists of a minimum of three members.

D_{MHI} and V_{MHI} are variables that weight the volume searched around a galaxy by the survey selection function. Assuming that the HIMF is independent of distance and position, then the volume of the search can be weighted by the fractional number density of galaxies observed above the completeness limit,

$$D_{MHI} = D_0 \Big[\frac{\int_M^\infty \Phi(M_{HI}) dM_{HI}}{\int_{M_{HI,lim}}^\infty \Phi(M_{HI}) dM_{HI}} \Big]^{-1/3}, \tag{4.4}$$

where $M = (M_{HI,i} + M_{HI,j})/2$, $\Phi(M_{HI})$ is the HIMF, and D_0 is a standard group size. The velocity difference can be weighted in the same way,

$$V_{MHI} = V_0 \Big[\frac{\int_M^\infty \Phi(M_{HI}) dM_{HI}}{\int_{M_{HI,lim}}^\infty \Phi(M_{HI}) dM_{HI}} \Big]^{-1/3}, \tag{4.5}$$

where V_0 is a standard velocity difference. That is, the group membership search volume is a function of group density interactively applied to each galaxy considered for membership. The values for $D_0 = 0.52$ Mpc and $V_0 = 600$ km s^{-1} are adopted from Geller & Huchra (1983).

Applying this method to nearby ALFA ZOA galaxies produces three galaxy groups made up of 14 detections (54% of nearby galaxies). This is very close to the expected fraction of all galaxies found in groups ($\sim 55\%$; Bahcall 1999). Once galaxy

Table 4.2 Overview of galaxy groups within 20 Mpc.

Group	Members	l	b	D_{LG}	M_{tot}
ALFA ZOA GG1	3	64.2°	-7.4°	9.0 Mpc	$5 \times 10^{11} M_{\odot}$
ALFA ZOA GG2	3	50.8°	-5.8°	9.4 Mpc	$3 \times 10^{10} M_{\odot}$
ALFA ZOA GG3	9	72.2°	$-10.6°$	19.1 Mpc	$9 \times 10^{12} M_{\odot}$

groups have been identified in the ALFA ZOA survey, the literature is then searched for additional group members a posteriori. Because the literature is not part of the ALFA ZOA selection function, an assumption is made that $D_{MHI} = D_0$, $V_{MHI} = V_0$. That is, the literature is searched for galaxies within 0.52 Mpc and 600 km s^{-1} of each ALFA ZOA group member. Counterparts in the literature without a known redshift are not considered for group membership. Only literature counterparts within 0.52 Mpc and 600 km s^{-1} of an ALFA ZOA group member are considered.

One additional galaxy is assigned to a group using these criteria. In addition, several galaxies are assigned to a group that were not listed in Table 4.1 because they have a redshift velocity that corresponds with a distance beyond 20 Mpc when using Hubble's Law, which does not take into account peculiar motion as the selection criteria does. An overview of nearby galaxy groups is listed in Table 4.2; Column 1 is the group name; Column 2 is the number of galaxies in the group; Columns 3 and 4 are Galactic longitude and latitude of the geometric group center, respectively; Column 5 is the Local Group-centered distance to the geometric group center, D_{LG}, from using Hubble's law; Column 6 is an estimate for the total mass of the group (explained in Sections 4-7). The error on distance estimates is ± 2 Mpc, as discussed in Section 4.2.1. The uncertainty on total mass estimates is quite high, about an order of magnitude, and is discussed in detail in Section 8.

A distribution of group membership is plotted in Figure 4.4. Details of group members are presented in Table 4.3; Column 1 is the group name; Column 2 is the name of the group member; Column 3 is the linear separation from the geometric

group center in kpc, $2D_{LG}sin(\theta/2)$, assuming all group members at the same Local Group centered distance; Column 4 is the Local-Group centered velocity in km s^{-1}; Column 5 is the H I mass in $M_{\odot}$; Column 6 is the velocity width at half peak flux in km s^{-1}. There is a small uncertainty on Local Group centered velocities and a larger uncertainty on linear separation as discussed in Section 4.2.1. Errors on other parameters can be seen in the full survey catalog. A wide range in linear separations from the geometric group center can be seen. These distances are different from the linear separation, D_{MHI}, used in the group identity algorithm, because D_{MHI} is applied to search for nearest neighbors, not distance from group center.

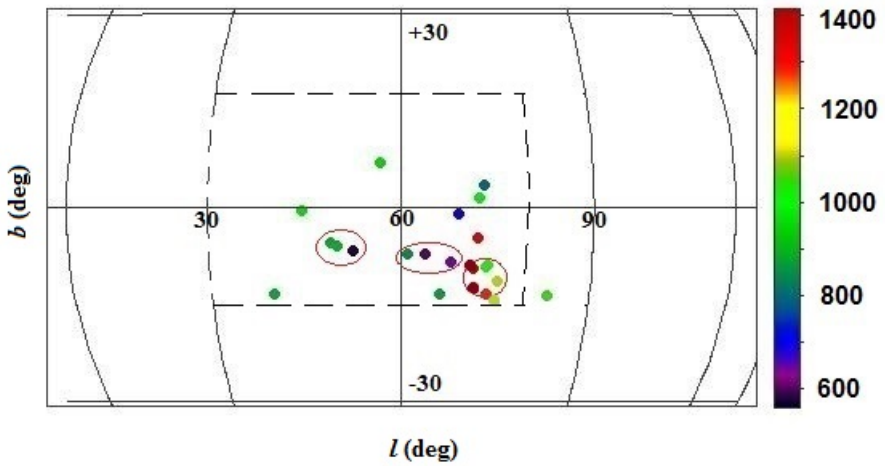

Figure 4.4 Angular distribution of ALFA ZOA galaxies within 20 Mpc in Galactic coordinates. Every gridline is 30° apart. Gridlines are labeled in degrees. Detections are color-coded by v_{LG} in km s^{-1}. The locations of the three groups discovered are circled in red. ALFA ZOA survey area outlined by dashed lines.

4.4 ALFA ZOA GG1

GG1 contains three galaxies located within 530 kpc of the geometric center, (l, b, D_{LG} = 64.2°, -7.4°, 9.0 Mpc), assuming that all galaxies are located at the same Local-Group

Table 4.3 Galaxy group members within 20 Mpc.

ALFA ZOA Group	Member Name	Separation (kpc)	v_{LG} (km s^{-1})	M_{HI} ($M_\odot$)	W_{50} (km s^{-1})
GG1	J2012+2114	530	767	1.6 $\times 10^7$	24
GG1	J2018+2319	80	532	1.9 $\times 10^7$	26
GG1	J2032+2559	530	585	1.1 $\times 10^8$	64
GG2	J1940+1154	290	755	3.8 $\times 10^7$	29
GG2	J1944+1238	90	772	3.3 $\times 10^7$	63
GG2	J1952+1429	300	465	9.5 $\times 10^6$	38
GG3	J2045+2811	565	1337	2.6 $\times 10^8$	69
GG3	J2050+2959	680	980	5.6 $\times 10^8$	66
GG3	J2050+2946	617	965	7.8 $\times 10^8$	60
GG3	J2103+2953	219	1048	1.1 $\times 10^9$	24
GG3	J2105+2708	919	1228	1.3 $\times 10^8$	178
GG3	J2057+2557	737	1752	1.8 $\times 10^9$	260
GG3	J2056+2554	739	1755	2.3 $\times 10^8$	82
GG3	J2037+2649	953	1763	1.0 $\times 10^8$	83
GG3	UGC 11707	1569	1199	5.0 $\times 10^9$	186

centered distance. None of the members have a counterpart in the literature within $2'$ in NASA Extragalactic Database (NED). None of the galaxies have a potential counterpart in Wide-Field Infrared Survey Explorer (WISE) images. The average linear separation between nearest neighbors is 360 kpc, and the maximum is 410 kpc.

4.4.1 ALFA ZOA J2018+2319

The H I profile of J2018+2319 is shown in Figure 4.5. Interferometric follow-up observations of ALFA ZOA J2018+2319 were carried out to obtain high-resolution H I imaging. J2018+2319 was observed on July 14th, 2011 with the Westerbork Synthesis Radio Telescope (WSRT) using the L-band-21cm receiver in mini-short configuration. Mini-short configuration is a telescope pattern adopted to reduce shadowing effects for sources below 30° declination, where the baselines of the outer four dishes along the movable railtracks are set to 96m. On source integration time

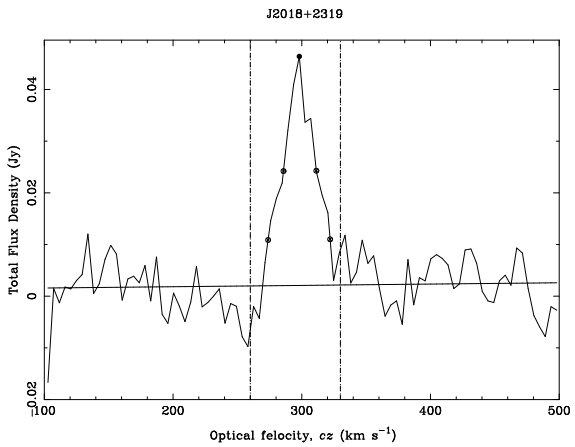

Figure 4.5 H I profile for J2018+2319. Notations are the same as described in Chapter 2.

was 12 hours with an additional 1 hour for calibration and overhead. Observations were conducted using a bandwidth of 5 MHz with 1024 channels giving a spectral resolution of 4.9 kHz (1.24 km s^{-1} at z = 0). 3C147 was used for calibration. The editing, calibration, deconvolution, and processing of the data were carried out in with the Miriad software package (Sault et al. 1995). Data were first inspected and interactively flagged for bad baselines using the task BLFLAG. Line free channels were extracted from the spectral-line data using task UVLIN and averaged to image the continuum in the field of the H I source and to refine the phase and amplitude calibration using task UVMODEL. The resulting phase and amplitude solutions were applied to the spectral-line data set using task UVCAT, and bandpass calibrated UV data was constructed by subtracting the continuum emission. A total intensity (Stokes I) H I image cube was built (the flux calibrator applied) and CLEANed using robust weighting giving a synthesized beamwidth of $26.7'' \times 11.7''$ and an rms noise level of 3.0 mJy beam^{-1} channel^{-1}. Moment 0 (H I flux density) and moment 1 (velocity field) maps were produced from the H I image cube by clipping at 3.0 mJy (1σ). These maps can be seen in Figure 4.6 along with a $3.4\mu m$ band image from the WISE data archive. Galaxies with WISE counterparts are always identified in the

3.4μm and 4.6μm bands and sometimes also in the 12μm and 22μm bands. There is an extended source in WISE near the top right of the image, but it is not determined to be associated with the H I emission.

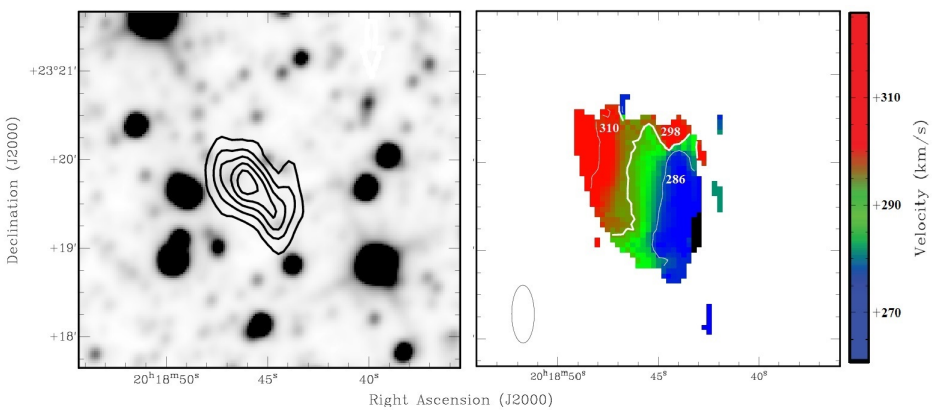

Figure 4.6 WISE 3.4μm band image and WSRT moment maps of J2018+2319. Left. H I flux density map overlayed on a WISE 3.4μm band image. Contours are at 3, 6, 9, 12, 15 σ. Right. Color coded velocity field clipped at 1 σ showing uniform rotation, with contours at 286, 298, 310 km s^{-1}. The WSRT synthetic beam size is shown in the bottom left.

The H I mass, velocity width, and profile shape of J2018+2319 are consistent with a small dwarf galaxy, though high resolution imaging shows uniform rotation as seen in Figure 4.6, indicating a clear axis of rotation. The angular extent of the H I out to 1 M$_\odot$ pc^{-2} is 72$''$ × 30$''$, corresponding with a linear size of 3.1 kpc × 1.3 kpc at the distance of GG1. The elongated shape of the galaxy and its uniform rotation indicate a disk-like galaxy distribution. The inclination, i, can be estimated very generally from the ratio of axes, i = cos^{-1}(1.3/3.1) = 65° assuming a circular distribution, where i = 90° when the galaxy is edge-on. Its total mass, in $M_\odot$, can then be estimated (Rohlfs & Wilson 1996) from the virial Theorem,

$$M_{tot} = 250\ v_{1/2}^2\ R, \tag{4.6}$$

where $v_{1/2} = W_{50}/sin(\mathrm{i})$ is the inclination-corrected velocity width, in km s^{-1}, of the galaxy at 50% peak flux, and R is the radius inside which M_{tot} is estimated, in

parsecs. The virialized mass of J2018+2319 is $M_{tot} = 3 \times 10^9 M_\odot$, making its H I mass fraction around 10^{-2}. This is on the low side compared to the typical H I mass fraction for irregular or dwarf-type galaxies. It is possible that J2018+2319 is a dwarf spiral galaxy given its mass, size, and disk-like structure (Schombert et al. 1995). Also, dwarf spirals are low surface brightness galaxies and there is no counterpart in the literature or image archives, though extinction in the area is high, A_B=2.4 (Schlafly & Finkbeiner 2011).

4.4.2 ALFA ZOA J2032+2559

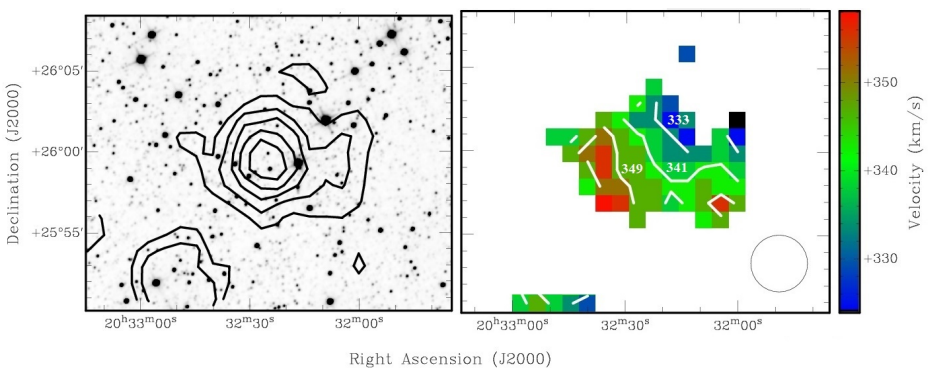

Figure 4.7 WISE 3.4μm band image and ALFA ZOA moment maps of J2032+2559. Left. H I flux density map overlayed on a WISE 3.4μm band image. Contours are at 3, 6, 9, 12, 15 σ. Right. Color coded velocity field showing rotation, with contours at 286, 298, 310 km s^{-1}. The Arecibo FWHM is shown in the bottom right.

J2032+2559 is resolved by ALFA ZOA. The H I flux density and velocity maps are shown in Figure 4.7. There do not appear to be any extragalactic WISE sources in the image. The angular extent of the H I out to 3 σ (16 mJy pixel^{-1}) is $11' \times 8'$, corresponding to a linear size of 28 kpc $\times$ 20 kpc at the distance of GG1. The H I flux density shows mostly circular distribution of hydrogen around the central peak but there is a significant extension of structure to the west. Rotation is seen across the bulk of the H I emission from northwest to southeast, though there is high velocity

dispersion to the southwest. It looks like there is an axis of rotation in the main portion of the galaxy and some type of interaction event happening in the southwest. The angular extent of H I along the rotation axes is $7' \times 6'$ indicating a linear size of 18 kpc $\times$ 15 kpc for the main, disk-like portion of the galaxy and an inclination of 30°. The virialized mass of the disk is $M_{tot} = 3 \times 10^{10} M_{\odot}$ and the H I mass fraction is 10^{-2}, calculated the same as in the last section. J2032+2559 is quite similar to Triangulum in size and total mass, though it has about 10 times less hydrogen content (Corbelli & Schneider 1997). It could be possible that the interaction event is consuming hydrogen and triggering star formation, though this would cause stellar brightness to increase and there are no counterparts in the literature or image archives (including all 2MASS and WISE bands) and the extinction in the area is not particularly high ($A_B = 1.5$). The H I profile of J2032+2559 is shown in Figure 4.8. A follow-up observation of J2032+2559 was taken with WSRT but has not yet been processed.

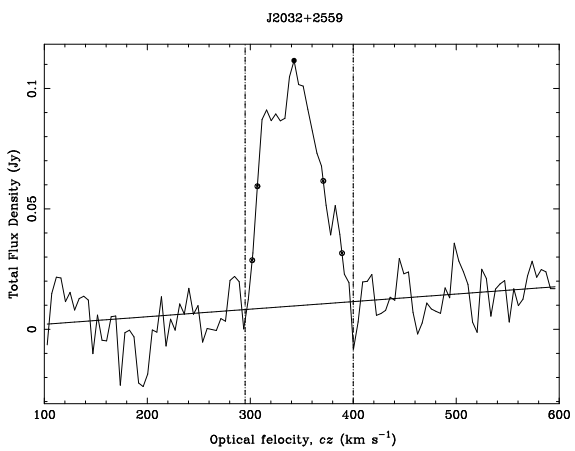

Figure 4.8 H I profile for J2032+2559.

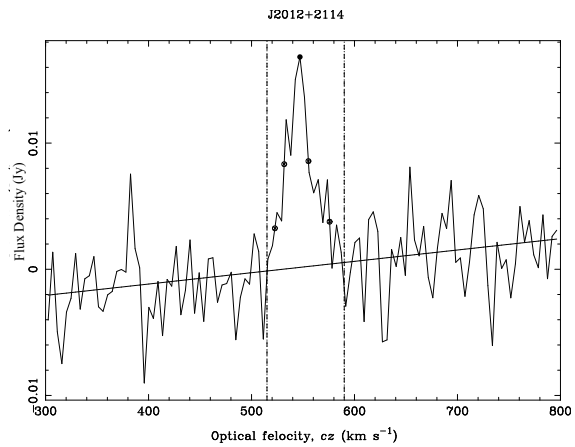

Figure 4.9 H I profile for J2012+2114.

4.4.3 ALFA ZOA J2012+2114

J2012+2114 has the lowest H I mass in the group. It has no counterparts in the literature and is not resolved by ALFA ZOA, putting an upper limit of 9 kpc on the extent of its H I emission. Its H I profile is shown in Figure 4.9. Judging from its H I mass, velocity width, and maximum size, it is likely a dwarf galaxy of some kind.

4.4.4 GG1 Overview

The total H I mass of the group, calculated by summing over M_{HI} for the member galaxies, is $M_{GG1\,HI} = 1.5 \times 10^8 M_\odot$. The lower limit on the total mass of GG1, from summing over the mass of its members galaxies, is $3 \times 10^{10} M_\odot$. This can be compared to the group's virialized mass (van den Bergh 1999), which can be estimated as,

$$M_{GG1} \sim 1.74 \times 10^6 \sigma_r^2 R_h, \tag{4.7}$$

where σ_r is the velocity dispersion in km s^{-1} and R_h is the radius at half mass in kpc. The velocity dispersion (Huchra & Geller 1982) of the group can be estimated

as the median of,

$$\sigma_r = \frac{\widetilde{|v_i - \widetilde{v}|}}{\sqrt{N-1}}, \tag{4.8}$$

where v_i is the velocity of the ith member, $\widetilde{v}$ is the median group velocity, N is the total number of group members. σ_r is determined using the median absolute deviation of velocities instead of the variance because of the low number of group members. The radius at half mass is estimated very generally as half of the average distance from the geometric center in order to obtain an order-of-magnitude estimate for the total mass of the group. The velocity dispersion of GG1 is $\sigma_r = 38$ km s^{-1}. The virialized mass is $M_{GG1} = 5 \times 10^{11} M_\odot$. The uncertainty on the group's virial mass is high because of the number of assumptions and low sample size that go into it. It is not a very robust estimate, in the sense that a change in the method of calculating velocity dispersion or what radius to choose for the measurement can change the estimate non-negligibly. If this estimate is off by an order of magnitude, then the total mass of the group is in good agreement with the lower limit calculated from summing over the mass of members. If this estimate is not off, then there are three likely explanations for the discrepancy between the total group mass and the masses of the members summed. (1) GG1 contains one or more large elliptical or gas-poor spiral or lenticular galaxies containing $\sim 10^{11} M_\odot$ of total mass. ALFA ZOA is complete above $M_{HI} = 4 \times 10^7 M_\odot$ at the distance of GG1 and fully samples the GG1 area of sky. Any galaxy that is contributing meaningfully to the total mass of the group did not go undetected if it has an H I mass fraction greater than 10^{-4}. (2) None of the members of GG1 are actually in the same galaxy group because they are detected as a false positive in the selection criteria. Follow-up observations to determine a redshift-independent distance estimate should constrain linear separations of group members further. (3) GG1 is not a relaxed system and so the virial theorem does not apply.

All three explanations are entirely possible. It may also be possible that the

virialized mass estimate is overly conservative and the total mass is even higher than $5 \times 10^{11} M_{\odot}$. This would indicate that there is some gas deficient massive galaxy with $\sim 10^{12} M_{\odot}$ or $\sim 10^{13} M_{\odot}$ in the group. It is not clear how easily such a galaxy could be discovered at such low Galactic latitude, but discovering more low mass group members could help improve confidence in the virial mass estimate.

4.5 ALFA ZOA GG2

GG2 contains three galaxies located within 300 kpc of the geometric center (l, b, v_{LG} = 50.8°, -5.8°, 9.4 Mpc), assuming that all galaxies are near the same Local-Group centered distance. Two galaxies have counterparts in the literature though none have a potential counterpart in WISE image data. The average linear separation between nearest neighbors is 220 kpc, and the maximum is 300 kpc. The velocity dispersion of the group is $\sigma_r = 12$ km s^{-1}.

4.5.1 ALFA ZOA J1952+1429

Arecibo Observations

J1952+1429 was initially detected with ALFA ZOA at low reliability. In order to confirm the detection, it was followed up with the L-band Wide receiver on the Arecibo telescope for 180 seconds of integration time using a total power on-off observation. Data were taken with the WAPP spectrometer with 4096 channels across a bandwidth of 25 MHz giving a velocity resolution of 1.3 km s^{-1} and rms = 2.5 mJy. The spectrum from the follow-up observation can be seen in Figure 4.10.

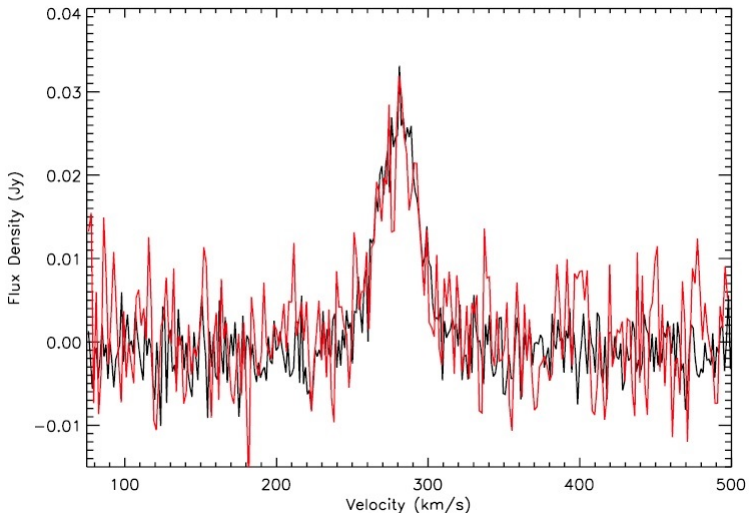

Figure 4.10 Integrated H I spectrum of J1952+1429. The black line is from a follow-up observation with the Arecibo telescope and the red line is from the JVLA observations. The JVLA recovered all H I emission to within 1σ.

JVLA Observations

Follow-up observations were carried out with the Karl Jansky Very Large Array (JVLA) in C-configuration to obtain high-resolution H I imaging of J1952+1429. The observations were scheduled dynamically for 3 × 1 hour sessions and observed on December 3rd and 4th, 2010. Observations utilized the Wideband Interferometric Digital ARchitecture (WIDAR) correlator with 2 MHz bandwidth over 256 spectral channels, resulting in 7.8 kHz (1.6 km s^{-1}) channel width. The on-source integration time was two hours. 3C48 was used to calibrate the flux density scale and the source J1925+2106, 9° from the target source, was used to calibrate the complex gains. The editing, calibration, deconvolution, and processing of the data were carried out in Astronomical Image Processing System (AIPS). Line free channels were extracted from the spectral-line data cube and averaged to image the continuum in the field of the H I source and to refine the phase and amplitude calibration. The resulting phase and amplitude solutions were applied to the spectral-line data set, and a bandpass

calibrated UV data cube was constructed by subtracting the continuum emission. A total intensity (Stokes I) H I image cube was built and CLEANed using natural weighting giving a synthesized beamwidth of $15.13'' \times 13.13''$ and an rms noise level of 2.6 mJy beam^{-1} channel^{-1}. Moment 0 (H I flux density) and moment 1 (velocity field) maps were produced from the H I image cube by smoothing across 3 velocity channels (5 km s^{-1}) and 5 pixels spatially ($20''$ at $4''$ per pixel) and clipping at 2.6 mJy (the 1σ level of the unsmoothed cube). These maps can be seen in Figure 4.11.

The angular extent of the H I out to 1 $M_\odot$ pc^{-2} is $44'' \times 40''$. The H I flux density shows a main peak and a secondary peak $16''$ away that overlaps a region of high velocity as well as significant velocity dispersion. The velocity field shows structure but non-uniform rotation. The integrated flux from the Arecibo and JVLA spectra are 0.94 ± 0.07 Jy km s^{-1} and 0.80 ± 0.13 Jy km s^{-1}, respectively. The JVLA recovered all integrated flux to within 1σ. A comparison of the H I profile between Arecibo and the JVLA can be seen in Figure 4.10.

Optical Observations

Digitized Sky Survey[1] (DSS) images show what looks to be a very faint, uncatalogued galaxy that may be the optical counterpart. The DSS magnitudes of this object from SuperCOSMOS[2] are $m_B = 17.5 \pm 0.3$ mag, $m_R = 17.0 \pm 0.3$ mag. The extinction in the area is relatively low for the ZOA with values estimated to be $A_B = 1.1$ and $A_R = 0.7$, from the DIRBE/*IRAS* extinction maps (Schlafly et al. 2011) though these

[1]The Digitized Sky Surveys were produced at the Space Telescope Science Institute under U.S. Government grant NAG W-2166. The images of these surveys are based on photographic data obtained using the Oschin Schmidt Telescope on Palomar Mountain and the UK Schmidt Telescope. The plates were processed into the present compressed digital form with the permission of these institutions.

[2]This research has made use of data obtained from the SuperCOSMOS Science Archive, prepared and hosted by the Wide Field Astronomy Unit, Institute for Astronomy, University of Edinburgh, which is funded by the UK Science and Technology Facilities Council.

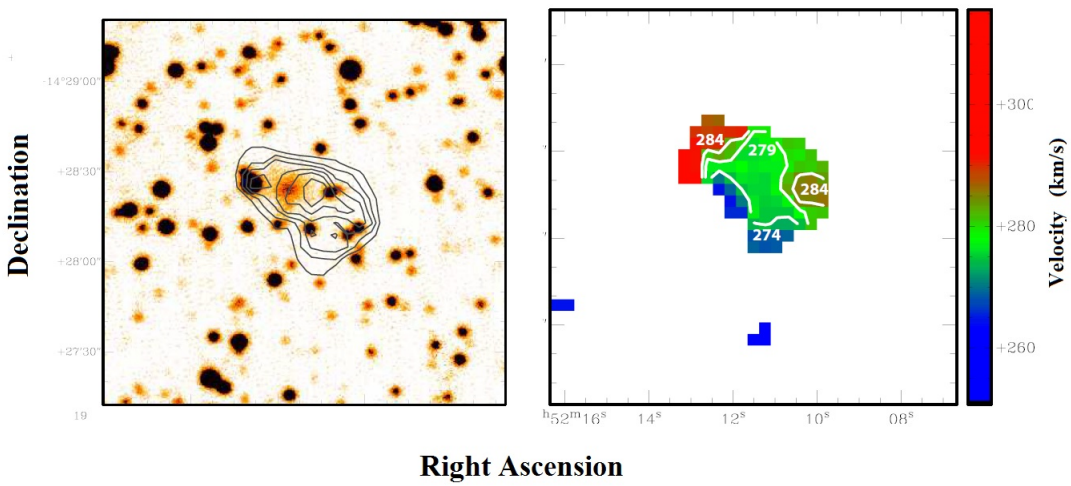

Figure 4.11 $2' \times 2'$ SARA B-band image and JVLA moment maps. Left Panel. H I column density map overlayed on a SARA B-band image. Contours are set at 1, 2, 3, 4, 5, 6 $\times 10^{20}$cm^{-2}. The H I peak is offset by 8.7″ from the apparent optical counterpart. Right Panel. Velocity field of J1952+1429 showing structure but not uniform rotation with contours at 274, 279, 284 km s^{-1}.

values are somewhat uncertain at such low Galactic latitudes. Applying extinction corrections gives $B - R = 0.1$ mag.

In order to obtain more accurate photometry, J1952+1429 was observed using a Bessell B-band filter on April 12, 2011 with the 0.9-m Southeastern Association for Research in Astronomy (SARA) telescope at Kitt Peak National Observatory using an Apogee Alta U 42 2048 × 2048 CCD. The field of view was $13.8' \times 13.8'$, giving a plate scale of 0.4″ pixel^{-1}. The source was low on the horizon with an average airmass of 1.7 and an average seeing of 2″. Nine 5-minute exposures were taken on-source for a total exposure time of 45 minutes and calibration was done using the equatorial standard star PG1657+078A (Landolt 1992).

The CCD images were bias-subtracted, dark-corrected, flat-fielded and co-added in Image Reduction and Analysis Facility (IRAF). The image can be seen in Figure

4.11. The APPHOT package was used for standard star photometry. The reduced image reaches a 1σ surface brightness level of 25 mag arcsec^{-2}. Astrometric calibration and aperture photometry of J1952+1429 was carried out interactively with the Graphical Astronomy and Image Analysis Tool (GAIA). Flux from the galaxy is recovered out to a radius of $8''$, reaching a surface brightness of 23.5 mag arcsec^{-2}, after which stellar contamination became significant. The recovered flux within this radius is $m_B = 16.9 \pm 0.1$ magnitudes, which is statistically a 2σ difference from the SuperCOSMOS estimate of the DSS image.

Follow up observations of J1952+1429 in H_α were conducted by Kaisin & Karachentsev (2013), giving a value of log $F_{H\alpha} = 14.00 \pm 0.02$ erg/(cm^2 s). This corresponds with an extinction-corrected integrated star formation rate of $10^{-3.08} M_\odot$ yr^{-1}.

Object Classification

As can be seen in the JVLA and SARA images, the H I peak is slightly offset ($\Delta\theta = 8.7''$) from the optical emission, indicating either a false counterpart or a disturbed H I distribution. The offset is ∼300 pc at 7 Mpc, which is not uncommon even for isolated galaxies (c.f. ∼400 pc offset in VV124, Bellazzini et al. 2011). This could conceivably be a pair of low-surface brightness dwarf galaxies (c.f. HIZSS 3 with separation of ∼900 pc, Begum et al. 2005), but there is no evidence for a second peak in the high signal-to-noise H I spectrum shown in Figure 1. Further, J1952+1429 has half the velocity width that the pair in HIZSS 3 appeared to have; $W_{50} = 55$ km s^{-1} for HIZSS 3 (Henning et al. 2000) compared to $W_{50} = 28$ km s^{-1} here. Any second galaxy would have to be much closer both spatially and in velocity than the pair in HIZSS 3 in order to escape detection. Deeper interferometric observations would be needed to be entirely conclusive.

J1952+1429 appears to be a dwarf galaxy judging from its Gaussian H I profile

and low H I mass. At a distance of 7 Mpc, $M_{HI} = 10^{7.0}$ $M_\odot$, which is significantly lower than the gaseous content of spiral-type galaxies (Roberts and Haynes 1994). Its low luminosity ($L_B = 10^{7.5}$ $L_\odot$ at 7 Mpc), H I content, and blue colors are strong evidence that it is not an early-type galaxy.

Morphological Type

Compared to other dwarf galaxies (Roberts & Haynes 1994; O'Neil et al. 2000), J1952+1429 is not particularly gas rich, $M_{HI}/L_B = 0.3$ $M_\odot/L_\odot$, but it is very compact and blue with an H I linear size of 1.4 × 1.3 kpc at 7 Mpc and B - $R = 0.1$ mag. The H I mass, M_{HI}/L_B ratio, blue optical colors, and linear size of J1952+1429 are similar to those of blue compact dwarf (BCD) galaxies (Huchtmeier et al. 2007). BCDs are small, blue, irregular dwarf galaxies which have low surface brightness features, ongoing star formation, and higher metallicities than typical dwarf galaxies. The velocity field of J1952+1429 shows structure, but non-uniform rotation which is common in blue compact dwarf galaxies (Ramya et al. 2011). J1952+1429 is most likely not a BCD, however, due to its low star formation rate, SFR = $10^{-3.08} M_\odot$ yr^{-1}. A typical BCD has SFR $\sim 10^{-1} - 10^{-2} M_\odot$ yr^{-1}.

Alternatively, there is evidence for the existence of blue, metal-poor, gas-rich ($M_{HI}/L_B > 1 M_\odot/L_\odot$) dwarf galaxies on the margins of galaxy groups (Grossi et al. 2007). These dwarfs are old (2 - 10 Gyrs) but have had remarkably little star formation in their history SFR $\sim 10^{-3} M_\odot$ yr^{-1}. They are thought to be galaxies in transition between dwarf irregular and dwarf spheroidal galaxies. J1952+1429 differs from the Grossi et al. galaxies because it has a lower M_{HI}/L_B ratio.

There is a recently discovered Local Group galaxy, VV124 (Bellazzini et al. 2011), which is similar to J1952+1429 in size, H I mass, M_{HI}/L_B ratio, and star formation rate, so they may be similar objects. VV124 is considered to be a precursor of modern

dwarf spheroidal galaxies that did not undergo an interaction-driven evolutionary path. The major difference between the two is that VV124 appears to be an isolated galaxy.

4.5.2 ALFA ZOA J1940+1154 and ALFA ZOA J1944+1238

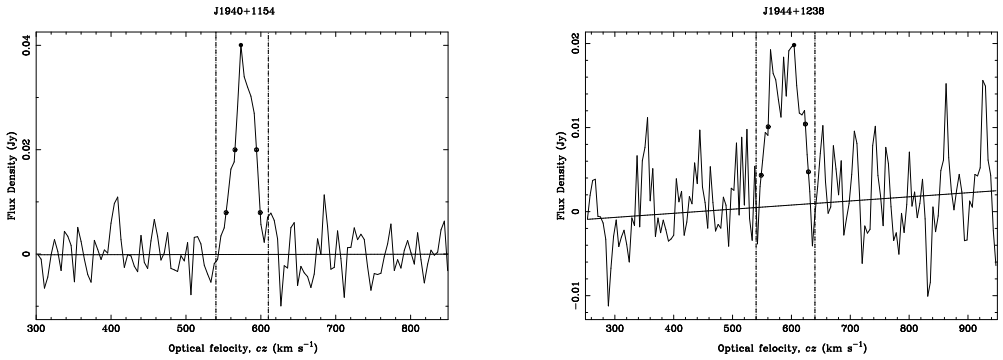

Figure 4.12 H I profiles for J1940+1154 and J1944+1238.

J1940+1154 has an H I counterpart in the literature from the HI Parkes Zone of Avoidance survey (HIZOA). The parameters are in good agreement; velocity is within 1 km s^{-1} and integrated flux is within 5% of each other. There are no other counterparts in the literature for either J1940+1154 or J1944+1238 and they are not resolved by ALFA ZOA or HIZOA, so neither their linear size nor total mass can be determined. Their profiles are shown in Figure 4.12. Their H I masses, velocity widths, and profile shapes are consistent with small dwarf galaxies.

4.5.3 GG2 Overview

The masses, velocity widths, and profile shapes of GG2 members are consistent with small dwarf galaxies. Not a single member has an H I mass greater than $4 \times 10^7 M_\odot$.

The virialized mass of the group is $M_{GG2} = 3 \times 10^{10} M_{\odot}$, using the same equations for the estimate described above. The total H I mass of the group is $M_{GG2\,HI} = 8.0 \times 10^{7} M_{\odot}$, giving an H I mass fraction of $10^{-2.5}$. This is quite small though it is not unreasonable; dwarf-type galaxies typically have an H I mass fraction around 10^{-1} and large spirals around 10^{-2}. Dwarf spheroidal galaxies have H I mass fractions as low as 10^{-5} (Grcevich & Putman 2009), though dwarf spheroidals typically have much smaller H I masses than the galaxies in GG2 (Spekkens et al. 2014). The survey is complete above $M_{HI} = 5 \times 10^{7} M_{\odot}$ at the distance of GG2 and fully covers the GG2 area of sky, so any H I sources in the group that may have gone undetected could contribute a few integer factors but probably not an order of magnitude to the H I mass fraction. Not too much can be said about the total masses of the GG2 galaxies, and so they are not found to be in disagreement with the estimated viralized group mass at the moment. The extinction in the area is rather low ($A_B \sim 1.3$ mag at group center), so follow-up observations in the visual bands are quite feasible and can provide useful morphological information, as was demonstrated for J1952+1429.

4.6 ALFA ZOA GG3

GG3, the largest nearby galaxy group in ALFA ZOA, contains nine galaxies located within 1.4 Mpc of their geometric center ($l, b, v_{LG} = 73.2°$, -10.3°, 19.1 Mpc), assuming that all galaxies are at the same Local-Group centered distance. Six galaxies have counterparts in the literature and four have counterparts at multiple wavelengths. The average linear separation between nearest neighbors is 340 kpc, and the maximum is 670 kpc. The velocity dispersion is $\sigma_r = 117$ km s^{-1}.

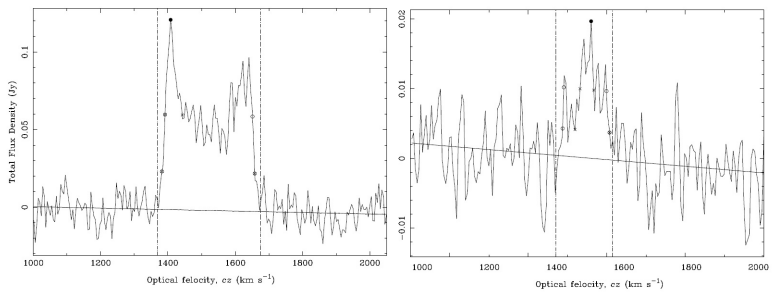

Figure 4.13 H I profiles for J2057+2557 and J2056+2554.

4.6.1 ALFA ZOA J2057+2557 and ALFA ZOA J2056+2554

J2057+2557 is considered by the literature to be an isolated galaxy (Karachentseva et al. 2010), though it is shown here to have a close companion, J2056+2554, and is part of a major group of galaxies. J2057+2557 has counterparts in optical, infrared, and 21 cm wavelengths. Its companion, J2056+2554, has no counterparts in the literature. The H I profiles of the galaxies are shown in Figure 4.13. There have been extensive observations of J2057+2557 in the literature and it is characterized as an Sdm-type spiral galaxy. High resolution imaging from the literature, using the JVLA in D-configuration, measures an H I diameter of $5.3'$ and $W_{50} = 120$ km s^{-1} with an inclination of $i = 81°$, giving an estimated virial mass of $6 \times 10^{10} M_{\odot}$ and an H I mass fraction of 0.045 (Pisano et al. 2002). J2057+2557 is resolved by ALFA ZOA and the ALFA ZOA moment maps for J2057+2557 and J2056+2554 are shown in Figure 4.14.

J2057+2557 exhibits uniform rotation along the major axis and its companion can be seen to the southwest. An H I diameter of $9'$ out to 3 σ is measured along the major axis, about twice as large as the JVLA estimate. ALFA ZOA measures a much larger velocity width as well, $W_{50} = 260$ km s^{-1}. The estimated virial mass of the system using ALFA ZOA measurements is $9 \times 10^{11} M_{\odot}$ and the H I mass fraction is $10^{-2.4}$. Even if the ALFA ZOA diameter is overestimated because of the

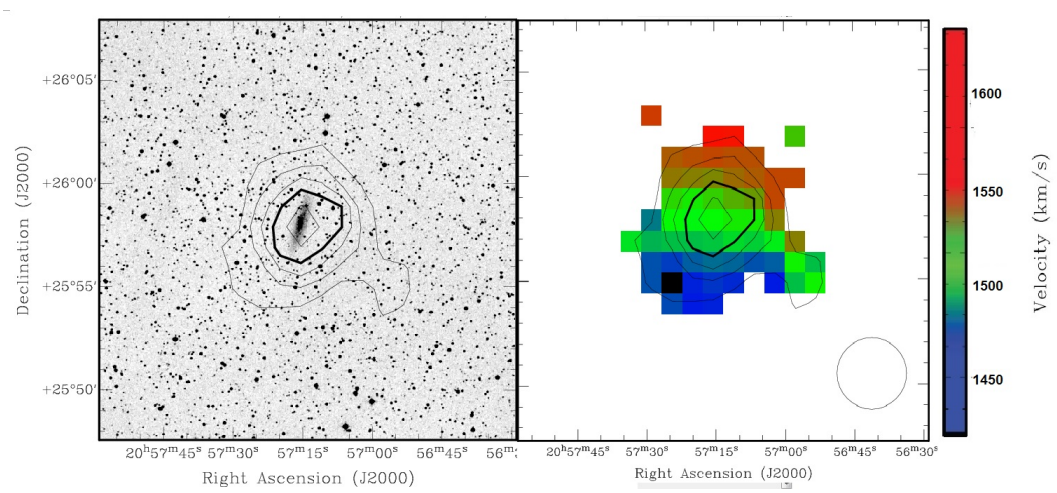

Figure 4.14 Left Panel. DSS B-band image and Arecibo flux density maps of J2057+2557 and J2056+2554. Contours are at 3, 6, 9, 12, 15 σ. Right Panel. Velocity field color coded as indicated by the scale on the right. The Arecibo FWHM is shown in the bottom right corner.

poorer resolution compared to the JVLA, the total mass estimate is still an order of magnitude larger than what is in the literature. It seems likely that J2057+2557 has been mischaracterized as Sdm-type when it is probably a more massive, earlier-type spiral galaxy. J2056+2554 is not resolved by ALFA ZOA and so its total mass cannot be estimated.

4.6.2 ALFA ZOA J2103+2953

J2103+2953 has the second highest H I mass in the group and is resolved by ALFA ZOA, but unfortunately it cannot be parameterized because of corrupted data. Luckily, it doesn't matter in this case because J2103+2953 is NGC 7013, which has counterparts in every observation wavelength from radio to x-ray. NGC 7013 is an SA(r)0/a-type lenticular galaxy (Sil'chenko & Afanasiev 2002). It is quite similar in size and mass to Triangulum with a total mass of $6 \times 10^{10} M_{\odot}$ (Knapp et al. 1984) spanning a diameter of $2R_{25} = 16.2$ kpc. The H I mass is $M_{HI} = 1.1 \times 10^{9} M_{\odot}$, and

the H I mass fraction is $10^{-1.7}$, in the range of what one would expect for a lenticular ($\sim 10^{-1} - 10^{-2}$).

4.6.3 ALFA ZOA J2050+2959 and ALFA ZOA J2050+2946

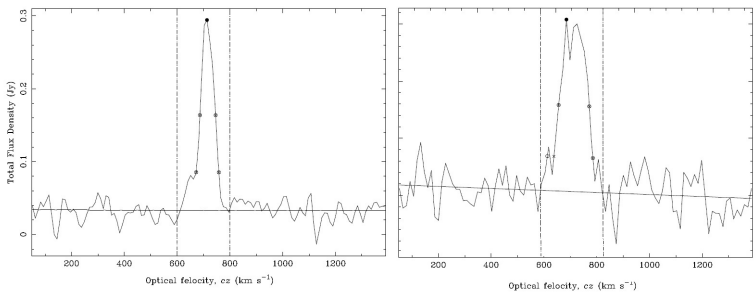

Figure 4.15 H I profiles for J2050+2959 (left) and J2050+2946 (right).

J2050+2959 and J2050+2946 are another close pair of galaxies in GG3, though they share more similar features to each other than the J2057+2557 and J2056+2554 pair do. The H I profiles of the galaxies are shown in Figure 4.15. J2050+2946 has one counterpart in the literature, 2MASX J20502688+2945370. It is located in an area of high stellar confusion and so it is difficult to determine morphological type from photometry, though it appears to have a "fuzzy", elongated shape. J2050+2959 is very similar to J2050+2946 in size, profile shape, and H I mass, though it has no counterpart in the literature. It is not visible in WISE data or 2MASS, however, it is seen in DSS I-band. J2050+2959 and J2050+2946 are both resolved by ALFA ZOA and their H I distributions and velocity fields can be seen in Figure 4.16.

The angular extent of the H I emission out to 3 σ is $13'$ and $11'$ corresponding with a linear size of 60 kpc and 51 kpc for J2050+2946 and J2050+2959, respectively. The peak of the H I distribution for J2050+2946 lines up nicely with 2MASX J20502688+2945370 and the J2050+2959 peak H I is centered on an uncataloged object in the DSS image. A second, and even brighter uncataloged object overlaps with

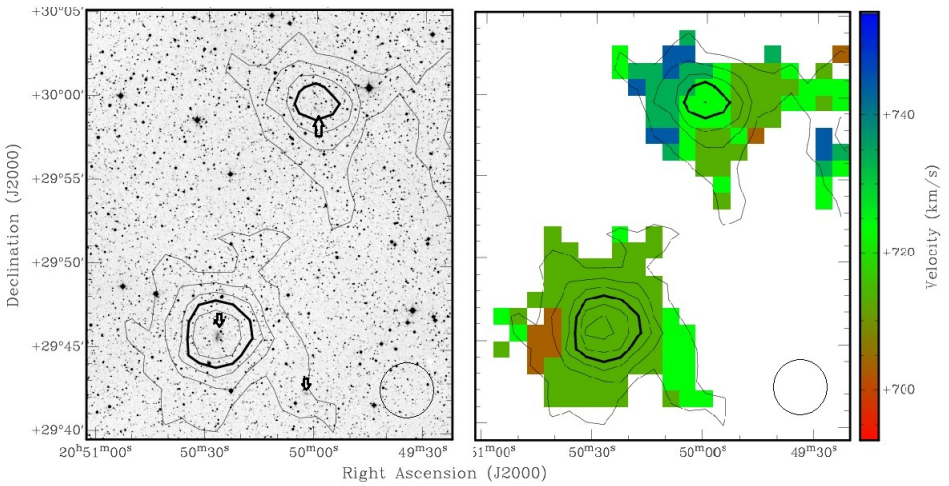

Figure 4.16 DSS I-band image and Arecibo flux density maps of J2050+2959 and J2050+2946. Left. Contours are at 3, 6, 9, 12, 15 σ. The arrows point towards suspected counterparts. The only counterpart in the literature is 2MASX J20502688+2945370 in the bottom left. Right Panel. Velocity field color coded as indicated by the scale on the right. The Arecibo FWHM is shown in the bottom right corner.

the large H I extension of J2050+2946 to the southwest. All three of these sources were probably confused with very bright Galactic emission in B- and R-band and so none were ever cataloged as extragalactic detections by galaxy catalogs constructed from the Palomar plates. The I-band source located in the J2050+2946 H I emission to the southwest was not detected by the ALFA ZOA selection function, and so it is not included in the ALFA ZOA catalog.

Some uniform rotation can be seen for both ALFA ZOA galaxies, though the velocity widths are not very large and the dispersion is more apparent in J2050+2959. J2050+2946 has a more pronounced plane of rotation, though the velocity width is too narrow to be an edge-on spiral. Its H I major axis lies almost perpendicular to the major axis of the visual counterpart, though the visual emission is heavily obscured. It is possible that J2050+2946 could be a face on spiral with a bright barred feature. The stellar morphology of J2050+2946 is too difficult to determine because of the

faintness of the detection. The geometry of these galaxies is too uncertain to estimate inclination angle. The major axes of rotation are 37 kpc and 28 kpc for J2050+2946 and J2050+2959, respectively, and with no inclination angle calculated, the lower limit for the virial mass of each galaxy is $3 \times 10^{10} M_{\odot}$. Their H I mass fraction is about $10^{-1.5}$. J2050+2946 and J2050+2959, located 60 kpc apart from peak to peak, seem very much like more massive versions of the Magellanic Clouds; not quite spiral galaxies though exhibiting some rotation. H I emission located spatially between the two galaxies appears to be a Magellanic Stream-type H I bridge.

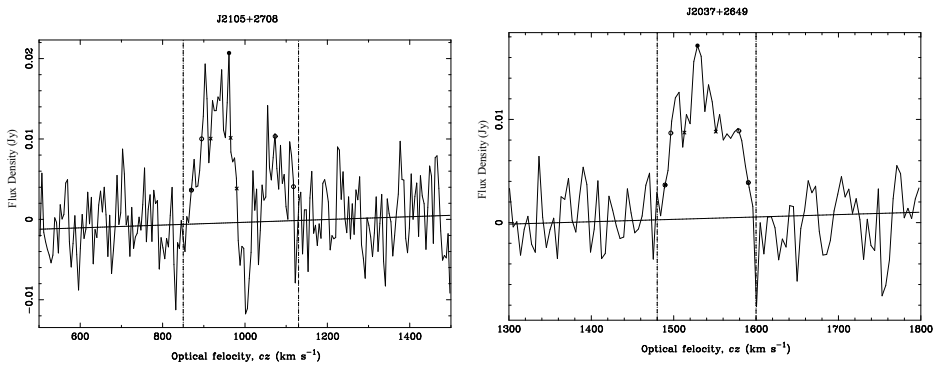

Figure 4.17 H I profiles for J2105+2708 and J2037+2649.

4.6.4 ALFA ZOA J2105+2708 and ALFA ZOA J2037+2649

J2105+2708 and J2037+2649 have the two lowest H I masses in GG3. J2037+2649 does not have any counterparts in the literature or in WISE image data. It is not resolved by ALFA ZOA so its size and total mass cannot be estimated. Judging from its H I mass, velocity width, and profile shape, it is likely a dwarf galaxy of some kind.

J2105+2708 has the lowest H I mass in the group, though it does have a large velocity width ($W_{50} = 178$ km s^{-1}, $W_{50} = 248$ km s^{-1}) and a bizarre, double triangle-

looking H I profile. It has an H I counterpart in the literature, ADBS J210538+2709, with a similar double triangle profile shape , though with lower derived velocity width (W_{50} = 92 km s^{-1}, W_{50} = 168 km s^{-1}). It is possible that J2105+2708 is really two galaxies that are confused. High resolution H I imaging would be required to find out.

4.6.5 ALFA ZOA J2045+2811 and UGC 11707

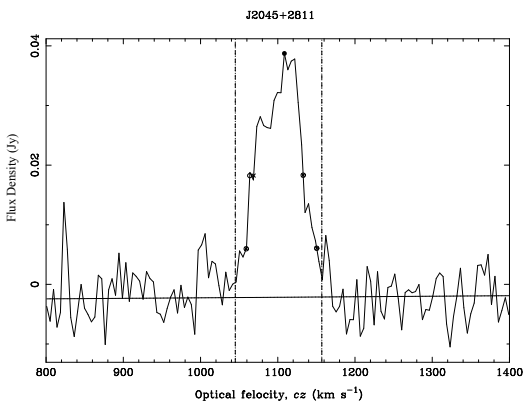

Figure 4.18 H I profile for J2045+2811.

Both J2045+2811 and UGC 11707 have multiple counterparts in the literature. UGC 11707 has optical and H I counterparts in the literature, and it is detected in WISE image data. UGC 11707 is classified as an SAdm-type galaxy, though its total mass is estimated to be $3 \times 10^{11} M_{\odot}$ (Popolo & Cardone 2012), which is quite high for a typical Magellanic spiral galaxy. UGC 11707 has the highest H I mass $= 5 \times 10^{9} M_{\odot}$ in GG3, but it does not have an ALFA ZOA counterpart as it lies outside of the survey area. UGC 11707 was selected for group membership from the literature after GG3 was formed from the ALFA ZOA selection function.

J2045+2811 has counterparts in visual (CGCG 491-001), far infrared (IRAS

20435 + 2759), and 21cm bands (AGC 300056). J2045+2811 also has counterparts in 2MASS and short wavelength WISE image data, though it is located in an area of high Galactic confusion, and so its morphology is difficult to determine. There appears to be a Galactic source that dominates the galaxy in brightness in the long wavelength WISE bands. It would be interesting to determine if the IRAS counterpart is actually this Galactic emission and whether it has been mischaracterized as an extragalactic source in far infrared. The H I emission is not resolved by ALFA ZOA and so no linear size or virial mass can be determined. Its H I mass, velocity width, and profile shape are consistent with an irregular or dwarf-type galaxy.

GG3 Overview

GG3 has a lot of similarities to the Local Group. Two massive spirals, J2057+2557 ($\sim 9 \times 10^{11} M_{\odot}$) and UGC 11707 ($\sim 3 \times 10^{11} M_{\odot}$), dominate the dynamical mass of the group, a small galaxy, J2056+2554, is a satellite of the most massive spiral like Andromeda and M32, there is a Triangulum-type spiral, J2103+2953=NGC 7013, and a pair of galaxies similar to the Magellanic clouds, J2050+2959 and J2050+2946, have a stream of hydrogen gas between them. J2057+2557 is very similar in mass to the Milky Way and has almost certainly been mischaracterized as an Sdm-type.

The total H I mass of the group is $M_{GG3\,HI} = 1 \times 10^{10} M_{\odot}$. The lower limit on the total mass of GG3, from summing over the mass of its member galaxies, is $1.3 \times 10^{12} M_{\odot}$. By comparison the virial mass of the group is $9 \times 10^{12} M_{\odot}$, in agreement within an order of magnitude. Due to the uncertainty in the group's virial mass estimate, it is possible that there are no more massive galaxies left undiscovered in GG3. The survey is complete above $M_{HI} = 2 \times 10^{8} M_{\odot}$ at the distance of GG3 though it does not fully cover the GG3 area of sky. There are two additional galaxies in the literature (CGCG 471-006 and KKR 61) outside of the ALFA ZOA survey area but within a couple degrees and with the same recessional velocity of UGC

11707. However, they are slightly too far outside of the ALFA ZOA selection criteria and so did not qualify for membership with the galaxy group algorithm used here. The group identity method applied in this chapter was chosen to utilize the selection function of the ALFA ZOA survey, and so has acted conservatively towards non-survey counterparts. These galaxies may very well be group members and should be looked at using a different identity algorithm for a future project.

4.7 Group Dynamical Mass Uncertainty

The uncertainty on the dynamical mass estimate for each group is not calculated statistically because of how heavily dependent the virial mass is on subjective choices. The virial theorem is not a very robust estimate. That is, changing decisions about how to calculate velocity dispersion or what linear size contains the correct virialized mass can change the total mass estimate by many factors. Applying the virial theorem to a galaxy group with only a few members also carries a lot of uncertainty because the assumption that their velocity dispersion can be approximated only from the radial component that can be measured becomes statistically less accurate. Additionally, there is a large error on distance estimates from using Hubble's law in the local universe because of the unknown peculiar velocities of galaxies. However, it should be noted that distance error only linearly affects a group's impact on the mass dipole. That is, gravitational influence increases inversely with distance squared, but dynamical mass estimates decreases inversely with distance. For example, if a group is moved to half the distance, its distance component contributes 4 times more to its gravitational influence but its virialized mass estimate decreases by a factor of 2 at the same time.

In an attempt to quantify the uncertainty on group masses, a range of values corresponding with vastly different assumptions can be calculated. For GG1 for

example, the velocity dispersion is estimated as $\sigma_r = 38$ km s^{-1}, calculated from the median absolute deviation divided by $\sqrt{N-1}$ of the galaxies' recessional velocities, a rather conservative estimate. If the velocity dispersion is calculated instead as the square root of the variance of recessional velocities, than it becomes $\sigma_r = 101$ km s^{-1}, a decidedly more liberal estimate. This change in deciding how to calculate virial mass increases the total estimated mass by nearly an order of magnitude. Similarly, deciding on a half-mass distance to use for the calculation of virial mass can change the estimate of total mass by several factors. For GG1, if the radius used to calculate the virial mass is changed to the median distance from group center, instead of half the average distance, then the total estimated mass increases by a factor of four. Using these liberal choices to estimate the dynamical mass of GG1 adjusts the value upwards to $M_{GG1} = 10^{13} M_{\odot}$. If the vector of the peculiar velocity for GG1 points entirely away from the Local Group, then its Local Group centered distance is overestimated. Subtracting one standard deviation of peculiar velocities in the local universe ($\sigma = 298 \pm 34$ km s^{-1} Masters 2008) from GG1's Local Group-centered recessional velocity reduces the distance to the group nearly by a factor of two, to $D_{LG} = 4.7$ Mpc. If a group has $10^{13} M_{\odot}$ at 3 Mpc, then it could recover the dipole vector. GG1 is close to these values within the uncertainty of their estimates.

4.8 Conclusion

From a list of nearby ALFA ZOA sources within 20 Mpc of the Local Group, criteria to identify group membership is discussed and three new galaxy groups are discovered. GG1 and GG2 are made up of dwarf and irregular galaxies and GG3 is comprised of a Local Group-like combination of spirals, dwarfs and irregulars.

Discovering mass behind the Milky Way with $\sim 10^{12} M_{\odot}$ at 1Mpc or $\sim 10^{15} M_{\odot}$ at 20Mpc may explain the discrepancy between the cosmic microwave background

dipole and 2MASS mass density dipole. None of the nearby galaxy groups discovered by ALFA ZOA clearly surpass this threshold as estimated here, but it is shown that GG1 may be close enough and massive enough within the uncertainty of the estimates of its parameters. It is unlikely that another group is close and massive enough as GG2 needs to be about 1000 times more massive at 9 Mpc and GG3 needs to be 100 times more massive at 20 Mpc to explain the dipole discrepancy.

4.8.1 Future Work

Of the three nearby galaxy groups, GG1 is certain to have massive group member(s) still undiscovered, or it has been falsely identified as a group or as virialized. Follow-up observations to help determine the answer to this may be of interest as GG1 is in the best position of the three to influence the mass dipole vector. A redshift-independent distance estimate could help address the distance uncertainty. The extinction in the area of the group is $A_B = 2$ mag. Ontaining a tip of the red giant branch distance may be possible, though none of the galaxies currently have any counterparts in the literature. Follow-up observations of GG1 group member, J2032+2559, have been taken with WSRT but not yet processed. High resolution imaging may help explain the apparent interaction event that's causing high velocity dispersion toward the southwest of the galaxy. It will also provide a more accurate estimate for the size of the H I emission and therefore, a better estimate for the dynamical mass of the galaxy.

GG2 and GG3 may or may not have undiscovered massive members. Not much is currently known about GG2 as a whole, though a good deal is now known about one of its members, J1952+1429. GG2 is in an area of relatively low extinction ($A_B \sim 1.3$ mag at group center), and so follow-up observations in visual bands may be feasible. GG3 is the most massive nearby group discovered by ALFA ZOA, though it is also the farthest away of the three. Though redshift information was known for six of its

nine galaxies, it was not identified as a group until ALFA ZOA was able to apply a group identity algorithm to its member galaxies using the survey's selection function. There are two candidates for GG3 group membership that are not included in the group in this chapter because they fell slightly outside of the membership criteria. These galaxies should be looked at for possible group membership using a different identity algorithm in the future.

Chapter 5

Conclusions

5.1 Summary

5.1.1 Survey Performance

The ALFA ZOA Deep Survey has detected 61 galaxies so far, 55% of which are new discoveries. The Deep survey achieves its expected noise level of 1 mJy (at 9 km s^{-1} resolution) and it is complete above $F_{HI} = 0.5$ Jy km s^{-1}. First results display the ability to detect galaxies out to nearly 190 h^{-1} Mpc and at extinctions that surveys at other wavelengths struggle to penetrate. ALFA ZOA Deep has completed 15 square degrees in the outer Galaxy and is continuing to take data, intending to cover about 300 square degrees in both the inner ($30° \leq l \leq 75°; b \leq |2°|$) and outer ($175° \leq l \leq 207°; -2° \leq b \leq +1°$) Galaxy, over the next several years.

The ALFA ZOA Shallow Survey has so far detected 454 galaxies in over 1100 square degrees of sky behind the Milky Way. The survey reached its expected sensitivity of rms = 5.4 mJy at 9 km s^{-1} channel resolution in 45% of the area (B+C fields), but the sensitivity worsens to rms = 7 mJy at 20.3 km s^{-1} channel resolution

for the rest of the area (A+D fields). The positional accuracy of the survey is shown to be 26″ on average, though it is a function of signal-to-noise for an individual source. ALFA ZOA is shown to have no Zone of Avoidance outside of H I emission from the Milky Way (v_{hel} <100 km s^{-1}). 152 B+C field detections (55% of sources) have a possible counterpart in the literature, though this is reduced to 21% within $|b| < 5°$. A fully adjudicated source catalog shows the survey to be complete above integrated flux, $F_{HI} = 2.2$ Jy km s^{-1} for B+C fields. An HIMF is estimated using the survey's selection function and the values of the best-fit parameters are very similar to ALFALFA. The values for the ALFA ZOA fit are $\Phi_* = 4.8 \pm 1.1 \times 10^{-3}$, $\log M_* = 9.87 \pm 0.11$, and $\alpha = 1.34 \pm 0.11$. The estimate for the H I critical density is $\Omega_{HI} = 4.3 \pm 1.1 \times\ 10^{-4}$.

ALFA ZOA has increased the number of known galaxies in the area by 100%, and has increased galaxies with known redshifts in the area by over 800%. From a list of nearby ALFA ZOA sources within 20 Mpc of the Local Group, a criteria to identify group membership is discussed and three new galaxy groups are discovered. GG1 and GG2 are made up of dwarf and irregular galaxies and GG3 is comprised of a Local Group-like combination of spirals, dwarfs and irregulars.

5.1.2 Large Scale Structure Results

ALFA ZOA confirms the extent of the C7, Cξ, and Pegasus overdensities, as well as the Aquarius void behind the Milky Way. The Corona Borealis, Delphinus, and Cygnus voids are not where predicted. An unpredicted overdensity, starting at (l, b, v = 30°, +13°, 1500 km s^{-1}) and connecting with the C7 overdensity at (l, b, v = 42°, +13°, 4500 km s^{-1}) is also discovered. Four out of seven predicted structures in the Zone of Avoidance are confirmed to be where expected while the other three are not. ALFA ZOA demonstrates that density reconstructions from galaxies above and below the plane are not completely accurate.

5.1.3 Mass Density Dipole Vector

Discovering mass behind the Milky Way with $\sim 10^{12} M_{\odot}$ at 1 Mpc or $\sim 10^{15} M_{\odot}$ at 20 Mpc may explain the discrepancy between the cosmic microwave background dipole and 2MASS mass density dipole. None of the nearby galaxy groups discovered by ALFA ZOA surpass this mass threshold as estimated here. However, the virial theorem was used to determine the total mass of nearby groups, and the virial theorem is not a very robust estimate. That is, changing decisions about how to calculate velocity dispersion or what linear size contains the correct virialized mass can change the total mass estimate by many factors. Additionally, there is a large error on distance estimates from using Hubble's law in the local universe because of the unknown peculiar velocities of galaxies. It appears unlikely that the mass dipole vector has been recovered by current ALFA ZOA detections, though it is not entirely conclusive within the uncertainty of the estimates.

5.2 Future Work

ALFA ZOA A+D fields have not yet been searched by multiple team members, and so this is planned for the near future. Why these fields have a much lower sensitivity than B+C is not currently known. A+D should not be at a lower sensitivity because they were observed in the same way. It would be ideal to solve this problem though ideas by current team members have been exhausted. Z field has not gone through the data reduction process yet and so this is also planned. Once A+D+Z fields are searched and adjudicated, their selection function can be determined and used to estimate an HIMF.

B+C fields have yet to be searched at velocities beyond v_{hel} = 11,500 km s^{-1}, though the data exists out to 50,000 km s^{-1} and has been reduced and made into

cubes. Similar to the deep survey, a useful velocity range to search will probably be out to $v_{hel} = 20{,}000$ km s^{-1} as RFI increases dramatically at higher velocities. These velocity ranges should be searched for detections and should increase the number of detections in the catalog by 10%.

ALFA ZOA Deep Survey observations are ongoing for several more years. Observations began in December 2010 and the survey area is about 25% complete so far. The observing plan in the outer Galaxy is to focus on Nyquist sampling 20 square degree contiguous sections at a time so that data cubes can be made and results analyzed ad hoc. In the inner galaxy, a 20 square degree area agreed upon by commensal partners is loosely focused on as the current objective for the observing plan.

Of the three nearest galaxy groups, GG1 is certain to have massive group member(s) still undiscovered, or it has been falsely identified as a group or as virialized. Uncertainty on distance and mass estimates are high enough that GG1 could recover the mass density dipole vector, though it cannot be known for certain without a redshift-independent distance estimate.

GG2 and GG3 may or may not have undiscovered massive members. Not much is currently known about GG2 as a whole, though a good deal is now known about one of its members, J1952+1429. GG2 is in an area of relatively low extinction ($A_B \sim 1.3$ mag at group center), and so follow-up observations in visual bands may be feasible. GG3 is the most massive nearby group discovered by ALFA ZOA, though it is also the farthest away. There are multiple candidates for GG3 group membership that are not included in the group in this dissertation because they fell slightly outside of the membership identity criteria. These galaxies should be looked at for possible group membership using a separate set of criteria (e.g. different values for the search volume, different selection function, etc.) in the future.

References

[1] Anderson, D. P., Cobb, J., Korpela, E., Lebofsky, M., & Werthimer, D., 2002, ACM 45, 56

[2] Abazajian, K., et al., 2003, AJ, 126, 2081

[3] Bahcall, Neta A., 1988, ARAA, 26, 631

[4] Bahcall, Neta A., 1999, fsu, conf, 135

[5] Barnes, D. G., et al. 2001, MNRAS, 322, 486

[6] Begum, A., Chengalur, J. N., Karachentsev, I. D., & Sharina, M. E. 2005, MNRAS, 359, 53

[7] Begum, A., Stanimirovic, S., Peek, J.E., Ballering, N.P., Heiles, C., Douglas, K.A., Putman, M., Gibson, S.J., Grcevich, J., Korpela, E.J., Lee, M., Saul, D., & Gallagher, J.S. 2010, ApJ, 722, 395

[8] Bellazzini, M., Beccari, G., Oosterloo, T. A., Galleti, S., Sollima, A., Correnti, M., Testa, V., Mayer, L., Cignoni, M., Fraternali, F., Gallozzi, S. 2011, A&A, 527, 58

[9] Bosma, Albert, 1978, PhD Thesis, Groningen Univ.

[10] Briggs, F. H., Sorar, E., Kraan-Korteweg, R. C., van Driel, W., 1997, PASA, 14, 37

[11] Cobb, J., Lebofsky, M., Werthimer, D., Bowyer, S., 2000, ASPC, 213, 485

[12] Colless M.M., et al., 2001, MNRAS, 328, 1039

[13] Corbelli & Schneider 1997, ApJ, 479, 244

[14] Cordes, J. M., Freire, P. C. C., Lorimer, D. R., et al. 2006, ApJ, 637, 44

[15] Courteau, S., & van den Bergh, S. 1999, AJ, 118, 337

[16] Davies, J. I., et al., 2011, MNRAS, 415, 1883

[17] Donley, J.L., et al., 2005, AJ, 129,220

[18] Erdogdu, P., Lahav, O., Huchra, J. P., et al. 2006, MNRAS, 373, 45

[19] Fouquée, P.; Durand, N.; Bottinelli, L.; Gouguenheim, L.; Paturel, G., 1990, A&AS, 86, 473

[20] Fouquée, P., Gourgoulhon, E., Chamaraux, P., Paturel, G., 1992, A&AS, 93, 211

[21] Freudling, W., et al., 2011, ApJ, 727, 40

[22] Garcia-Gomez, C. & Athanassoula, E., 1991, A&ASS, 89, 159

[23] Geller & Huchra, 1983, ApJS, 52, 61

[24] Gibbs, 1898, Nature, 59, 200

[25] Giovanelli, R., et al. 2005, AJ, 130, 2598

[26] Giovanelli, R., et al. 2007, Astron. J., 133, 2569

[27] P. Goldsmith, 2002, "Analysis of Arecibo 305m antenna performance and surface errors," Arecibo Observatory, Arecibo, PR, Tech. Memo. 2002-02

[28] Gooch, R.E., 1996, ASP Conf. Ser., 101, 80

[29] Grcevich, Jana & Putman, Mary E.,2009, ApJ, 696, 385

[30] Grossi, M., Disney, M. J., Pritzl, B. J., Knezek, P. M., Gallagher, J. S., Minchin, R. F., & Freeman, K. C. 2007, MNRAS, 374, 107

[31] Haynes, M. P., et al., 2011, AJ, 142, 170

[32] Haynes, M. P., Giovanelli, R., & Chincarini, G. L. 1984, ARA&A, 22, 445

[33] Henning et al., 2010, AJ, 139, 2130

[34] Henning, P. A., et al. 2000, AJ, 119, 2686

[35] Henning, P. A., Kraan-Korteweg, R. C., & Staveley-Smith, L. 2005, in ASP Conf. Ser. 329, 199

[36] Henning, P. A., Kraan-Korteweg, R. C., Rivers, et al., 1998, AJ, 115, 584

[37] Henning, P. A., Springob, C. M., Minchin, R. F., Momjian, E., Catinella, B., McIntyre, T. P., Day, F., Muller, E., Koribalski, B., Rosenberg, J. L., Schneider, S., Staveley-Smith, L., & van Driel, W. 2010, AJ, 139, 2130

[38] Huchra & Geller, 1982, AJ, 257, 423

[39] Huchra, Davis, Latham and Tonry, 1983, ApJS 52, 89

[40] Huchra et al., 2012, ApJS, 199, 26

[41] Jarrett, T. H., 2000a, PASP, 112, 1008

[42] Jarrett, T. H., Chester, T., Cutri, R., Schneider, S., Skrutskie, M., & Huchra, J. P. 2000b, AJ, 119, 2498

[43] Jarrett, T. H., et al., 2000c, AJ, 120, 298

[44] Jarrett, T. H., et al., 2013, AJ, 145, 6

[45] Jones et al., 2004, MNRAS 355, 747

[46] Jones et al., 2009, MNRAS, 399, 683

[47] Kalberla & Kerp, 2009, ARA&A, 47, 27

[48] Karachentseva et al., 2010, AstBu, 65, 1

[49] Kerp, J. et al. 2011, AN, 332, 637

[50] Kerr, Frank J.; Henning, Patricia A., 1987, ApJ, 320, 99

[51] Knapp et al., 1984, A&A, 133, 127

[52] Kolatt T., Dekel A., Lahav O.: 1995, MNRAS 275, 797

[53] Kogut A. et al., 1993, ApJ 419, 1

[54] Koribalski, B. S., et al., 2004, AJ, 128, 16

[55] Kraan-Korteweg, R. C., Loan, A. J., Burton, et al., 1994, Nature, 372, 77

[56] Kraan-Korteweg, R. C. & Lahav, Ofer, 2000, A&ARv, 10, 211

[57] Kraan-Korteweg, R. C. & Jarrett, T., 2005, ASPC, 329, 119

[58] Kraus, 1966, Radio Astronomy, McGraw-Hill

[59] Landolt, A. U. 1992, AJ, 104, 340

[60] Lavaux, G. & Hudson, M.J. 2011 MNRAS,416, 2840

[61] Lavaux, G. et al. 2010, ApJ, 709, 484

[62] Liu, B., McIntyre, T., Terzian, et al., 2013, AJ, 146, 80

[63] Lockman, F. J., Benjamin, R. A., Heroux, A. J., & Langston, G. I. 2008, ApJ, 679, 21

[64] Loeb, A., & Narayan, R. 2008, MNRAS, 386, 2221

[65] Loeb, A., & Narayan, R. 2008, MNRAS, 386, 2221

[66] Martin, A.M., Papastergis, E., Giovanelli, R., et al., 2010, Ap.J. 723, 1359

[67] Massey, P., Henning P.A., & Kraan-Korteweg, R.C. 2003 AJ, 126. 2362

[68] Masters, K. 2008, ASP Conf. Ser., 395, 137

[69] McIntyre, T. P., 2013a, "Spectral Line Bandpass Removal Using a Median Filter," Arecibo Observatory, Arecibo, PR, Tech. Memo. 2013-01

[70] McIntyre, T. P., 2013b, "Position Switching Separation Tolerance with Arecibo in L-Band," Arecibo Observatory, Arecibo, PR, Tech. Memo. 2013-02

[71] McIntyre, T. P., et al., 2011, ApJL, 739, 26

[72] Meyer et al., 2004, MNRAS, 350, 1195

[73] Morras, R., Bajaja, E., Arnal, E. M., & Poppel, W. G. L. 2000, A&AS, 142, 25

[74] Neugebauer et al., 1984, ApJ, 278, 1

[75] O'Neil, K., Bothun, G. D., & Schombert, J. 2000, AJ, 119, 1360

[76] P. Goldsmith, 2002, "Analysis of Arecibo 305m antenna performance and surface errors," Arecibo Observatory, Arecibo, PR, Tech. Memo. 2002-02

[77] Park, G., et al., 2013, AJ, 77, 14

[78] Paturel, G. et al., 2003, A&A, 412, 45

[79] Pisano, D. J.; Wilcots, Eric M.; Liu, Charles T., 2002, ApJS, 142, 161

[80] Popolo & Cardone, 2012, MNRAS, 423, 1060

[81] Ramya, S., Kantharia, N. G., & Prabhu, T. P. 2011, ApJ, 728, 124

[82] Rauzy S., 2001, MNRAS, 324, 51

[83] Riad et al. 2010, MNRAS, 401, 924

[84] Roberts, Morton & S., Haynes, M. P., 1994, ARA&A, 32, 115

[85] Rohlfs, K., & Wilson, T. L. 1996, Tools of Radio Astronomy (Berlin: Springer)

[86] Rosenberg, J.L. & Schneider, S.E., 2002, ApJ, 567, 247

[87] Rowan-Robinson, M. et al., 2000, MNRAS 314, 375

[88] Saintonge, A. 2007, Astron. J., 133, 2087

[89] Sault, R. J., Teuben P. J., & Wright, M. C. H. 1995, ASP Conf. Ser. 77, 433

[90] Saunders W et al. 2000 Mon. Not. R. Astron. Soc. 317 55

[91] Schechter, P. 1976, ApJ, 203, 297

[92] Schlafly & Finkbeiner, 2011, ApJ, 737, 103

[93] Schlegel, Finkbeiner & Davis 1998, ApJ, 500, 525

[94] Schmidt M., 1968, ApJ, 151, 393

[95] Schmoldt I. M. et al., 1999, AJ, 118, 1146

[96] Schombert et al., 1995, AJ, 110, 2067

[97] Shafi, N. 2008, MSc thesis, Univ. of Cape Town

[98] Sil'chenko, O. K.; Afanasiev, V. L., 2002, A&A, 385, 1

[99] Skrutskie, M. F., et al., 2006, AJ, 131, 1163

[100] Spekkens, Kristine et al., 2014, ApJ, 795, 5

[101] Spitler et al., 2014, ApJ, 790, 101

[102] Taylor, A. R.; Salter, C. J, 2010, ASPC, 438, 402

[103] Taylor, M. B., 2005, ASP Conf. Ser. vol. 347, 29

[104] van den Bergh, 1999, A&A Rev, 9, 273

[105] Verhulst, Pierre-François, 1845, Nouveaux Mémoires de l'Académie Royale des Sciences et Belles-Lettres de Bruxelles, 18, 1

[106] Von Korff, J., et al., 2013, ApJ, 767, 40

[107] Watkins, R. et al. 2009, MNRAS, 392, 743

[108] Whiting, M., 2012, MNRAS, 421, 3242

[109] Whiting, M.; Humphreys, B., 2012, PASA, 29, 371

[110] Zwaan et al., 2003, AJ, 125, 2842

[111] Zwaan et al., 2004, MNRAS, 350, 1210

[112] Zwaan, M. A., Meyer, M. J., Staveley-Smith, L., Webster, R. L., 2005, MNRAS, 359, 30

Appendix A

Data Reduction Code

First, the data reduction programs used for processing ALFA ZOA Shallow Survey A+D field raw data into .sdfits files that can be operated on by Gridzilla. There are five main programs that make up the data reduction pipeline.

1. spec2sdfits.pro is the umbrella program that takes a list of .spec file locations, runs data reduction on the files, and writes them out as .sdfits files. It runs the following four programs from start to finish. 2. lowcal.pro opens a .spec file, loads it into a structure, identifies, and removes the low flux noise diode. It also identifies and applies the high flux noise diode and reads in and applies a table of Gain per beam per zenith angle for each polarization. 3. livedatazoa.pro runs bandpass correction 4. masveltrans.pro converts from topo- to bary-centric frequency 5. mas2sdfits.pro writes the data out in .sdfits format with the correct header information for Gridzilla.

Next, the data reduction programs used for processing ALFA ZOA Deep Survey raw data into .sdfits files that can be operated on by Gridzilla. There are four main programs that make up the data reduction pipeline.

1. coverage.pro is the umbrella program that takes the raw files, runs data reduction on the files, and writes them out as .sdfits files. It runs the following four programs from start to finish. 2. coordmatch.pro looks at every pointing from one observing date and finds the closest spatial on-off pair within the separation tolerence of the survey 3. zoaredfiles.pro runs bandpass correction 4.

mas2sdfits.pro writes the data out in .sdfits format with the correct header information for Gridzilla. It is the same program used for the Shallow Survey A+D data, and so the code is not listed again.

The program scripts are presented below. Individual scripts are commented in lines that start with a semi-colon, ;.

```
spec2sdfits
pro spec2sdfits
file='/home/zoa/speclist.cat'
nrows = File_Lines(file)
filelist=strarr(nrows)
openr,lun,file,/get_lun
readf,lun,filelist
close,/all

print,systime()
for i =0,nrows-1 do begin

    ;remove the low cal and combine calons and caloffs into .2s records
    lowcal,filelist[i],bxsubcal,bysubcal,bonx,bony,boffx,boffy

    ;bandpass correct lambdas for each polarization
    livedatazoa,bxsubcal,bxred
    livedatazoa,bysubcal,byred

    ;find the high cal records (calons) and derive the high cal for the
   lambda
    findspeccals2,boffx,calons
    hicalxnorm=boffx[calons].d/boffx[calons+35].d-1.
    hicalynorm=boffy[calons].d/boffy[calons+35].d-1.
    hicalx=median(hicalxnorm,dimen=2)
    hicaly=median(hicalynorm,dimen=2)

    ;create the ratio (calrat) for high cal value per measured high cal
    recs=n_elements(boffx)
    chans=n_elements(boffx[0].d)
    beam=boffx[0].h.beam
```

```
    freqTopo=(dindgen(chans)-(bxred[0].h.crpix1-1))*bxred[0].h.cdelt1*1d-6
      +bxred[0].h.crval1*1d-6
    ;call the value for the high cal (1) for alfa (17) for the
    bandwidth freqtopo
    is=calget1(17,1,freqtopo,calval,alfabmnum=beam)
    calx={cal:calval[0,*]/hicalx}
    caly={cal:calval[1,*]/hicaly}
    calratx=replicate(calx,recs)
    calraty=replicate(caly,recs)

    ;calibrate the data into antenna temperature
    bxredcal=bxred
    byredcal=byred
    bxredcal.d=bxred.d*calratx.cal
    byredcal.d=byred.d*calraty.cal

    ;scale the calibration into Jy and combine polarizations
    bxredjy=bxredcal
    byredjy=byredcal
    cfreq = boffx[0].h.crval1
    gains=fltarr(2,recs)
    for j=0L,recs-1 do begin
   gains[*,j]=alfagetgain(beam,cfreq=cfreq,za=90.-boffx[j].h.elevatio)
        bxredjy.d=bxredcal.d/gains[0,j]
        byredjy.d=byredcal.d/gains[1,j]
    endfor

    ;convert to barycentric frequency
    masveltrans2,bxredjy,bxout,/bary,/resamp
    masveltrans2,byredjy,byout,/bary,/resamp

    ;write out the sdfits file
    filexout=strsplit(filelist[i],'.spec',/regex,/extract)+'x.sdfits'
    fileyout=strsplit(filelist[i],'.spec',/regex,/extract)+'y.sdfits'
    mas2sdfits2,bxout,filexout
    mas2sdfits2,byout,fileyout

endfor
```

```
print,systime()
end



lowcal
pro lowcal2,file,bxjy,byjy,bjy
;this program extracts the lowcal from the data and subtracts it from
    the records where the lowcal is on. input is the name of the .spec
    file to operate on and outputs are normalized and low cal subtracted
    bx and by structures (bxsublcal and bysublcal). optional output is
    raw data called, bonx, bony, boffx, boffy.
;print,systime()
;open the spec file and load it into structures
spec2,file,bonx0,bony0,boffx0,boffy0
close,/all

;bin the structures from 0.2s integrations into 1s integrations in
    order to reduce processing time
records0=n_elements(bonx0)
bonx=bonx0[0:records0/5-1]
bony=bony0[0:records0/5-1]
boffx=boffx0[0:records0/5-1]
boffy=boffy0[0:records0/5-1]
records=n_elements(boffx)
chans=n_elements(boffx[0].d)

for i=0L,records-1 do begin
    bonx[i]=bonx0[2+i*5]
    bonx[i].d=median(bonx0[i*5:4+i*5].d,dimen=2)
    bonx.h.exposure=1d
    bony[i]=bony0[2+i*5]
    bony[i].d=median(bony0[i*5:4+i*5].d,dimen=2)
    bony.h.exposure=1d
    boffx[i]=boffx0[2+i*5]
    boffx[i].d=median(boffx0[i*5:4+i*5].d,dimen=2)
    boffx.h.exposure=1d
    boffy[i]=boffy0[2+i*5]
    boffy[i].d=median(boffy0[i*5:4+i*5].d,dimen=2)
```

```
    boffy.h.exposure=1d
endfor

;use the 0.2s structure to derive the high cal because the process is
   quick and more accurate to derive the cal with more records
findspeccals2,boffx0,calons
hicalxnorm=boffx0[calons].d/boffx0[calons+35].d-1.
hicalynorm=boffy0[calons].d/boffy0[calons+35].d-1.
hicalx=median(hicalxnorm,dimen=2)
hicaly=median(hicalynorm,dimen=2)

;create the structures without the lowcal bu subtracting it and
   combining when the lowcal is on and off together
boffxnorm=boffx
lowcalxnorm=bonx
bonxnormsubcal=bonx
lowcalx=fltarr(chans)
for i=0L,records-1 do begin
    lowcalxnorm[i].d=(bonx[i].d-boffx[i].d)/median(boffx[i].d)
endfor
lowcalx=median(lowcalxnorm.d,dimen=2)
for i=0L,records-1 do begin
    bonxnormsubcal[i].d=bonx[i].d/median(boffx[i].d)-lowcalx
    boffxnorm[i].d=boffx[i].d/median(boffx[i].d)
endfor
bxsublcal=bonx
bxsublcal.d=(bonxnormsubcal.d+boffxnorm.d)/2.

boffynorm=boffy
lowcalynorm=bony
bonynormsubcal=bony
lowcaly=fltarr(chans)
for i=0L,records-1 do begin
    lowcalynorm[i].d=(bony[i].d-boffy[i].d)/median(boffy[i].d)
endfor
lowcaly=median(lowcalynorm.d,dimen=2)
for i=0L,records-1 do begin
    bonynormsubcal[i].d=bony[i].d/median(boffy[i].d)-lowcaly
    boffynorm[i].d=boffy[i].d/median(boffy[i].d)
```

```
endfor
bysublcal=bony
bysublcal.d=(bonynormsubcal.d+boffynorm.d)/2.

;apply the high cal
beam=boffx[0].h.beam
freqTopo=(dindgen(chans)-(boffx[0].h.crpix1-1))
*boffx[0].h.cdelt1*1d-6+boffx[0].h.crval1*1d-6
;call the value for the high cal (1) for alfa (17) for the bandwidth
    freqtopo
is=calget1(17,1,freqtopo,calval,alfabmnum=beam)
calx={cal:calval[0,*]/hicalx}
caly={cal:calval[1,*]/hicaly}
calratx=replicate(calx,records)
calraty=replicate(caly,records)
;calibrate the data into antenna temperature
bxcal=bxsublcal
bycal=bysublcal
bxcal.d=bxsublcal.d*calratx.cal
bycal.d=bysublcal.d*calraty.cal

;apply gain per beam per za, scale the calibration into Jy and combine
    polarizations
bxjy=bxcal
byjy=bycal
cfreq = boffx[0].h.crval1
gains=fltarr(2,records)
for j=0L,records-1 do begin
    gains[*,j]=alfagetgain(beam,cfreq=cfreq,za=90.-boffx[j].h.elevatio)
    bxjy[j].d=bxcal[j].d/gains[0,j]
    byjy[j].d=bycal[j].d/gains[1,j]
endfor
bjy=bxjy
bjy.d=(bxjy.d+byjy.d)/2.
;print,systime()
end
```

```
livedatazoa
pro livedatazoa2,bin,bout,test=test

;bandpass correct a meridian nodding mode lambda using the technique of
    aips++ package, LiveData.

;telescope drives 0.75' per second
;5' = about 7 seconds = 35 .2s integrations
;300 integrations = 60'
;print,systime()
;b=mrdfits(filein,1,onheader)
ints=n_elements(bin)
chans=n_elements(bin[0].d)
off=median(bin[7:60].d,dimen=2)
bout=bin

for i=0L,ints-1 do begin
    if (i/5 gt (i-1)/5) then begin
        if(i lt 60) then begin
            off=median(bin[i+7:i+60].d,dimen=2)
        endif else begin
       if(i lt ints-61) then begin
                off1=median(bin[i-60:i-7].d,dimen=2)
                off2=median(bin[i+7:i+60].d,dimen=2)
                off=(off1+off2)/2.
            endif else begin
                off=median(bin[i-60:i-7].d,dimen=2)
       endelse
        endelse
    endif
    goodchan1 = fix(chans/10.0)
    goodchan2 = chans - goodchan1
    offmed = median(off[goodchan1-1:goodchan2-1])
    normoff = off/offmed
    reduced=(bin[i].d-off)/normoff
    is=corblauto(reduced,yout,deg=1,sub=1,raw=n_elements(reduced))
    bout[i].d=yout
```

```
endfor
;mwrfits,bout,fileout,onheader
;print,systime()
end
```

```
masveltrans
pro masveltrans2,b,bout,bary=bary,lsr=lsr,topo=topo,
resamp=resamp,spline=spline,lsquadratic=lsquadratic,
quadratic=quadratic,errcode=errcode,rest=rest,redshift=redshift,vel=vel

; Transform frequency from topocentric to another frame
; Uses formulae from http://www.gb.nrao.edu/~fghigo/gbtdoc/doppler.html

nrows=n_elements(b)
crval1 = b.h.crval1
cdelt1 = b.h.cdelt1
specsys=b.h.specsys
c=299792458D
bout=b
if (n_elements(resamp) eq 0) then resamp = 1
if (n_elements(bary) eq 0) then bary = 0
if (n_elements(lsr) eq 0) then lsr = 0
if (n_elements(topo) eq 0) then topo = 0
if (n_elements(rest) eq 0) then rest = 0
if (n_elements(vel) eq 0) then vel = 0
errcode = 0
```

```
if (rest) then begin
    if (n_elements(redshift) ne 1) then begin
        redshift = b.h.req_vel
        vel = 0
    endif
    if (vel) then redshift = redshift * 1000
```

```
    veltype = b.h.req_vel_type
    if (strcmp(veltype,'v',1,/fold_case)) then vel = 1
    if (vel) then redshift = redshift/c
    restfactor = 1.0 + redshift
endif else restfactor = 1.0



if ((topo + bary + lsr) EQ 0) then begin
    print, 'Error: no target coordinate system specified!'
    errcode = 1
endif else if ((topo + bary + lsr) GT 1) then begin
    print, 'Error: only one target coordinate system may be specified!'
    errcode = 1
endif



; Look for input specsys
; If LSR or Barycent, set topo to convert to topocentric before
; converting back out

if (strcmp(b[0].h.specsys,'TOPOCENT',/fold_case)) then begin
    oldsys = 'topo'
    if (topo) then begin
         print, 'Error: Requested transform is from topocentric to
   topocentric!'
         errcode = 1
     endif
endif else if (strcmp(b[0].h.specsys,'BARYCENT',/fold_case)) then begin
    oldsys = 'bary'
    if (bary) then begin
         print, 'Error: Requested transform is from barycentric to
   barycentric!'
         errcode = 1
     endif
     topo = 1
endif else if (strcmp(b[0].h.specsys,'LSRK',/fold_case)) then begin
    oldsys = 'lsr'
```

```
    if (lsr) then begin
         print, 'Error: Requested transform is from LSR to LSR!'
         errcode = 1
     endif
     topo = 1
endif else begin
    print,'Error: specsys not recognized: ',b[0].h.specsys
    errcode = 1
endelse

if (errcode EQ 0) then begin
    for i = 0L, nrows-1 do begin
;        freqs = masfreq(b[i].h) * 1E6
        nchans = b[i].nchan
        oldcrval1 = b[i].h.crval1
        relbary = b[i].h.vel_bary/c
        rarad = b[i].h.crval2*!pi/180.d
        decrad = b[i].h.crval3*!pi/180.d
        radec3vec = anglestovec3(rarad,decrad)
        rellsr = vellsrproj(radec3vec,relbary)
   freqs=(dindgen(nchans) - (b[i].h.crpix1 -1))*b[i].h.cdelt1*1d-6
   +b[i].h.crval1

        if (topo) then begin
            if (oldsys EQ 'bary') then begin
                relold = relbary
            endif else if (oldsys EQ 'lsr') then begin
                relold = rellsr
            endif else begin
                print, 'something weird has happened!'
                errcode = 1
                relold = 0
            endelse

            tfreq = freqs * sqrt(1 - relold^2)/(1 - relold)
            tcrval1 = oldcrval1 * sqrt(1 - relold^2)/(1 - relold)
            relframe = 0
            newspecsys = 'TOPOCENT'
```

```
        endif else begin
            tfreq = freqs
            tcrval1 = oldcrval1

        endelse

        if (bary) then begin
            relframe = relbary
            newspecsys='BARYCENT'
        endif else if (lsr) then begin
            relframe = rellsr
            newspecsys='LSRK'
        endif

        bfreq = tfreq * (1 - relframe) / sqrt(1 - relframe^2)
        newcrval1 = tcrval1 * (1-relframe)/sqrt(1-relframe^2)
        specsys[i] = newspecsys

        if (resamp) then begin
            bfreqresamp = freqs - (oldcrval1 - newcrval1)
            npols = b[i].npol
            resampled = fltarr(nchans,npols)
            for j = 0,npols - 1 do begin
                resampled[*,j] = interpol(b[i].d[*,j],bfreq,bfreqresamp,

   spline=spline,lsquadratic=lsquadratic,quadratic=quadratic)
            endfor
            bout[i].d = resampled
        endif
        crval1[i] = newcrval1
    endfor
endif

bout.h.crval1 = crval1*restfactor
bout.h.cdelt1 = cdelt1
bout.h.specsys = specsys

return
end
```

```
mas2sdfits
pro mas2sdfits4,bin,file,bary=bary,resamp=resamp

; Take in mas structure b and write out to an sdfits file similar to
; the output from Livedata.
; /bary will transform from topo to bary
; /resamp will resample (using interpol) into a uniform freq. grid after
; transforming to bary


;this program does not use an exact relativistic solution
when transforming channel widths as the gridding program, Gridzilla,
only operates on data with uniform channel width.

b = bin

fxhmake,header,/extend,/date,/initialize
fxwrite,file,header

nrows=n_elements(b)

;if(n_elements(bary) LT 1) then bary = 0

;if (bary) then begin
;    masveltrans,b,bout,bary=bary,resamp=resamp
;    b = bout
;endif

crval1 = b.h.crval1
cdelt1 = b.h.cdelt1
specsys=b.h.specsys
c=299792458D

polval=float(strmid(string(b[0].h.crval4,format='(f+0)'),0,2))
polinc = polval/abs(polval)
```

```
;dimen=size(b[0].d,/dimensions)
;if (n_elements(dimen) EQ 2) then begin
;    data=reform(b[0].d,dimen[0],dimen[1],1,1)
;endif else if (n_elements(dimen) EQ 1) then begin
;    data=reform(b[0].d,dimen[0],1,1,1)
;endif else begin
;    print,'Problem with data dimension!'
;endelse

data = reform(b[0].d,b[0].nchan,b[0].npol,1,1)

calfctr=fltarr(nrows,b[0].npol)+1.0

fxbhmake,bheader,nrows,'SINGLE DISH','name of this binary table
    extension',/initialize
fxaddpar,bheader,'TELESCOP','ARECIBO 305m','Telescope name'
fxaddpar,bheader,'OBSGEO-X',2.390586900E+06,'[m] Antenna ITRF
    X-coordinate'
fxaddpar,bheader,'OBSGEO-Y',-5.564731440E+06,'[m] Antenna ITRF
    Y-coordinate'
fxaddpar,bheader,'OBSGEO-Z',1.994720450E+06,'[m] Antenna ITRF
    Z-coordinate'
fxbaddcol,index,bheader,b[0].h.datexxobs,'DATE-OBS'
fxbaddcol,index,bheader,b[0].h.crval5,'TIME',tunit='s'
fxbaddcol,index,bheader,b[0].h.exposure,'EXPOSURE',tunit='s'
fxbaddcol,index,bheader,b[0].h.object,'OBJECT'
fxbaddcol,index,bheader,b[0].h.restfrq,'RESTFRQ',tunit='Hz'
fxbaddcol,index,bheader,b[0].h.obsmode,'OBSMODE'
fxbaddcol,index,bheader,b[0].h.beam+1,'BEAM'
fxbaddcol,index,bheader,b[0].h.ifn+1,'IF'
fxbaddcol,index,bheader,abs(cdelt1[0]),'FREQRES',tunit='Hz'
fxbaddcol,index,bheader,b[0].h.bandwid,'BANDWID',tunit='Hz'
fxaddpar,bheader,'CTYPE1','FREQ    ','DATA array axis 1: frequency in
    Hz'
fxbaddcol,index,bheader,b[0].h.crpix1,'CRPIX1'
fxbaddcol,index,bheader,crval1[0],'CRVAL1'
fxbaddcol,index,bheader,cdelt1[0],'CDELT1'
```

```
fxaddpar,bheader,'CTYPE2','STOKES  ','DATA array axis 2: polarization
    code'
fxaddpar,bheader,'CRPIX2',1.0,'Polarization code reference pixel'
fxaddpar,bheader,'CRVAL2',polval,'Polarization code at reference pixel'
fxaddpar,bheader,'CDELT2',polinc,'Polarization code axis increment'
fxaddpar,bheader,'CTYPE3','RA      ','DATA array axis 3 (degenerate):
    RA (mid-int)'
fxaddpar,bheader,'CRPIX3',1.0,'RA reference pixel'
fxbaddcol,index,bheader,b[0].h.crval2,'CRVAL3',tunit='deg'
fxaddpar,bheader,'CDELT3',1.0,'RA axis increment'
fxaddpar,bheader,'CTYPE4','DEC     ','DATA array axis 4 (degenerate):
    Dec (mid-int)'
fxaddpar,bheader,'CRPIX4',1.0,'Dec reference pixel'
fxbaddcol,index,bheader,b[0].h.crval3,'CRVAL4',tunit='deg'
fxaddpar,bheader,'CDELT4',1.0,'Dec axis increment'
fxaddpar,bheader,'SPECSYS','BARYCENT'
fxaddpar,bheader,'SSYSOBS','TOPOCENT','Doppler reference frame of
    observation'
fxaddpar,bheader,'EQUINOX',2000,'Equinox of equatorial coordinates'
fxaddpar,bheader,'RADESYS','FK5','Equatorical coordinate frame'
fxbaddcol,index,bheader,fltarr(2),'TSYS'
fxbaddcol,index,bheader,data,'DATA',tunit='Jy/beam'
fxbaddcol,index,bheader,fltarr(b[0].npol),'CALFCTR'
fxbaddcol,index,bheader,b[0].h.azimuth,'AZIMUTH',tunit='deg'
fxbaddcol,index,bheader,b[0].h.elevatio,'ELEVATIO',tunit='deg'
fxbaddcol,index,bheader,b[0].h.vel_bary,'VEL_BARY',tunit='m/s'

fxbcreate,lun,file,bheader,ext

;The number in 'indgen' in fxbwritem (below) should reflect the number
; of columns!

fxbwritm,lun,indgen(21)+1,b.h.datexxobs,b.h.crval5,b.h.exposure
,b.h.object,b.h.restfrq,b.h.obsmode,b.h.beam+1,b.h.ifn+1,abs(cdelt1)
,b.h.bandwid,b.h.crpix1,crval1,cdelt1,b.h.crval2,b.h.crval3,fltarr(nrows,2)
+30.0,b.d,calfctr,b.h.azimuth,b.h.elevatio,b.h.vel_bary

fxbfinish,lun
```

```
return
end



coverage
pro coverage3

; this program performs ALFAZOA deep field bandpass calibration on all
    observations and writes them out in sdfits format ready to be fed
    into gridzilla
; the user needs to first make a list of all project aofits files by
    typing ls /share/pdata8/pdev/a2611*b0s0* > /home/zoa/filesum.cat
;this program works by iterating each file named in filesum.cat
    sequentially in ON-OFF/OFF data reduction with it's neighboring file

file='/home/zoa/filesum.cat'
nrows = File_Lines(file)
filelist=strarr(nrows)
openr,lun,file,/get_lun
readf,lun,filelist
close,/all
istest = -1
is1 = -1
is2 = -1

;for k=0,ndates-1 do begin
for j=1,nrows-1 do begin

            file1 = filelist[j]
            is1=masopen(file1,desc1)
            dored = 0
            if (is1 eq 0) then begin

                is=masgetfile(desc1,b1)

                file2 = filelist[j+1]
                is2=masopen(file2,desc2)
```

```
            if (is2 eq 0) then begin

                is=masgetfile(desc2,b2)

                dec_on=b1[0].h.REQ_DECJ
                dec_off1=b2[0].h.REQ_DECJ

                ra_on=b1[0].h.REQ_RAJ
                ra_off1=b2[0].h.REQ_RAJ

                decsep1 = abs(dec_on - dec_off1) * 60.0

                if ((decsep1 lt 1.5) AND (ra_off1 GT ra_on)) then
begin
                    k = j+1
                    dored=1

                endif

            endif
            if (dored eq 0) then begin

                masclose,desc2

                file2 = filelist[j-1]
                is2=masopen(file2,desc2)

                if (is2 eq 0) then begin
                    is=masgetfile(desc2,b2)

                    dec_off2=b2[0].h.REQ_DECJ

                    ra_off2=b2[0].h.REQ_RAJ

                    decsep2 = abs(dec_on - dec_off2)*60.0


                    if ((decsep2 lt 1.5) AND (ra_off2 LT ra_on))
then begin
```

```
                        k = j-1
                        dored=1
                    endif
                endif
            endif
            if(dored) then begin

filebase1=strsplit(file1,'/share/pdata8',/regex,/extract)

filebase2=strsplit(file2,'/share/pdata8',/regex,/extract)
                for beam = 0,6 do begin
                    sclcal=1

                    pdata=beam+8
                    pdatas=string(pdata,format='(I0)')
                    beams=string(beam,format='(I0)')

                    file1='/share/pdata'+pdatas+filebase1
                    beamnum=strpos(file1,'b0')
                    strput,file1,beams,beamnum+1

                    file2='/share/pdata'+pdatas+filebase2
                    beamnum=strpos(file2,'b0')
                    strput,file2,beams,beamnum+1

                    zoaredfiles,file1,file2,b,avg=0,sclcal=sclcal,

/scljy,matches=matches,/median,velrange=[-2000,12000]

                    if (matches GT 20) then begin
                        if (sclcal eq 1) then begin

fileout='/proj/a2611/all/sdfitsa2611/'+strs

plit(strsplit(file1,'/share/pdata'+pdatas+'

/pdev/',/regex,/extract),'.fits',/regex,/ex
                                                tract)+'_out.sdfits'
                        endif else begin
```

```
    fileout='/proj/a2611/all/sdfitsa2611/'+strsp

    lit(strsplit(file1,'/share/pdata'+pdatas+'/p

    dev/',/regex,/extract),'.fits',/regex,/extra
                                                ct)+'_out_nocal.sdfits'
                            endelse
                            mas2sdfits,b,fileout,/bary,/resamp
                            print,fileout+' written'
                        endif
                    endfor
                endif else begin
                    name=b1.h.object
                    print, name[0]+' has no match'
                endelse



            endif else begin
                print,file1+' not found'
                i = imax
            endelse

            if (is1 EQ 0) then masclose,desc1
            if (is2 EQ 0) then masclose,desc2
            if (istest EQ 0) then masclose,desctest


endfor
end


coordmatch
pro coordmatch,bon,boff,on_index,off_index,offsets,time=time,maxd=maxd

;
; bon - mas struct for on
; boff - mass struct for off
```

```
; maxd - max allowable offset (arcmin)
;
; Returns:
; on_index - matched spectra in on
; off_index - matched spectra in off
; offsets - offset between matched spectra (arcmin)
;

if(n_elements(maxd) ne 1) then maxd=3.5
maxoff = maxd * !pi/(180.0*60.0)
theta_on=(!pi/180.0)*bon.h.azimuth
phi_on=(!pi/180.0)*bon.h.elevatio
theta_off=(!pi/180.0)*boff.h.azimuth
phi_off=(!pi/180.0)*boff.h.elevatio
;got ons and offs
c=fltarr(n_elements(theta_off),n_elements(theta_on))
for j=0,(n_elements(theta_on)-1) do begin
   for n=0,(n_elements(theta_off)-1) do begin
       if (phi_on[j] gt phi_off[n]) then begin

    c[n,j]=((cos(phi_on[j]))^2*(theta_off[n]-theta_on[j])^2+(phi_off[
                n]-phi_on[j])^2)^0.5
       endif else begin

    c[n,j]=((cos(phi_off[n]))^2*(theta_off[n]-theta_on[j])^2+(phi_of
                f[n]-phi_on[j])^2)^0.5
       endelse
   endfor
endfor
;made array c of seperations
;print,c*((180*60)/!pi)
f=min(c,dimension=1)
;produced values of smallest seperations for each on
h=indgen(n_elements(f))
g=intarr(n_elements(f))
for l=0,(n_elements(f)-1) do begin
    g[l]=where(c[*,l] eq f[l])
endfor
if (min(f) gt maxoff) then begin
```

```
    print,'Minimum offset of ',min(f),' greater than maximum allowed of
    ',maxoff
    on_index=-1
    off_index=-1
    offsets=180*60
    time=0
endif else begin
    on_index = h[where(f lt maxoff)]
    off_index = g[where(f lt maxoff)]
    offsets= ((180*60)/!pi)*f[where(f lt maxoff)]

;made two arrays, on_index and off_index, of indices of theta ons and
   offs
;that match and have seperation less than maxd
;print,'on_index=',on_index
;print,'off_index=',off_index
    time=n_elements(offsets)
endelse
print,time

end



zoaredfiles
pro zoaredfiles,filename1,filename2,b,sclcal=sclcal,scljy=scljy,avg=avg,
median=median,offs=offs,maxoff=maxoff,dobl=dobl,deg=deg,matches=matches,
velrange=velrange,polAVG=polAVG

if(n_elements(beam)) eq 0 then beam=0
if(n_elements(spectrum)) eq 0 then spectrum=0
if(n_elements(deg)) eq 0 then deg=1
if(n_elements(dobl)) eq 0 then dobl=1

;file1='/share/pdata'+string(beam+8,format='(I0)')+'/pdev/'+projid+'.'+st
ring(date1,format='(I0)')+'.b'+string(beam,format='(I0)')+'s'+string(spe
ctrum,format='(I0)')+'g1.'+string((100*num1),format='(I05)')+'.fits'

;file2='/share/pdata'+string(beam+8,format='(I0)')+'/pdev/'+projid+'.'+s
```

```
tring(date2,format='(I0)')+'.b'+string(beam,format='(I0)')+'s'+string(spe
ctrum,format='(I0)')+'g1.'+string((100*num2),format='(I05)')+'.fits'

is=masopen(filename1,desc1)
is=masopen(filename2,desc2)

if(n_elements(sclcal) eq 0) then sclcal=0
if(n_elements(sclJy) eq 0) then sclJy = 0
if(n_elements(avg) eq 0) then avg=1
if(n_elements(median) eq 0) then median = 0
if(median) then avg = 1
if(n_elements(maxoff) eq 0) then maxoff = 1.7

if (scljy) then sclcal = 1

if(sclcal) then begin
    masgetcalib,desc1,b1,caltime=cal1
    masgetcalib,desc2,b2,caltime=cal2
endif else begin
    is=masgetfile(desc1,b1,/double)
    is=masgetfile(desc2,b2,/double)
    cal1=0
    cal2=0
endelse

if ((cal1 eq 0) or (cal2 eq 0)) then begin
    sclcal = 0
    scljy = 0
    print, 'Cals not found!'
endif


coordmatch,b1,b2,on_ind,off_ind,offs,time=matches,maxd=maxoff

if(matches GT 20) then begin
    bred = replicate(b1[on_ind[0]],matches)
    for i = 0,matches-1 do begin
        bred[i] = b1[on_ind[i]]
    endfor
```

```
    for i = 0, matches-1 do begin
        masonoff,b1[on_ind[i]].d,b2[off_ind[i]].d,tempspec
        bred[i].d = tempspec
;    print,i,on_ind[i],off_ind[i]
    endfor

    if (avg) then begin
        b = masmath(bred,/avg,/median,polAVG=polAVG)
;        if (median) then begin
;            b = masmath(bred,/median)
;        endif else begin
;            is = masaccum(bred,b,/avg,/new)
;        endelse
    endif else begin
   is = masaccum(bred,b,/avg,/new)
        b = bred
    endelse

    if(dobl) then begin
        masbl,b,bbl,/auto,/sub,deg=deg,velrange=velrange,/hi
        b = bbl
    endif

    if(scljy) then begin
        masalfagain, b, bcal, cfreq = 1400, bw = 60
        b = bcal
    endif
endif else begin
    print,'No matching positions found!'
endelse

masclose,/all

end
```

Appendix B

ALFA ZOA Profiles

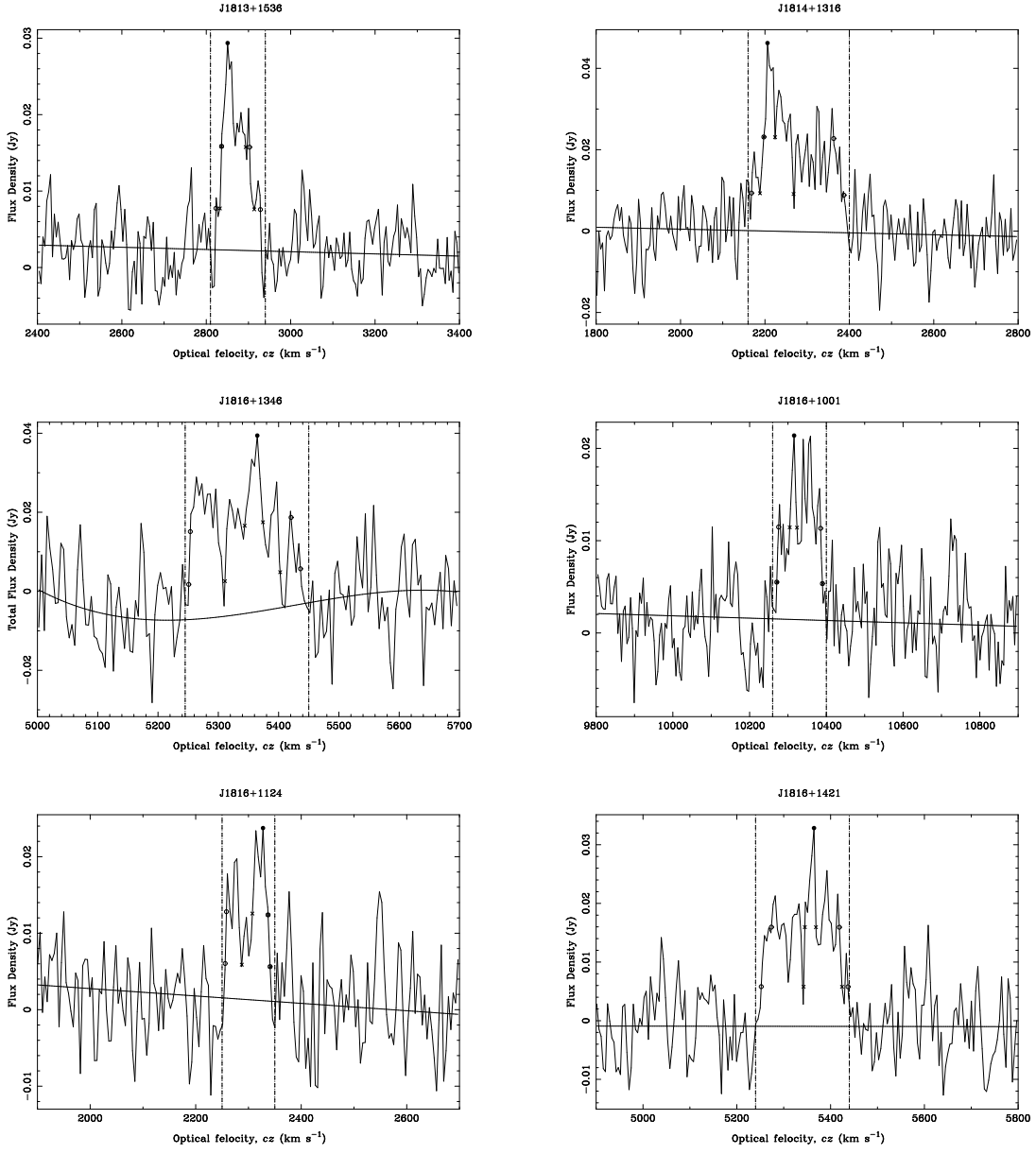

Figure B.1 HI profiles of ALFA ZOA Shallow survey detections in flux density (Jy) versus heliocentric velocity (km s^{-1}).

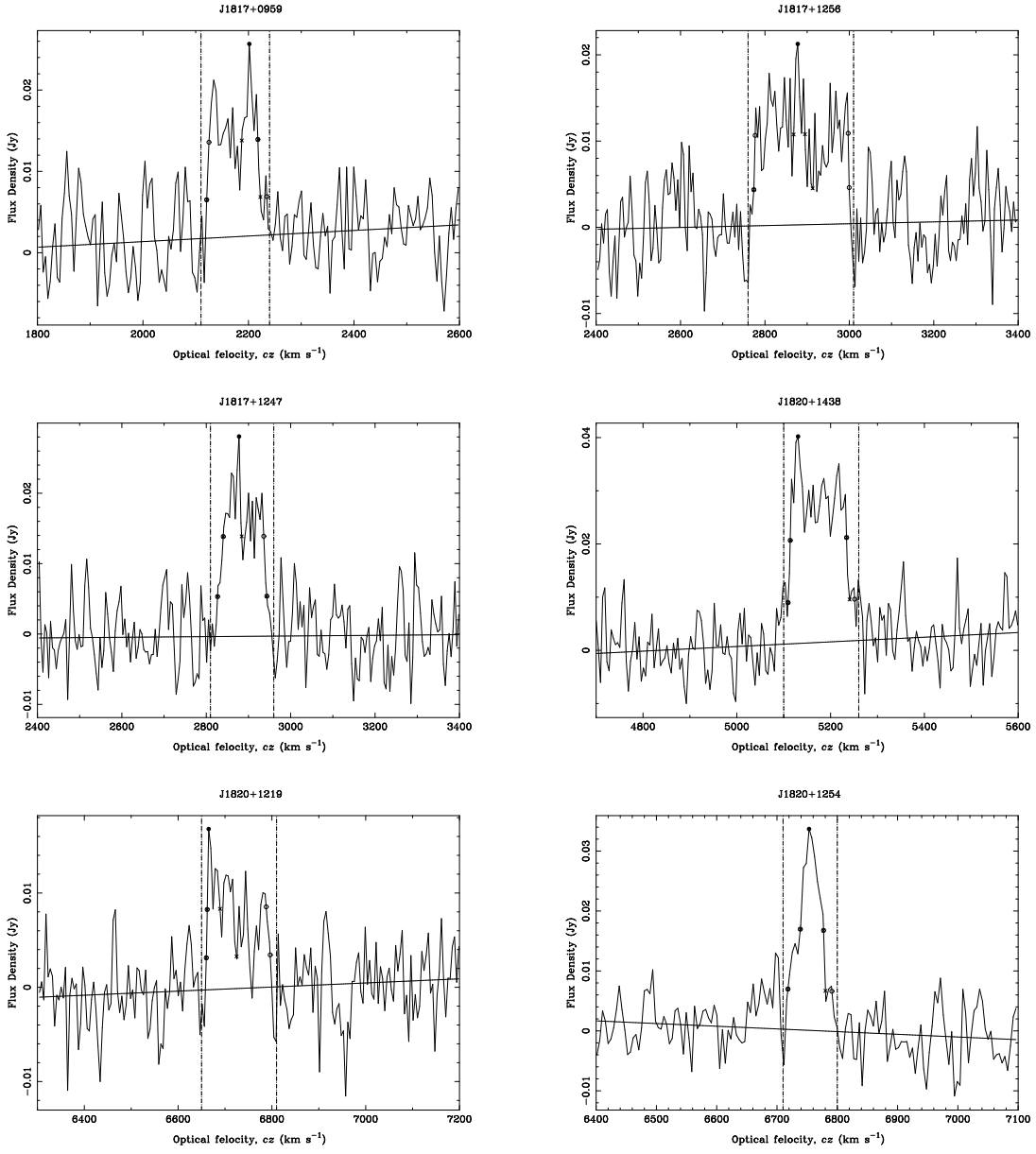

Figure B.1 (continued)

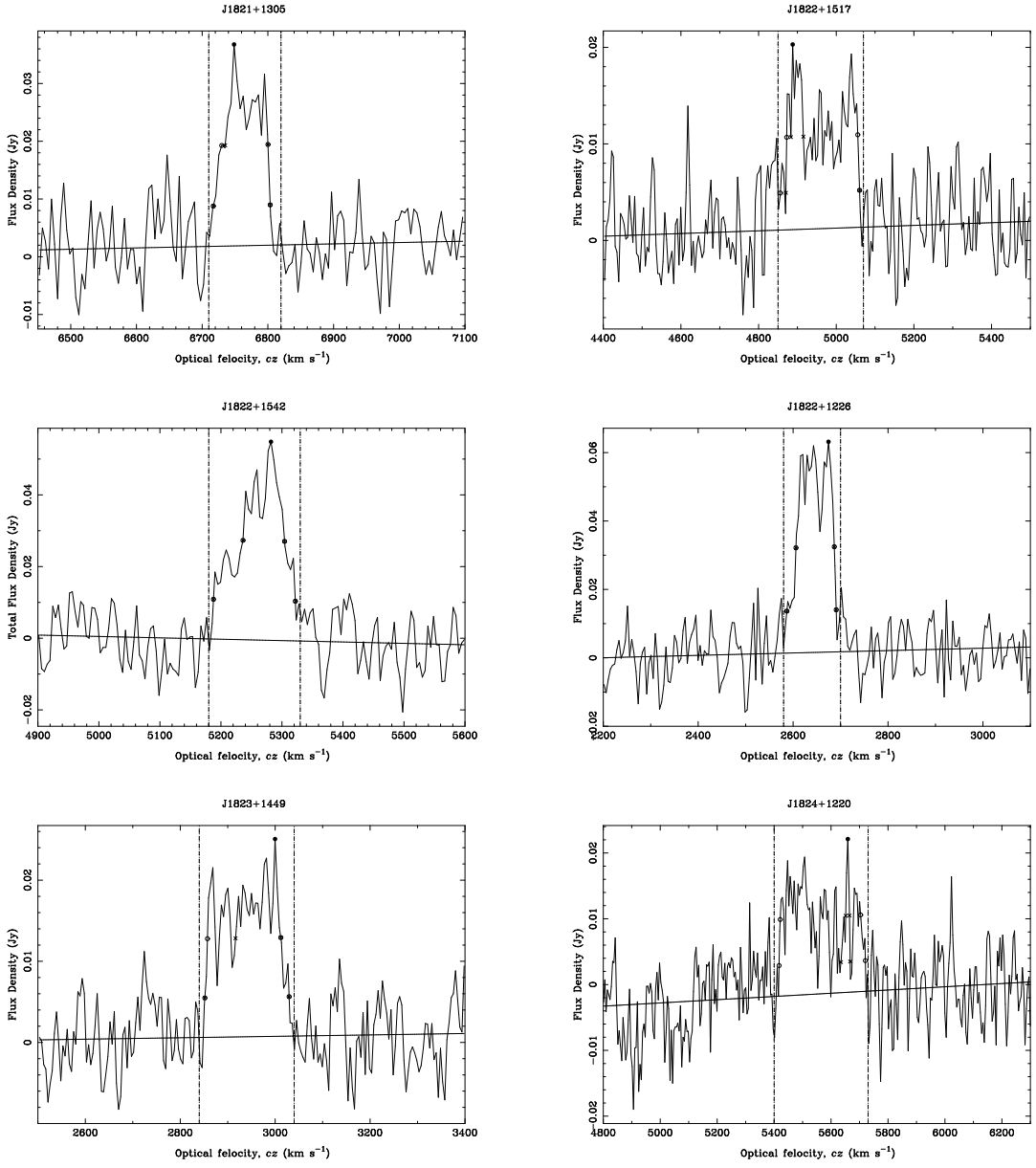

Figure B.1 (continued)

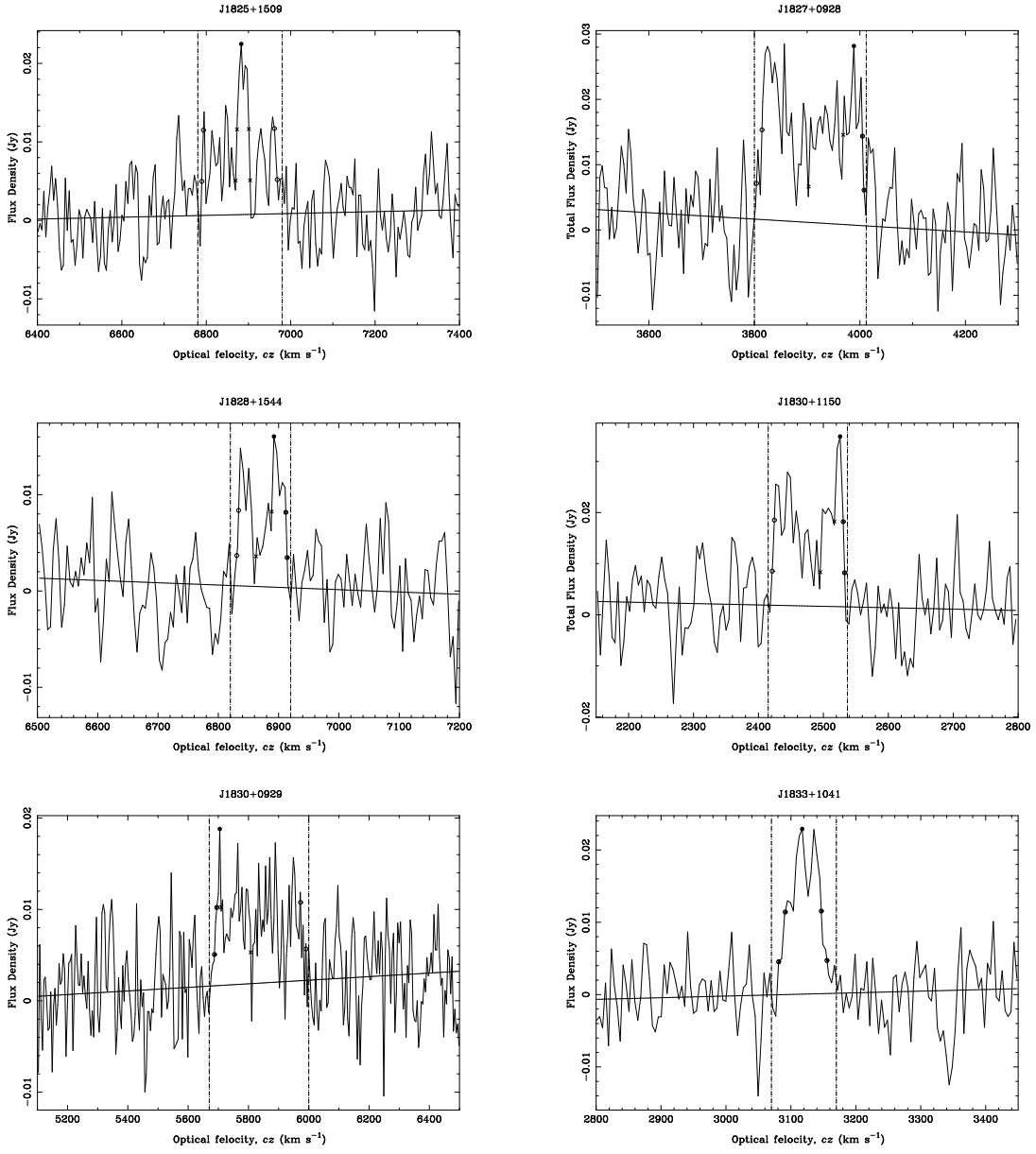

Figure B.1 (continued)

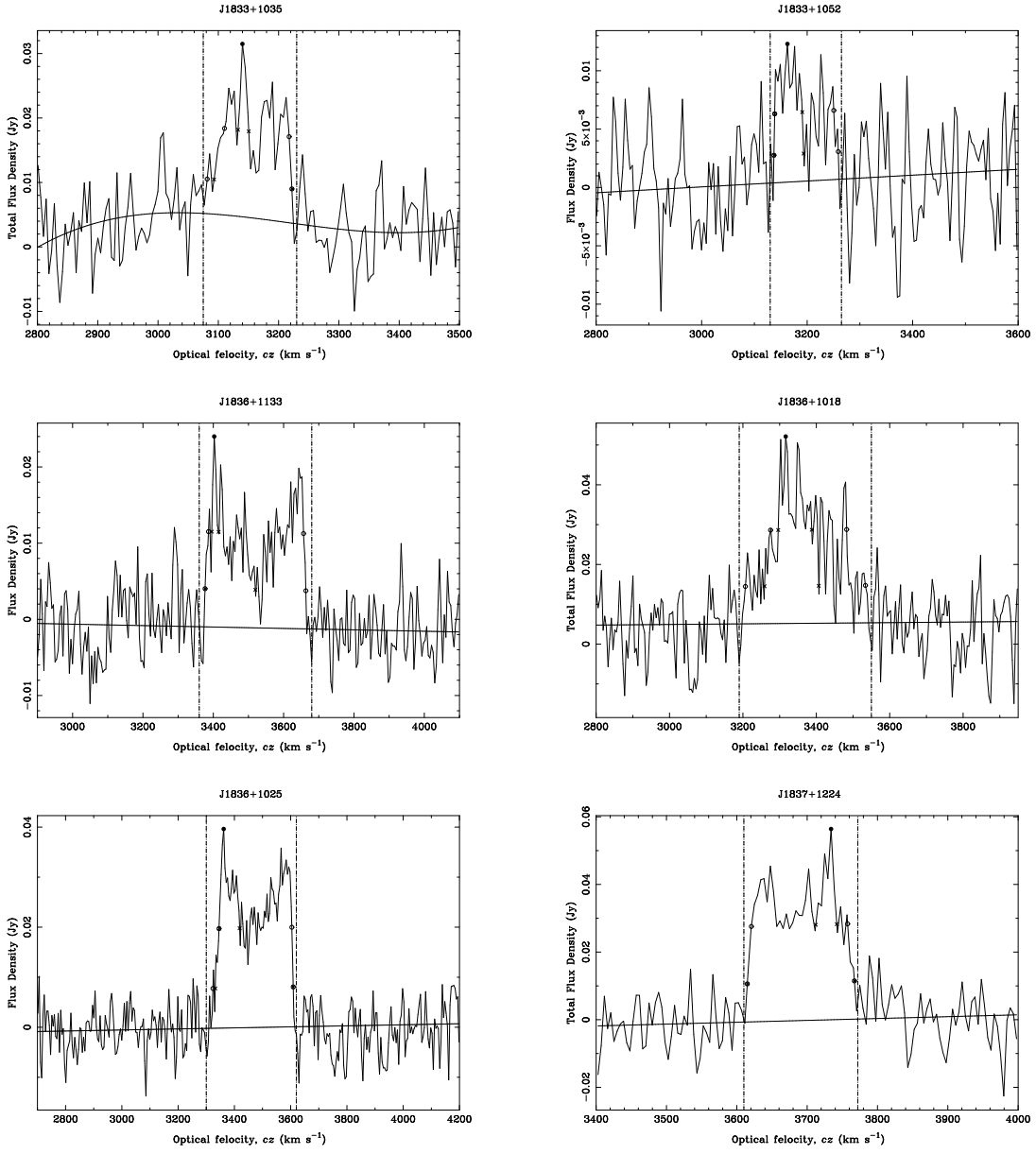

Figure B.1 (continued)

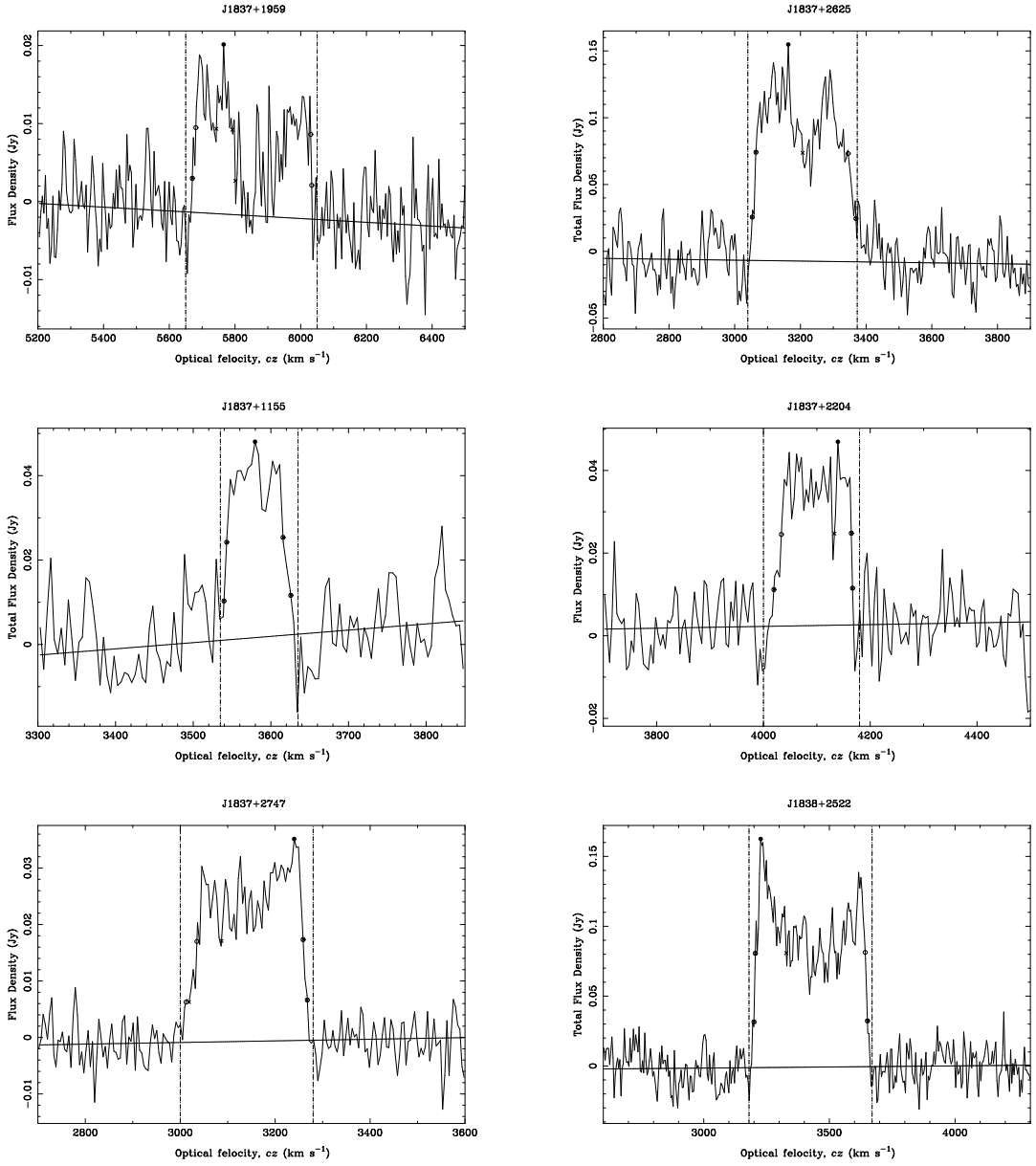

Figure B.1 (continued)

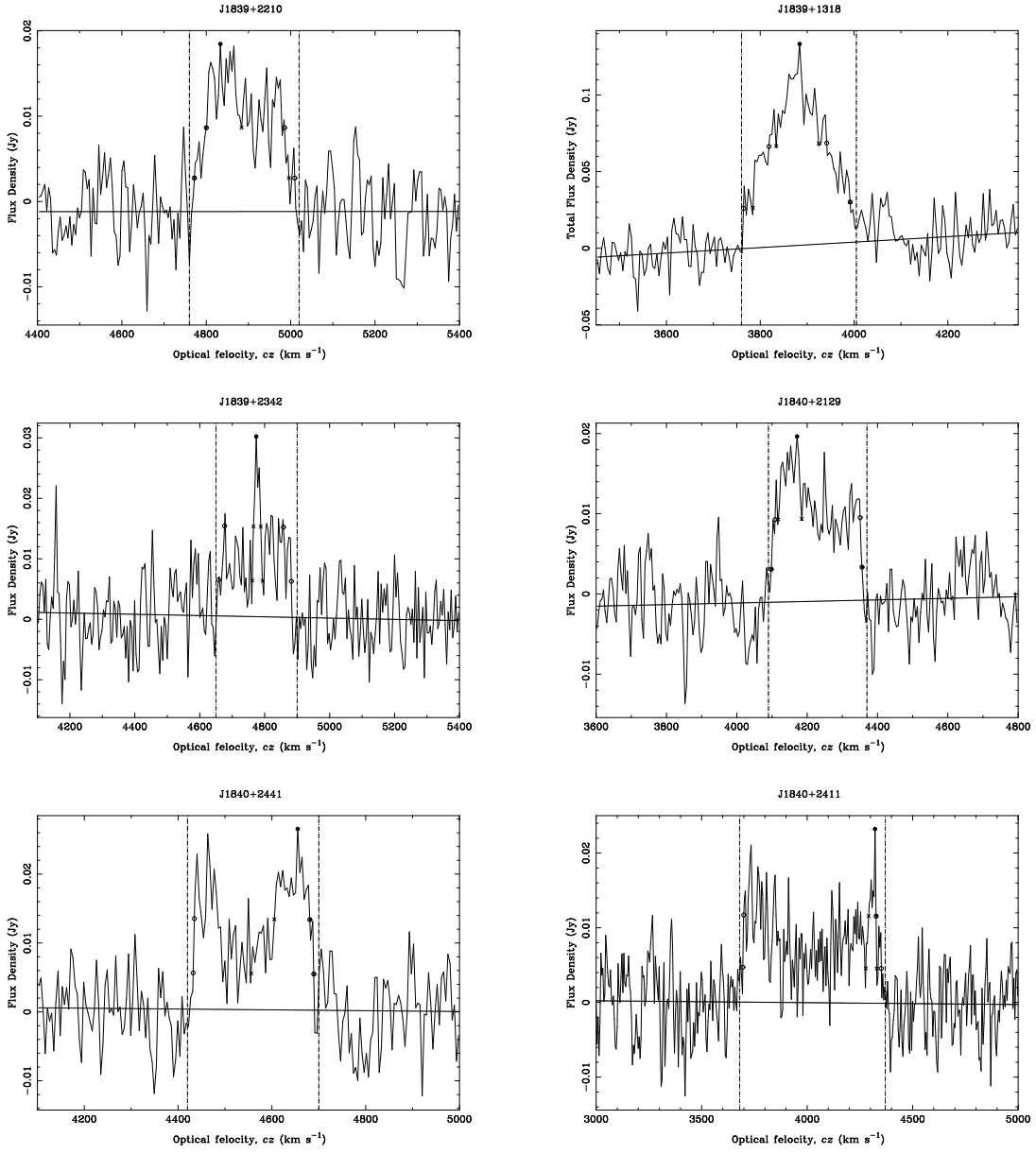

Figure B.1 (continued)

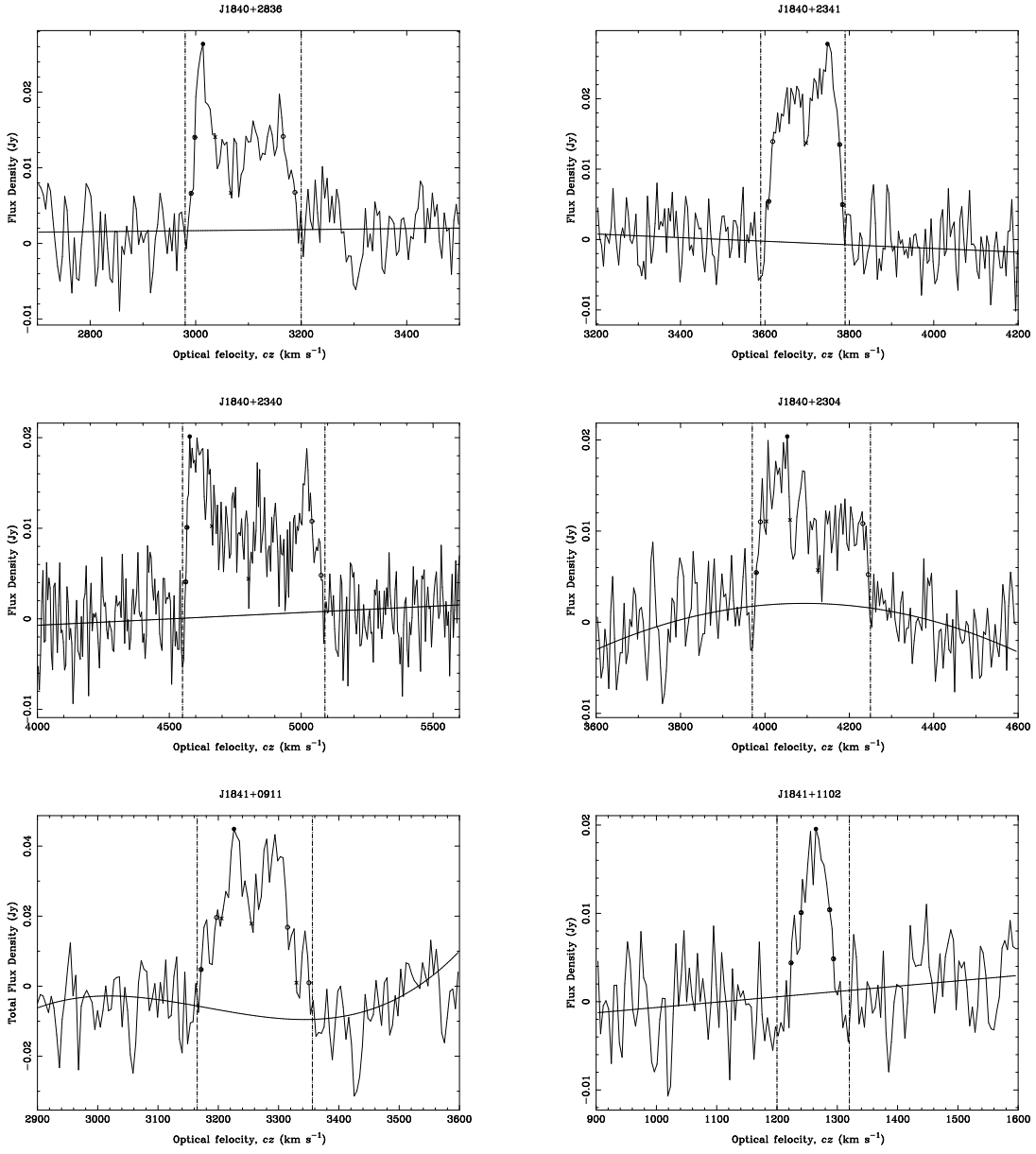

Figure B.1 (continued)

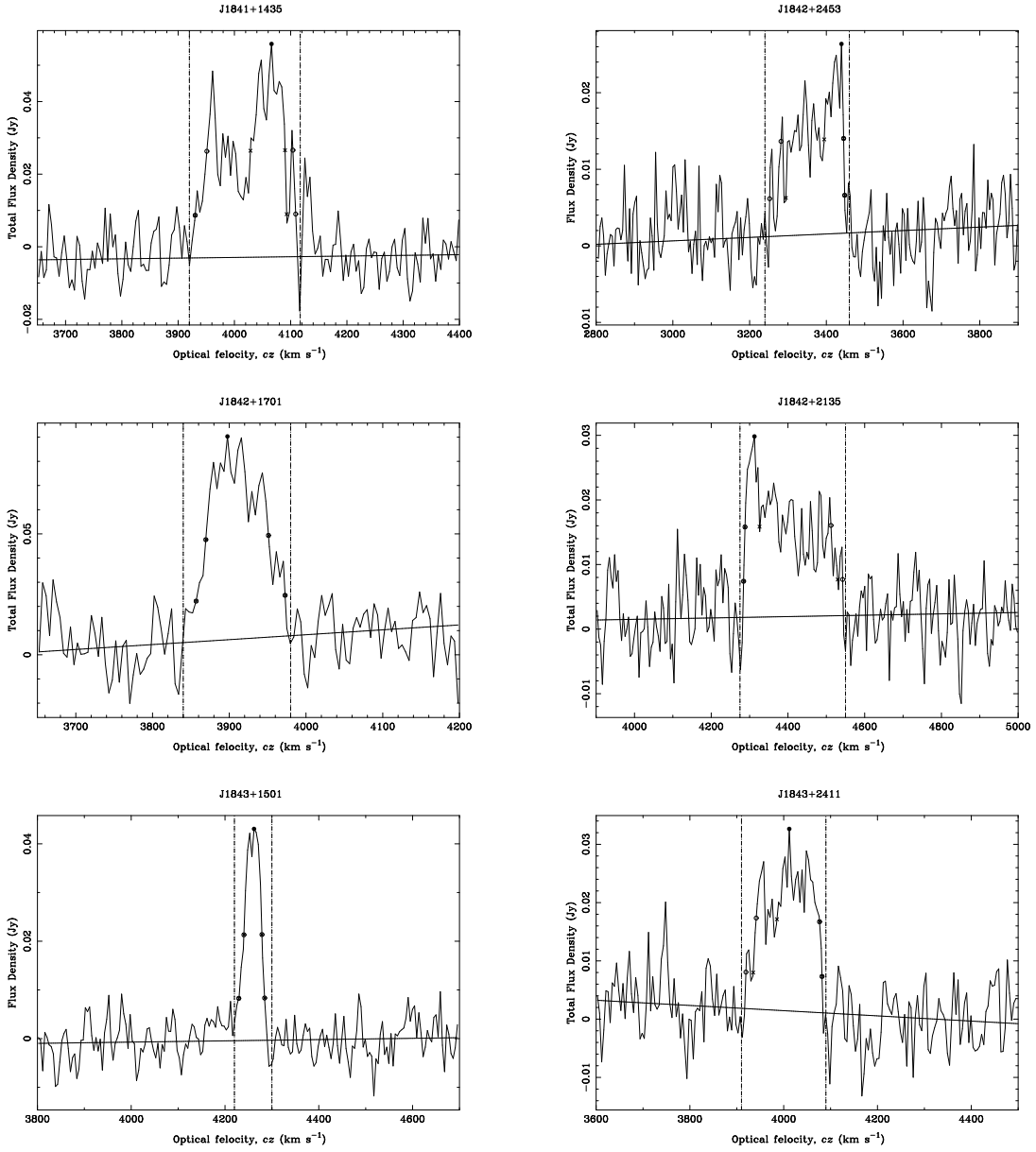

Figure B.1 (continued)

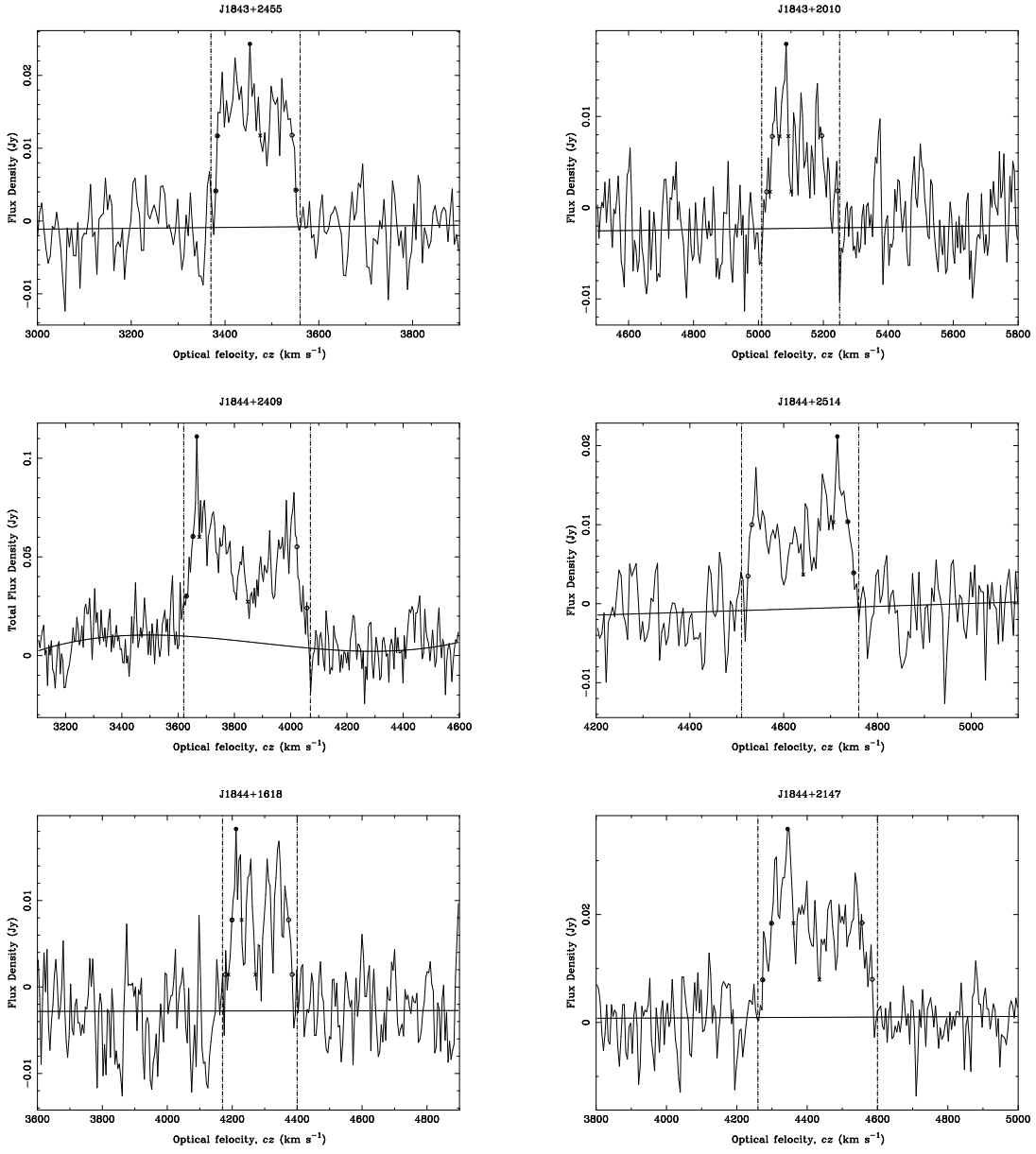

Figure B.1 (continued)

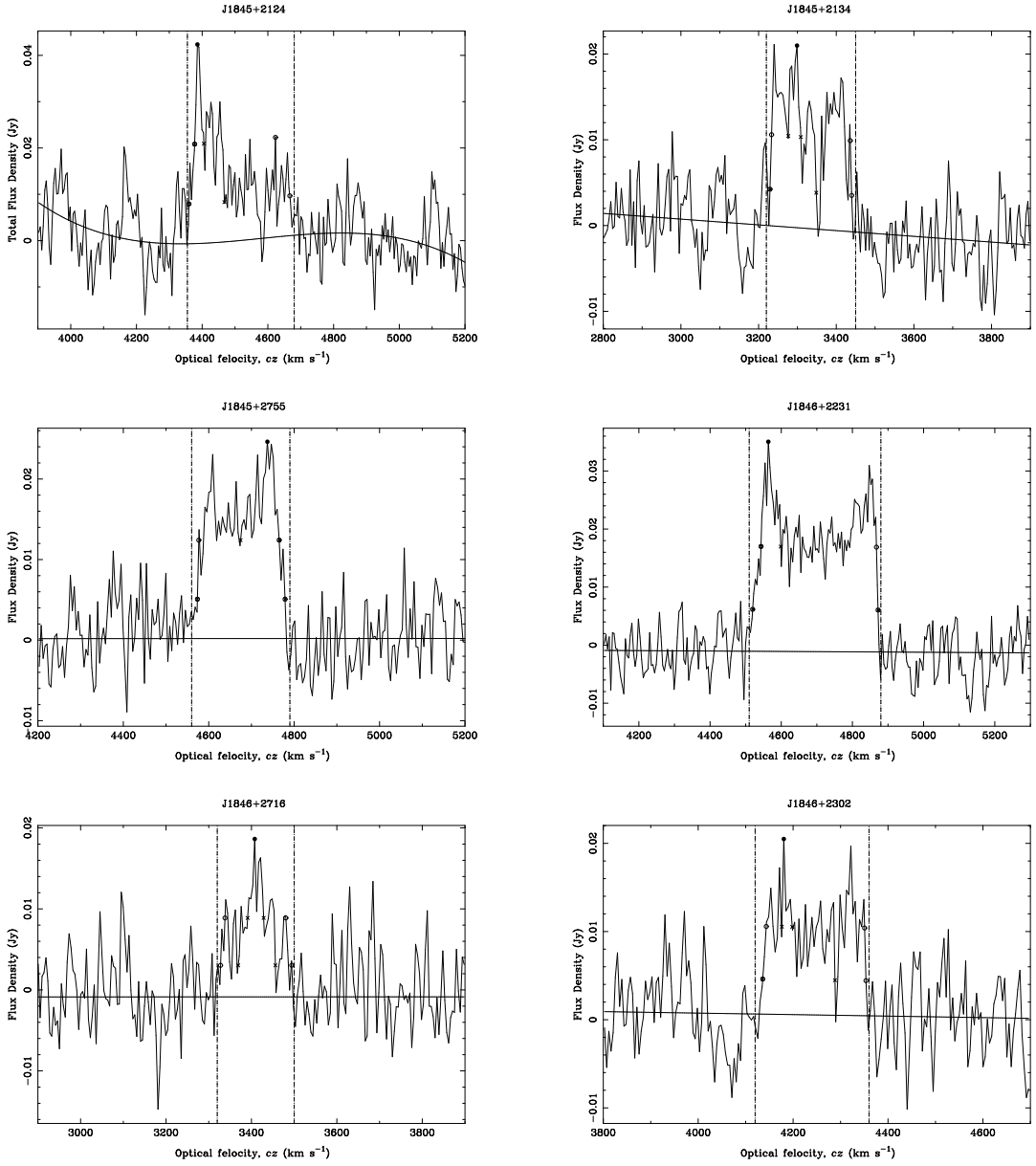

Figure B.1 (continued)

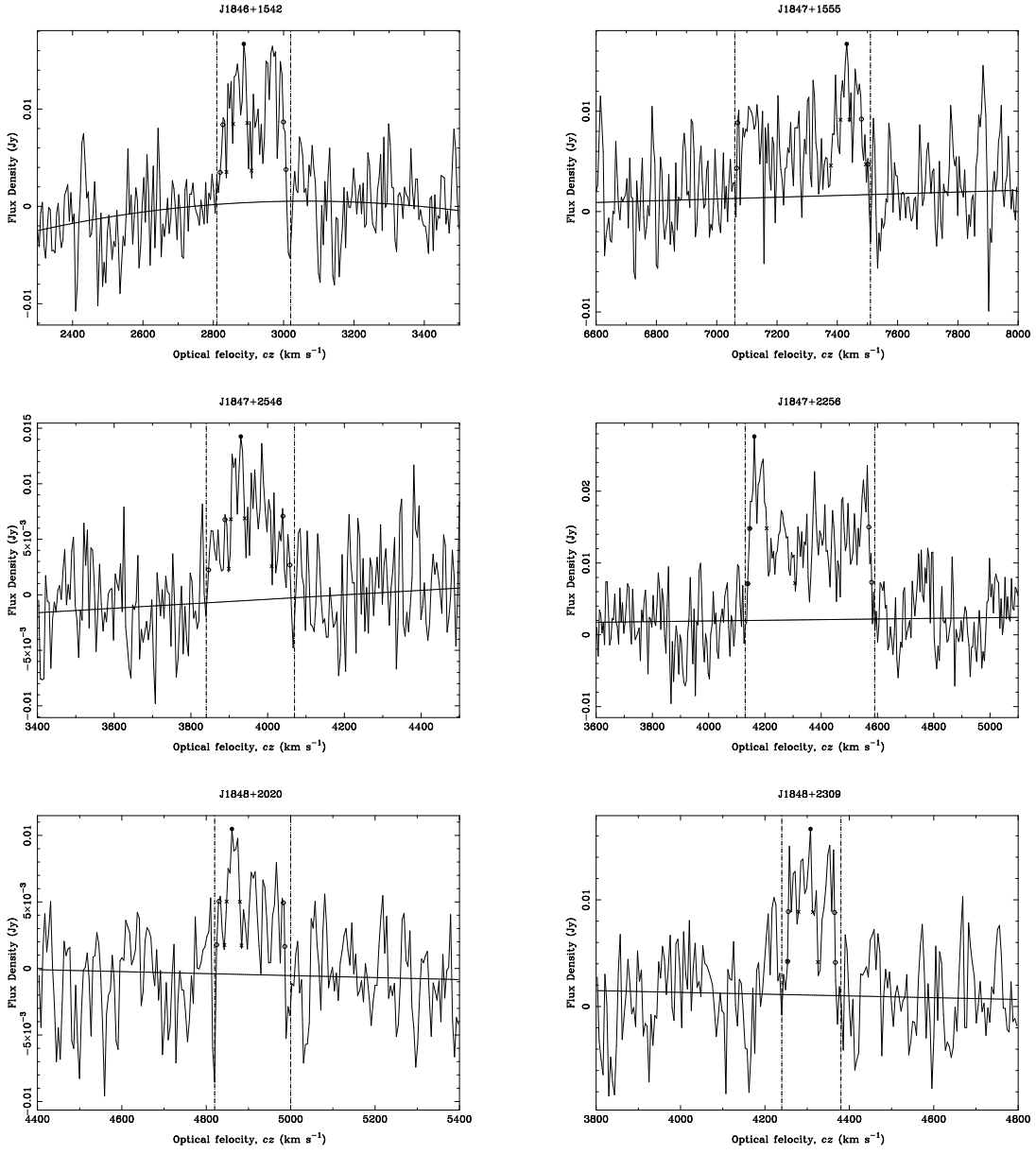

Figure B.1 (continued)

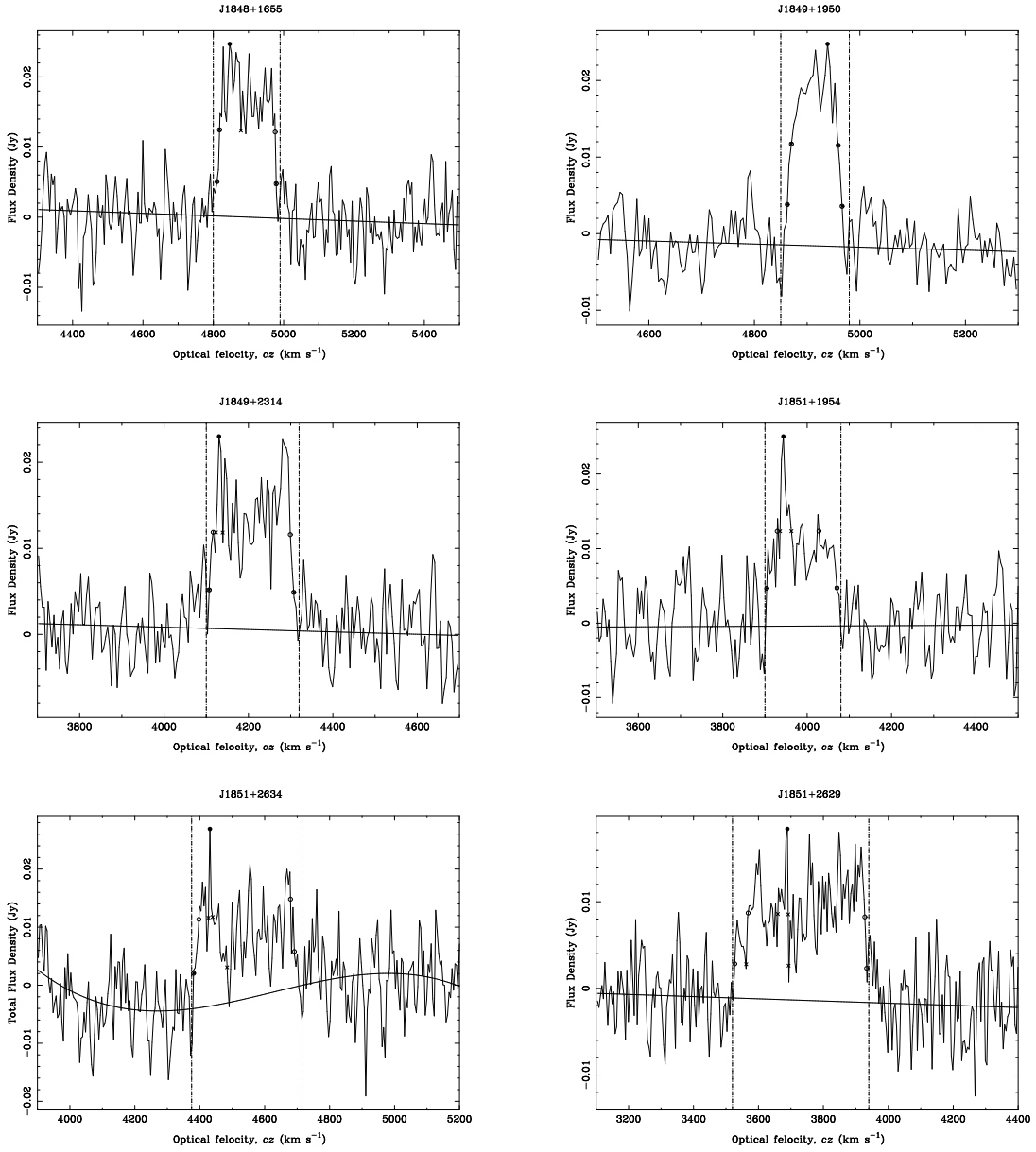

Figure B.1 (continued)

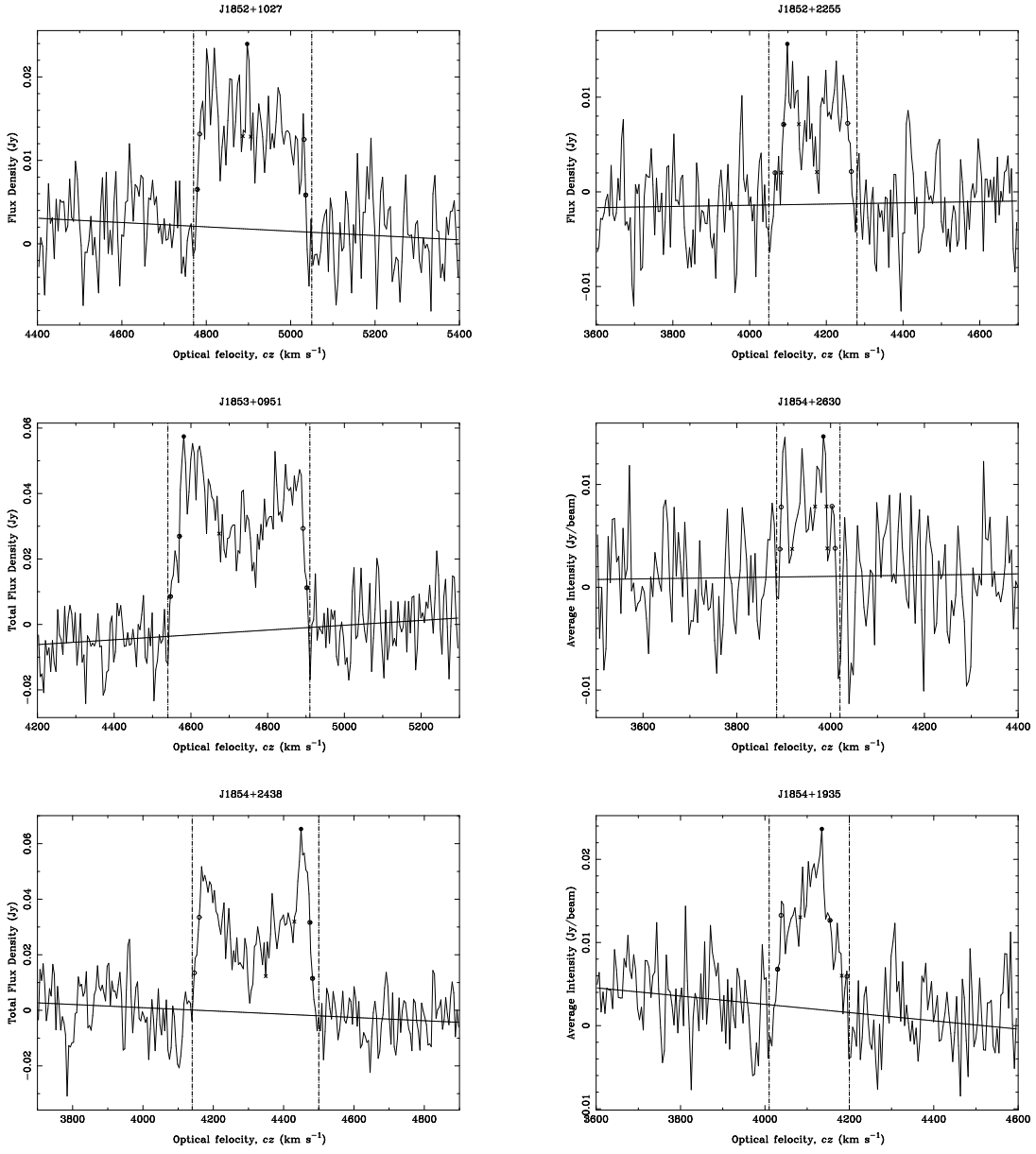

Figure B.1 (continued)

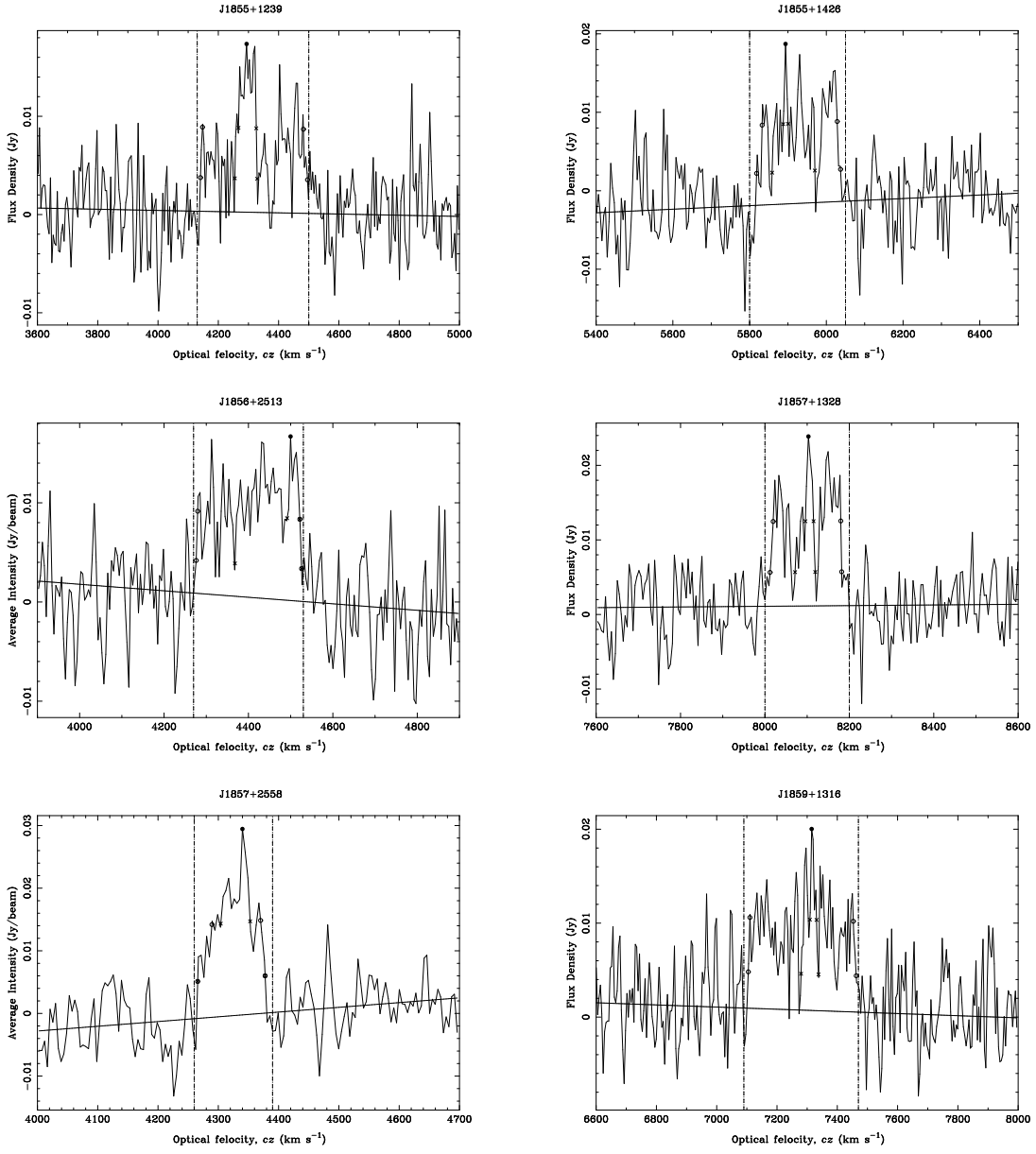

Figure B.1 (continued)

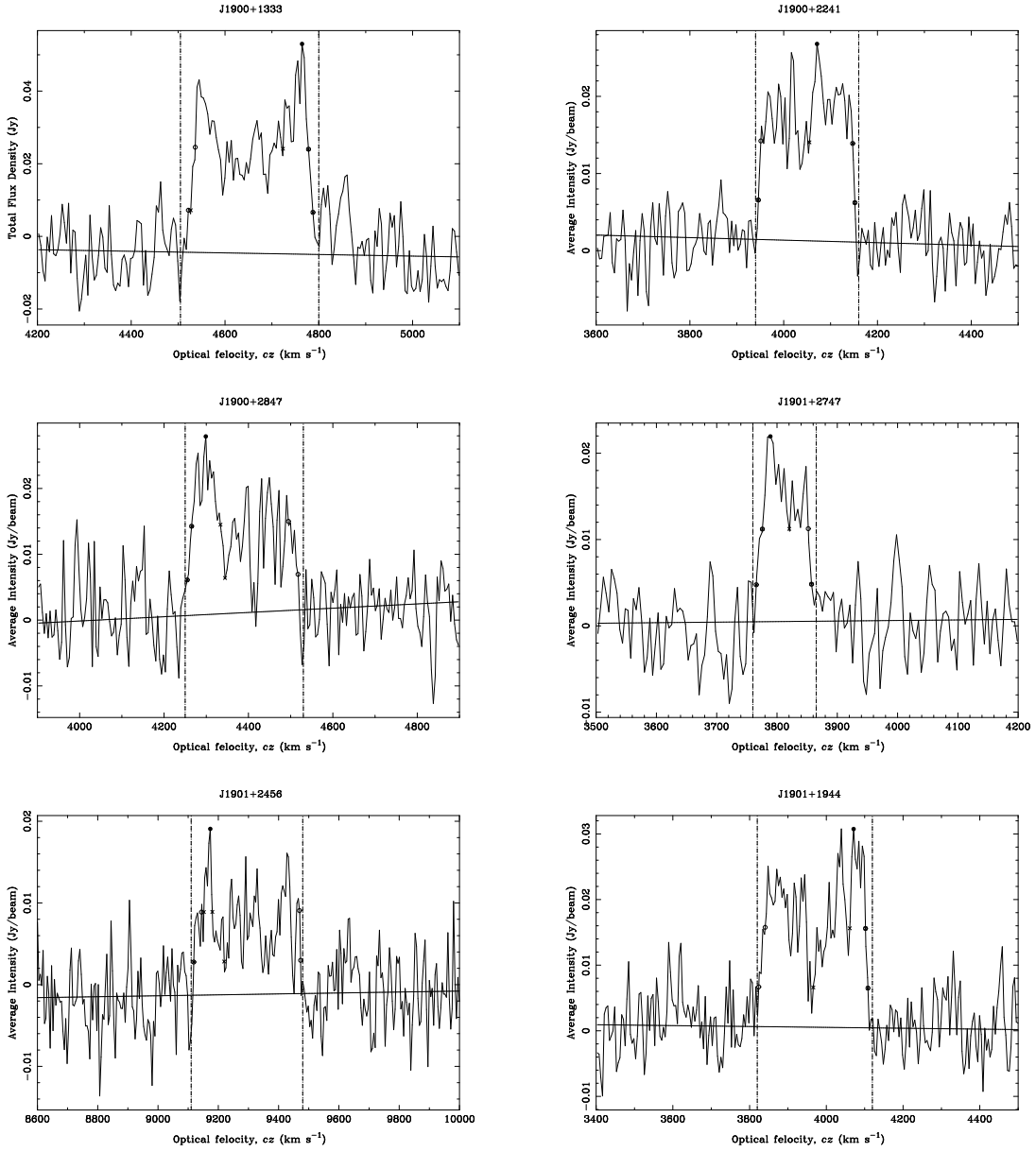

Figure B.1 (continued)

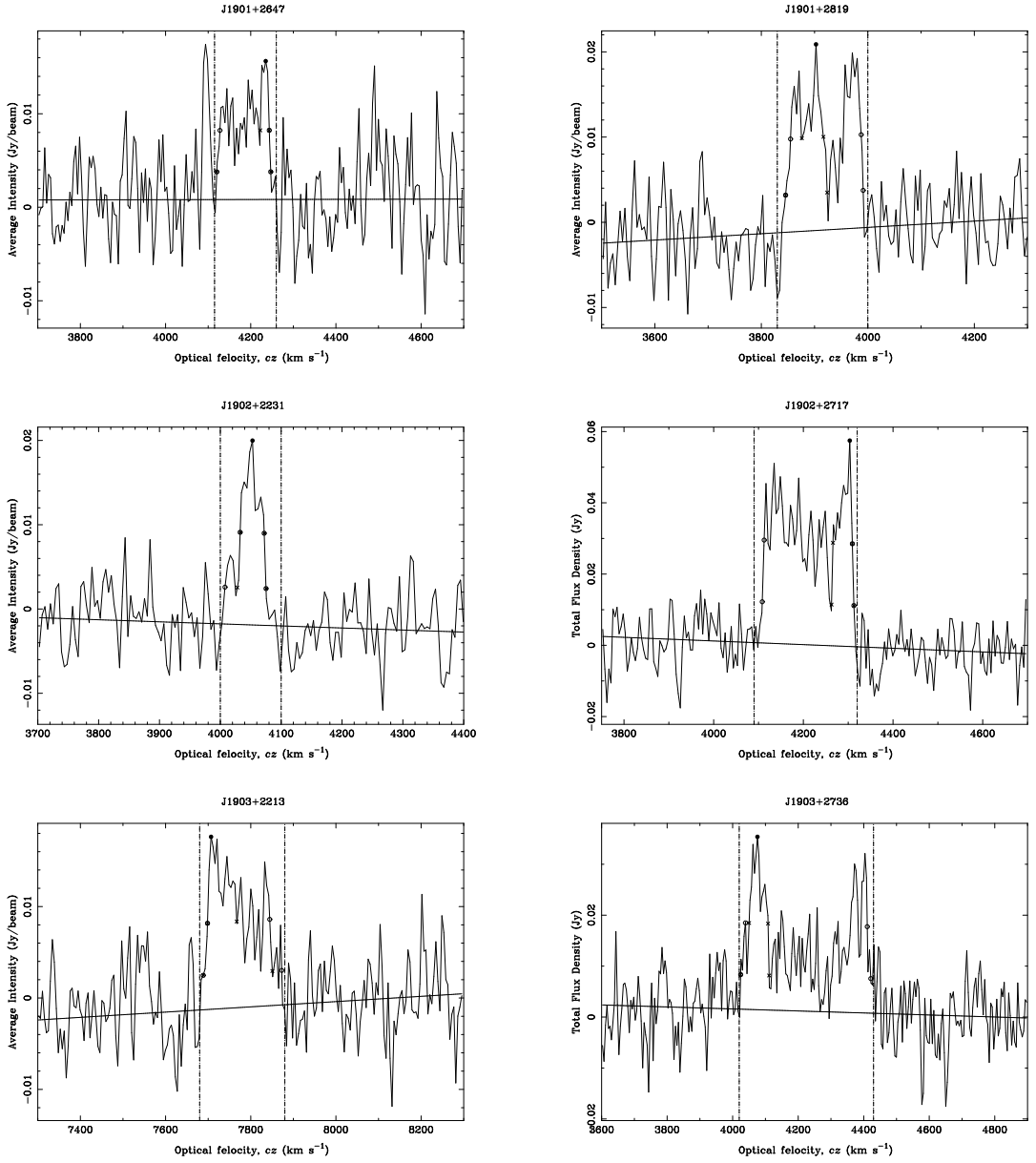

Figure B.1 (continued)

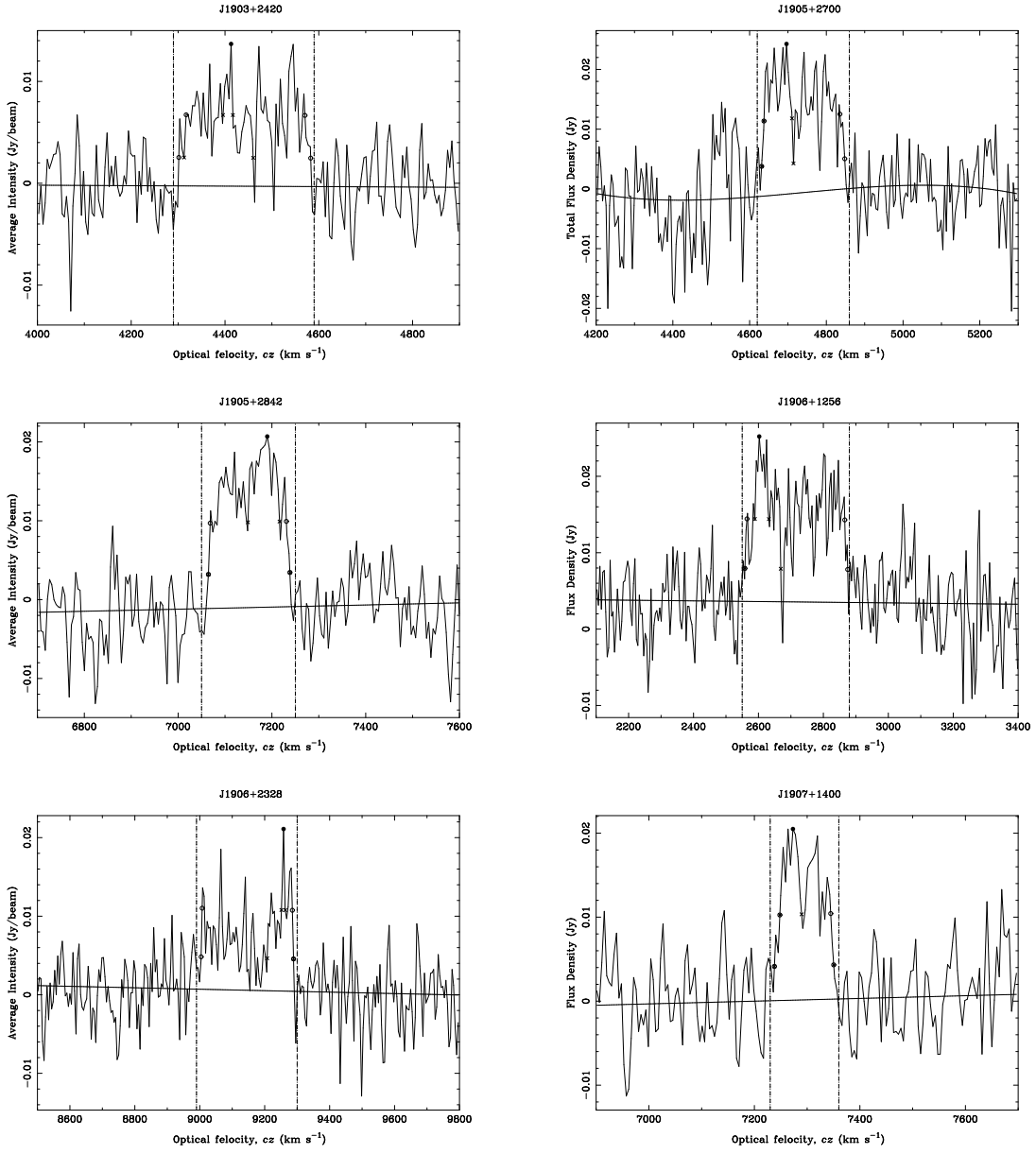

Figure B.1 (continued) Figure B continued

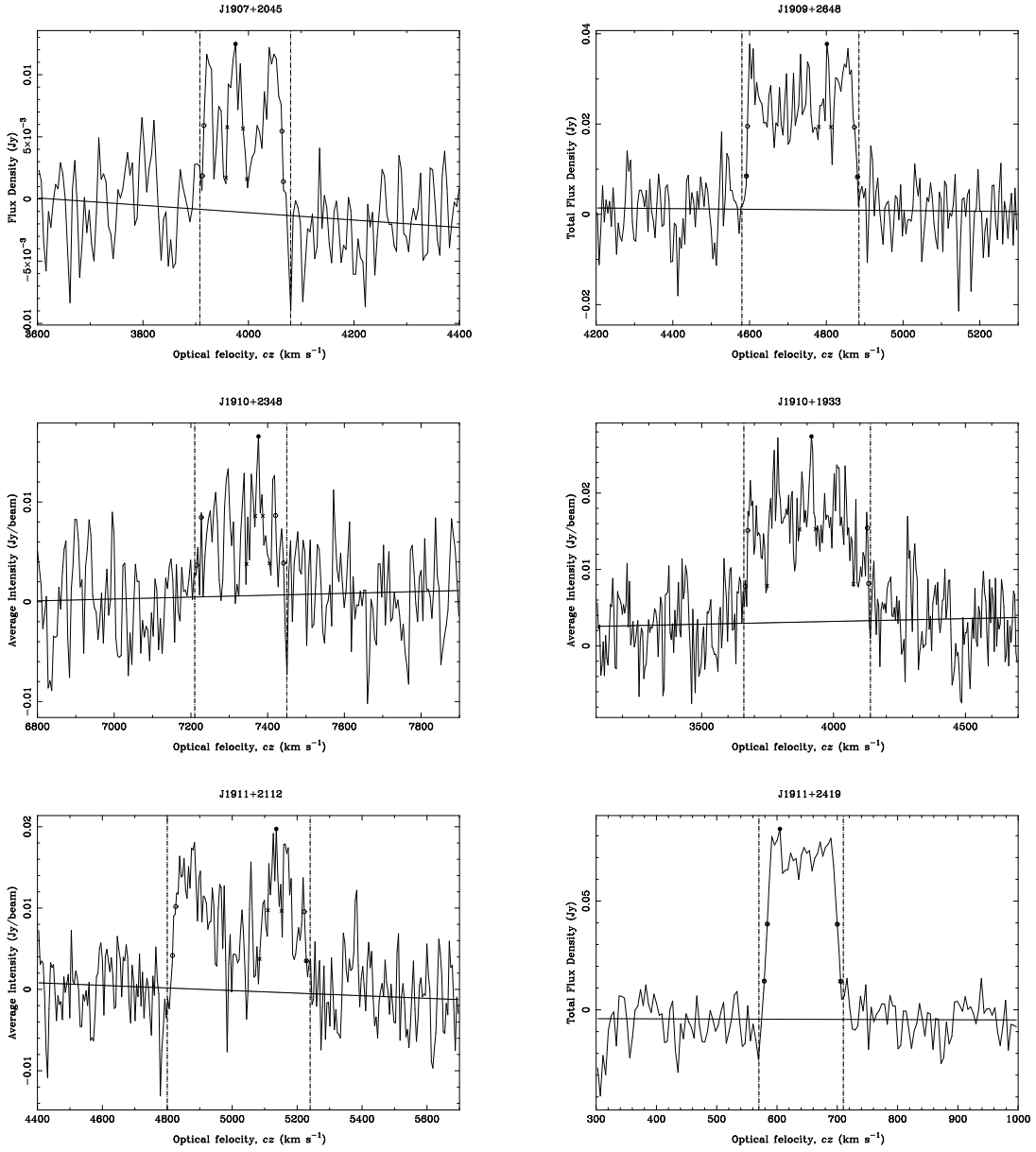

Figure B.1 (continued)

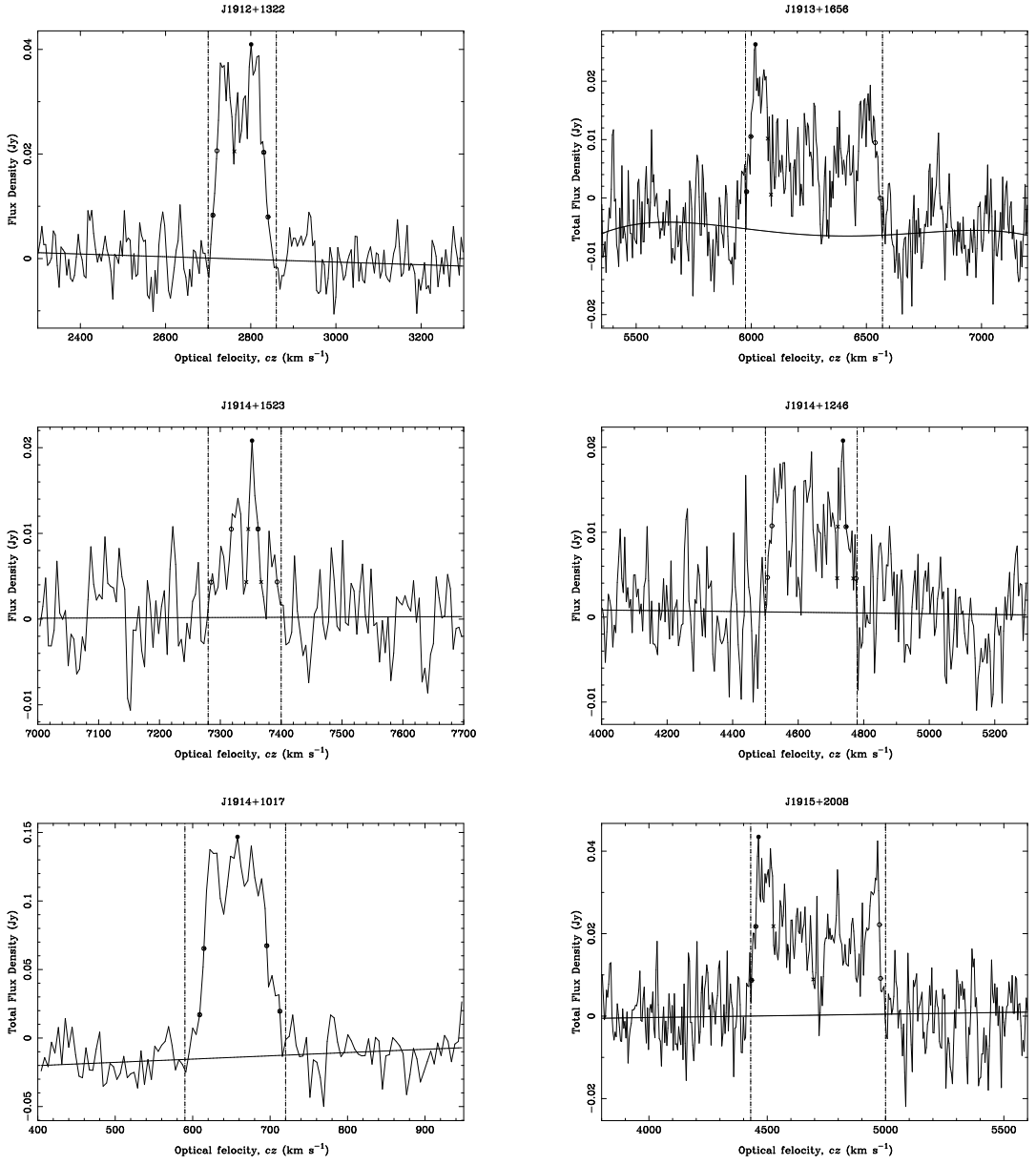

Figure B.1 (continued)

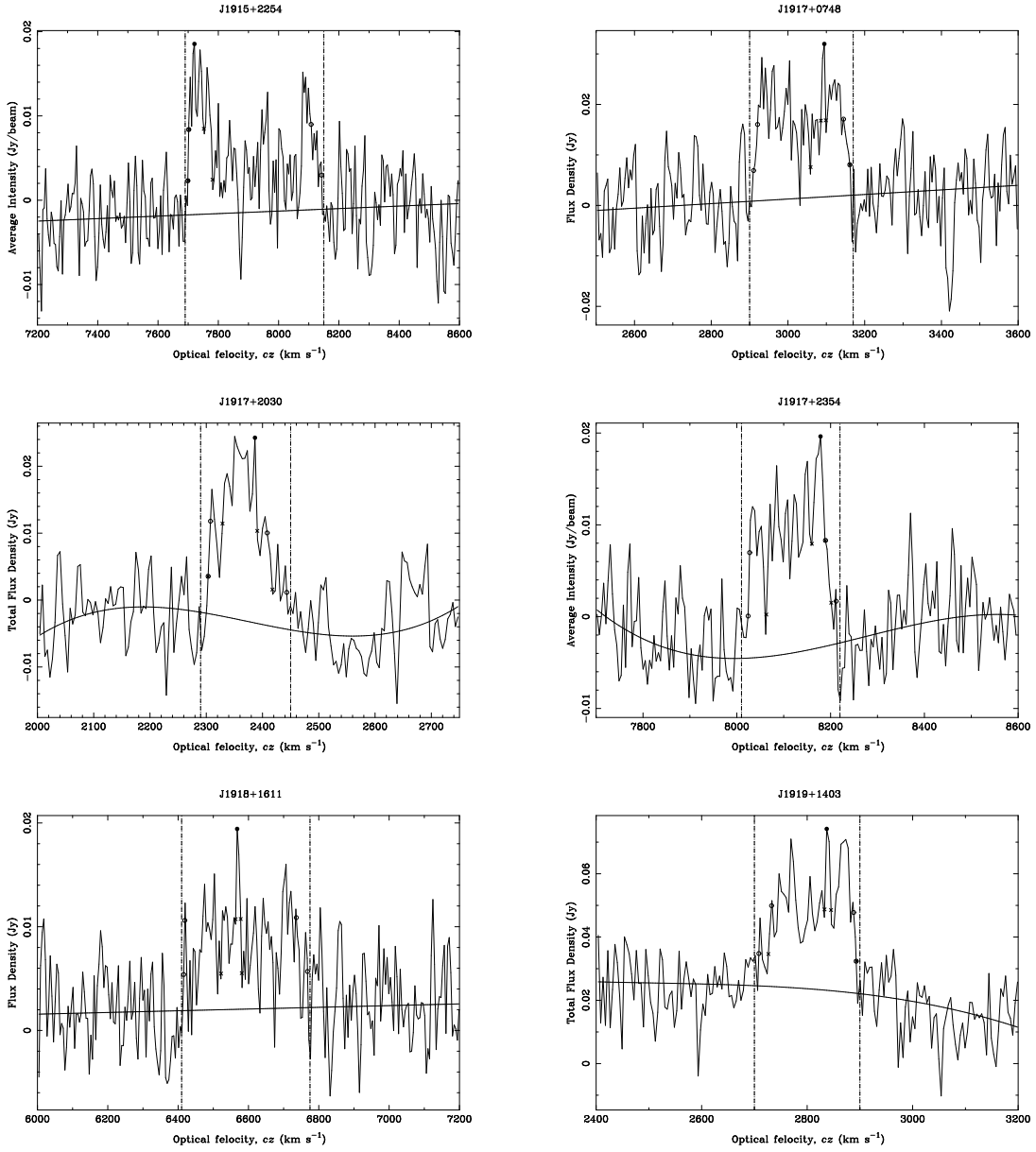

Figure B.1 (continued)

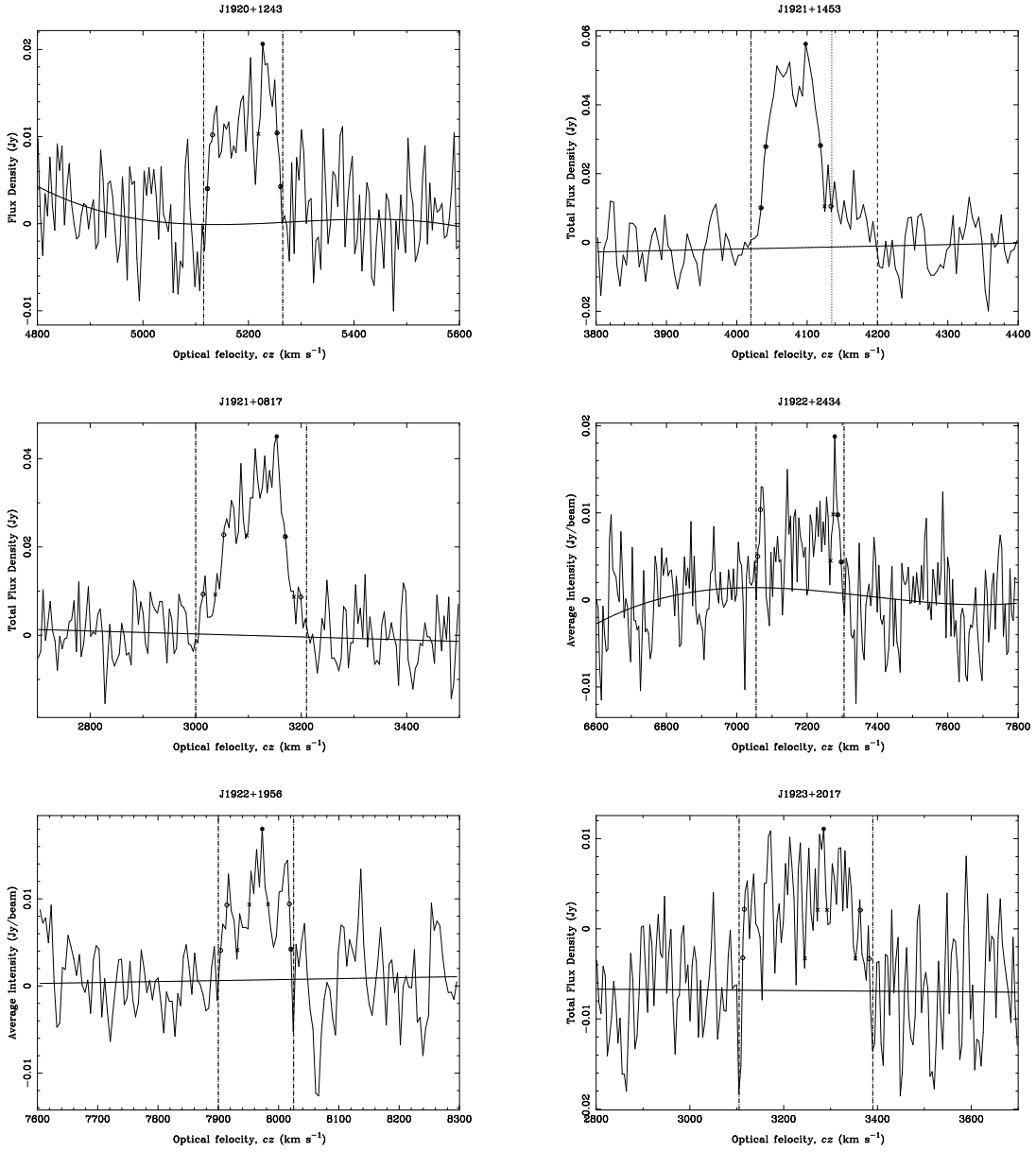

Figure B.1 (continued)

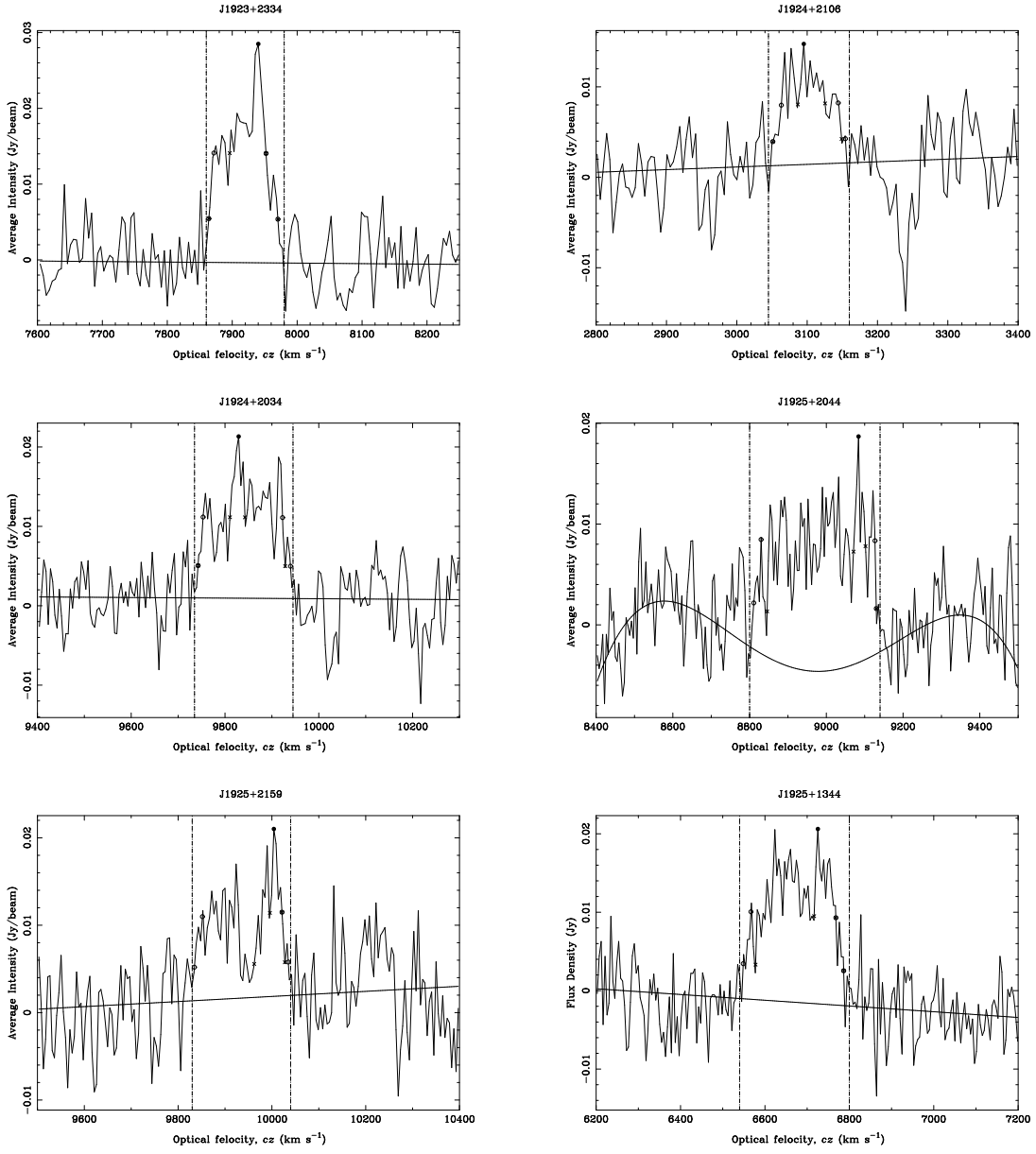

Figure B.1 (continued)

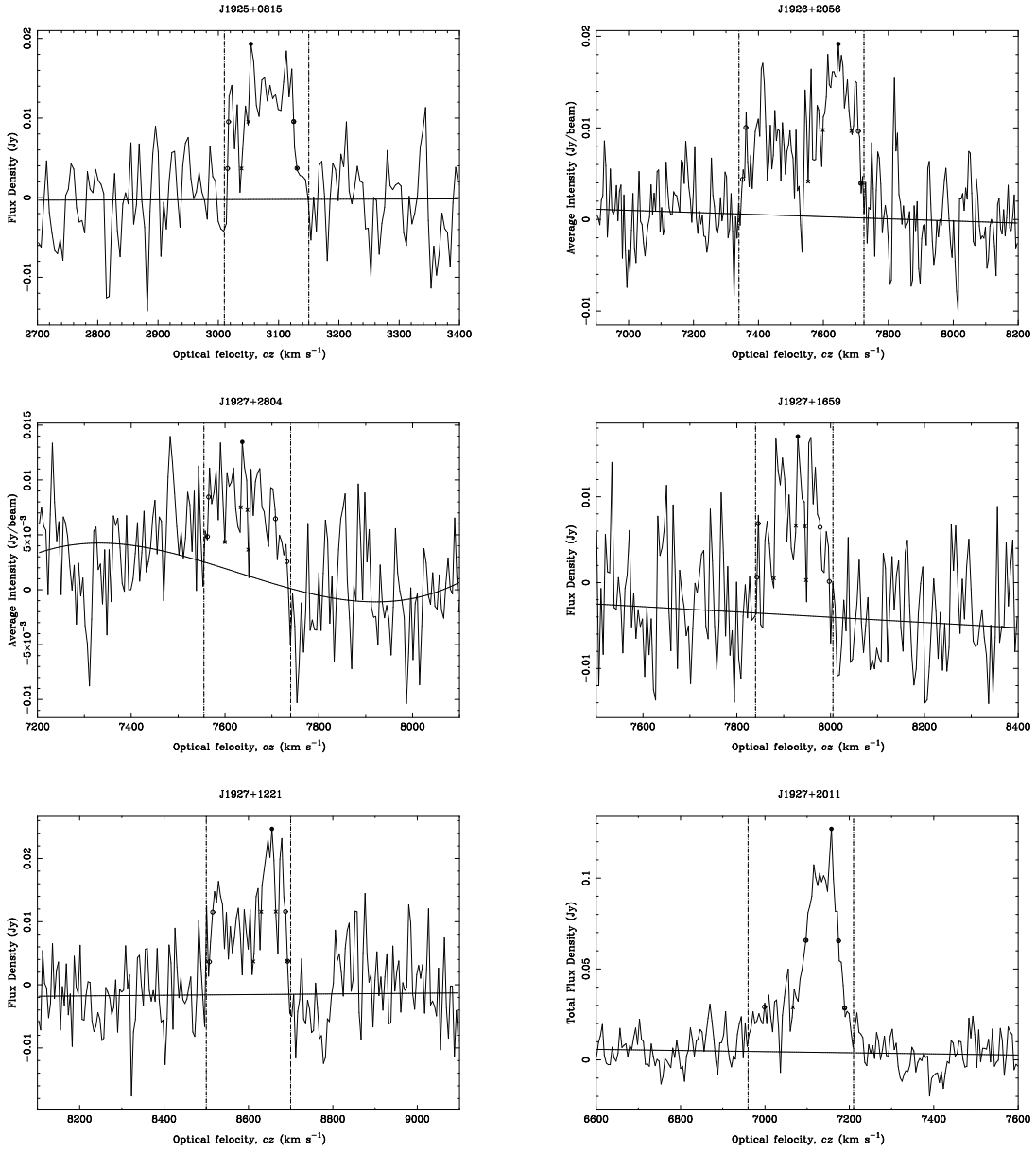

Figure B.1 (continued)

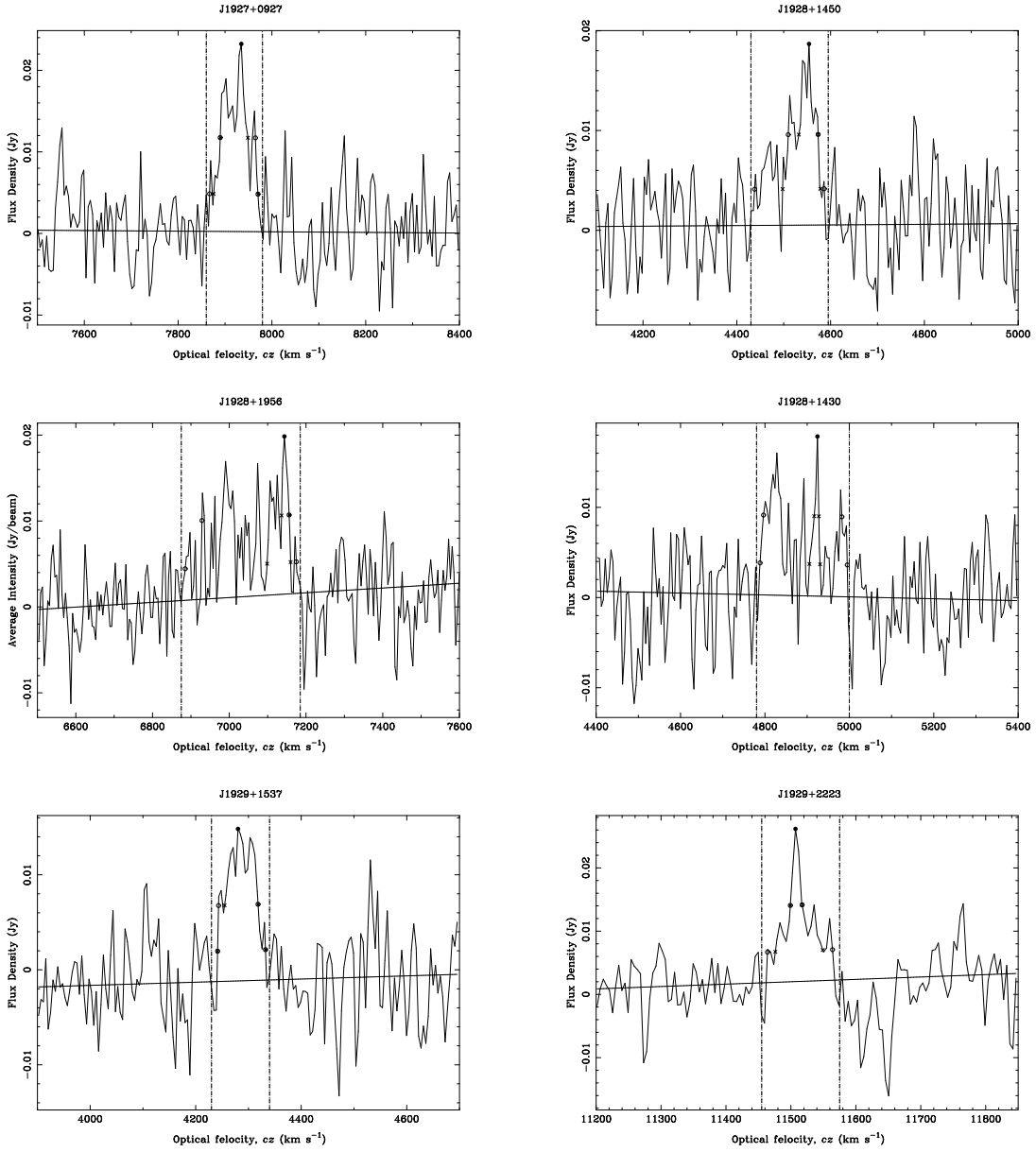

Figure B.1 (continued)

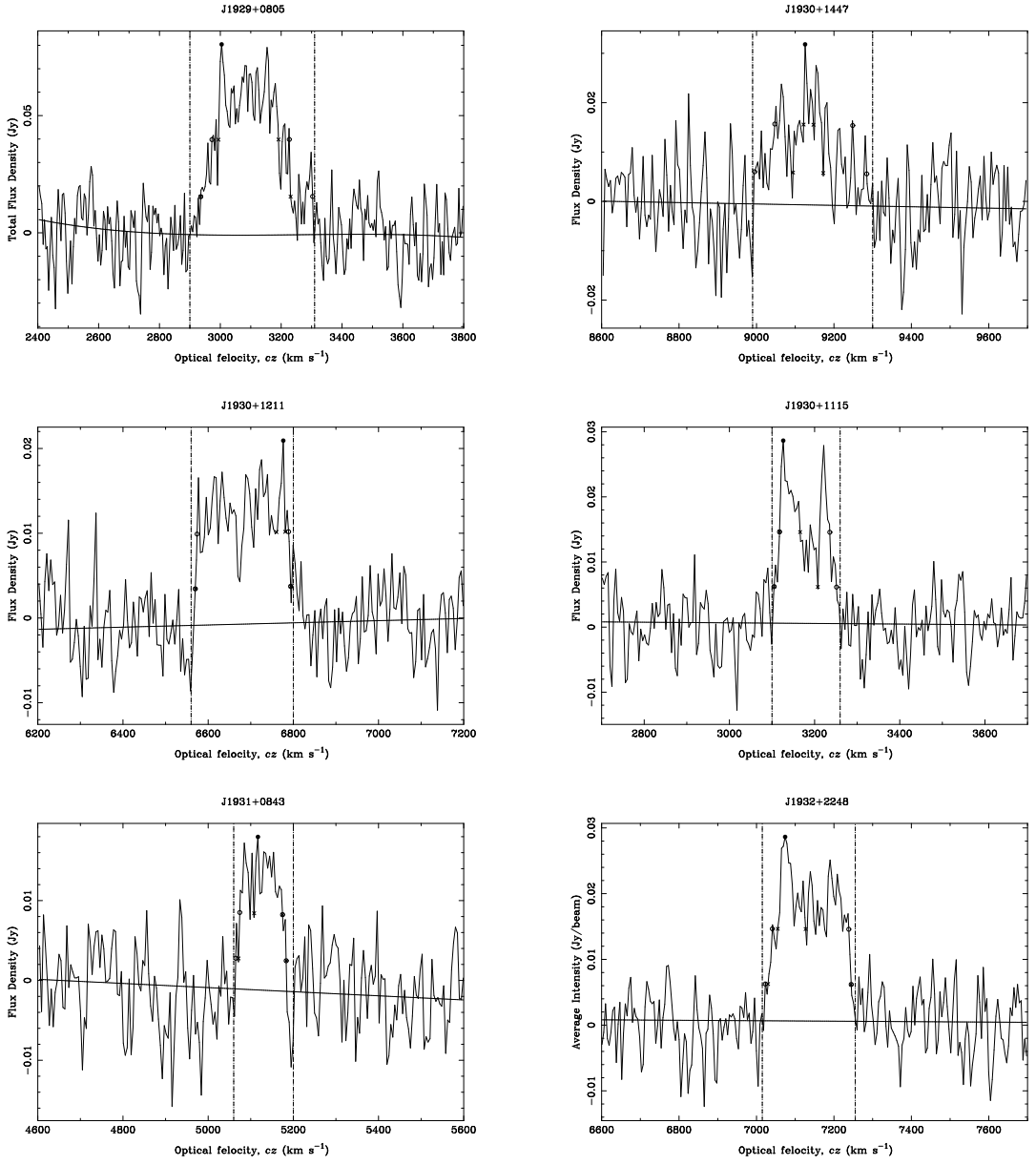

Figure B.1 (continued)

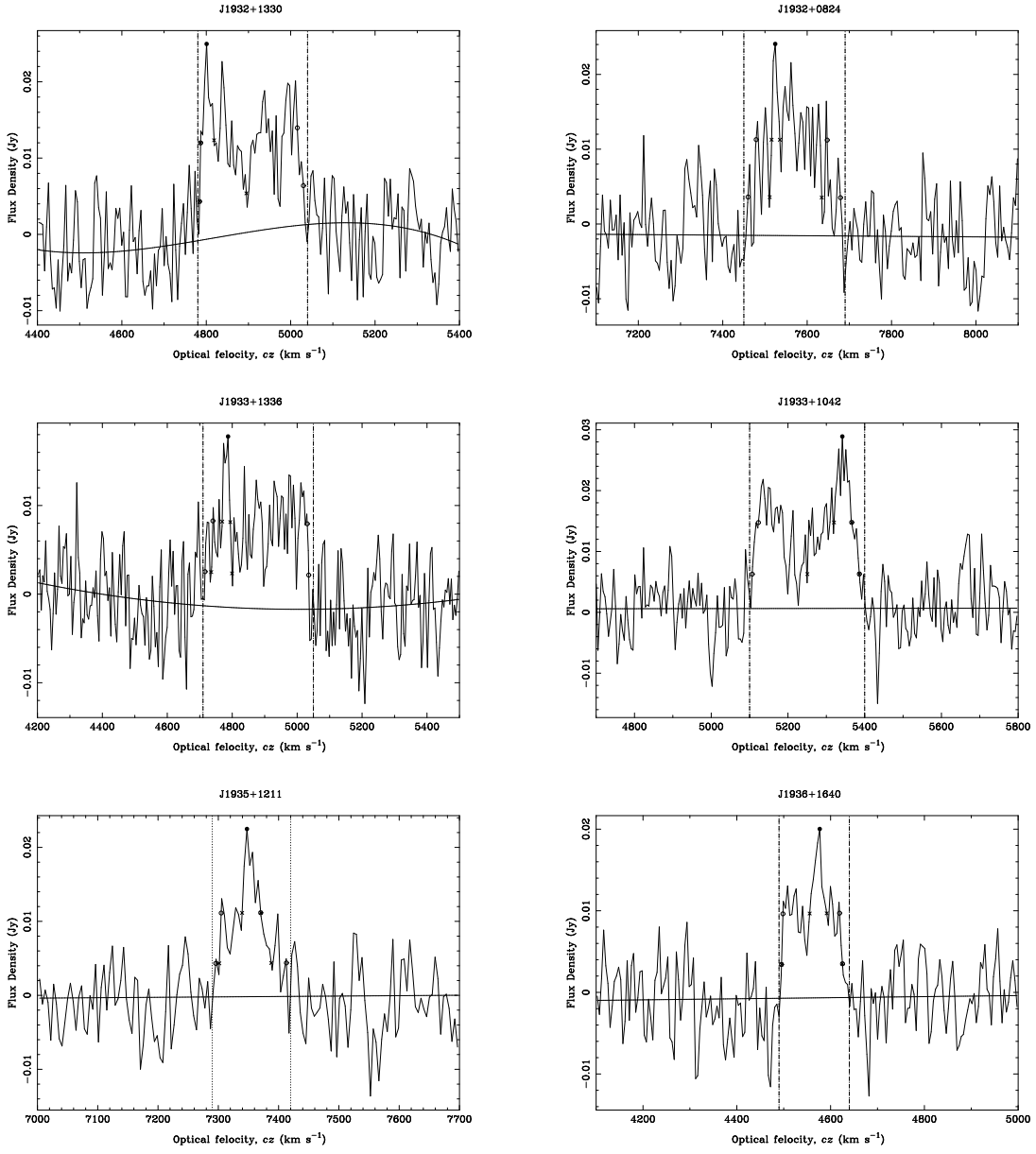

Figure B.1 (continued)

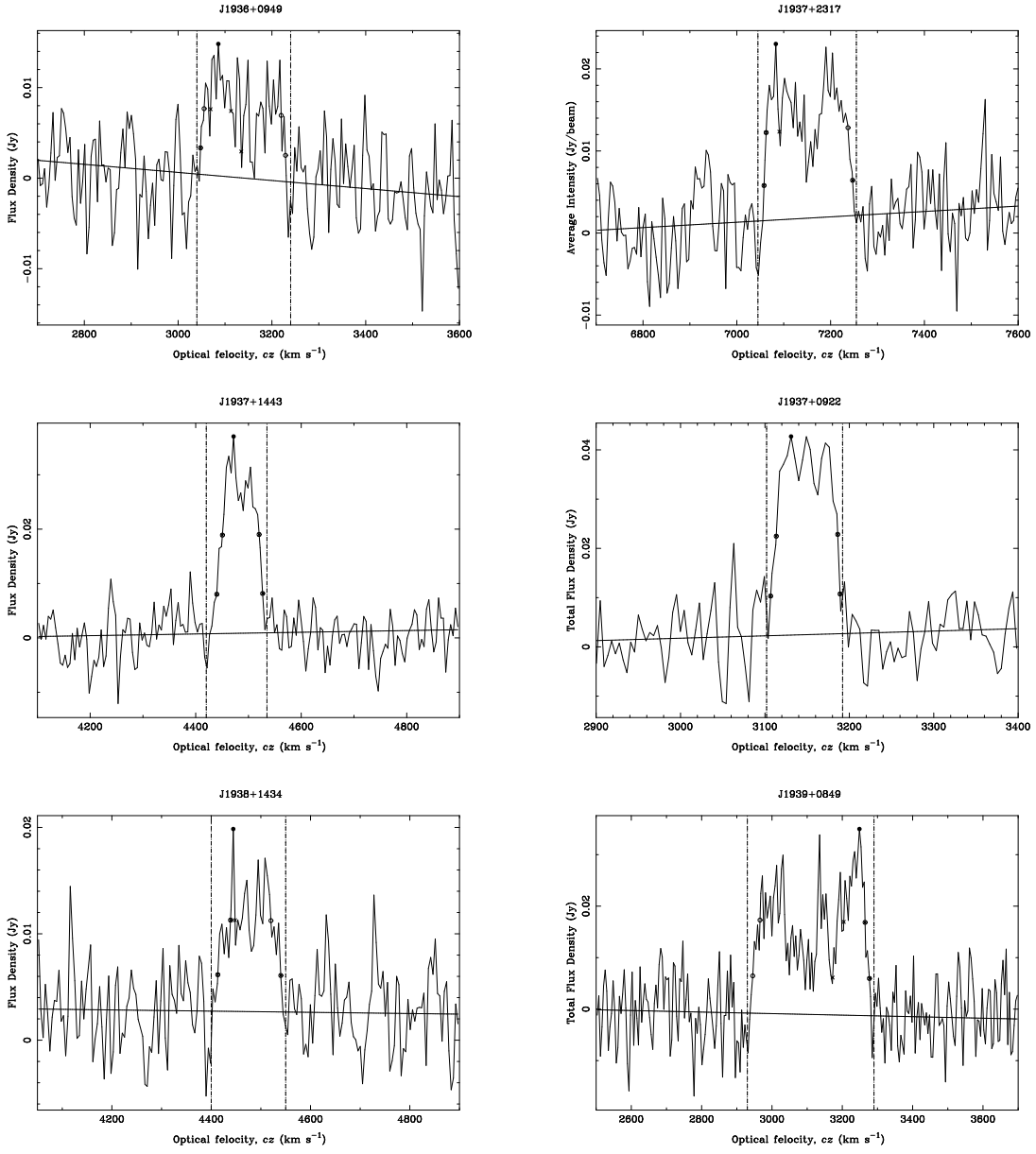

Figure B.1 (continued)

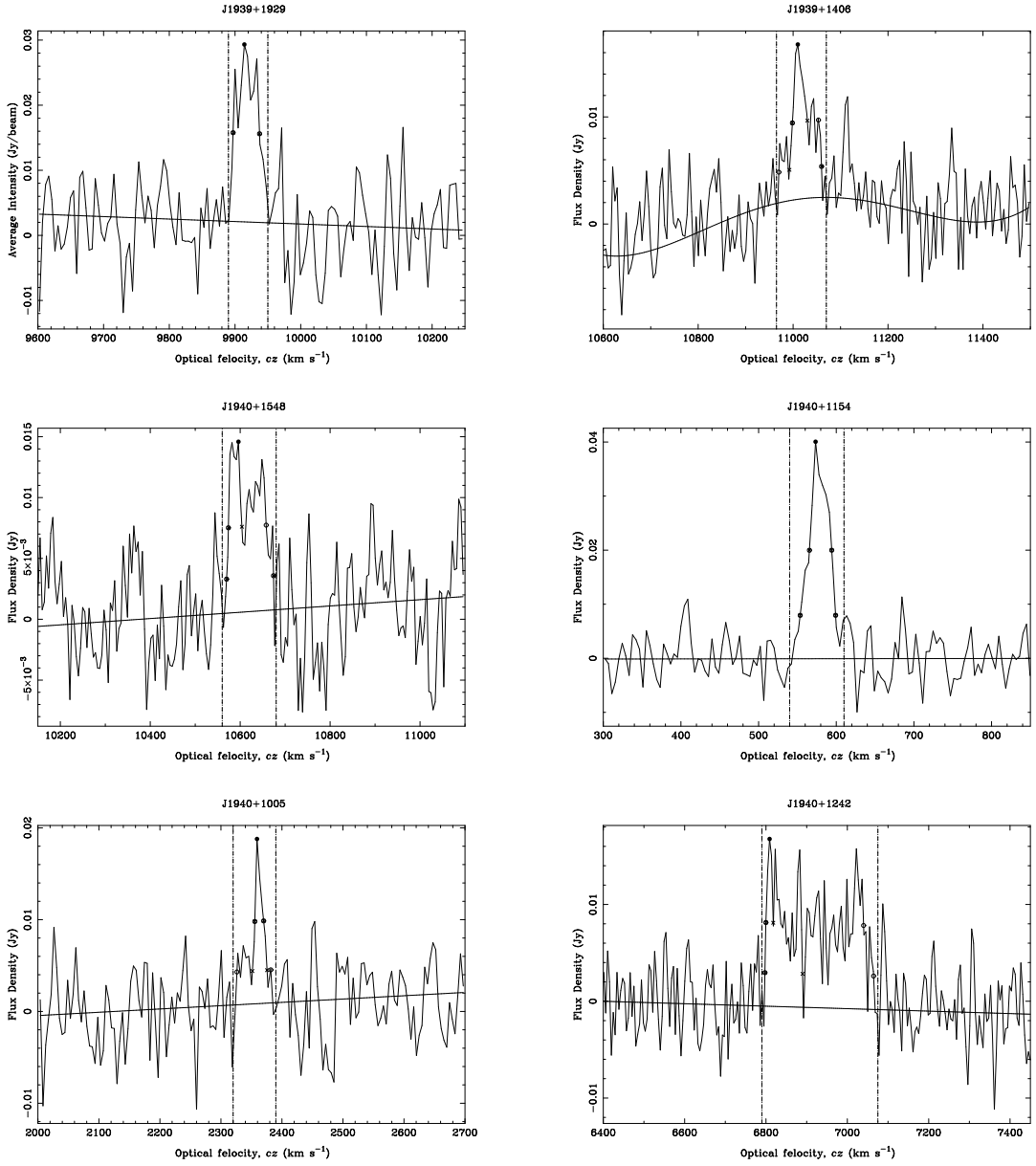

Figure B.1 (continued)

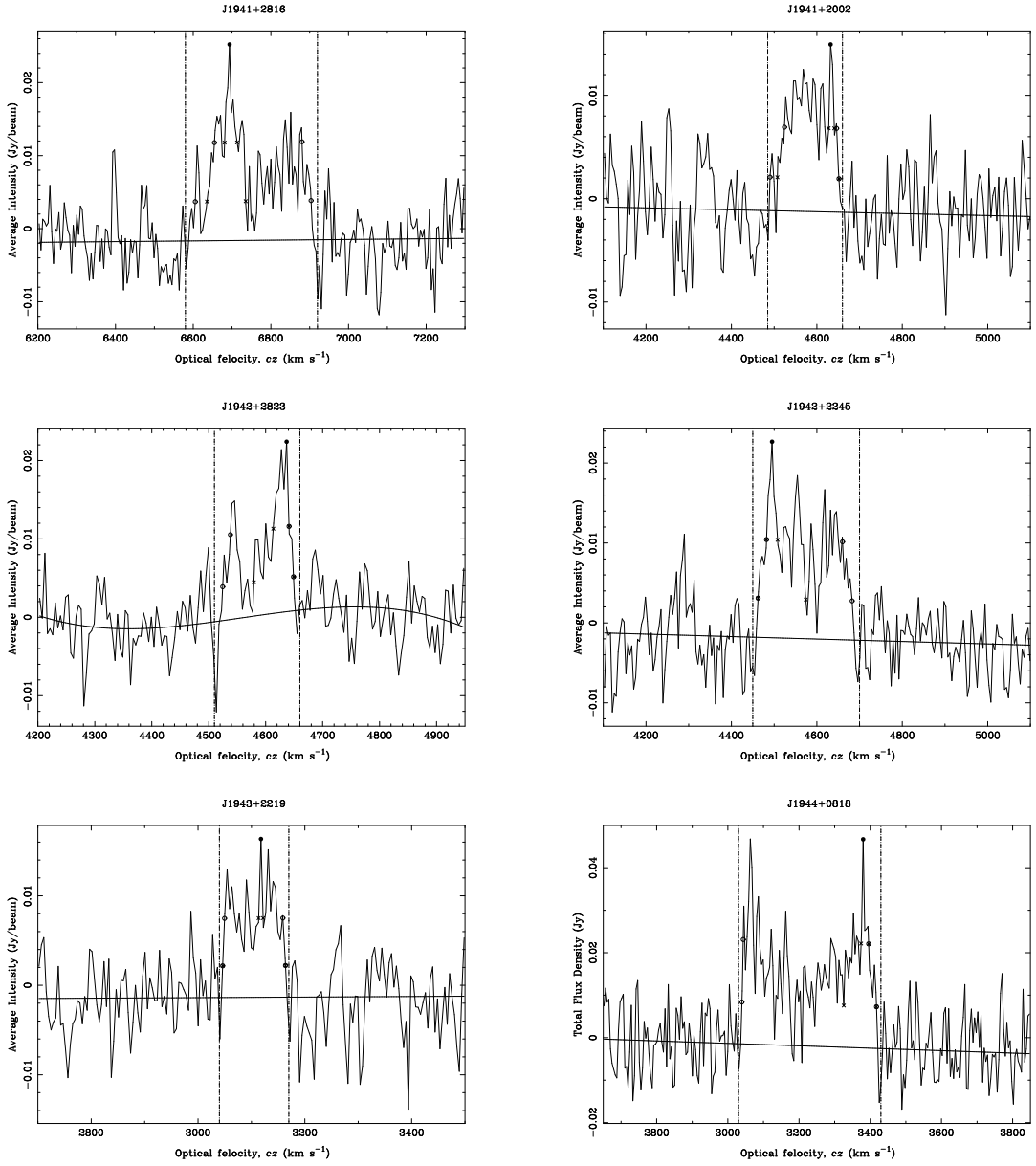

Figure B.1 (continued)

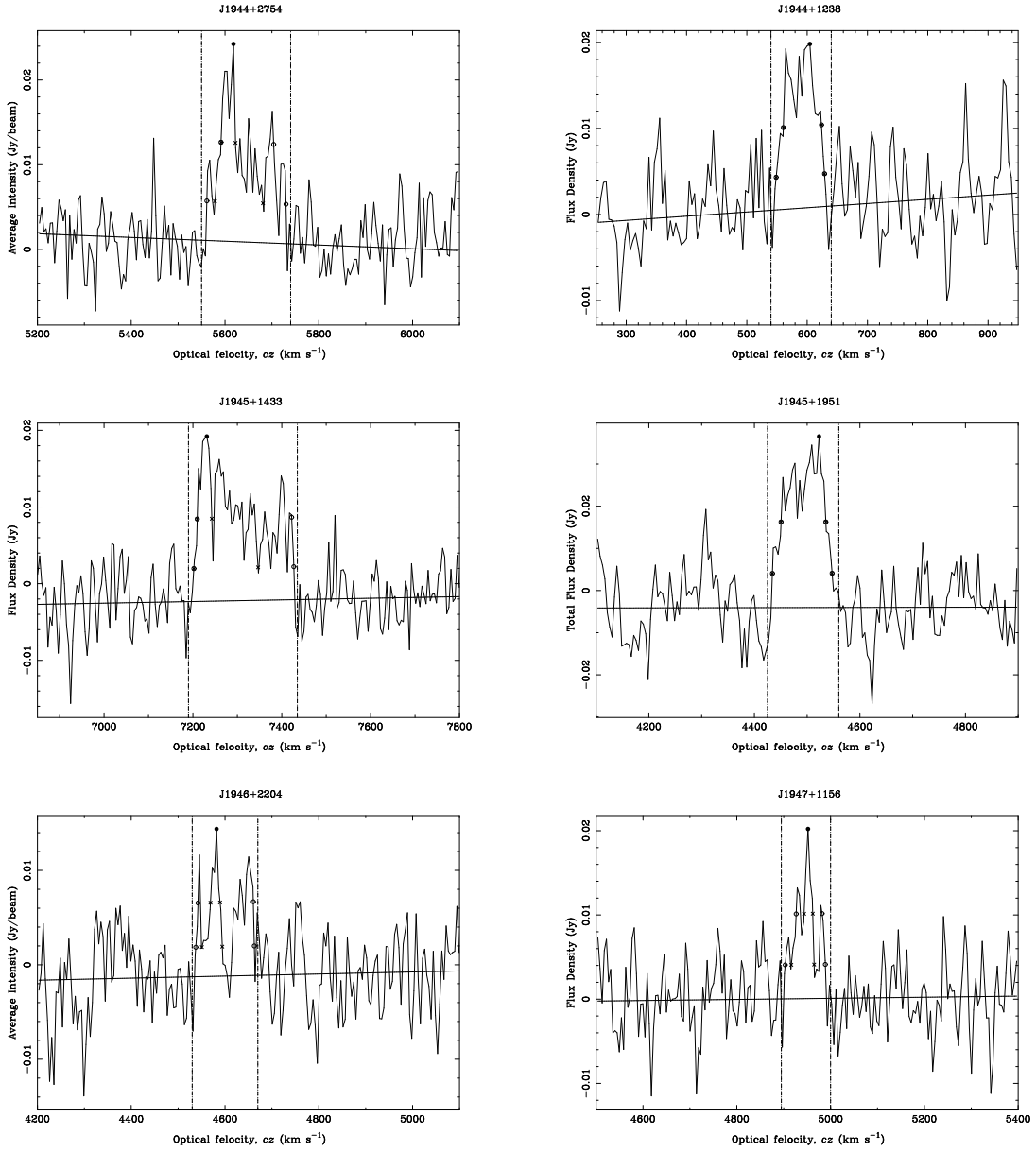

Figure B.1 (continued)

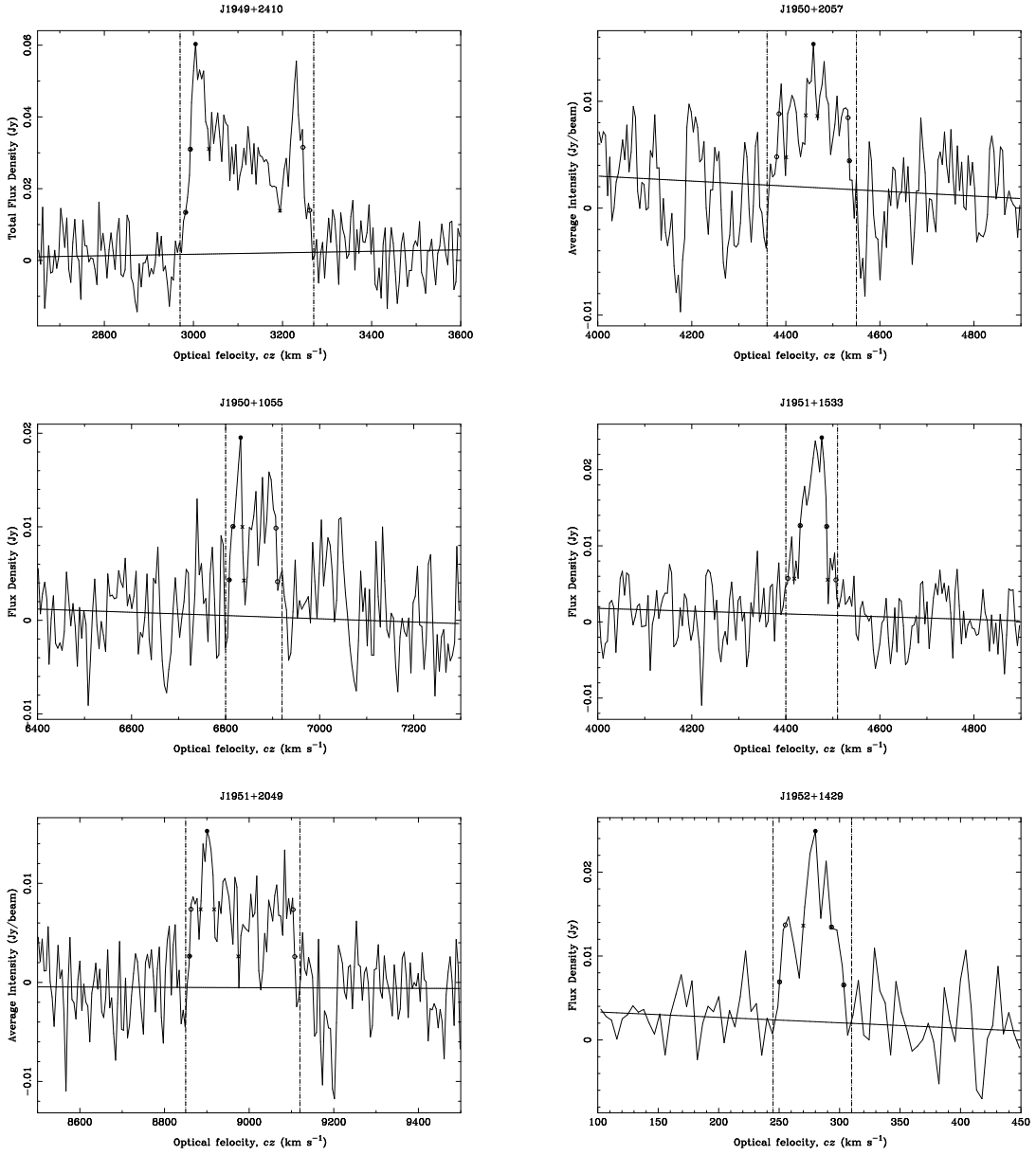

Figure B.1 (continued)

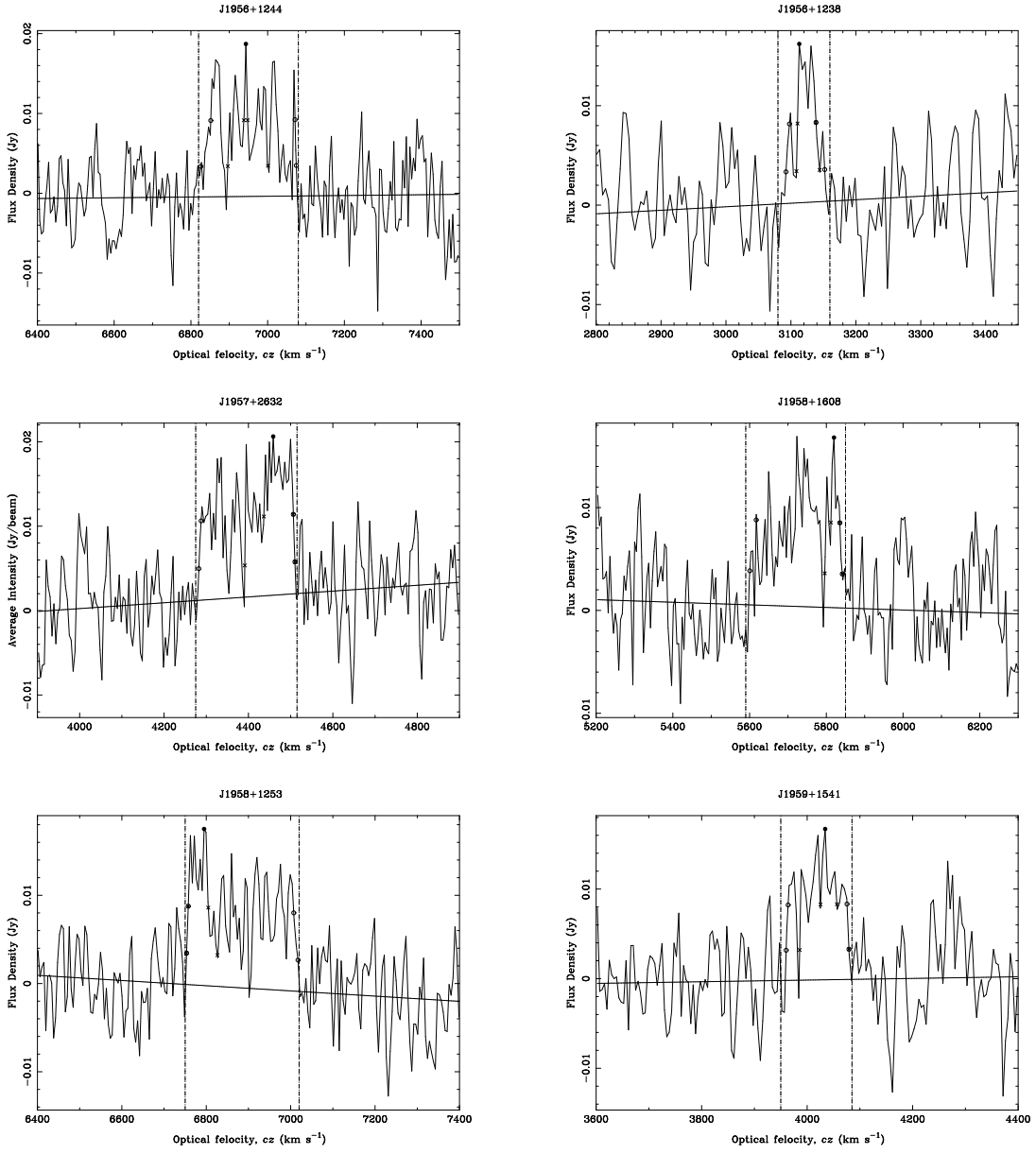

Figure B.1 (continued)

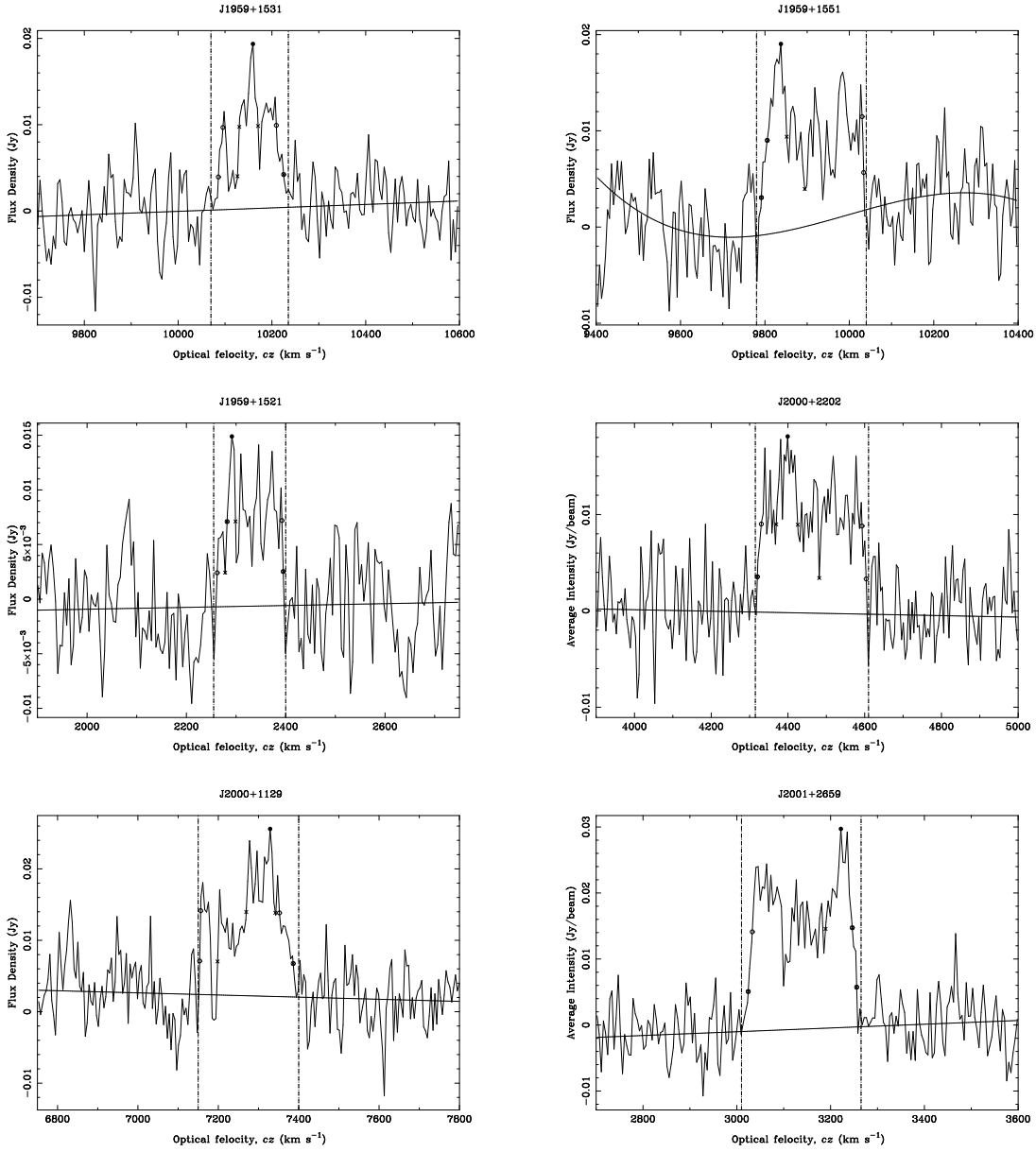

Figure B.1 (continued)

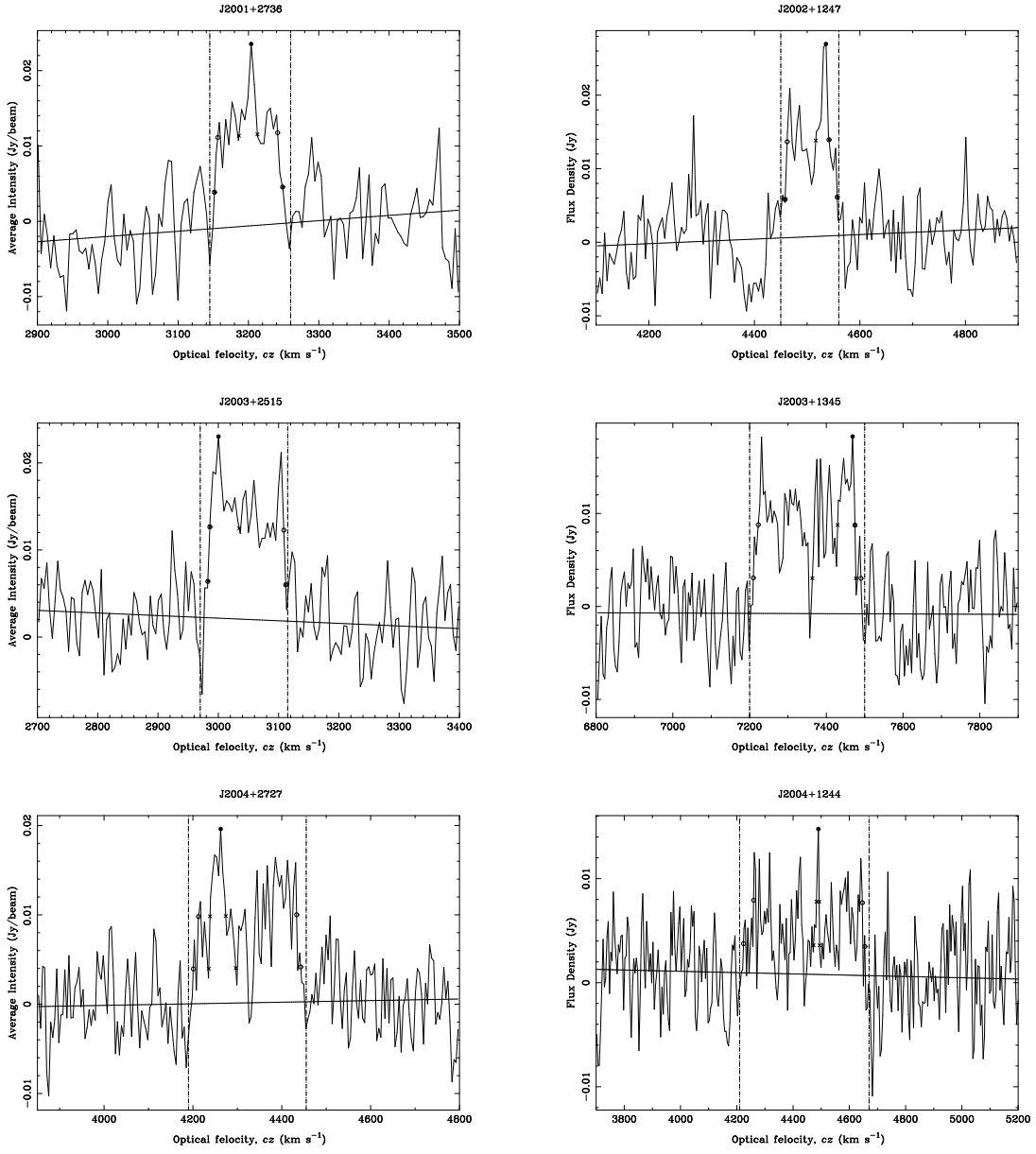

Figure B.1 (continued)

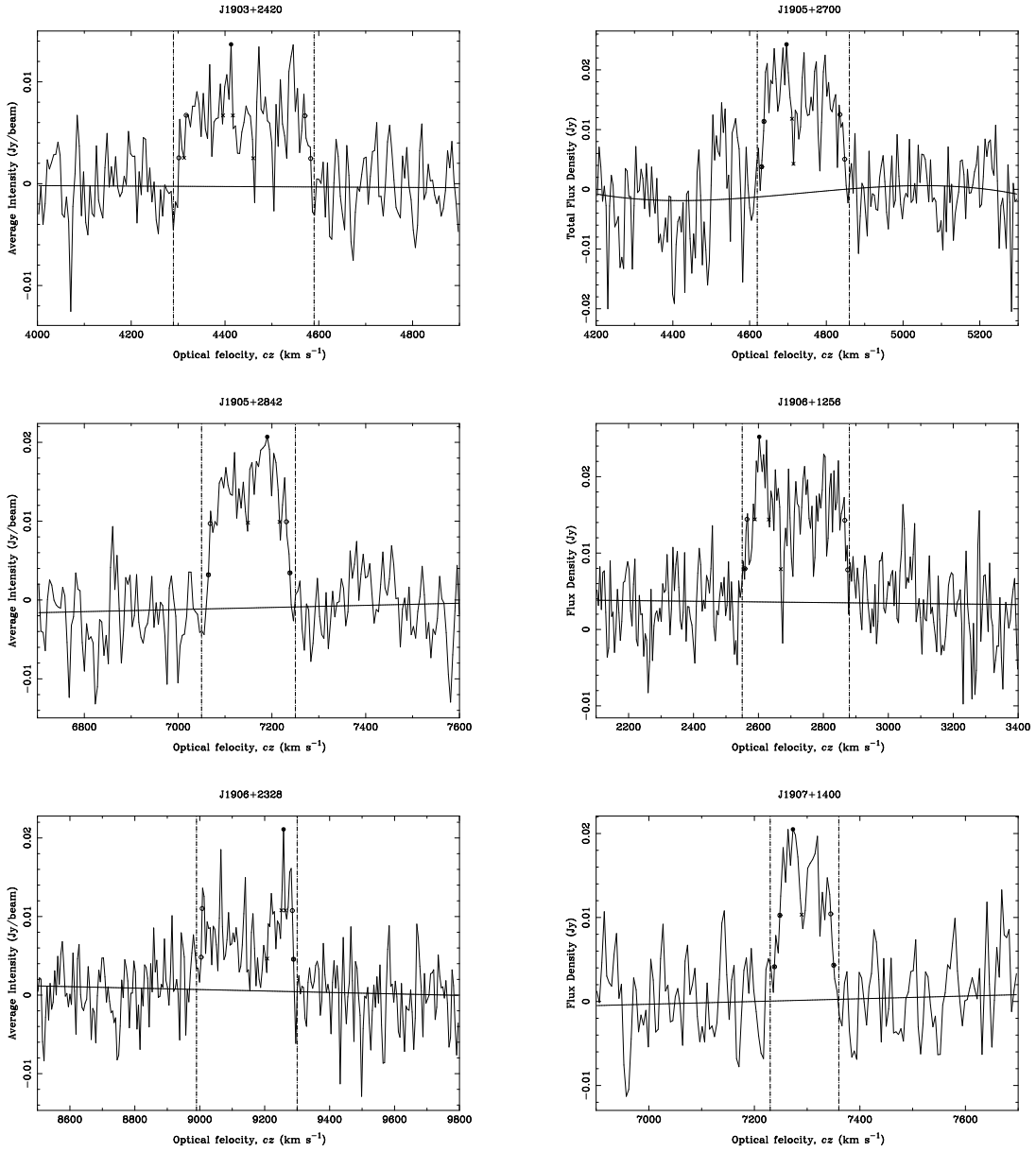

Figure B.2 (Figure B.1 continued)

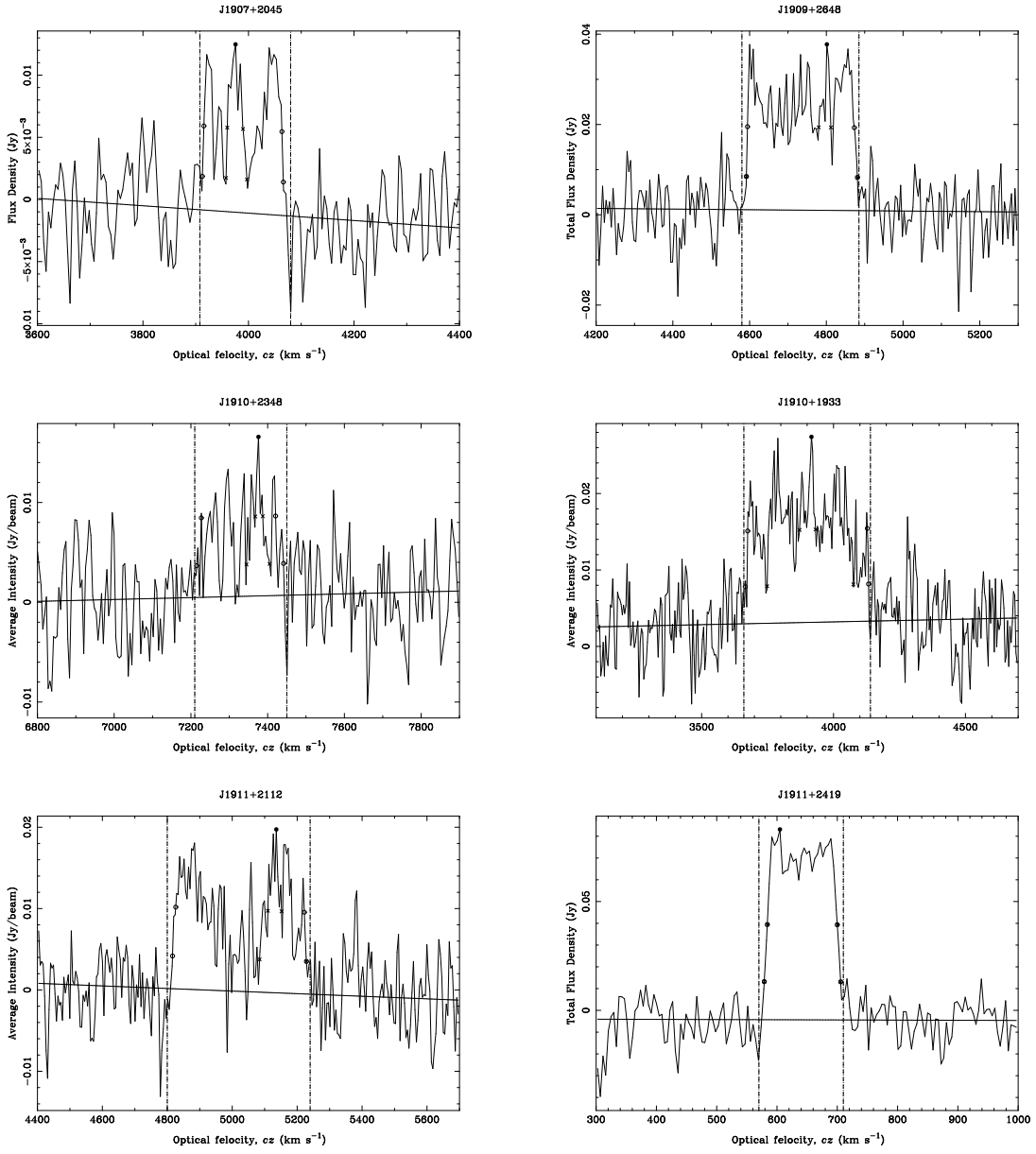

Figure B.2 (continued)

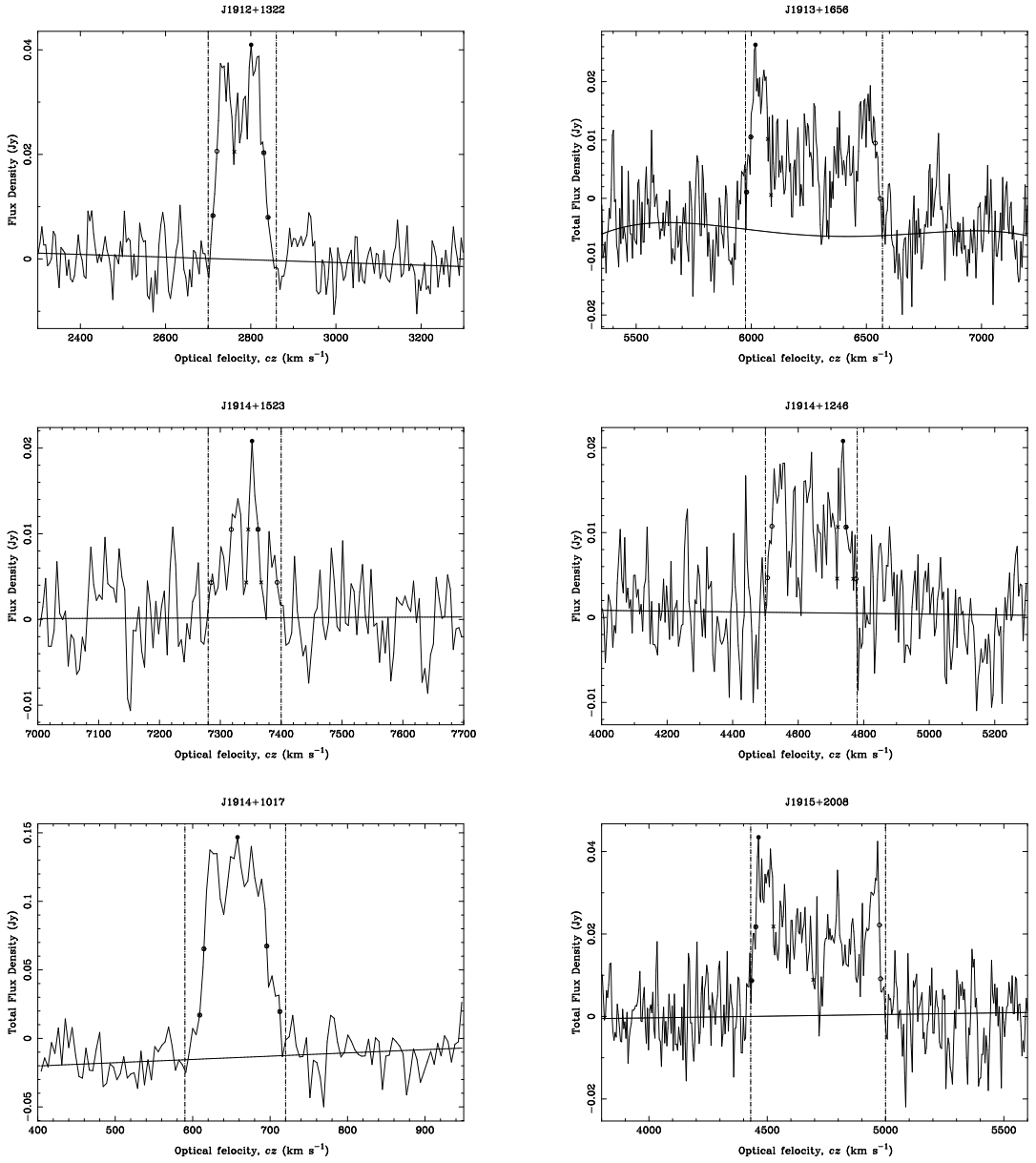

Figure B.2 (continued)

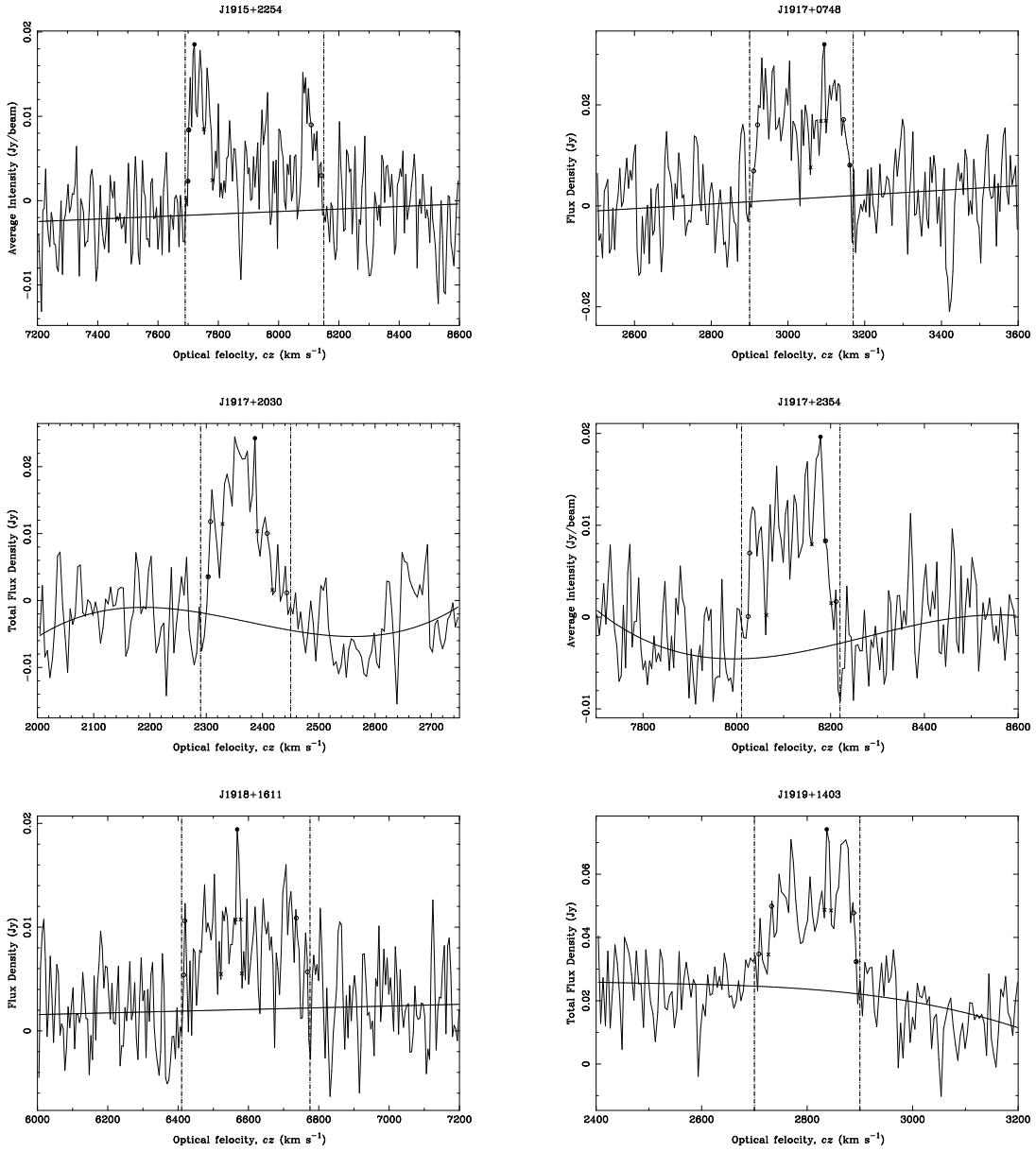

Figure B.2 (continued)

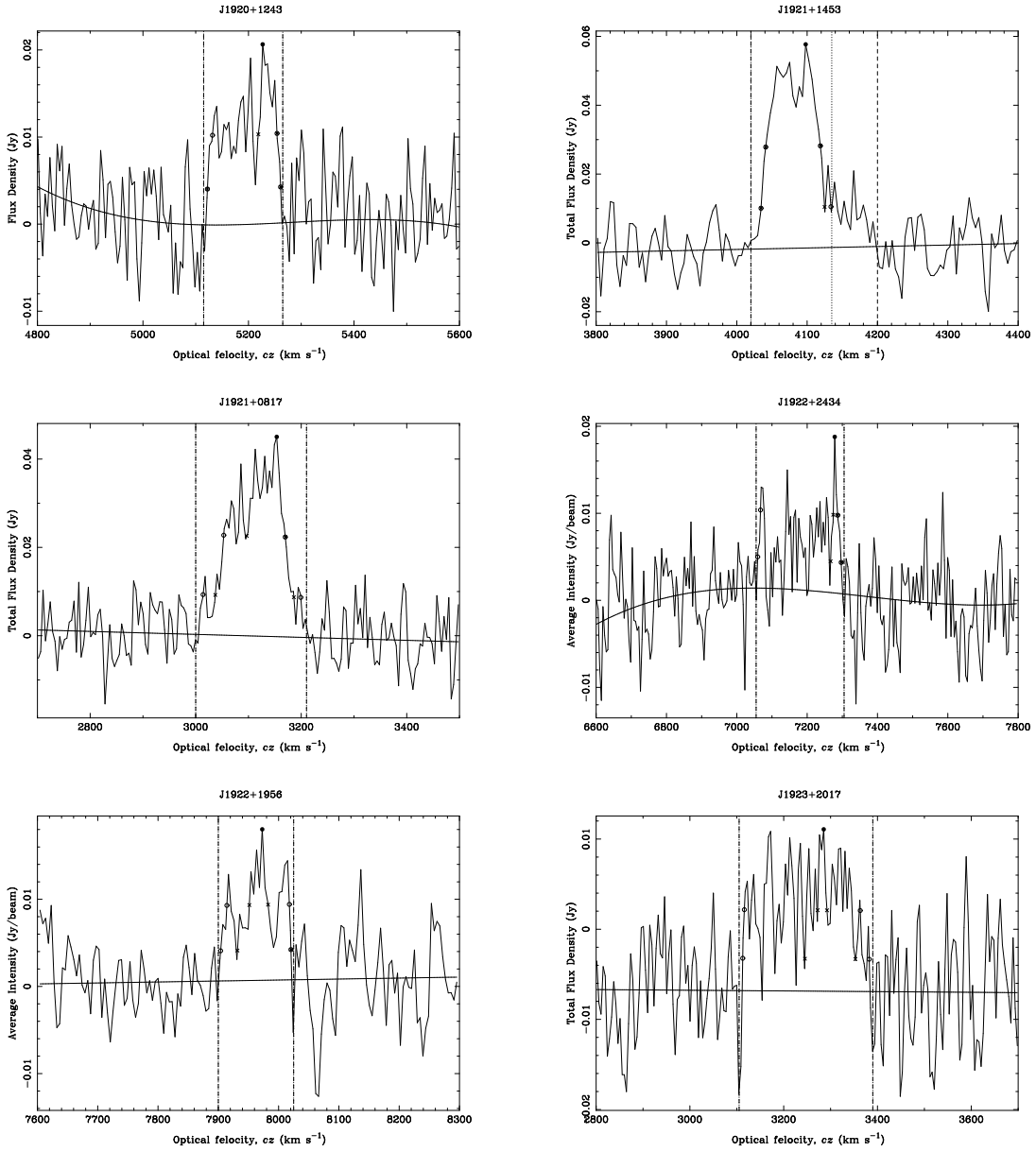

Figure B.2 (continued)

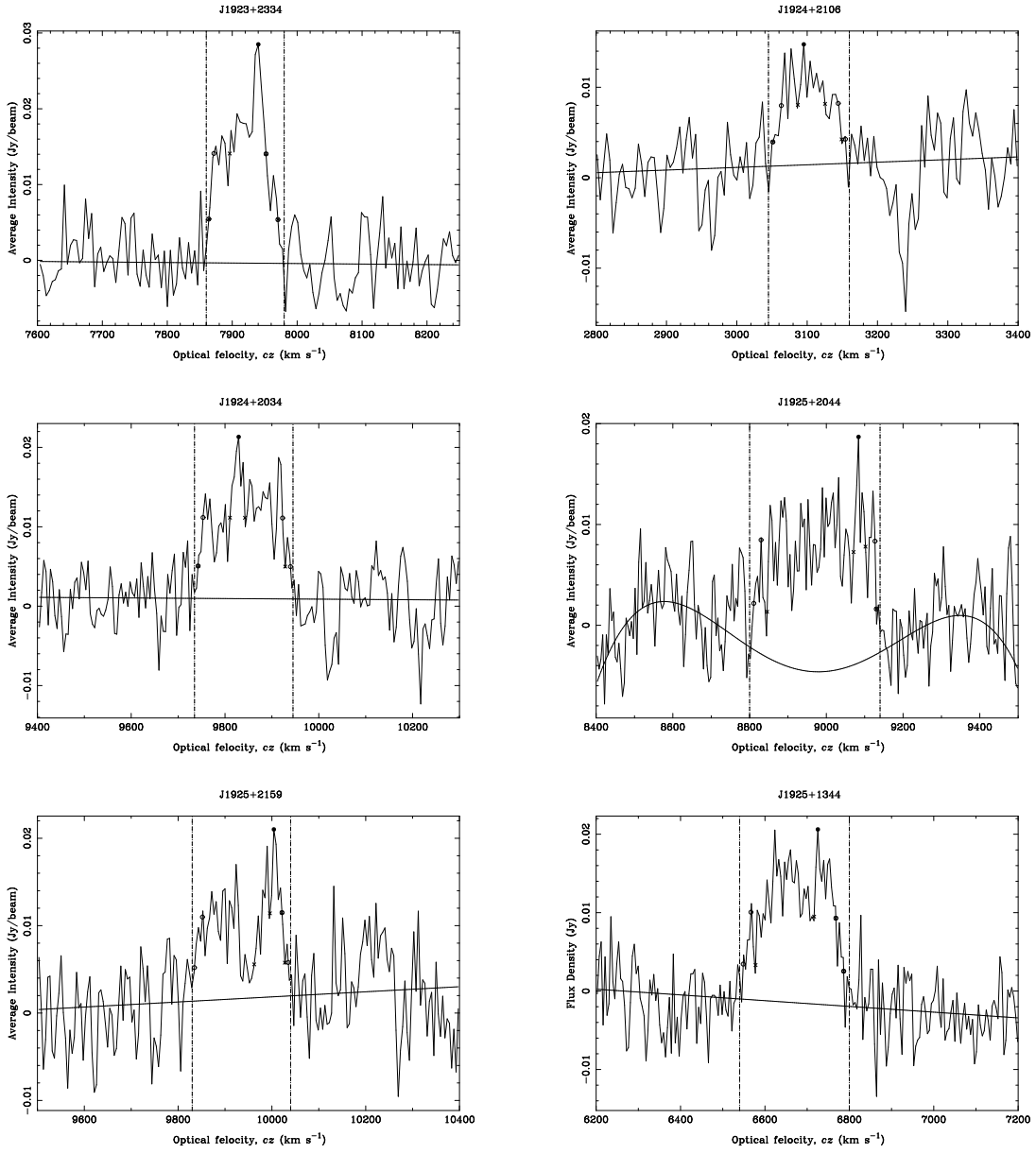

Figure B.2 (continued)

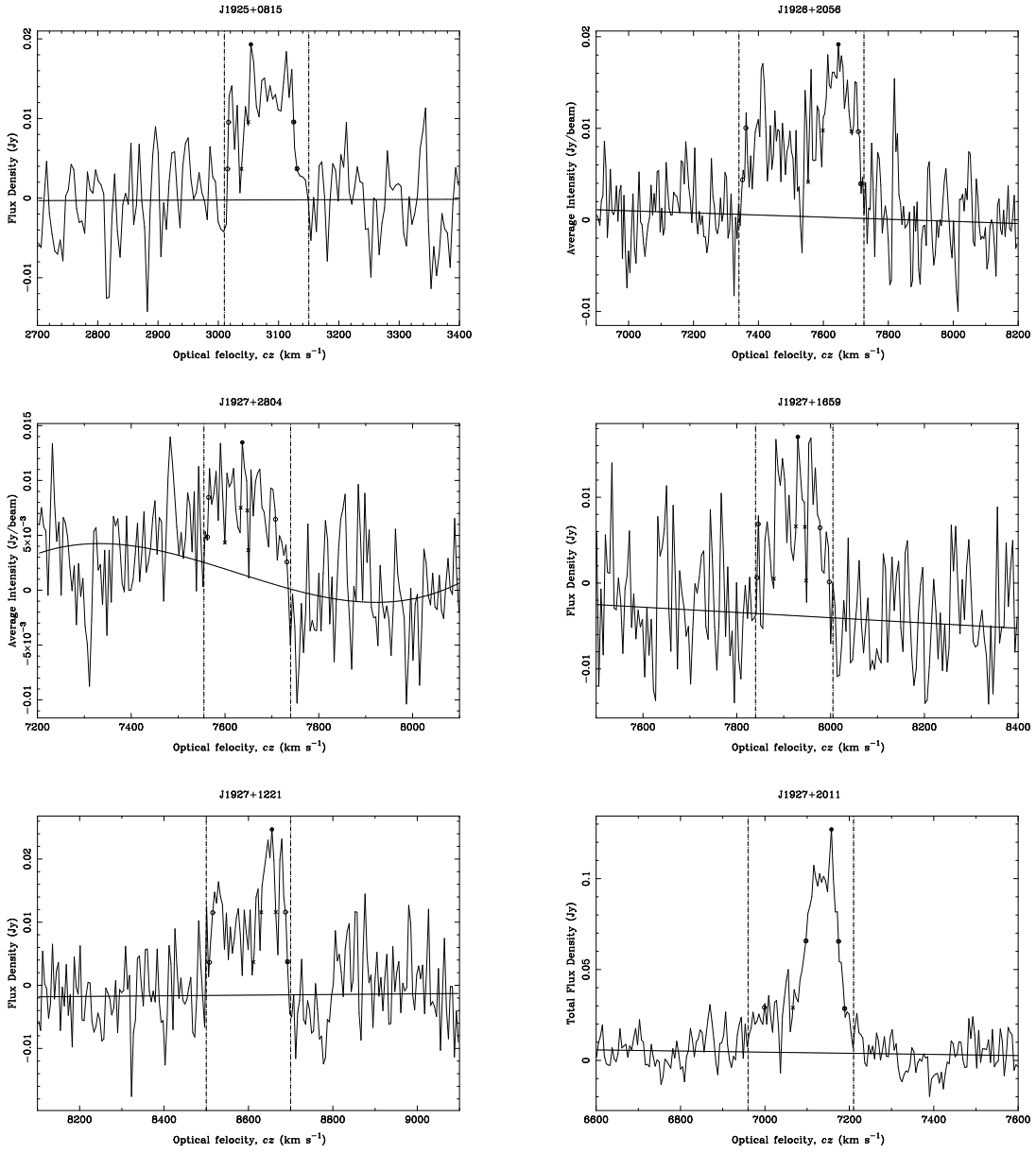

Figure B.2 (continued)

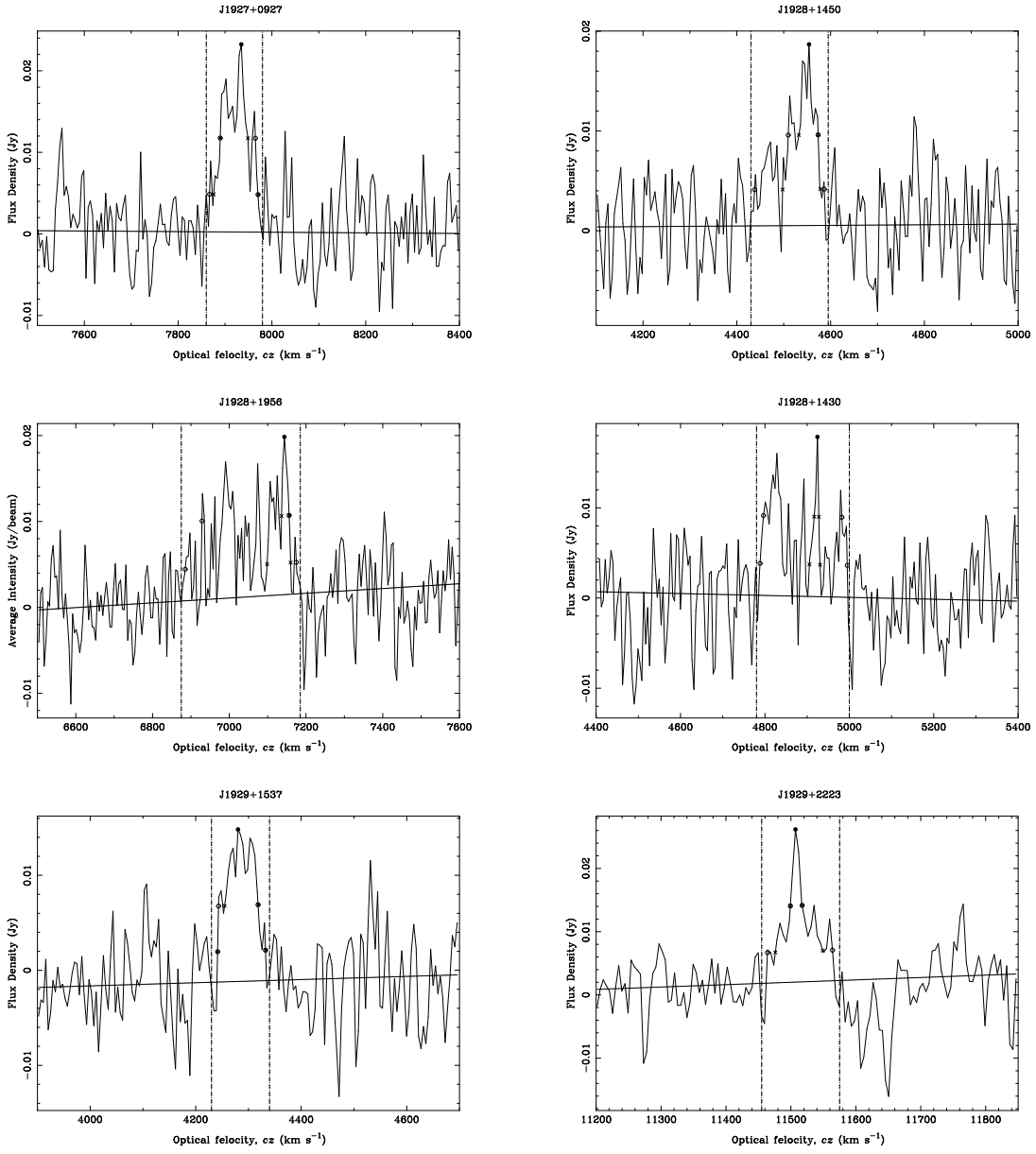

Figure B.2 (continued)

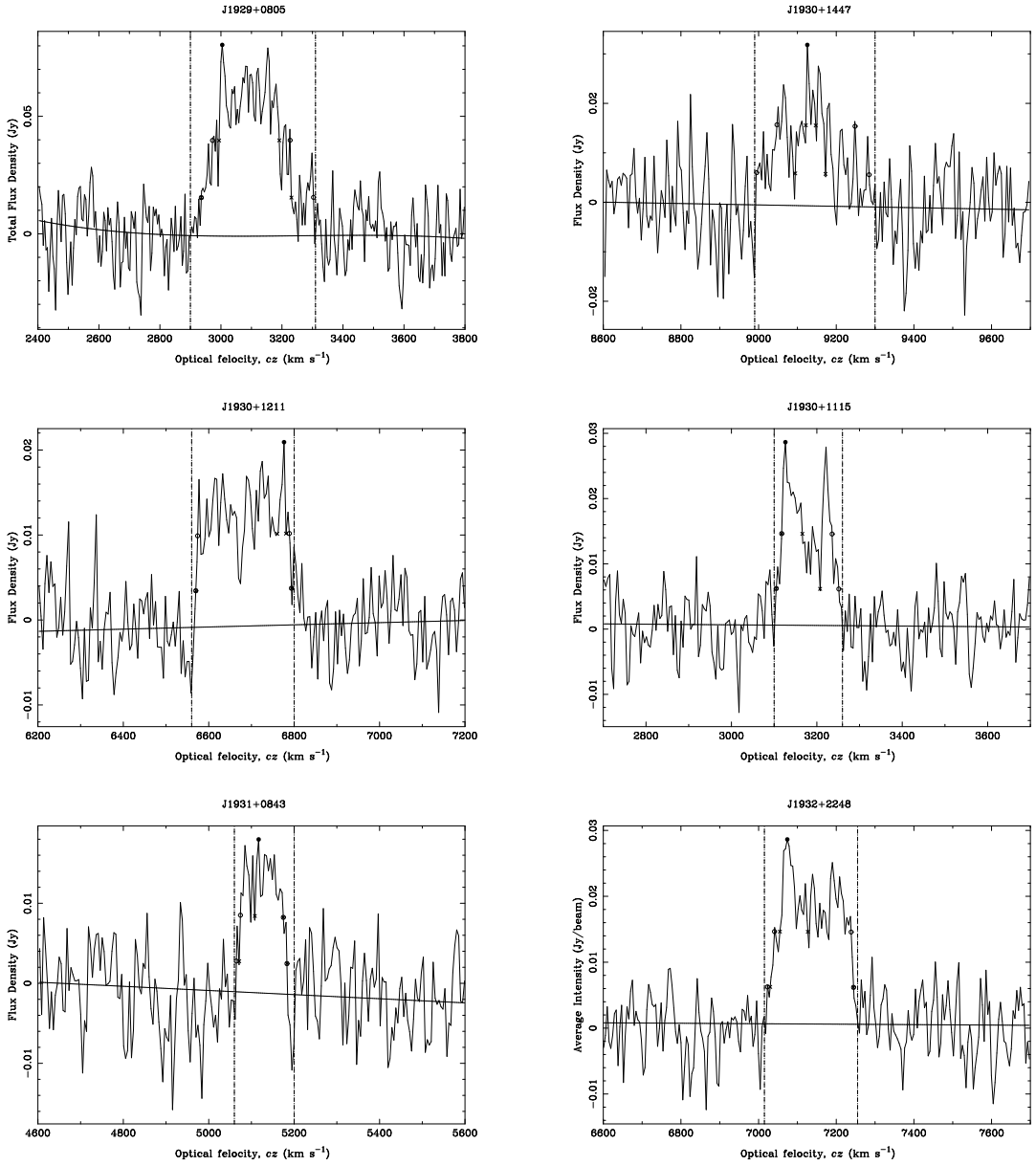

Figure B.2 (continued)

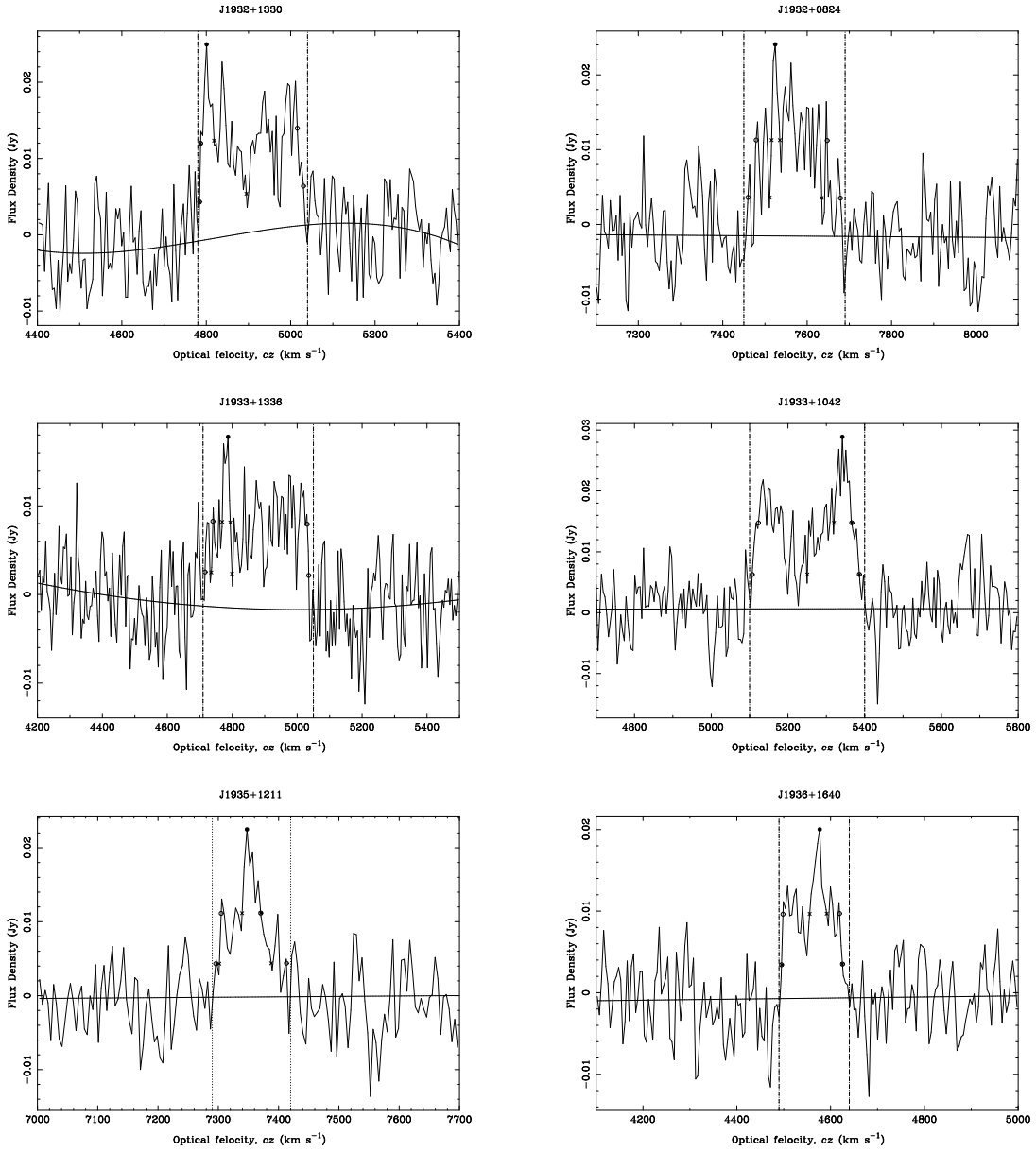

Figure B.2 (continued)

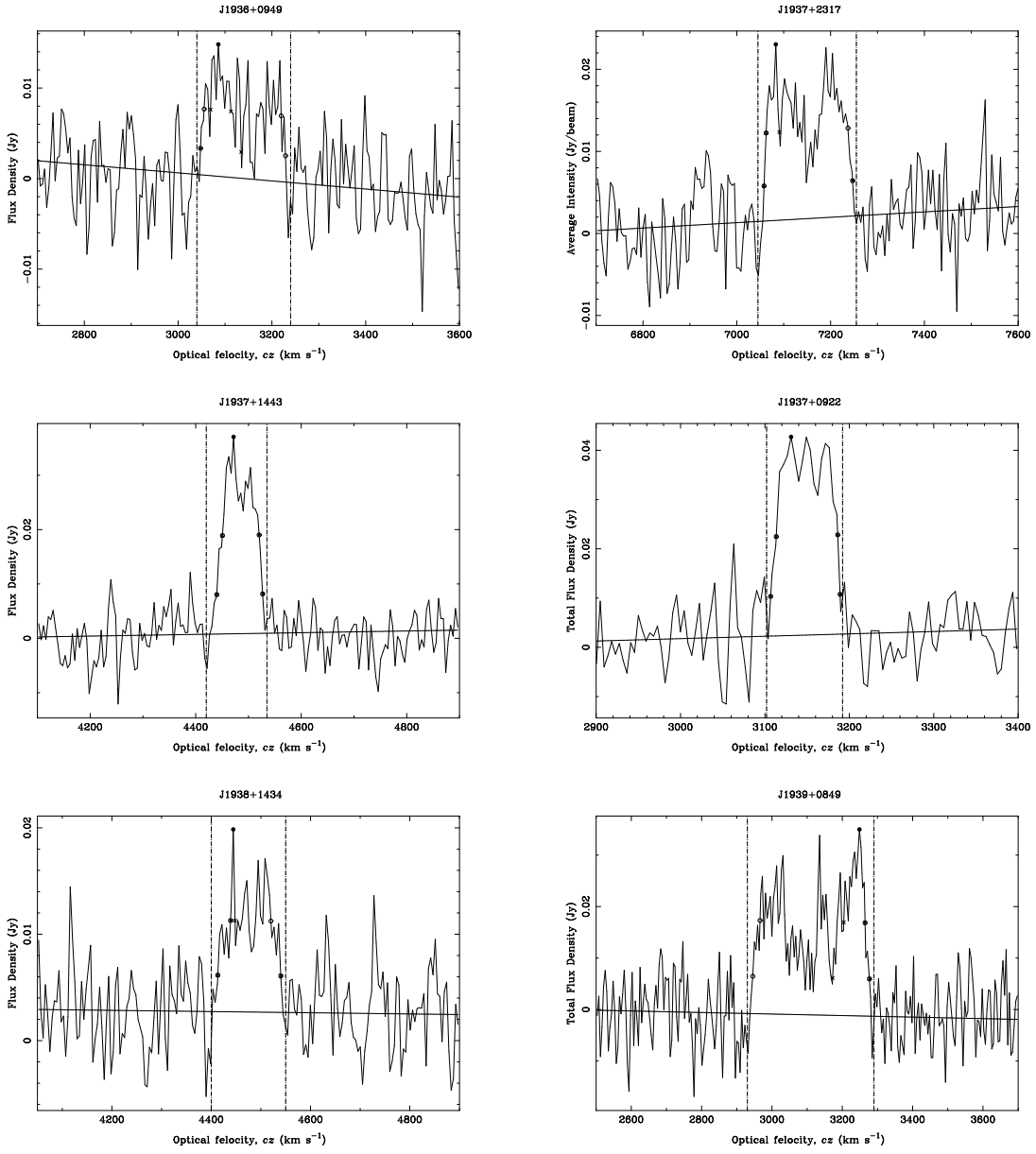

Figure B.2 (continued)

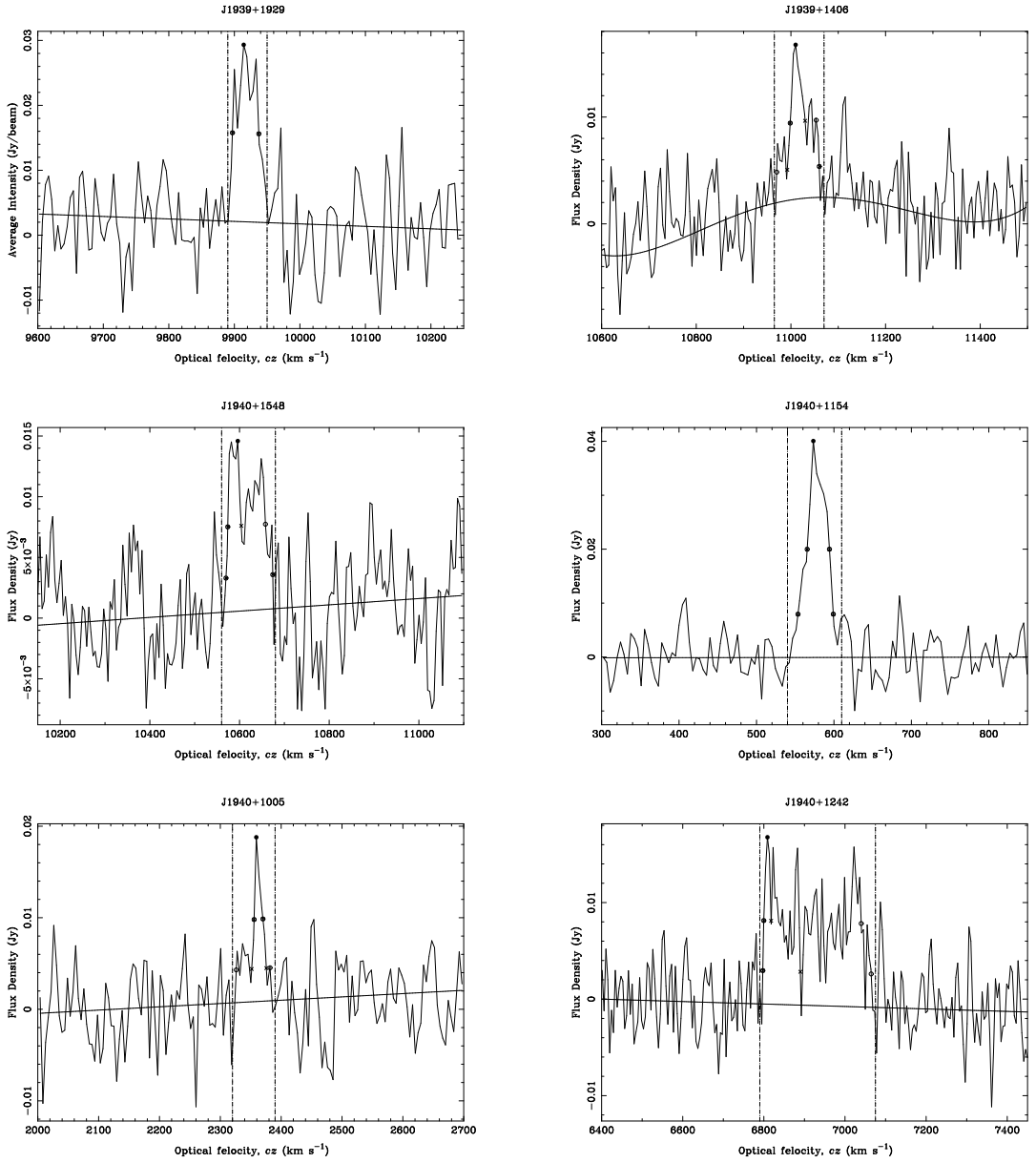

Figure B.2 (continued)

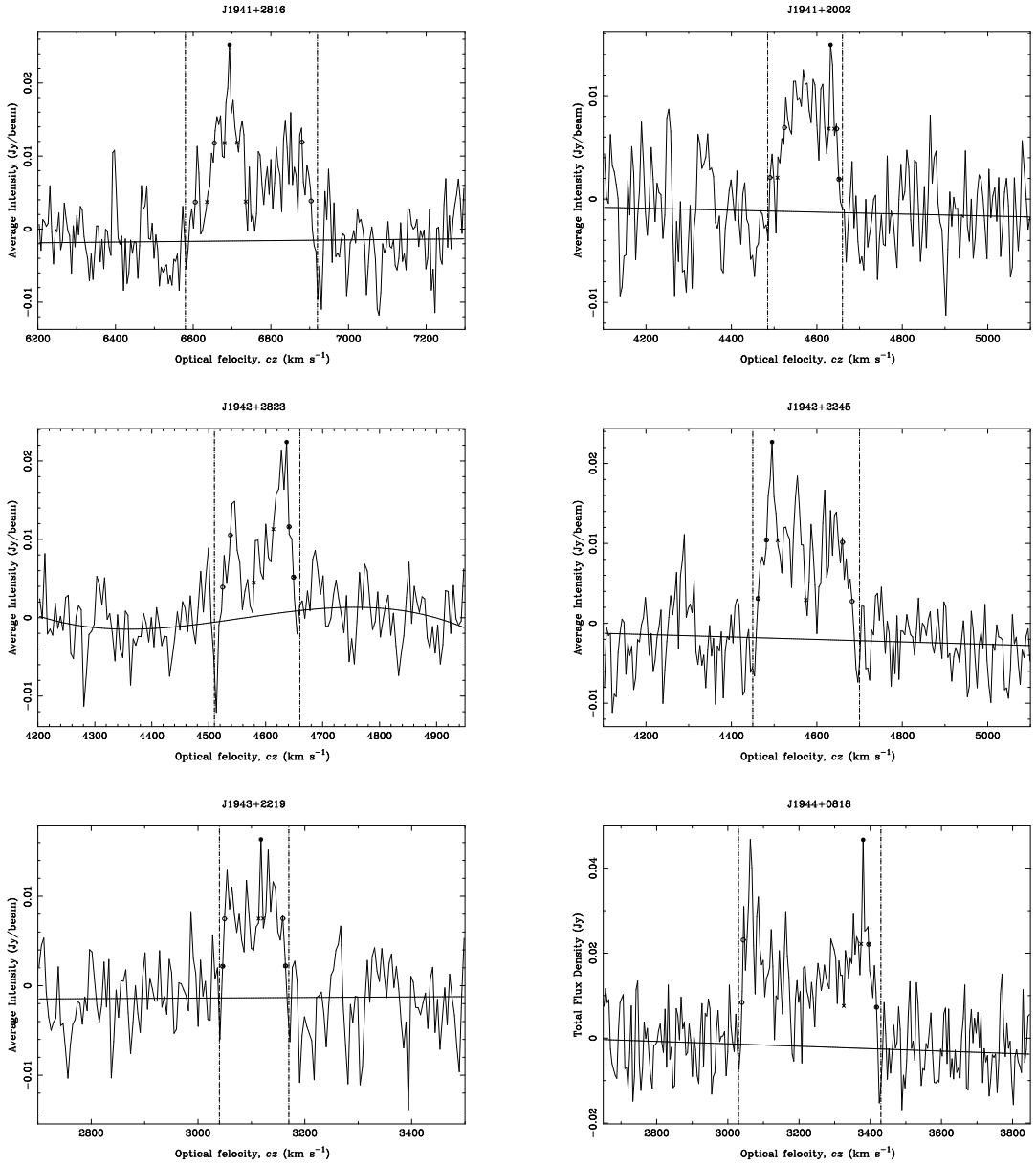

Figure B.2 (continued)

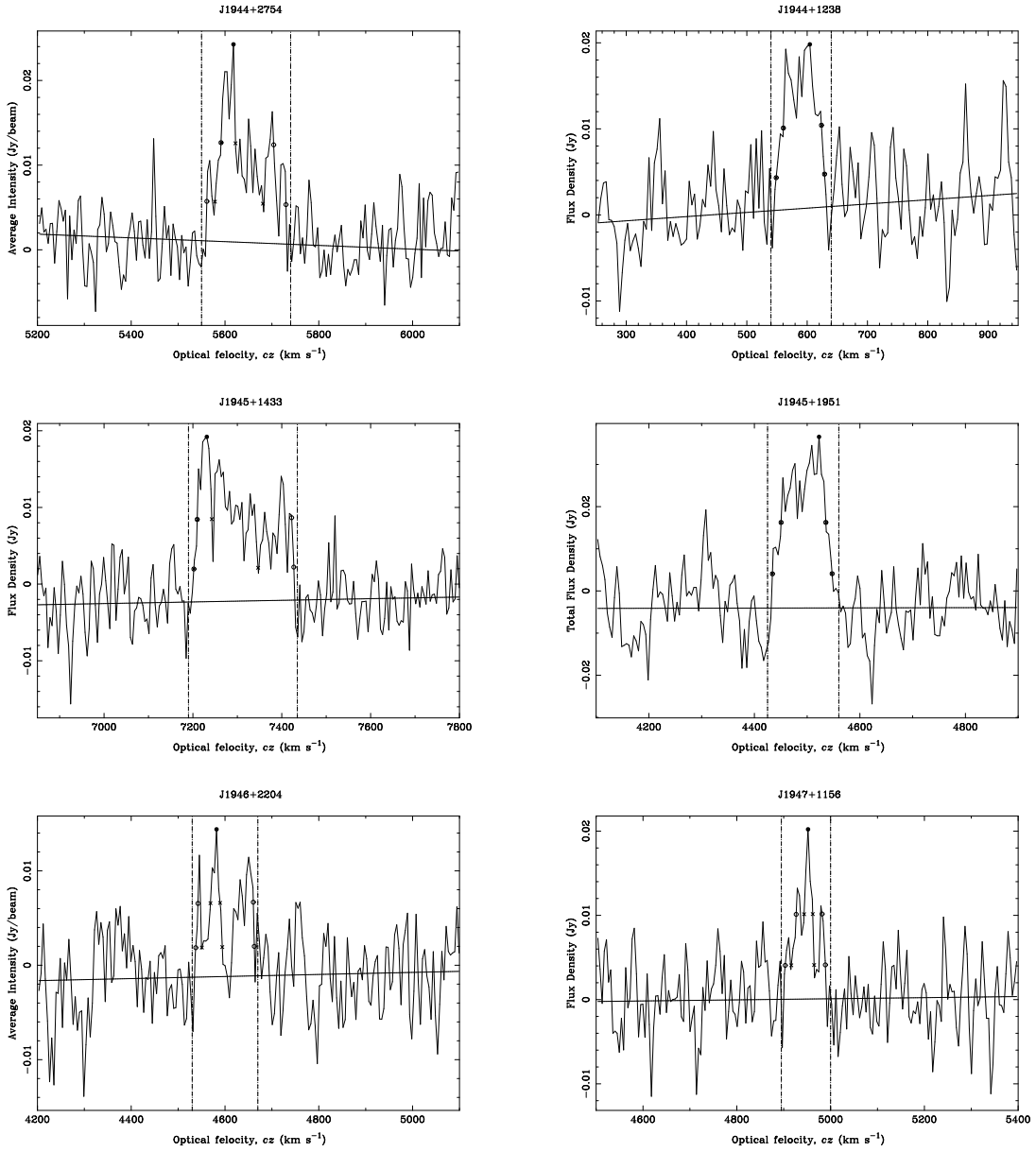

Figure B.2 (continued)

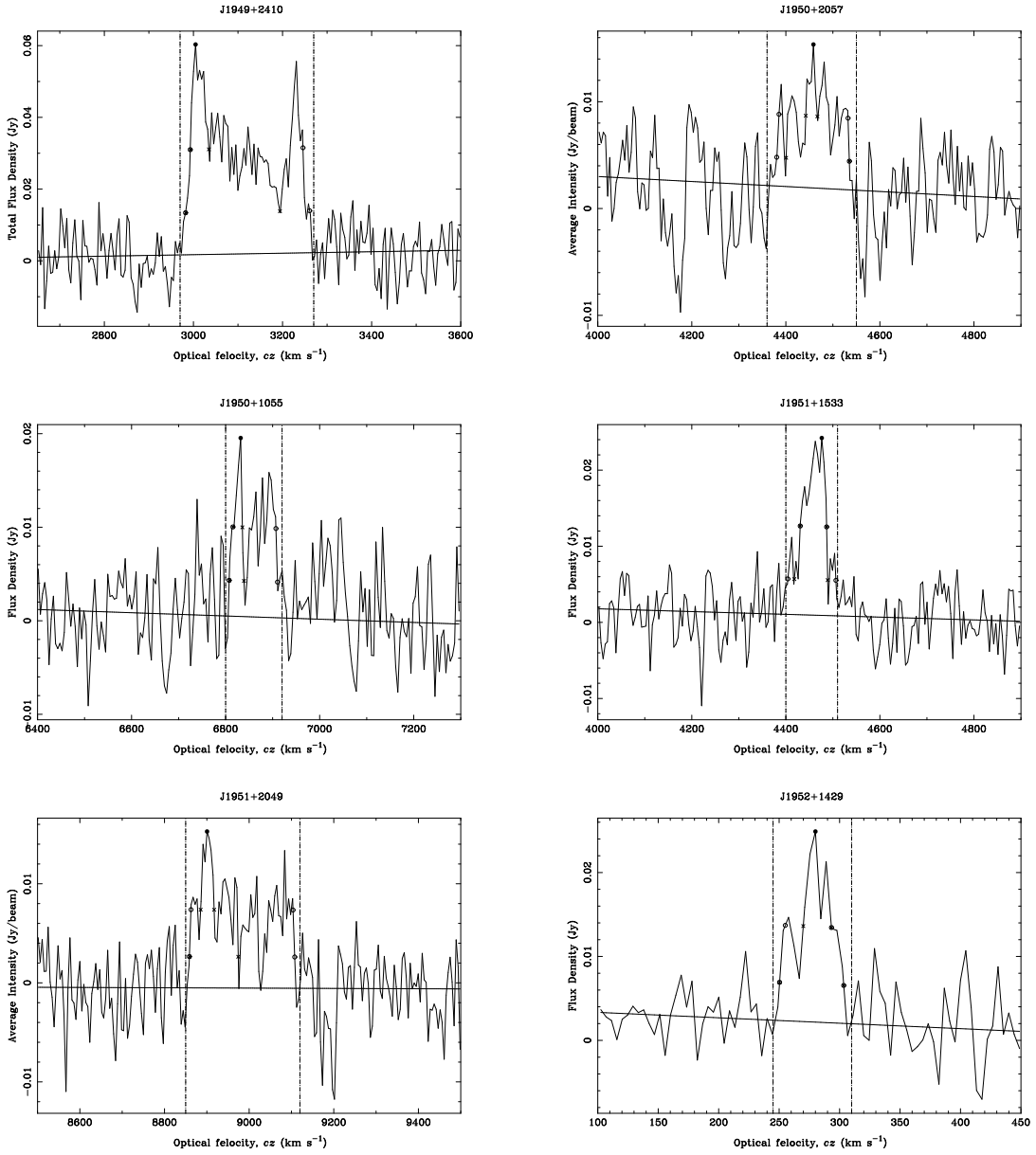

Figure B.2 (continued)

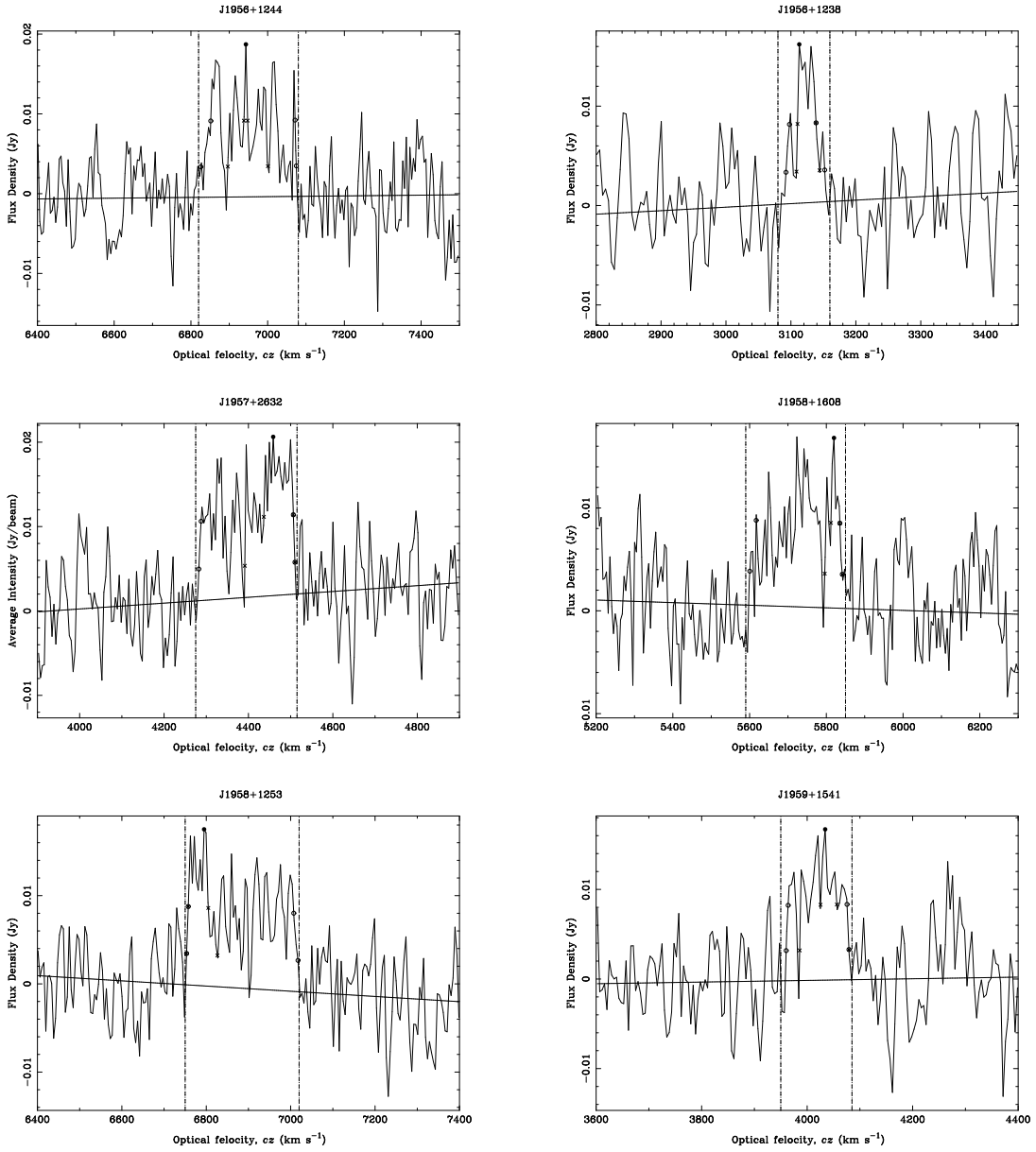

Figure B.2 (continued)

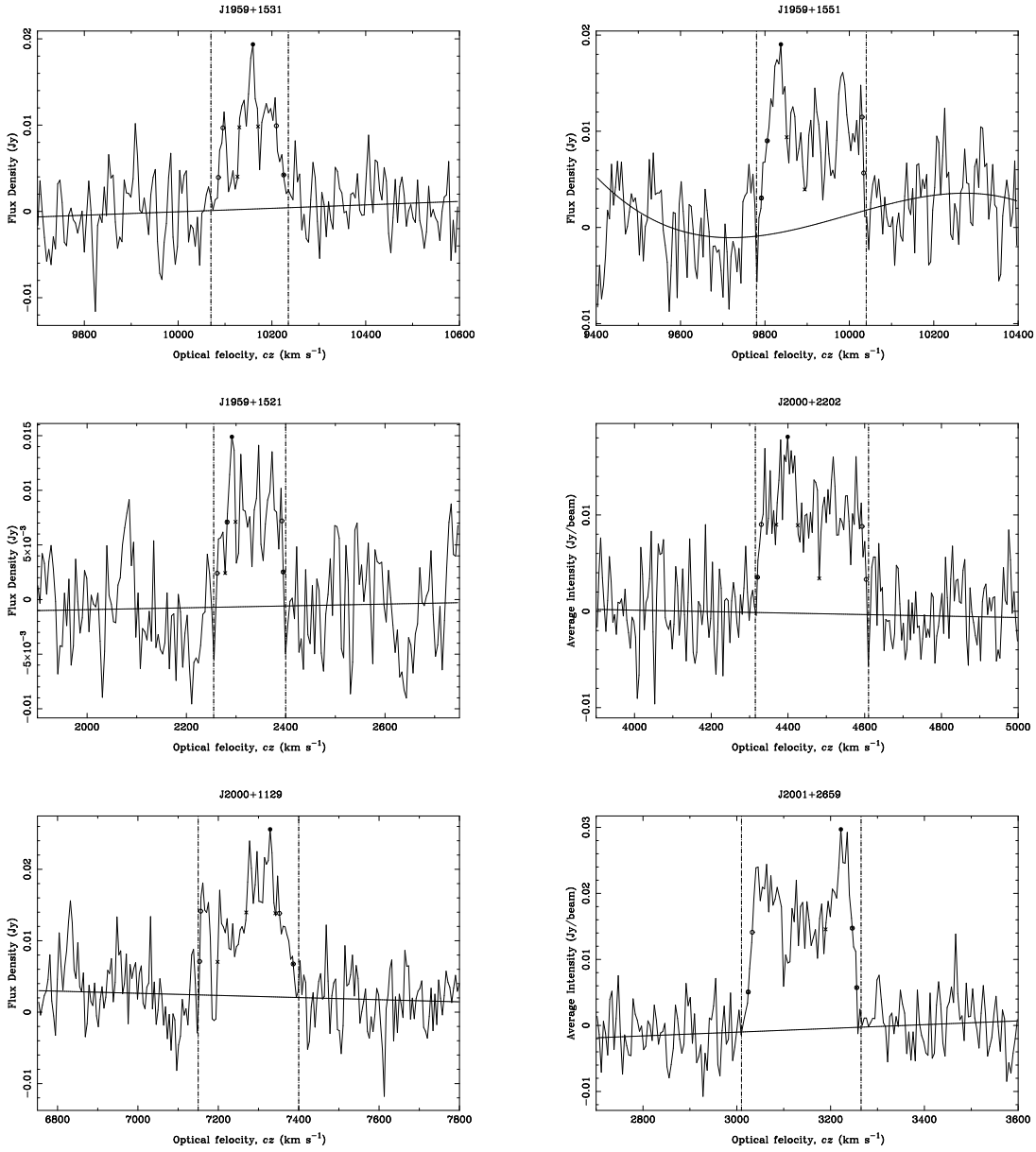

Figure B.2 (continued)

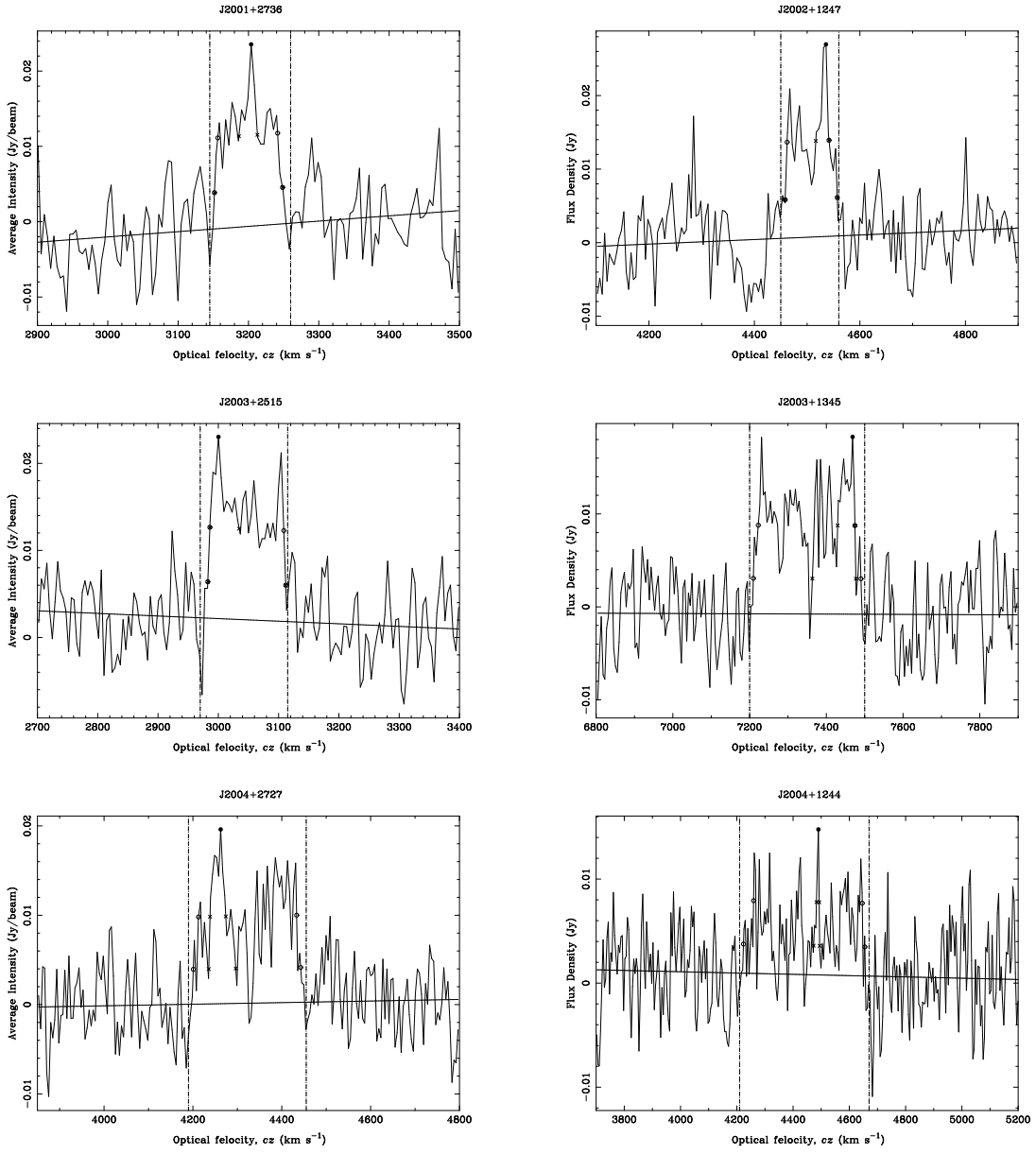

Figure B.2 (continued)

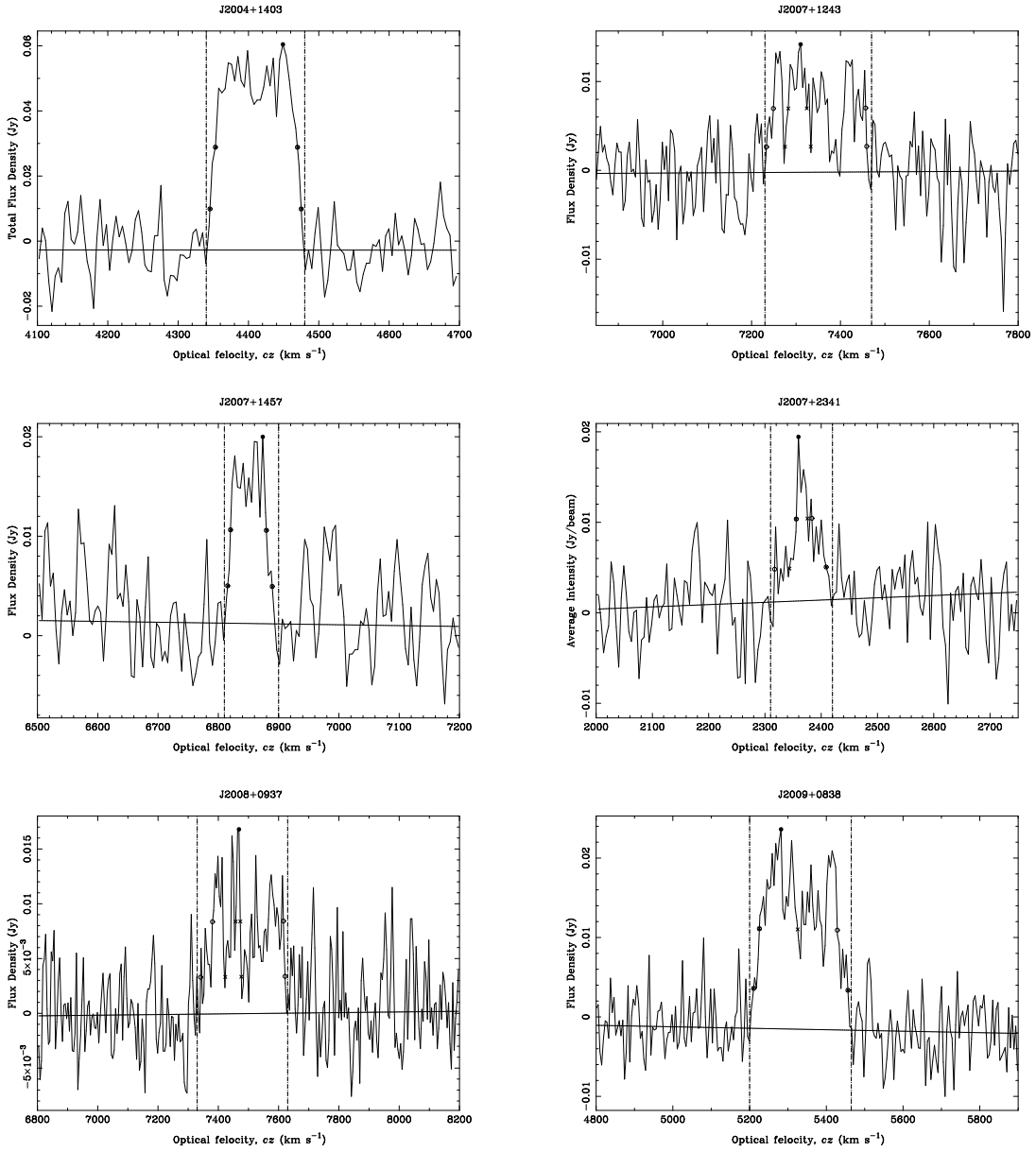

Figure B.3 (Figure B.1 continued)

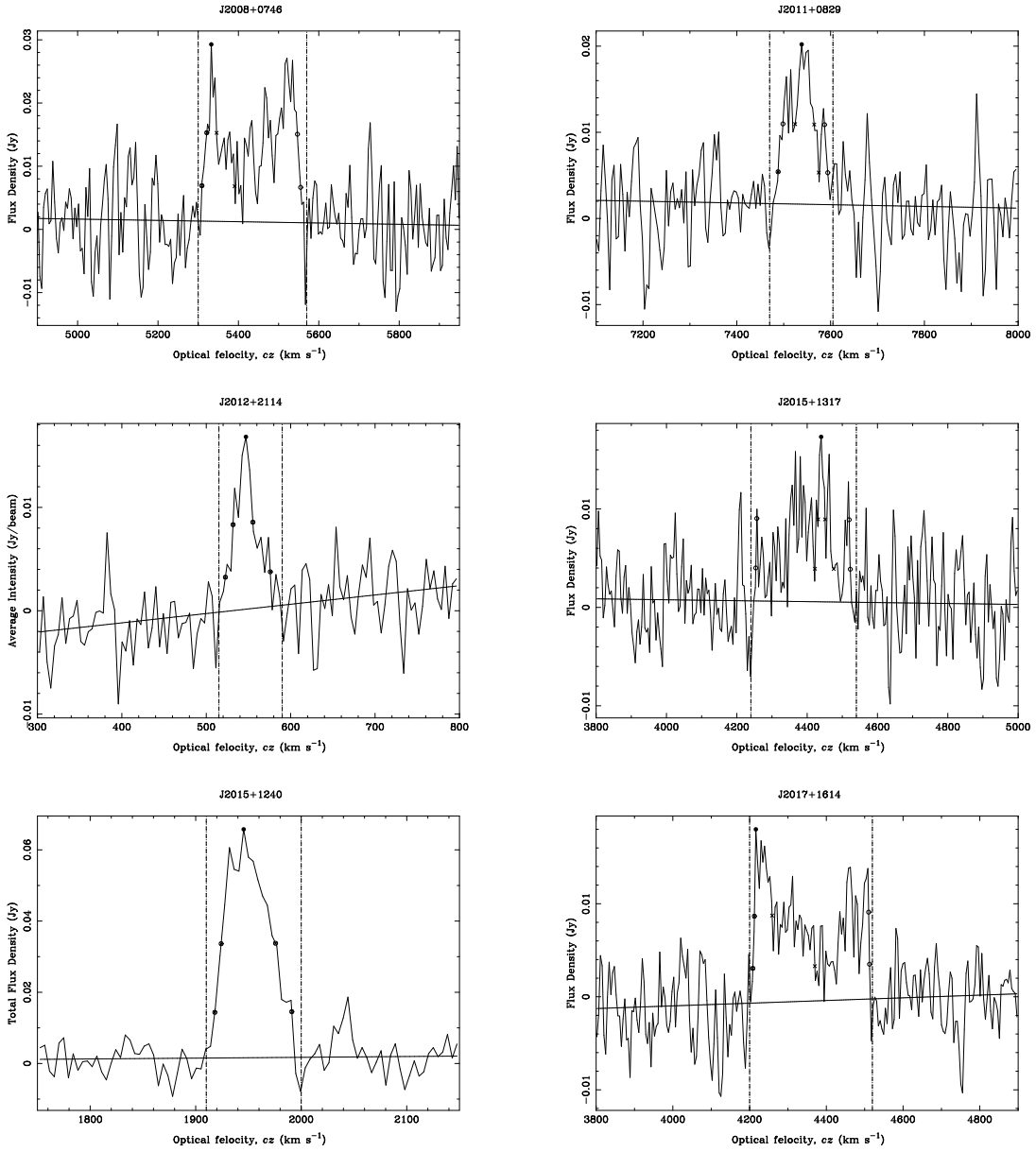

Figure B.3 (continued)

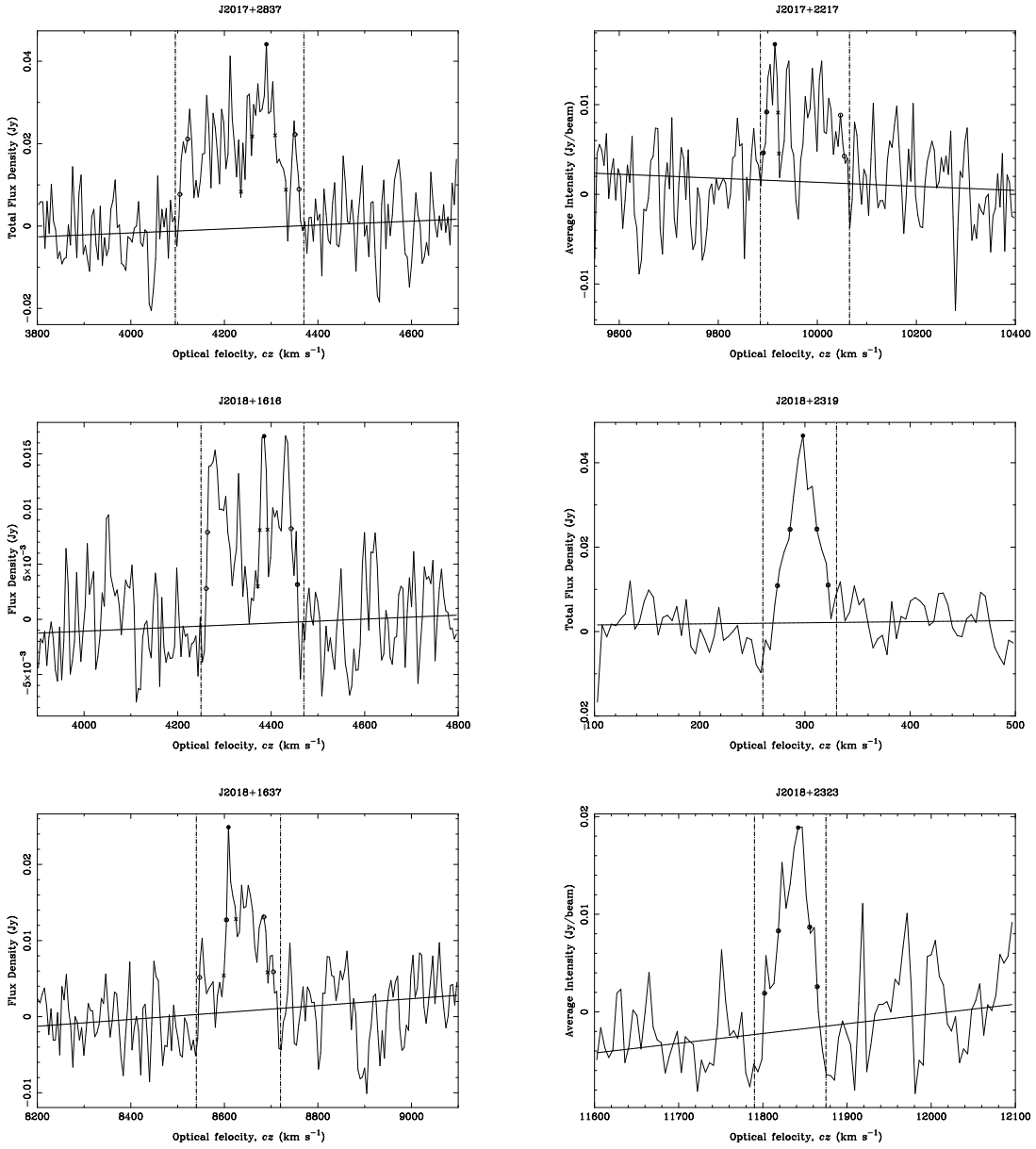

Figure B.3 (continued)

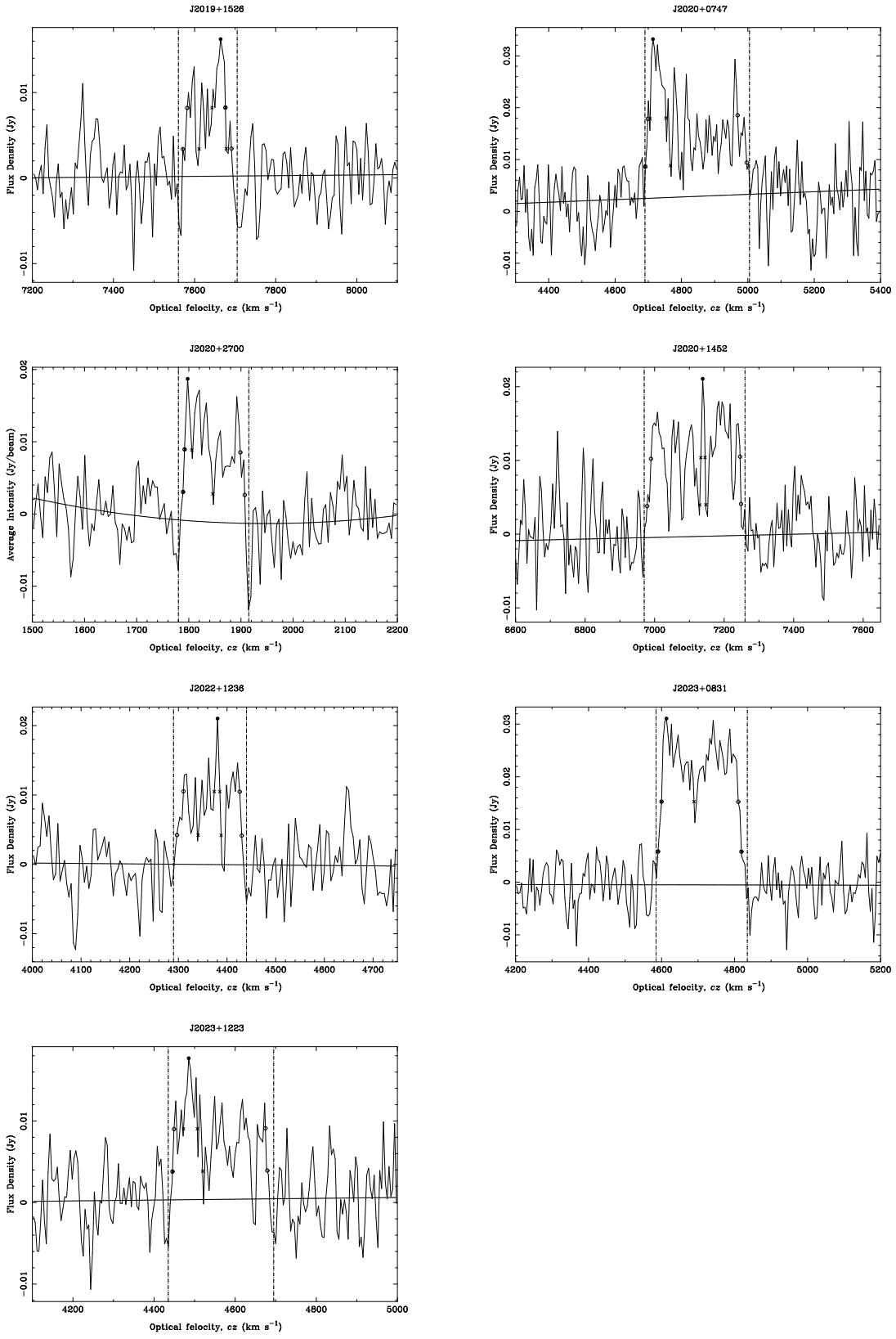

Figure B.3 (continued)

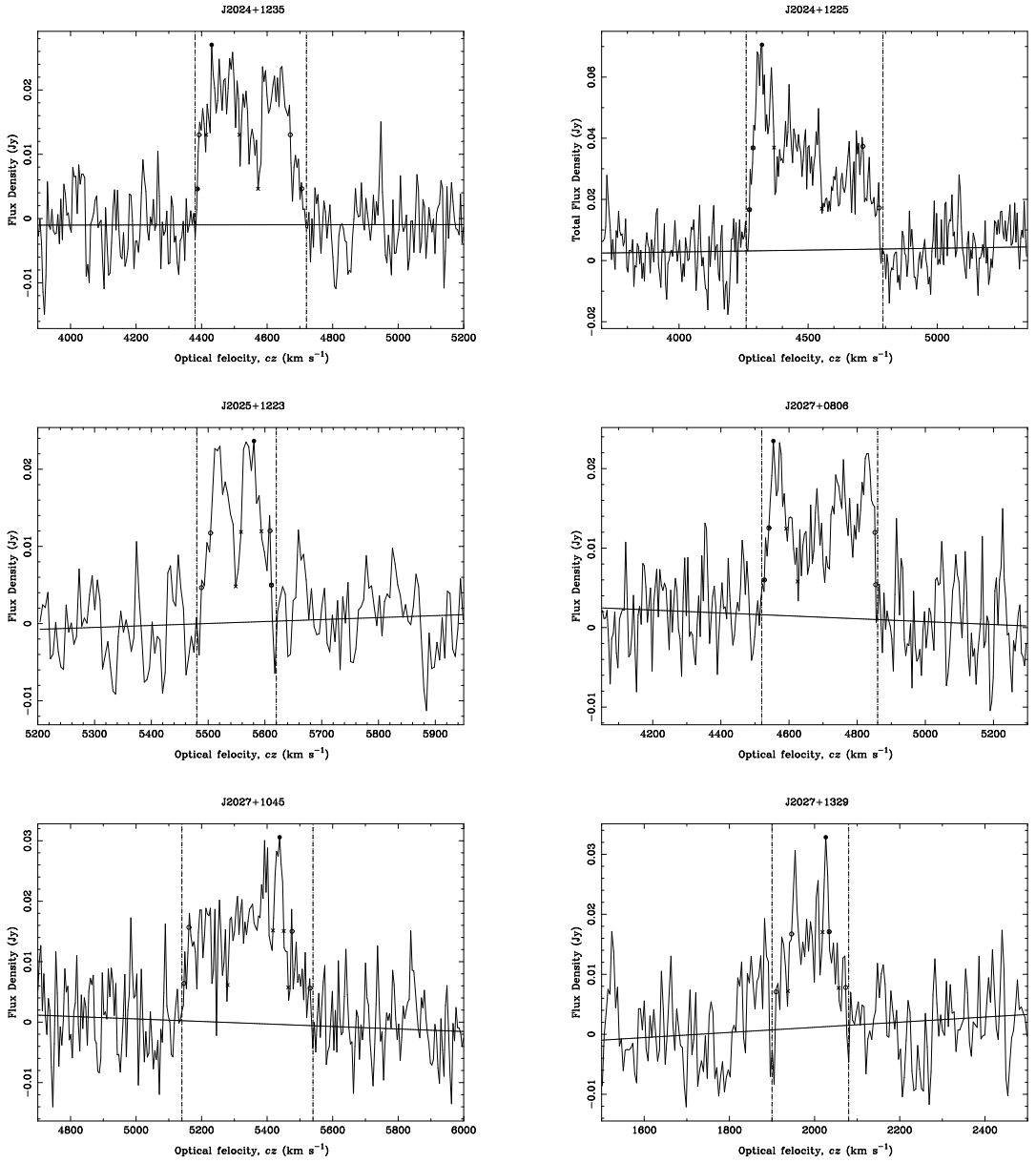

Figure B.3 (continued)

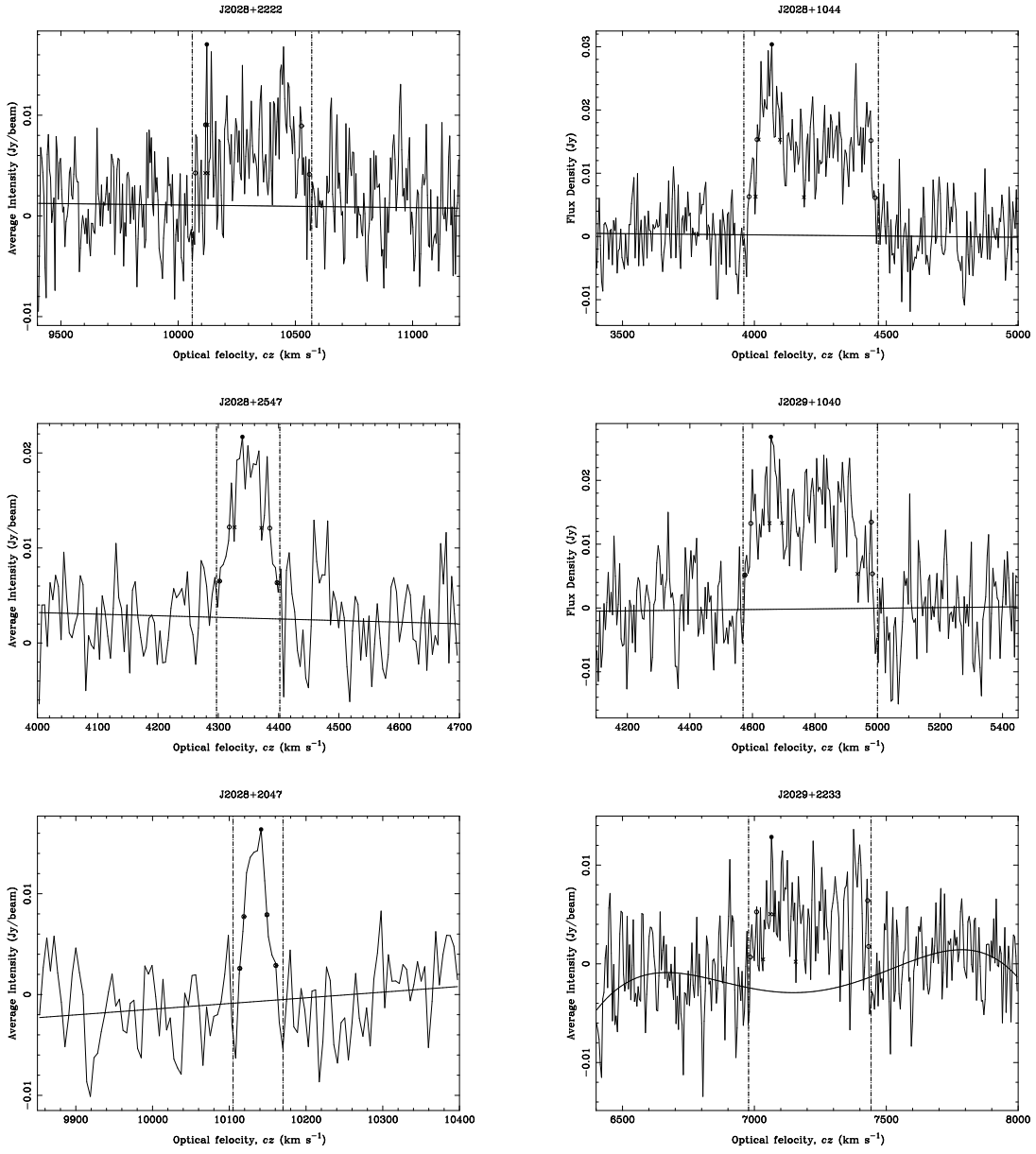

Figure B.3 (continued)

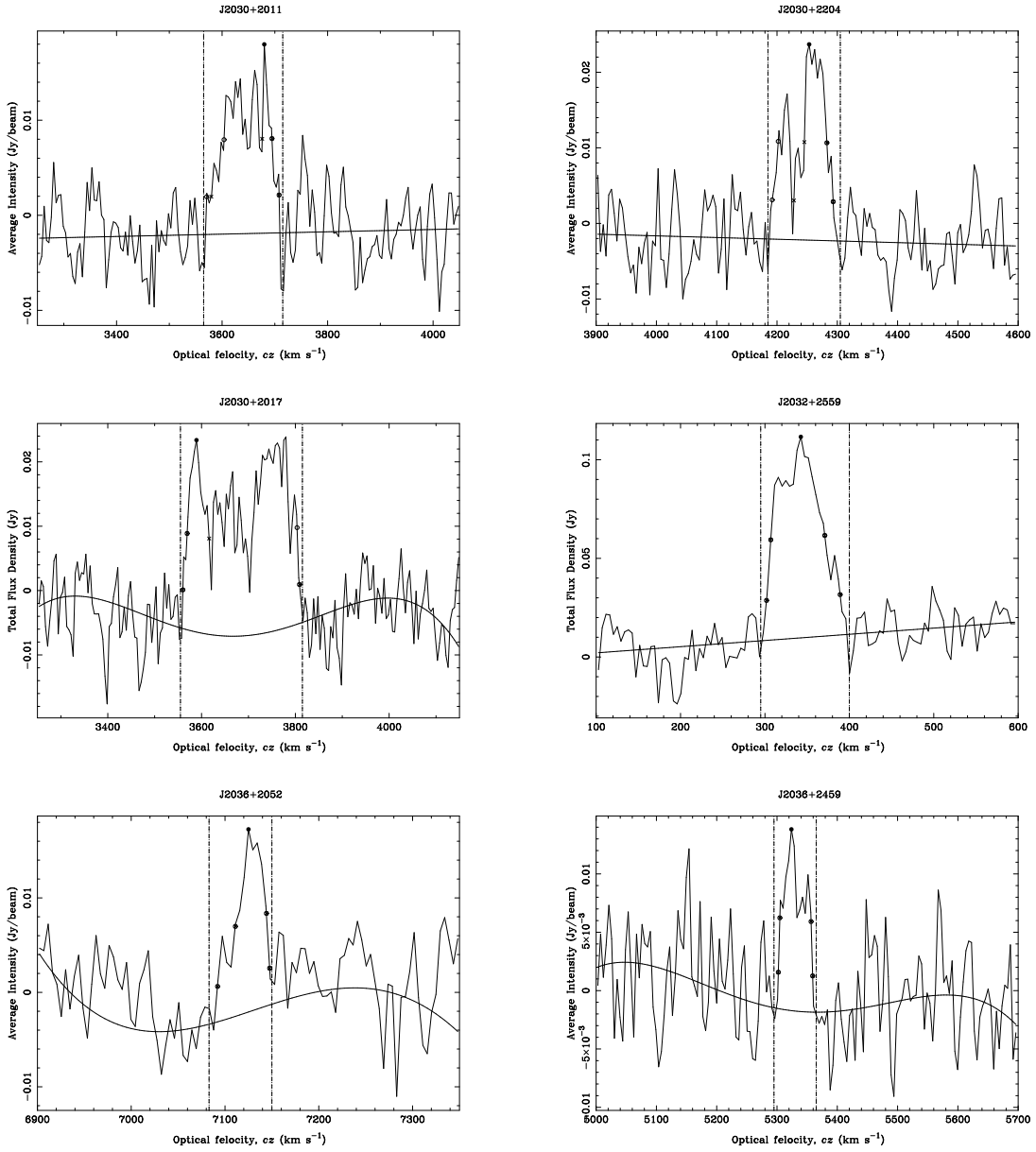

Figure B.3 (continued)

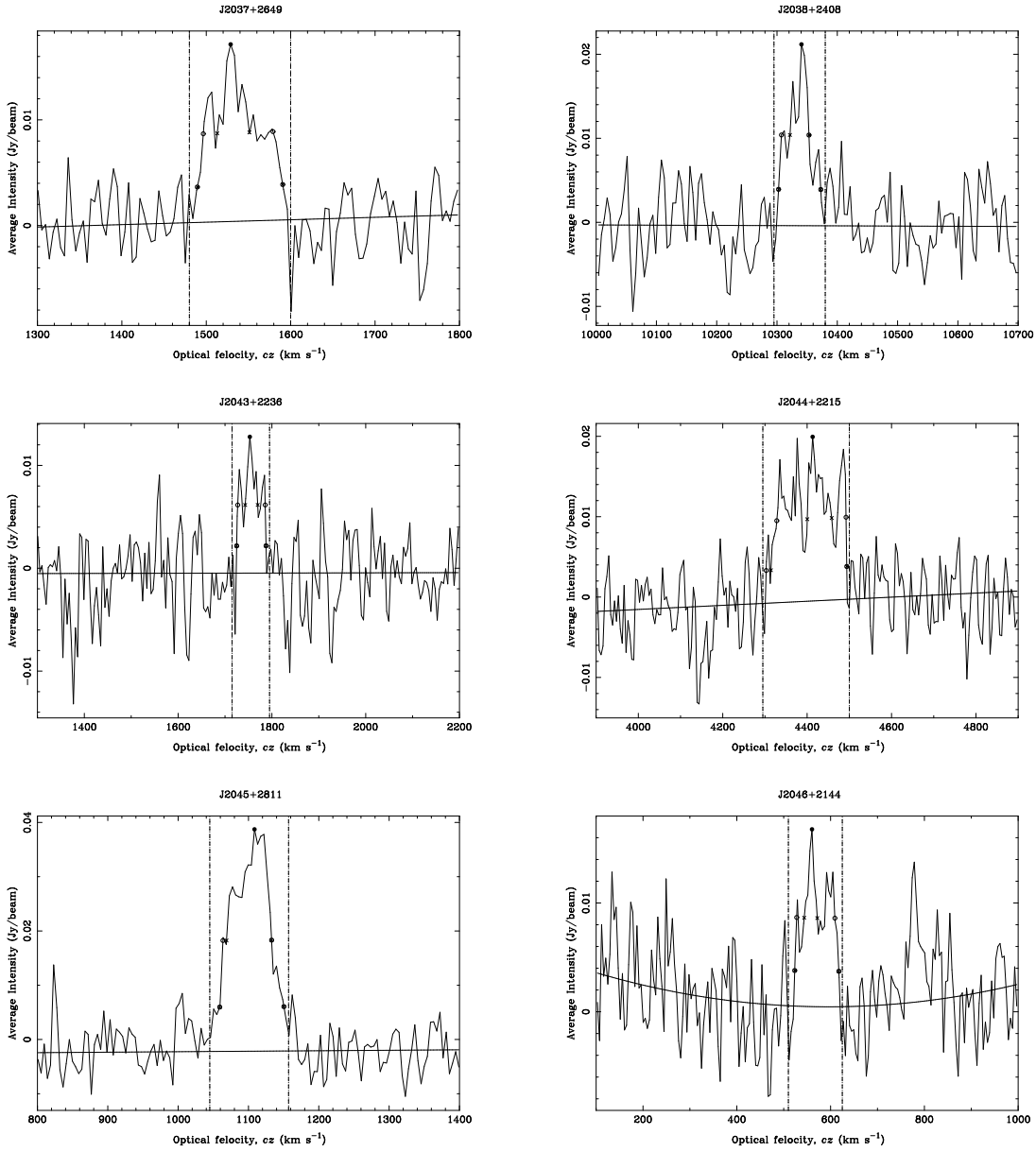

Figure B.3 (continued)

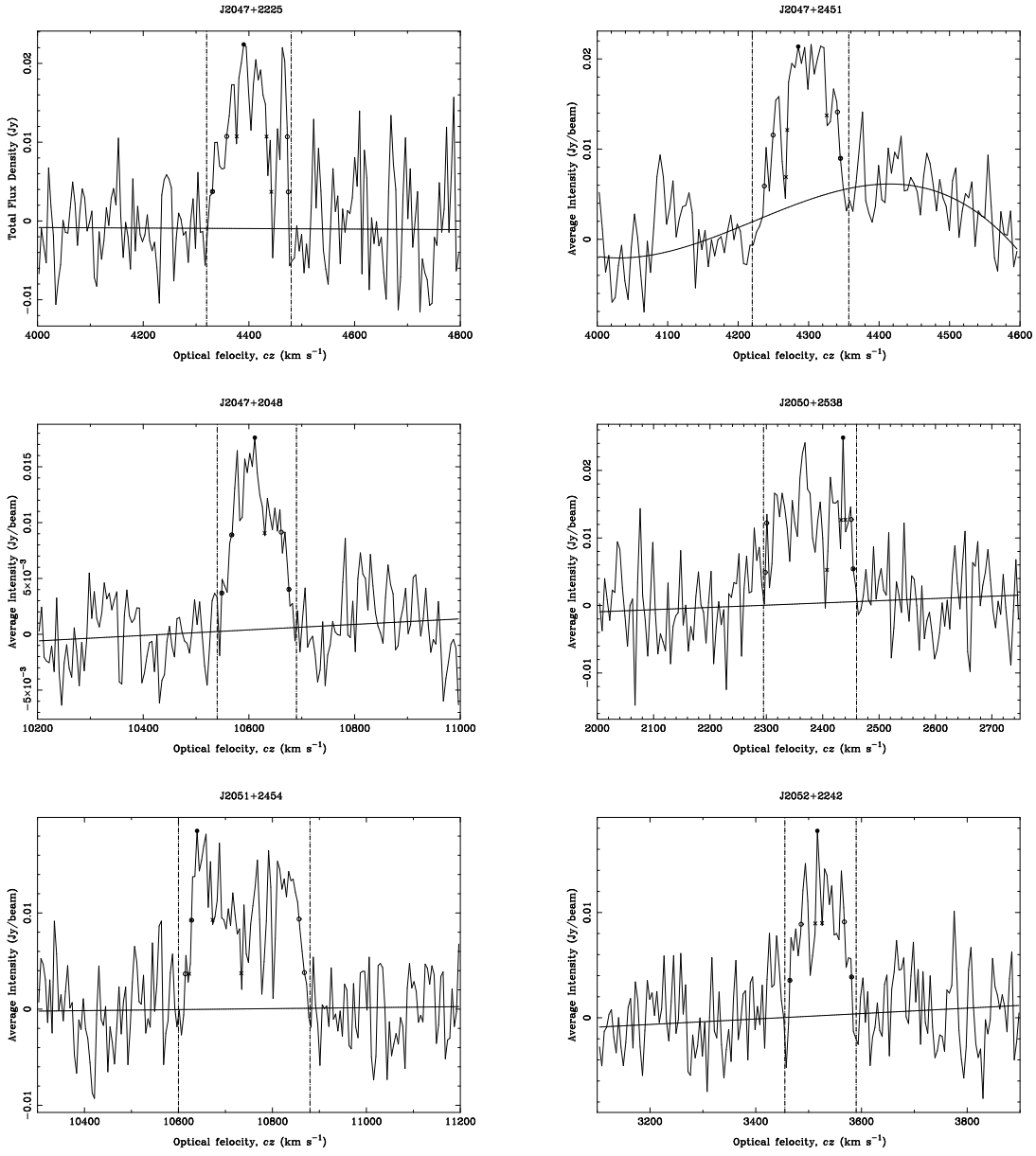

Figure B.3 (continued)

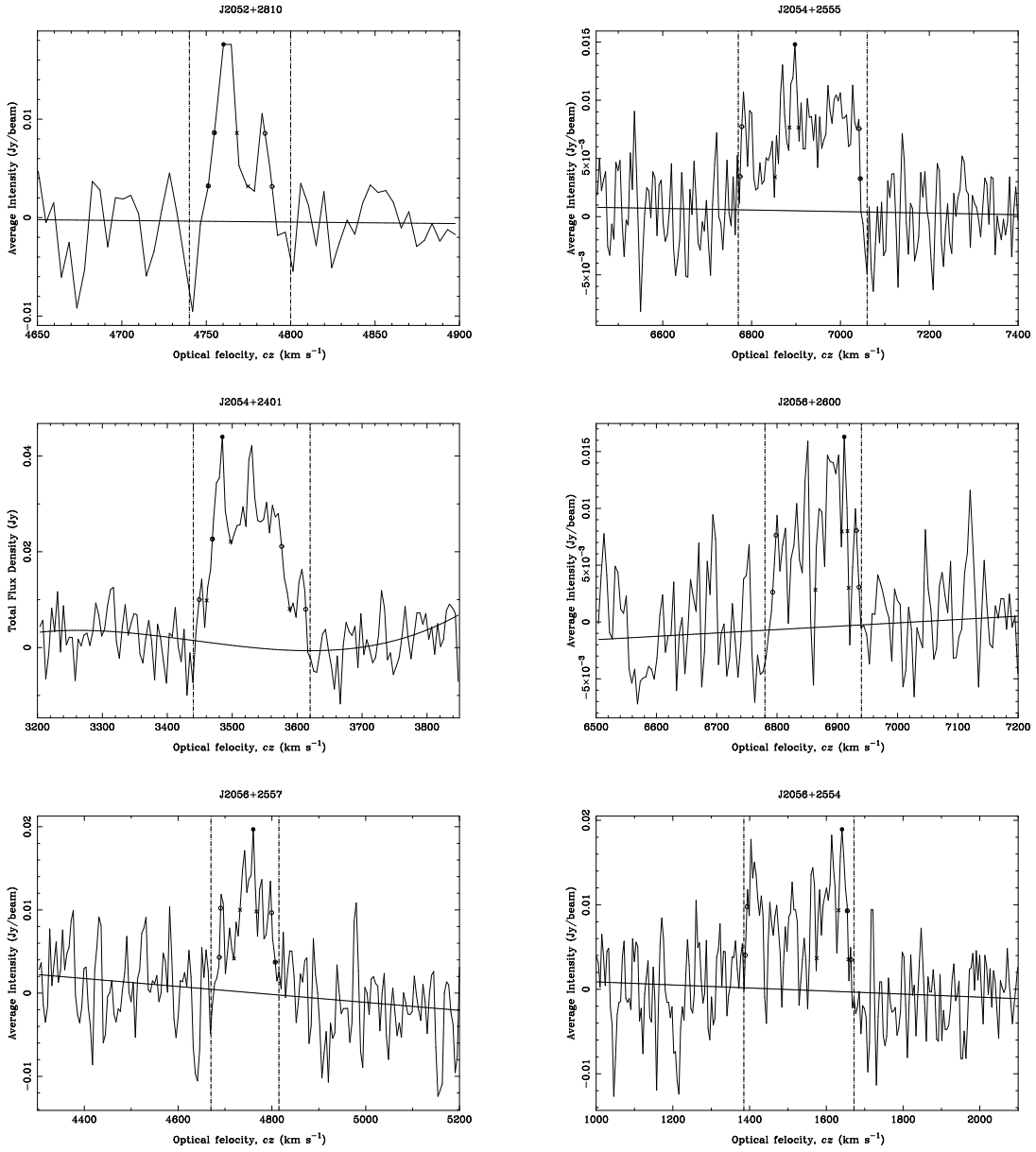

Figure B.3 (continued)

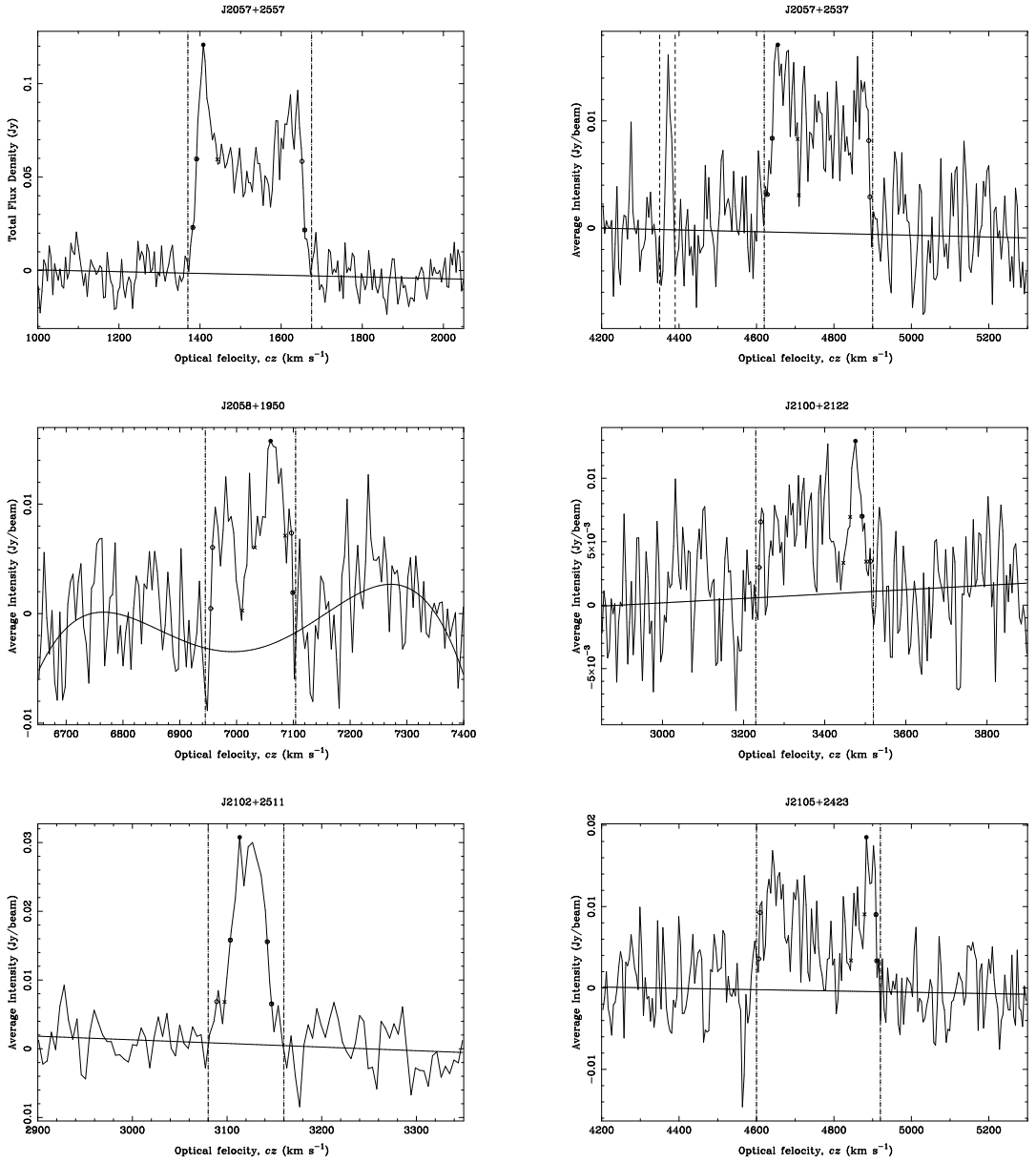

Figure B.3 (continued)

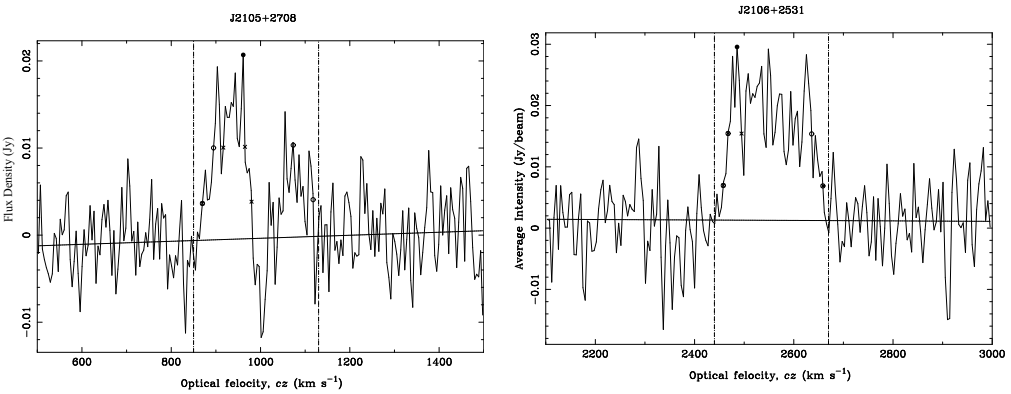

Figure B.3 (continued)

Appendix C

ALFA ZOA Catalogs

Table C.1. ALFA ZOA Deep Survey: First Results Catalog.

ALFAZOA	RA (J2000.0)	Dec (J2000.0)	l (°)	b (°)	F_{HI} (Jy km s^{-1})	v_{hel} (km s^{-1})	W_{50} (km s^{-1})	W_{20} (km s^{-1})	D_{LG} (Mpc)	$logM_{HI}$ (M$_\odot$)
J0555+1531	05 55 43 :	+15 31 54 :	192.73 :	−4.84 :	···	6620 :	···	···	···	···
J0556+1520[e]	05 56 11	+15 20 41	192.95	−4.84	2.5±0.2	7870±1	210±3	222±4	116	9.9
J0556+1450	05 56 30	+14 50 34	193.43	−5.02	4.7±0.3	6774±6	326±12	367±19	100	10.0
J0556+1513	05 56 54	+15 13 22	193.14	−4.74	0.6±0.1	7999±6	137±13	184±19	118	9.3
J0556+1448	05 56 55	+14 48 25	193.51	−4.95	0.6±0.1	5474±4	152±8	170±11	81	8.9
J0557+1450	05 57 02	+14 50 16	193.49	−4.91	0.8±0.1	8070±7	176±14	230±21	119	9.4
J0558+1708[e]	05 58 08	+17 08 51	191.61	−3.53	1.0±0.1	4966±4	164±8	193±12	73	9.1
J0558+1557[e]	05 58 48	+15 57 31	192.73	−3.98	1.1±0.1	6966±3	168±5	190±8	103	9.4
J0558+1656	05 58 52	+16 56 03	191.89	−3.48	0.8±0.1	8222±2	114±5	141±7	121	9.5
J0559+1636	05 59 29	+16 36 40	192.24	−3.52	1.7±0.1	8039±2	327±5	352±7	118	9.8
J0559+1543[e]	05 59 31	+15 43 43	193.02	−3.95	2.1±0.2	6529±3	74±6	112±9	96	9.7
J0559+1532[e]	05 59 49	+15 32 23	193.22	−3.98	6.6±0.3	5451±1	188±2	203±3	80	10.0
J0600+1644[e]	06 00 31	+16 44 39	192.25	−3.24	0.6±0.1	8109±3	26±6	102±9	119	9.3
J0600+1654	06 00 37	+16 54 34	192.12	−3.13	1.5±0.1	7006±2	251±4	265±6	103	9.6
J0600+1642[e]	06 00 39	+16 42 40	192.31	−3.21	1.0±0.1	8170±2	139±4	157±6	120	9.5

Table C.1 (cont'd)

ALFAZOA	RA (J2000.0)	Dec (J2000.0)	l (°)	b (°)	F_{HI} (Jy km s^{-1})	v_{hel} (km s^{-1})	W_{50} (km s^{-1})	W_{20} (km s^{-1})	D_{LG} (Mpc)	$logM_{HI}$ (M$_\odot$)
J0600+1640^e	06 00 48	+16 40 41	192.32	−3.21	0.9±0.1	8206±4	72±8	148±11	121	9.5
J0600+1651^e	06 00 52	+16 51 08	192.20	−3.11	4.5±0.4	6907±5	211±10	284±15	102	10.0
J0600+1529	06 00 59	+15 29 16	193.40	−3.76	1.2±0.1	5579±3	165±5	194±8	82	9.3
J0601+1540	06 01 02	+15 40 14	193.25	−3.66	1.1±0.1	5509±1	214±3	220±4	81	9.2
J0601+1709^e	06 01 11	+17 09 18	191.97	−2.89	2.5±0.2	6863±2	283±4	297±6	101	9.8
J0601+1620^e	06 01 34	+16 20 20	192.73	−3.22	2.9±0.3	4010±2	132±5	159±7	59	9.4
J0602+1558	06 02 03	+15 58 14	193.11	−3.30	1.1±0.1	5397±3	135±7	163±10	80	9.2
J0602+1450^e	06 02 26	+14 50 51	194.13	−3.77	149±0.9	769±0	233±0	250±0	11	9.7
J0602+1449	06 02 27	+14 49 44	194.15	−3.77	0.3±0.1	18668±5	61±10	90±16	275	9.7
J0602+1438	06 02 37	+14 38 19	194.34	−3.83	0.5±0.1	14213±5	152±10	179±15	209	9.7
J0603+1601	06 03 05	+16 01 08	193.19	−3.06	1.9±0.1	6332±2	233±5	261±7	93	9.6
J0603+1607^e	06 03 06	+16 07 29	193.09	−3.00	3.6±0.3	5444±3	310±6	337±10	80	9.7
J0603+1642	06 03 14	+16 42 02	192.61	−2.69	0.7±0.1	8295±4	73±8	118±12	122	9.5
J0605+1526^e	06 05 54	+15 26 07	194.03	−2.75	3.9±0.3	5452±2	153±4	180±6	80	9.8
J0606+1459	06 06 47	+14 59 08	194.52	−2.78	1.3±0.1	3911±2	146±5	162±7	58	9.0

Table C.1 (cont'd)

ALFAZOA	RA (J2000.0)	Dec (J2000.0)	l (°)	b (°)	F_{HI} (Jy km s^{-1})	v_{hel} (km s^{-1})	W_{50} (km s^{-1})	W_{20} (km s^{-1})	D_{LG} (Mpc)	$logM_{HI}$ (M$_\odot$)
J0607+1505	06 07 17	+15 05 55	194.48	−2.62	1.9±0.1	5376±3	126±7	243±10	79	9.4
J0607+1606	06 07 29	+16 06 00	193.63	−2.09	2.6±0.1	5637±3	130±5	238±8	83	9.6
J0607+1615	06 07 33	+16 15 00	193.51	−2.01	1.2±0.1	5515±6	153±11	268±17	81	9.3
J0607+1543	06 07 39	+15 43 45	193.97	−2.24	0.4±0.1	12862±5	80±9	105±14	189	9.6
J0607+1507	06 07 43	+15 07 43	194.51	−2.52	1.1±0.1	5436±5	170±10	216±14	80	9.2
J0607+1607^e	06 07 45	+16 07 00	193.65	−2.03	4.4±0.1	5573±2	188±4	253±5	82	9.9
J0607+1611a	06 07 46	+16 11 00	193.59	−1.99	3.3±0.1	5539±2	127±4	203±5	82	9.7
J0607+1611b	06 07 46	+16 11 00	193.59	−1.99	0.7±0.1	5217±2	187±5	196±7	77	9.0
J0608+1527	06 08 50	+15 27 27	194.35	−2.12	1.0±0.2	13787±5	150±10	182±15	203	10.0
J0610+1709	06 10 20	+17 09 11	193.04	−0.99	2.4±0.2	13453±3	215±6	249±9	198	10.3
J0610+1704	06 10 57	+17 04 55	193.17	−0.89	0.5±0.1	13558±4	143±8	161±11	200	9.7
J0611+1552^e	06 11 07	+15 52 16	194.25	−1.44	12±0.5	5443±3	387±7	484±10	80	10.3
J0611+1553	06 11 26	+15 53 00	194.28	−1.37	0.9±0.1	5589±3	108±6	141±9	82	9.1
J0611+1643^e	06 11 31	+16 43 18	193.55	−0.95	0.9±0.1	5241±2	89±4	101±5	77	9.1
J0612+1636	06 12 37	+16 36 29	193.78	−0.77	0.6±0.1	5146±3	184±5	196±8	76	8.9

Table C.1 (cont'd)

ALFAZOA	RA (J2000.0)	Dec (J2000.0)	l (°)	b (°)	F_{HI} (Jy km s^{-1})	v_{hel} (km s^{-1})	W_{50} (km s^{-1})	W_{20} (km s^{-1})	D_{LG} (Mpc)	$logM_{HI}$ (M$_\odot$)
J0613+1545	06 13 41	+15 45 07	194.65	−0.96	1.4±0.2	13307±3	202±6	215±9	196	10.1
J0613+1707	06 13 59	+17 07 41	193.48	−0.23	0.5±0.1	16308±7	64±14	148±20	240	9.8
J0614+1641	06 14 23	+16 41 30	193.91	−0.36	0.6±0.1	13366±4	256±8	267±12	197	9.8
J0615+1547	06 15 08	+15 47 38	194.78	−0.63	0.3±0.1	13062±4	47±8	64±12	192	9.3
J0615+1705	06 15 40	+17 05 47	193.70	0.10	0.5±0.1	4841±5	91±10	139±14	71	8.8
J0616+1639	06 16 00	+16 39 58	194.12	−0.03	0.3±0.1	2144±4	38±7	65±11	32	7.9
J0616+1526	06 16 03	+15 26 10	195.20	−0.61	0.7±0.1	11735±5	178±10	213±16	173	9.7
J0616+1641[e]	06 16 10	+16 41 54	194.11	0.02	6.8±0.3	5555±3	210±5	272±8	82	10.0
J0616+1704	06 16 25	+17 04 56	193.80	0.25	0.8±0.1	5040±2	170±4	190±6	74	9.0
J0616+1705	06 16 34	+17 05 12	193.81	0.29	1.3±0.1	5704±1	56±2	86±384	9.3	9.3
J0616+1626	06 16 45	+16 26 54	194.39	0.02	1.2±0.1	11584±3	386±5	397±8	170	9.9
J0616+1536	06 16 58	+15 36 41	195.15	−0.33	1.3±0.1	11761±2	148±4	159±5	173	10.0
J0617+1655	06 17 15	+16 55 43	194.03	0.36	1.2±0.1	5373±4	369±7	389±11	79	9.3
J0617+1648[e]	06 17 19	+16 48 26	194.14	0.31	1.4±0.2	5696±3	111±5	123±8	84	9.4
J0617+1644	06 17 43	+16 44 55	194.24	0.37	0.3±0	5313±3	22±6	74±9	78	8.7

Table C.1 (cont'd)

ALFAZOA	RA (J2000.0)	Dec (J2000.0)	l (°)	b (°)	F_{HI} (Jy km s^{-1})	v_{hel} (km s^{-1})	W_{50} (km s^{-1})	W_{20} (km s^{-1})	D_{LG} (Mpc)	$logM_{HI}$ ($M_\odot$)
J0618+1430	06 18 18 :	+14 30 53 :	196.27 :	−0.57 :	...	13667 :	...	...	...	...

Table C.2. Catalog of possible counterparts for ALFA ZOA Deep detections.

ALFAZOA	l (°)	b (°)	A_B (mag)	Counterpart	Sep. (′)	Δv (km s^{-1})
J0556+1450	193.43	−5.02	1.2	2MASX J05563099+1450236	0.3	2
J0556+1513	193.14	−4.74	1.4	2MASX J05565515+1513206	0.3	···
J0556+1520	192.95	−4.84	1.3	2MASX J05561201+1520386	0.5	···
	···	···	···	ZOAG G192.97–04.82	1.3	···
	···	···	···	2MASX J05561519+1520186	1.3	···
J0558+1557	192.73	−3.98	2.2	2MASX J05584846+1557068	0.4	···
J0558+1708	191.61	−3.53	2.6	2MASX J05581034+1708233	0.7	···
J0559+1543	193.02	−3.95	2.0	2MASX J05593112+1542527	0.8	···
	···	···	···	ZOAG G193.03–03.9	0.9	···
J0559+1636	192.24	−3.52	2.9	2MASX J05593052+1636117	0.6	···
J0601+1540	193.25	−3.66	2.5	2MASX J06010160+1540102	0.1	···
J0600+1640	192.32	−3.21	5.3	2MASX J06004860+1641193	1.0	···
J0600+1651	192.20	−3.11	4.0	2MASX J06005403+1649473	1.4	···
	···	···	···	2MASX J06005104+1649293	1.7	···
J0600+1654	192.12	−3.13	3.0	2MASX J06003585+1654227	0.3	···
J0601+1709	191.97	−2.89	4.6	2MASX J06011037+1709532	0.6	···
J0602+1438	194.34	−3.83	3.2	2MASX J06023859+1438273	0.4	···

Table C.2 (cont'd)

ALFAZOA	l (°)	b (°)	A_B (mag)	Counterpart	Sep. (′)	Δv (km s^{-1})
J0602+1450	194.13	−3.77	3.2	2MASX J06022660+1450540	0.2	2
J0603+1601	193.19	−3.06	3.9	2MASX J06030641+1601033	0.3	...
J0603+1607	193.09	−3.00	4.2	2MASX J06030454+1607413	0.4	...
J0605+1526	194.03	−2.75	4.4	2MASX J06055511+1526548	0.8	...
J0607+1506	194.48	−2.62	3.6	2MASX J06072476+1505517	1.9	...
J0607+1543	193.97	−2.24	7.0	2MASX J06074014+1544206	0.7	...
J0607+1607	193.65	−2.03	5.4	2MASX J06074379+1608036	1.1	...
J0608+1527	194.35	−2.12	5.3	2MASX J06085110+1526540	0.6	...
J0611+1552	194.25	−1.44	4.8	2MASX J06110597+1551441	0.5	...
J0614+1641	193.91	−0.36	7.4	2MASX J06142201+1641578	0.5	...
J0616+1626	194.39	0.02	5.9	2MASX J06164466+1627254	0.5	...
J0616+1641	194.11	0.02	5.3	2MASX J06161202+1641266	0.7	...
J0617+1655	194.03	0.36	5.0	2MASX J06171616+1655575	0.4	...

Table C.3. ALFA ZOA Shallow Survey B+C Catalog.

ALFAZOA	RA (J2000.0)	Dec (J2000.0)	l (°)	b (°)	F_{HI} (Jy km s^{-1})	v_{hel} (km s^{-1})	W_{50} (km s^{-1})	W_{20} (km s^{-1})	D_{LG} (Mpc)	$logM_{HI}$ (M$_\odot$)
J1813+1536	18 : 14 : 08	15 36 40	42.96	15.20	1.6±0.4	2869±6	66±11	105±17	42	8.84
J1814+1316	18 : 14 : 13	13 16 08 :	40.77 :	14.19 :	···	2280 :	···	···	···	···
J1816+1346[e]	18 : 16 : 03	13 47 09	41.34	14.01	3.3±0.6	3008±5	126±11	161±16	44	9.18
J1816+1001	18 : 16 : 37	10 03 08	38.05	12.28	1.6±0.4	10330±4	110±7	119±11	147	9.92
J1816+1124	18 : 16 : 45	11 24 23	39.31	12.84	1.3±0.5	2298±4	79±7	85±11	34	8.53
J1816+1421	18 : 16 : 59	14 24 04	42.12	14.06	3.6±0.8	5346±7	145±14	185±22	77	9.71
J1817+0959	18 : 17 : 25	09 59 46	38.08	12.08	1.6±0.5	2171±6	93±12	114±18	32	8.60
J1817+1256	18 : 17 : 29	12 57 04	40.82	13.34	2.8±0.6	2887±3	220±6	226±9	42	9.08
J1817+1247	18 : 18 : 02	12 46 42	40.72	13.14	2.2±0.5	2888±5	96±10	117±15	42	8.98
J1820+1438	18 : 20 : 06	14 39 09	42.69	13.49	4.2±0.6	5174±3	120±7	142±10	75	9.75
J1820+1219	18 : 20 : 59	12 18 10	40.60	12.29	1.2±0.3	6725±4	126±7	136±11	96	9.43
J1820+1254	18 : 21 : 04	12 55 48	41.19	12.54	1.6±0.4	6758±4	39±9	73±13	97	9.56
J1821+1305	18 : 21 : 54	13 05 21	41.42	12.43	2.2±0.5	6765±4	70±8	87±12	97	9.70
J1822+1517	18 : 22 : 36	15 16 28	43.53	13.20	2.5±0.6	4964±6	183±13	204±19	72	9.49
J1822+1542[e]	18 : 22 : 43	15 42 06	43.94	13.35	4.9±1.1	5270±8	68±16	134±24	76	9.83

Table C.3 (cont'd)

ALFAZOA	RA (J2000.0)	Dec (J2000.0)	l (°)	b (°)	F_{HI} (Jy km s^{-1})	v_{hel} (km s^{-1})	W_{50} (km s^{-1})	W_{20} (km s^{-1})	D_{LG} (Mpc)	$logM_{HI}$ (M$_\odot$)
J1822+1226	18 : 23 : 02	12 24 06 :	40.91 :	11.88 :	...	2646 :	...	...	...	...
J1823+1449	18 : 24 : 07	14 50 40	43.29	12.69	3.0±0.6	2935±6	155±11	178±17	43	9.13
J1824+1220	18 : 24 : 49	12 20 23	41.05	11.46	4.1±1.0	5563±8	282±15	303±23	80	9.79
J1825+1509	18 : 25 : 42	15 09 50	43.75	12.47	1.8±0.5	6877±4	168±9	179±13	99	9.61
J1827+0928[e]	18 : 27 : 36	09 29 20	38.74	9.60	3.6±0.8	3910±5	190±9	204±14	57	9.44
J1828+1544[e]	18 : 28 : 23	15 55 54	44.57	12.14	0.8±0.4	6873±4	78±7	84±11	99	9.27
J1830+1150[e]	18 : 30 : 44	11 50 37	41.23	9.94	2.1±0.7	2478±3	106±6	112±9	37	8.83
J1830+0929	18 : 30 : 58	09 27 59	39.09	8.85	2.5±0.7	5834±9	278±18	304±26	84	9.61
J1833+1041	18 : 33 : 24	10 41 01	40.46	8.84	1.3±0.4	3119±5	56±10	74±16	46	8.79
J1833+1035	18 : 33 : 26	10 36 44	40.40	8.80	2.3±0.6	3164±7	107±14	140±21	46	9.06
J1833+1052	18 : 33 : 20	10 53 06	40.64	8.95	0.9±0.5	3194±7	112±13	122±20	47	8.68
J1836+1133	18 : 36 : 23	11 34 18	41.60	8.58	3.9±0.7	3521±4	270±9	287±13	51	9.39
J1836+1018[e]	18 : 36 : 33	10 19 34	40.48	8.00	7.7±1.2	3379±10	207±21	327±31	49	9.64
J1836+1025	18 : 36 : 50	10 26 25	40.62	7.98	7.9±0.8	3475±4	259±7	285±11	51	9.68
J1837+1224[e]	18 : 37 : 13	12 23 30	42.43	8.76	5.9±0.9	3689±3	137±6	152±10	54	9.60

Table C.3 (cont'd)

ALFAZOA	RA (J2000.0)	Dec (J2000.0)	l (°)	b (°)	F_{HI} (Jy km s^{-1})	v_{hel} (km s^{-1})	W_{50} (km s^{-1})	W_{20} (km s^{-1})	D_{LG} (Mpc)	$logM_{HI}$ (M$_\odot$)
J1837+1959	18 : 37 : 21	19 58 41	49.41	11.98	4.1±0.6	5856±4	350±7	363±11	85	9.84
J1837+2625^e	18 : 37 : 33	26 24 55	55.47	14.57	36.8±3.3	3205±4	281±8	316±12	48	10.30
J1837+1155^e	18 : 37 : 46	11 55 23	42.06	8.43	3.3±1.0	3579±5	73±9	86±14	52	9.33
J1837+2204	18 : 38 : 01	22 04 11 :	51.43 :	12.71 :	···	4099 :	···	···	···	···
J1837+2747	18 : 38 : 01	27 47 45	56.83	15.02	7.1±0.7	3147±4	224±7	255±11	47	9.57
J1838+2522^e	18 : 38 : 39	25 22 22	54.59	13.92	50.5±2.7	3424±2	437±4	452±5	51	10.49
J1839+2210	18 : 39 : 17	22 10 52	51.66	12.49	3.1±0.6	4893±9	185±18	238±27	71	9.57
J1839+1318^e	18 : 39 : 38	13 17 24	43.51	8.62	18.7±1.7	3880±5	123±11	227±16	57	10.15
J1839+2342	18 : 39 : 55	23 43 05	53.15	12.99	2.7±0.7	4767±7	181±15	224±22	70	9.50
J1840+2129	18 : 40 : 16	21 29 35	51.11	12.00	3.6±0.6	4230±4	242±8	258±13	62	9.51
J1840+2441	18 : 40 : 24	24 41 02	54.10	13.28	3.9±0.9	4558±5	246±9	257±14	67	9.61
J1840+2411	18 : 40 : 27	24 12 02	53.66	13.07	6.6±1.0	4013±7	627±14	656±21	59	9.73
J1840+2836	18 : 40 : 38	28 36 16	57.83	14.81	2.7±0.6	3082±6	167±13	197±19	46	9.13
J1840+2341	18 : 40 : 50	23 40 46	53.20	12.78	3.9±0.5	3698±3	158±6	175±9	55	9.44
J1840+2340	18 : 40 : 53	23 40 54	53.21	12.77	6.1±0.8	4804±7	474±14	514±21	70	9.85

Table C.3 (cont'd)

ALFAZOA	RA (J2000.0)	Dec (J2000.0)	l (°)	b (°)	F_{HI} (Jy km s^{-1})	v_{hel} (km s^{-1})	W_{50} (km s^{-1})	W_{20} (km s^{-1})	D_{LG} (Mpc)	$logM_{HI}$ (M$_\odot$)
J1840+2304	18 : 41 : 04	23 04 54	52.67	12.49	2.9±0.6	4111±6	243±12	265±18	60	9.40
J1841+0911^e	18 : 41 : 39	09 12 51	40.04	6.38	6.6±1.1	3256±7	118±14	179±21	48	9.55
J1841+1102	18 : 41 : 56	11 01 42	41.71	7.12	0.8±0.4	1264±7	47±14	70±21	20	7.88
J1841+1435^e	18 : 41 : 58	14 35 46	44.95	8.69	6.5±0.9	4028±4	153±7	179±11	59	9.72
J1842+2453	18 : 42 : 22	24 53 40	54.49	12.96	3.0±0.5	3364±5	163±11	196±16	50	9.25
J1842+1701^e	18 : 42 : 58	17 03 43	47.30	9.54	7.5±1.4	3910±5	82±10	116±15	57	9.77
J1842+2135^e	18 : 43 : 04	21 36 15	51.49	11.45	4.2±0.7	4400±6	224±12	258±17	64	9.62
J1843+1501	18 : 43 : 10	15 01 35	45.47	8.61	2.0±0.3	4259±2	38±5	55±7	62	9.26
J1843+2411^e	18 : 43 : 24	24 10 52	53.92	12.46	3.5±0.7	4009±5	135±11	162±16	59	9.46
J1843+2455	18 : 43 : 29	24 55 25	54.62	12.75	3.1±0.5	3463±3	159±6	171±9	51	9.29
J1843+2010	18 : 43 : 58	20 10 58	50.27	10.66	2.2±0.5	5119±10	153±21	219±31	74	9.46
J1844+2409^e	18 : 44 : 21	24 08 12	53.97	12.24	21.3±1.8	3837±5	369±9	429±14	57	10.21
J1844+2514	18 : 44 : 22	25 15 29	55.02	12.70	2.7±0.6	4634±5	204±11	225±16	68	9.46
J1844+1618	18 : 44 : 36	16 18 46	46.79	8.86	2.7±0.6	4286±7	174±14	206±22	63	9.39
J1844+2147	18 : 45 : 02	21 47 35	51.86	11.12	6.4±0.7	4427±5	257±11	312±16	65	9.80

Table C.3 (cont'd)

ALFAZOA	RA (J2000.0)	Dec (J2000.0)	l (°)	b (°)	F_{HI} (Jy km s^{-1})	v_{hel} (km s^{-1})	W_{50} (km s^{-1})	W_{20} (km s^{-1})	D_{LG} (Mpc)	$logM_{HI}$ (M$_\odot$)
J1845+2124[e]	18 : 45 : 13	21 25 09	51.54	10.92	5.4±0.9	4500±8	246±15	307±23	66	9.74
J1845+2134	18 : 45 : 32	21 35 39	51.73	10.93	3.1±0.6	3335±3	203±7	211±10	49	9.25
J1845+2755	18 : 45 : 35	27 54 53	57.62	13.53	3.7±0.7	4671±4	188±9	205±13	69	9.61
J1846+2231	18 : 46 : 25	22 36 45	52.76	11.18	8.4±0.9	4705±4	324±8	352±12	69	9.97
J1846+2716	18 : 46 : 27	27 16 28	57.10	13.10	1.7±0.5	3409±7	142±14	167±21	51	9.02
J1846+2302	18 : 46 : 40	23 02 53	53.19	11.30	2.5±0.6	4247±4	207±9	218±13	62	9.36
J1846+1542	18 : 46 : 41	15 42 06	46.46	8.14	2.1±0.4	2913±4	172±9	187±13	43	8.97
J1847+1555	18 : 47 : 15	15 55 42	46.72	8.12	2.8±0.6	7275±7	411±15	435±22	105	9.87
J1847+2546	18 : 47 : 18	25 47 31	55.80	12.32	1.7±0.5	3964±12	151±25	212±37	58	9.14
J1847+2256	18 : 48 : 02	22 56 44	53.23	10.97	6.1±0.8	4357±4	424±8	440±12	64	9.77
J1848+2020	18 : 48 : 07	20 20 33	50.84	9.85	0.9±0.4	4906±6	152±11	161±17	72	9.05
J1848+2309	18 : 48 : 43	23 09 37	53.49	10.92	1.3±0.5	4310±3	110±6	113±9	63	9.08
J1848+1655	18 : 48 : 43	16 55 43	47.79	8.24	3.4±0.5	4897±3	158±6	168±9	71	9.60
J1849+1950	18 : 49 : 20	19 50 30	50.51	9.38	2.2±0.4	4914±3	89±7	104±10	72	9.43
J1849+2314	18 : 50 : 03	23 14 51	53.70	10.68	3.1±0.6	4208±5	183±10	200±15	62	9.45

Table C.3 (cont'd)

ALFAZOA	RA (J2000.0)	Dec (J2000.0)	l (°)	b (°)	F_{HI} (Jy km s^{-1})	v_{hel} (km s^{-1})	W_{50} (km s^{-1})	W_{20} (km s^{-1})	D_{LG} (Mpc)	$logM_{HI}$ (M$_\odot$)
J1851+1954	18 : 51 : 47	19 54 14	50.82	8.88	2.2±0.6	3979±10	99±20	166±30	58	9.25
J1851+2634[e]	18 : 51 : 49	26 33 38	56.94	11.71	4.3±0.8	4538±6	282±12	310±18	67	9.66
J1851+2629	18 : 52 : 02	26 28 58	56.89	11.64	5.1±0.9	3748±9	359±18	406±28	56	9.57
J1852+1027	18 : 52 : 57	10 27 56	42.42	4.45	3.7±0.7	4908±4	247±7	257±11	71	9.64
J1852+2255	18 : 53 : 02	22 55 39	53.71	9.93	2.0±0.5	4172±7	167±15	199±22	61	9.24
J1853+0951[e]	18 : 53 : 54	09 51 21	41.98	3.96	14.9±1.6	4731±5	322±10	356±14	69	10.22
J1854+2630	18 : 54 : 13	26 29 47	57.11	11.20	0.9±0.4	3949±6	108±12	118±18	58	8.86
J1854+2438[e]	18 : 54 : 29	24 39 29	55.44	10.37	12.2±1.7	4317±4	315±8	336±13	63	10.07
J1854+1935	18 : 54 : 53	19 34 36	50.84	8.08	2.0±0.5	4096±8	116±15	164±23	60	9.24
J1855+1239	18 : 55 : 47	12 39 54	44.71	4.82	2.8±0.6	4315±6	335±12	355±18	63	9.42
J1855+1426	18 : 55 : 53	14 27 11	46.32	5.60	2.3±0.5	5930±6	196±11	219±17	86	9.61
J1856+2513	18 : 56 : 48	25 13 57	56.20	10.14	2.8±0.6	4401±4	242±7	250±11	65	9.44
J1857+1328	18 : 57 : 54	13 29 55	45.69	4.73	2.5±0.6	8100±4	160±7	170±11	116	9.89
J1857+2558	18 : 58 : 00	25 59 33	57.01	10.22	2.0±0.5	4330±6	81±11	112±17	64	9.29
J1859+1316	18 : 59 : 24	13 16 39	45.65	4.31	3.6±0.6	7282±5	343±9	358±14	105	9.97

Table C.3 (cont'd)

ALFAZOA	RA (J2000.0)	Dec (J2000.0)	l (°)	b (°)	F_{HI} (Jy km s^{-1})	v_{hel} (km s^{-1})	W_{50} (km s^{-1})	W_{20} (km s^{-1})	D_{LG} (Mpc)	$logM_{HI}$ (M$_\odot$)
J1900+1333^e	19 : 00 : 12	13 33 31	45.99	4.26	9.7±1.5	4657±5	241±10	266±15	68	10.02
J1900+2241	19 : 00 : 13	22 40 30	54.20	8.32	3.9±0.5	4049±3	196±5	206±8	60	9.51
J1900+2847	19 : 00 : 59	28 46 42	59.86	10.81	4.0±0.7	4380±6	229±12	262±19	65	9.59
J1901+2747	19 : 01 : 19	27 47 26	58.99	10.32	1.5±0.5	3814±5	76±11	92±16	57	9.06
J1901+2456	19 : 01 : 45	24 56 42	56.42	9.00	3.6±0.7	9307±7	325±14	354±21	134	10.19
J1901+1944	19 : 01 : 47	19 44 48	51.72	6.70	5.8±0.8	3971±5	261±9	285±14	58	9.67
J1901+2647	19 : 01 : 47	26 47 50	58.12	9.80	1.3±0.6	4186±7	116±13	127±20	62	9.08
J1901+2819	19 : 01 : 59	28 20 00	59.55	10.42	2.1±0.5	3921±4	133±9	146±13	58	9.23
J1902+2231	19 : 02 : 29	22 32 19	54.31	7.80	1.0±0.3	4052±6	39±11	67±17	60	8.91
J1902+2717^e	19 : 02 : 49	27 18 25	58.69	9.81	7.8±1.1	4211±2	197±4	204±6	62	9.85
J1903+2213	19 : 03 : 36	22 13 32	54.15	7.42	2.3±0.5	7771±7	146±14	184±22	112	9.83
J1903+2736^e	19 : 03 : 42	27 36 35	59.05	9.76	6.4±1.0	4225±5	372±11	397±16	62	9.77
J1903+2420	19 : 03 : 55	24 21 20	56.11	8.30	2.2±0.5	4444±8	253±16	281±24	65	9.34
J1905+2700^e	19 : 05 : 22	27 00 35	58.67	9.17	3.9±1.0	4736±7	198±13	217±20	70	9.65
J1905+2842	19 : 05 : 33	28 42 32	60.23	9.87	3.0±0.6	7150±4	162±7	174±11	104	9.88

Table C.3 (cont'd)

ALFAZOA	RA (J2000.0)	Dec (J2000.0)	l (°)	b (°)	F_{HI} (Jy km s^{-1})	v_{hel} (km s^{-1})	W_{50} (km s^{-1})	W_{20} (km s^{-1})	D_{LG} (Mpc)	$logM_{HI}$ (M$_\odot$)
J1906+1256	19 : 06 : 23	12 56 28	46.13	2.64	4.4±0.8	2715±5	301±10	317±16	40	9.23
J1906+2328	19 : 07 : 02	23 27 08	55.61	7.26	2.4±0.4	9146±3	278±5	285±8	132	10.00
J1907+1400	19 : 07 : 40	14 01 11	47.23	2.86	1.8±0.6	7296±6	96±13	112±19	105	9.68
J1907+2045	19 : 08 : 02	20 45 31	53.29	5.85	1.4±0.4	3989±4	148±7	153±11	59	9.07
J1909+2648[e]	19 : 09 : 35	26 49 12	58.91	8.24	8.0±1.1	4734±3	278±6	289±9	70	9.96
J1910+2348	19 : 10 : 25	23 49 04	56.29	6.73	1.7±0.6	7324±10	194±19	226±29	106	9.64
J1910+1933	19 : 10 : 26	19 33 04	52.47	4.79	7.0±1.0	3901±4	454±9	467±13	58	9.74
J1911+2112	19 : 11 : 36	21 12 20	54.07	5.31	4.5±0.8	5024±6	396±11	412±17	73	9.76
J1911+2419[e]	19 : 11 : 44	24 21 08	56.90	6.70	10.4±1.3	642±2	116±4	127±7	12	8.54
J1912+1322	19 : 12 : 44	13 23 41	47.24	1.47	4.3±0.5	2776±3	110±5	129±8	41	9.24
J1913+1656[e]	19 : 13 : 57	16 55 44	50.52	2.85	9.5±1.2	6268±7	540±14	580±20	91	10.27
J1914+1523	19 : 14 : 16	15 23 03	49.18	2.07	1.0±0.4	7340±10	44±19	108±29	106	9.43
J1914+1246	19 : 14 : 32	12 47 04	46.91	0.80	3.3±0.7	4633±9	226±17	270±26	68	9.55
J1914+1017[e]	19 : 15 : 05	10 17 36	44.76	−0.47	14.0±1.3	655±2	81±4	104±6	11	8.63
J1915+2008[e]	19 : 15 : 08	20 09 35	53.52	4.09	13.0±1.5	4713±5	522±10	545±14	69	10.17

Table C.3 (cont'd)

ALFAZOA	RA (J2000.0)	Dec (J2000.0)	l (°)	b (°)	F_{HI} (Jy km s^{-1})	v_{hel} (km s^{-1})	W_{50} (km s^{-1})	W_{20} (km s^{-1})	D_{LG} (Mpc)	$logM_{HI}$ (M$_\odot$)
J1915+2254	19 : 15 : 28	22 54 50	56.01	5.29	3.6±0.7	7905±8	406±16	443±25	114	10.04
J1917+0748	19 : 17 : 31	07 48 51 :	42.85 :	−2.16 :	···	3033 :	···	···	···	···
J1917+2030[e]	19 : 17 : 40	20 30 21	54.10	3.72	2.5±0.6	2358±8	101±15	140±23	36	8.88
J1917+2354	19 : 18 : 07	23 54 48	57.18	5.21	2.9±0.6	8108±6	162±12	188±18	117	9.97
J1918+1611	19 : 18 : 55	16 10 11	50.40	1.44	2.6±0.7	6578±9	317±18	352±27	95	9.74
J1919+1403[e]	19 : 20 : 07	14 04 54	48.69	0.21	5.8±1.4	2810±7	156±13	184±20	42	9.38
J1920+1243	19 : 20 : 17	12 44 08	47.51	−0.45	1.9±0.6	5193±6	122±12	139±19	75	9.40
J1921+1453[e]	19 : 21 : 42	14 53 56	49.59	0.25	4.7±0.8	4080±4	78±7	99±11	60	9.60
J1921+0817[e]	19 : 22 : 09	08 18 14	43.82	−2.94	5.1±0.9	3111±7	117±15	185±22	46	9.41
J1922+2434	19 : 22 : 24	24 34 51	58.23	4.65	1.5±0.5	7177±6	220±12	237±18	104	9.59
J1922+1956	19 : 22 : 37	19 56 40	54.14	2.44	1.2±0.5	7966±6	104±12	117±18	115	9.56
J1923+2017[e]	19 : 23 : 44	20 17 27	54.57	2.37	3.0±1.0	3240±10	247±20	270±31	48	9.22
J1923+2334	19 : 23 : 56	23 35 05	57.50	3.88	2.0±0.5	7912±5	80±9	106±14	114	9.80
J1924+2106	19 : 24 : 10	21 05 14	55.33	2.65	0.9±0.4	3104±9	81±18	103±27	46	8.66
J1924+2034	19 : 24 : 24	20 35 44	54.92	2.37	2.5±0.6	9838±7	169±13	197±20	141	10.07

Table C.3 (cont'd)

ALFAZOA	RA (J2000.0)	Dec (J2000.0)	l (°)	b (°)	F_{HI} (Jy km s^{-1})	v_{hel} (km s^{-1})	W_{50} (km s^{-1})	W_{20} (km s^{-1})	D_{LG} (Mpc)	$logM_{HI}$ (M$_\odot$)
J1925+2044	19 : 25 : 09	20 45 42	55.15	2.30	4.4±0.6	8978±4	297±9	319±13	129	10.24
J1925+2159	19 : 25 : 29	22 00 10	56.28	2.82	2.0±0.7	9937±10	170±19	200±29	143	9.99
J1925+1344	19 : 25 : 43	13 45 39	49.05	−1.14	3.6±0.6	6667±7	201±14	238±20	96	9.90
J1925+0815	19 : 26 : 01	08 15 59	44.23	−3.80	1.6±0.6	3071±4	108±8	115±12	45	8.90
J1926+2056	19 : 26 : 06	20 56 53	55.42	2.19	4.0±0.6	7534±4	346±8	365±13	109	10.05
J1927+2804	19 : 27 : 11	28 04 45	61.83	5.34	1.3±0.5	7636±11	143±21	169±32	111	9.57
J1927+1659	19 : 27 : 22	17 01 05	52.10	0.06	2.0±0.8	7912±9	132±17	154±26	114	9.78
J1927+1221	19 : 27 : 39	12 19 57	48.01	−2.23	3.0±0.7	8601±5	172±9	185±14	124	10.03
J1927+2011[e]	19 : 27 : 41	20 11 48	54.93	1.51	13.1±1.3	7136±5	77±11	190±16	103	10.52
J1927+0927	19 : 27 : 56	09 27 46	45.51	−3.66	1.6±0.4	7927±6	75±12	103±18	114	9.68
J1928+1450	19 : 28 : 16	14 51 00	50.30	−1.17	1.4±0.5	4542±15	64±31	149±46	66	9.15
J1928+1956	19 : 28 : 43	19 56 57	54.83	1.17	2.3±0.5	7042±10	227±21	290±31	102	9.75
J1928+1430	19 : 28 : 53	14 30 45	50.07	−1.46	1.5±0.6	4889±8	186±15	207±23	71	9.26
J1929+1537	19 : 29 : 08	15 37 26	51.08	−0.98	1.1±0.4	4281±6	75±13	91±19	63	9.02
J1929+2223	19 : 29 : 16	22 23 55	57.04	2.23	1.0±0.3	11508±8	18±17	100±25	165	9.82

Table C.3 (cont'd)

ALFAZOA	RA (J2000.0)	Dec (J2000.0)	l (°)	b (°)	F_{HI} (Jy km s^{-1})	v_{hel} (km s^{-1})	W_{50} (km s^{-1})	W_{20} (km s^{-1})	D_{LG} (Mpc)	$logM_{HI}$ (M$_\odot$)
J1929+0805[e]	19 : 29 : 22	08 04 01	44.45	−4.63	18.8±2.7	3100±11	254±23	368±34	46	9.97
J1930+1447	19 : 30 : 17	14 50 14	50.52	−1.60	4.0±1.1	9148±14	201±27	289±41	131	10.21
J1930+1211	19 : 30 : 40	12 11 57	48.24	−2.94	3.4±0.7	6681±4	215±7	224±11	96	9.88
J1930+1115	19 : 30 : 42	11 16 03	47.43	−3.39	2.6±0.5	3177±5	118±10	146±15	47	9.14
J1931+0843	19 : 31 : 27	08 43 45	45.28	−4.77	1.7±0.6	5124±7	100±14	118±22	74	9.34
J1932+2248	19 : 32 : 41	22 49 33	57.79	1.75	4.4±0.7	7140±5	197±10	222±14	103	10.05
J1932+1330	19 : 32 : 45	13 30 27	49.64	−2.76	3.6±0.9	4901±6	229±12	246±17	72	9.63
J1932+0824	19 : 33 : 05	08 27 04	45.23	−5.26	2.9±0.6	7563±8	168±16	219±25	109	9.91
J1933+1336	19 : 33 : 42	13 36 28	49.84	−2.91	3.5±0.8	4886±8	291±17	319±25	71	9.62
J1933+1042	19 : 33 : 59	10 42 31	47.32	−4.37	4.5±0.8	5244±6	243±13	279±19	76	9.79
J1935+1211	19 : 35 : 22	12 14 51	48.84	−3.93	1.3±0.5	7338±11	66±22	117±33	106	9.55
J1936+1640	19 : 36 : 15	16 39 49	52.81	−1.97	1.7±0.5	4559±4	121±8	130±12	67	9.26
J1936+0949	19 : 36 : 25	09 49 27	46.83	−5.32	1.6±0.6	3138±7	164±15	181±22	47	8.92
J1937+2317	19 : 37 : 17	23 17 10	58.71	1.04	2.8±0.7	7150±5	174±11	189±16	104	9.84
J1937+1443	19 : 37 : 19	14 43 24	51.24	−3.14	2.5±0.4	4485±3	70±6	87±9	66	9.40

Table C.3 (cont'd)

ALFAZOA	RA (J2000.0)	Dec (J2000.0)	l (°)	b (°)	F_{HI} (Jy km s^{-1})	v_{hel} (km s^{-1})	W_{50} (km s^{-1})	W_{20} (km s^{-1})	D_{LG} (Mpc)	$logM_{HI}$ (M$_\odot$)
J1937+0922[e]	19 : 37 : 51	09 21 16	46.59	−5.86	3.0±0.6	3150±3	73±5	82±8	47	9.19
J1938+1434	19 : 38 : 56	14 33 58	51.29	−3.56	1.3±0.4	4480±9	81±18	127±27	66	9.13
J1939+0849	19 : 39 : 15	08 48 18	46.27	−6.42	6.9±1.1	3115±6	299±13	332±19	46	9.54
J1939+1929	19 : 39 : 37	19 30 07 :	55.68 :	−1.28 :	···	9917 :	···	···	···	···
J1939+1406	19 : 40 : 01	14 06 07	51.02	−4.02	0.8±0.3	11026±7	55±14	90±21	158	9.67
J1940+1548	19 : 40 : 15	15 49 46	52.55	−3.22	1.1±0.4	10616±8	84±16	104±24	152	9.78
J1940+1154	19 : 40 : 50	11 55 25	49.21	−5.25	1.4±0.3	580±3	29±6	46±9	11	7.58
J1940+1005	19 : 41 : 02	10 05 42	47.62	−6.19	0.4±0.2	2363±9	15±17	56±26	36	8.13
J1940+1242	19 : 41 : 02	12 41 48	49.91	−4.92	2.7±0.6	6920±7	240±14	267±21	100	9.81
J1941+2816	19 : 41 : 40	28 16 40	63.55	2.64	3.6±0.5	6767±7	225±14	298±21	99	9.92
J1941+2002	19 : 41 : 45	20 02 28	56.40	−1.45	1.7±0.5	4585±10	122±20	161±31	67	9.25
J1942+2823	19 : 42 : 31	28 23 12	63.73	2.53	1.3±0.3	4590±4	103±8	124±12	68	9.14
J1942+2245	19 : 42 : 34	22 46 29	58.87	−0.27	2.9±0.5	4571±6	178±11	220±17	67	9.49
J1943+2219	19 : 43 : 39	22 20 17	58.61	−0.70	1.3±0.4	3104±4	109±8	118±12	47	8.81
J1944+0818[e]	19 : 44 : 12	08 19 38	46.45	−7.73	8.0±1.3	3219±5	352±10	378±15	48	9.63

Table C.3 (cont'd)

ALFAZOA	RA (J2000.0)	Dec (J2000.0)	l (°)	b (°)	F_{HI} (Jy km s^{-1})	v_{hel} (km s^{-1})	W_{50} (km s^{-1})	W_{20} (km s^{-1})	D_{LG} (Mpc)	$logM_{HI}$ (M$_\odot$)
J1944+2754	19 : 44 : 31	27 53 36	63.53	1.90	2.0±0.4	5648±7	112±13	169±20	83	9.50
J1944+1238	19 : 44 : 36	12 37 36	50.27	−5.71	1.2±0.4	592±5	63±11	80±16	11	7.52
J1945+1433	19 : 45 : 54	14 32 54	52.11	−5.03	3.0±0.5	7316±3	213±7	225±10	106	9.90
J1945+1951[e]	19 : 46 : 02	19 52 22	56.75	−2.41	3.4±0.9	4493±7	85±13	113±20	66	9.55
J1946+2204	19 : 46 : 47	22 04 23	58.74	−1.46	1.0±0.4	4601±5	118±9	125±14	68	9.03
J1947+1156	19 : 47 : 27	11 57 12	50.03	−6.65	0.9±0.3	4954±7	55±13	86±20	72	9.02
J1949+2410[e]	19 : 50 : 00	24 11 10	60.94	−1.03	9.6±1.2	3119±4	253±8	279±12	47	9.70
J1950+2057	19 : 50 : 26	20 58 21	58.22	−2.75	1.3±0.6	4459±6	147±12	154±18	66	9.11
J1950+1055	19 : 50 : 40	10 56 06	49.53	−7.84	1.2±0.4	6861±5	91±9	103±14	99	9.46
J1951+1533	19 : 51 : 11	15 33 41	53.63	−5.64	1.6±0.4	4459±7	56±14	102±21	66	9.20
J1951+2049	19 : 51 : 23	20 50 13	58.22	−3.01	2.3±0.6	8983±4	241±8	249±12	130	9.95
J1952+1429	19 : 52 : 17	14 29 01	52.83	−6.41	0.8±0.2	274±3	38±5	53±8	7	6.90
J1956+1244	19 : 56 : 13	12 43 44	51.78	−8.11	2.4±0.7	6962±9	220±17	249±26	101	9.77
J1956+1238	19 : 56 : 27	12 39 36	51.76	−8.20	0.6±0.3	3118±7	41±15	60±22	47	8.49
J1957+2632	19 : 57 : 44	26 33 21	63.87	−1.31	2.8±0.7	4397±4	219±9	228±13	65	9.45

Table C.3 (cont'd)

ALFAZOA	RA (J2000.0)	Dec (J2000.0)	l (°)	b (°)	F_{HI} (Jy km s^{-1})	v_{hel} (km s^{-1})	W_{50} (km s^{-1})	W_{20} (km s^{-1})	D_{LG} (Mpc)	$logM_{HI}$ (M$_\odot$)
J1958+1608	19 : 58 : 44	16 08 33	55.06	−6.90	2.2±0.7	5726±8	218±16	241±25	83	9.56
J1958+1253	19 : 58 : 52	12 53 56	52.27	−8.59	2.8±0.7	6882±6	250±12	264±18	100	9.82
J1959+1541	19 : 59 : 16	15 41 55	54.74	−7.24	1.3±0.5	4020±4	112±8	119±12	59	9.05
J1959+1531	19 : 59 : 19	15 31 00	54.59	−7.35	1.5±0.4	10153±6	114±12	139±18	146	9.88
J1959+1551	19 : 59 : 20	15 50 58	54.88	−7.18	2.8±0.5	9918±5	225±9	242±14	142	10.12
J1959+1521	19 : 59 : 28	15 21 25	54.47	−7.46	1.3±0.5	2337±9	110±18	133±27	36	8.58
J2000+2202	20 : 00 : 14	22 01 20	60.30	−4.16	3.6±0.6	4462±5	262±10	284±16	66	9.56
J2000+1129	20 : 00 : 22	11 29 55	51.23	−9.62	3.0±0.6	7254±7	196±13	233±20	105	9.89
J2001+2659	20 : 01 : 34	26 59 49	64.70	−1.80	4.9±0.7	3140±4	213±7	231±11	48	9.41
J2001+2736	20 : 02 : 07	27 36 51	65.29	−1.58	1.5±0.4	3199±4	85±8	97±12	48	8.92
J2002+1247	20 : 02 : 43	12 49 15	52.68	−9.44	1.6±0.5	4502±5	79±10	99±14	66	9.22
J2003+2515	20 : 03 : 37	25 15 12	63.46	−3.12	1.9±0.5	3047±3	123±7	129±10	46	8.97
J2003+1345	20 : 03 : 58	13 44 47	53.64	−9.22	3.3±0.8	7349±9	252±18	280±27	106	9.95
J2004+2727	20 : 04 : 17	27 27 58	65.42	−2.07	2.7±0.6	4323±6	221±12	242±17	64	9.41
J2004+1244	20 : 04 : 44	12 44 42	52.87	−9.89	2.1±0.6	4453±12	386±24	431±36	65	9.33

Table C.3 (cont'd)

ALFAZOA	RA (J2000.0)	Dec (J2000.0)	l (°)	b (°)	F_{HI} (Jy km s^{-1})	v_{hel} (km s^{-1})	W_{50} (km s^{-1})	W_{20} (km s^{-1})	D_{LG} (Mpc)	$logM_{HI}$ (M$_\odot$)
J2004+1403^e	20 : 04 : 47	14 07 15	54.07	−9.20	7.3±1.0	4411±3	117±6	130±8	65	9.86
J2007+1243	20 : 07 : 19	12 43 28	53.18	−10.45	2.1±0.7	7353±8	208±17	226±25	106	9.74
J2007+1457	20 : 07 : 35	14 57 35	55.16	−9.34	1.1±0.4	6850±5	59±10	74±16	99	9.41
J2007+2341	20 : 07 : 56	23 41 08	62.66	−4.79	0.8±0.3	2370±10	28±20	92±29	37	8.38
J2008+0937	20 : 08 : 37	09 38 20	50.65	−12.31	2.5±0.6	7498±9	235±18	280±27	108	9.84
J2009+0838	20 : 09 : 05	08 39 31	49.85	−12.90	4.4±0.6	5327±5	203±11	246±16	78	9.79
J2008+0746	20 : 09 : 07	07 47 45	49.09	−13.35	3.7±0.9	5434±6	225±12	246±18	79	9.74
J2011+0829	20 : 12 : 04	09 28 15	50.95	−13.12	1.4±0.4	7543±5	89±10	106±16	109	9.59
J2012+2114	20 : 12 : 13	21 15 18	61.14	−6.93	0.6±0.2	543±5	24±11	53±16	11	7.19
J2015+1317	20 : 15 : 54	13 18 12	54.80	−11.92	1.9±0.5	4388±3	263±7	269±10	65	9.28
J2015+1240^e	20 : 15 : 55	12 41 21	54.27	−12.26	3.4±0.4	1950±2	52±4	73±6	30	8.87
J2017+1614	20 : 17 : 36	16 14 16	57.56	−10.71	3.0±0.6	4361±3	298±6	304±9	64	9.47
J2017+2837^e	20 : 17 : 39	28 37 07	67.99	−3.91	6.2±1.1	4236±5	230±10	255±15	63	9.76
J2017+2217	20 : 18 : 00	22 17 34	62.75	−7.49	1.3±0.5	9972±7	149±14	164±21	144	9.80
J2018+1616	20 : 18 : 45	16 17 39	57.76	−10.91	2.0±0.5	4353±6	179±12	195±17	64	9.29

Table C.3 (cont'd)

ALFAZOA	RA (J2000.0)	Dec (J2000.0)	l (°)	b (°)	F_{HI} (Jy km s^{-1})	v_{hel} (km s^{-1})	W_{50} (km s^{-1})	W_{20} (km s^{-1})	D_{LG} (Mpc)	$logM_{HI}$ (M$_\odot$)
J2018+2319[e]	20 : 18 : 50	23 19 54	63.73	−7.07	1.4±0.4	299±4	26±8	48±11	7	7.28
J2018+1637	20 : 18 : 54	16 37 52	58.06	−10.76	1.7±0.4	8644±9	80±19	158±28	125	9.79
J2018+2323	20 : 18 : 59	23 25 39	63.83	−7.05	0.9±0.3	11837±6	37±12	63±18	170	9.77
J2019+1526	20 : 19 : 12	15 27 22	57.10	−11.46	1.0±0.3	7629±6	94±13	120±19	110	9.46
J2020+0747	20 : 20 : 18	07 47 43 :	50.55 :	−15.73 :	···	4834 :	···	···	···	···
J2020+2700	20 : 20 : 19	27 00 29	66.99	−5.30	1.5±0.4	1845±4	107±8	118±12	29	8.47
J2020+1452	20 : 20 : 26	14 53 10	56.77	−12.01	3.6±0.6	7118±4	256±9	270±13	103	9.96
J2022+1236	20 : 22 : 22	12 35 57	55.05	−13.64	1.4±0.4	4368±5	116±9	133±14	64	9.13
J2023+0831	20 : 23 : 57	08 32 24	51.70	−16.11	6.1±0.8	4705±4	210±7	228±11	69	9.83
J2023+1223	20 : 24 : 06	12 22 38	55.09	−14.11	2.0±0.6	4562±4	225±9	234±13	67	9.33
J2024+1235	20 : 24 : 30	12 34 59	55.32	−14.08	6.4±1.0	4531±7	278±14	319±22	67	9.83
J2024+1225[e]	20 : 24 : 40	12 26 44	55.23	−14.19	17.4±1.6	4499±6	425±13	503±19	66	10.26
J2025+1223	20 : 25 : 16	12 23 49	55.26	−14.34	2.1±0.6	5557±6	105±11	123±17	81	9.50
J2027+0806	20 : 27 : 34	08 06 01	51.80	−17.11	4.7±0.8	4697±5	311±10	327±15	69	9.72
J2027+1045	20 : 27 : 44	10 46 03	54.18	−15.73	6.5±1.0	5319±10	315±19	385±29	78	9.97

Table C.3 (cont'd)

ALFAZOA	RA (J2000.0)	Dec (J2000.0)	l (°)	b (°)	F_{HI} (Jy km s^{-1})	v_{hel} (km s^{-1})	W_{50} (km s^{-1})	W_{20} (km s^{-1})	D_{LG} (Mpc)	$logM_{HI}$ (M$_\odot$)
J2027+1329	20 : 28 : 01	13 30 28	56.60	−14.30	2.6±0.7	1990±11	88±22	164±33	31	8.77
J2028+2222	20 : 28 : 12	22 23 37	64.17	−9.39	3.0±0.7	10322±13	409±26	486±39	149	10.19
J2028+1044	20 : 28 : 25	10 45 19	54.26	−15.87	8.3±0.9	4226±6	432±13	478±19	62	9.88
J2028+2547	20 : 28 : 42	25 48 14	67.06	−7.53	1.3±0.4	4352±7	67±15	96±22	65	9.13
J2029+1040	20 : 29 : 08	10 40 33	54.29	−16.06	6.8±1.1	4787±6	385±12	408±18	70	9.90
J2028+2047	20 : 29 : 08	20 47 41	62.95	−10.47	0.5±0.3	10134±6	30±13	47±19	146	9.43
J2029+2233	20 : 30 : 00	22 33 16	64.54	−9.64	3.7±0.8	7219±8	421±16	448±24	105	9.99
J2030+2011	20 : 30 : 37	20 11 51	62.66	−11.10	1.7±0.4	3649±8	91±15	137±23	55	9.07
J2030+2204	20 : 30 : 38	22 03 15	64.21	−10.04	1.8±0.5	4242±5	81±10	101±15	63	9.22
J2030+2017[e]	20 : 30 : 57	20 17 42	62.78	−11.10	5.9±0.9	3686±4	234±8	249±12	55	9.62
J2032+2559[e]	20 : 32 : 31	25 59 28	67.72	−8.12	7.0±1.1	339±3	64±6	87±9	8	8.05
J2036+2052	20 : 36 : 37	20 49 41	64.00	−11.89	0.8±0.2	7128±4	33±8	56±12	104	9.29
J2036+2459	20 : 36 : 57	24 59 52	67.49	−9.51	0.7±0.3	5331±3	52±7	57±10	79	8.99
J2037+2649	20 : 37 : 21	26 49 25	69.04	−8.51	1.2±0.3	1538±5	83±10	101±15	25	8.24
J2038+2408	20 : 38 : 29	24 07 52	66.99	−10.30	1.0±0.4	10330±6	46±13	70±19	149	9.70

Table C.3 (cont'd)

ALFAZOA	RA (J2000.0)	Dec (J2000.0)	l (°)	b (°)	F_{HI} (Jy km s^{-1})	v_{hel} (km s^{-1})	W_{50} (km s^{-1})	W_{20} (km s^{-1})	D_{LG} (Mpc)	$logM_{HI}$ (M$_\odot$)
J2043+2236	20 : 44 : 06	22 37 04	66.53	−12.24	0.6±0.3	1756±3	59±6	63±10	28	8.05
J2044+2215	20 : 45 : 00	22 14 48	66.35	−12.63	2.7±0.7	4410±7	164±15	191±22	66	9.43
J2045+2811	20 : 45 : 46	28 10 26	71.27	−9.19	3.0±0.5	1098±3	69±6	91±10	19	8.41
J2046+2144	20 : 46 : 21	21 45 26	66.14	−13.17	0.9±0.4	568±6	81±12	94±18	11	7.46
J2047+2225[e]	20 : 47 : 26	22 26 16	66.85	−12.96	2.3±0.6	4415±7	115±15	143±22	66	9.38
J2047+2451	20 : 47 : 37	24 52 44	68.87	−11.52	1.4±0.4	4295±5	91±10	108±15	64	9.14
J2047+2048	20 : 47 : 42	20 48 39	65.55	−13.99	1.5±0.4	10614±7	94±13	127±20	153	9.93
J2050+2538	20 : 50 : 37	25 37 56	69.90	−11.60	2.3±0.7	2376±3	150±7	156±10	37	8.88
J2051+2454	20 : 51 : 22	24 54 16	69.42	−12.18	3.1±0.7	10742±7	229±14	254±20	155	10.24
J2052+2242	20 : 52 : 28	22 41 49	67.79	−13.73	1.2±0.4	3527±8	82±15	117±23	53	8.91
J2052+2810	20 : 52 : 55	28 09 27	72.24	−10.44	0.4±0.2	4770±4	30±8	38±11	71	8.62
J2054+2555	20 : 54 : 37	25 56 01	70.71	−12.12	2.2±0.5	6910±4	264±8	270±11	101	9.72
J2054+2401[e]	20 : 55 : 04	24 01 31	69.24	−13.39	4.4±0.6	3523±5	107±10	164±15	53	9.47
J2056+2600	20 : 56 : 36	25 59 55	71.05	−12.43	1.4±0.5	6865±5	133±10	143±14	100	9.51
J2056+2557	20 : 56 : 52	25 57 22	71.05	−12.50	1.4±0.4	4745±4	109±9	119±13	70	9.21

Table C.3 (cont'd)

ALFAZOA	RA (J2000.0)	Dec (J2000.0)	l (°)	b (°)	F_{HI} (Jy km s^{-1})	v_{hel} (km s^{-1})	W_{50} (km s^{-1})	W_{20} (km s^{-1})	D_{LG} (Mpc)	$logM_{HI}$ (M$_\odot$)
J2056+2554	20 : 57 : 06	25 56 08	71.07	−12.56	2.7±0.6	1524±5	262±10	275±15	25	8.60
J2057+2557[e]	20 : 57 : 22	25 57 54	71.13	−12.58	21.4±1.7	1521±2	260±4	276±6	25	9.50
J2057+2537	20 : 57 : 56	25 38 10	70.95	−12.89	3.3±0.6	4765±5	249±10	265±16	71	9.59
J2058+1950	20 : 59 : 02	19 50 49	66.43	−16.69	1.9±0.5	7027±3	139±6	145±8	102	9.66
J2100+2122	21 : 00 : 55	21 22 11	67.96	−16.09	1.7±0.6	3367±10	250±20	275±30	51	9.01
J2102+2511	21 : 02 : 51	25 11 49	71.33	−14.03	1.4±0.3	3123±3	39±6	58±9	48	8.86
J2105+2423	21 : 05 : 18	24 23 07	71.05	−14.97	2.9±0.7	4759±3	300±7	305±10	71	9.53
J2105+2708	21 : 05 : 44	27 10 24	73.31	−13.25	1.8±0.5	984±10	178±21	248±31	18	8.11
J2106+2531	21 : 06 : 19	25 51 38	72.37	−14.20	4.0±0.7	2552±6	169±12	201±18	40	9.17

Table C.4. ALFA ZOA Shallow Survey A+D Catalog.

ALFAZOA	RA (J2000.0)	Dec (J2000.0)	l (°)	b (°)	F_{HI} (Jy km s^{-1})	v_{hel} (km s^{-1})	W_{50} (km s^{-1})	W_{20} (km s^{-1})	D_{LG} (Mpc)	$logM_{HI}$ (M$_\odot$)
J1728+0722	17 27 48	+07 26 04	30.08	21.96	4.0±0.6	1678±6	137±12	195±19	25	8.8
J1728−0013	17 28 01	–00 12 06	22.89	18.37	2.4±0.6	2130±3	58±7	70±10	31	8.7
J1728+0723	17 28 12	+07 25 01	30.11	21.86	26.2±1.4	1695±1	128±2	146±4	25	9.6
J1732+0705	17 32 24	+07 03 24	30.26	20.77	115.2±1.9	1661±1	367±1	386±2	25	10.2
J1733+0528	17 33 56	+05 28 13	28.93	19.72	14.1±1.0	2837±2	168±4	190±5	41	9.8
J1734+0649	17 34 22	+06 50 33	30.28	20.24	4.5±0.5	6429±7	170±14	274±21	93	10.0
J1735+0656	17 35 50	+06 58 10	30.58	19.97	5.0±0.4	6537±2	243±4	261±6	94	10.0
J1738+0300	17 38 43	+03 00 23	27.19	17.53	1.9±0.6	10029±8	52±17	104±25	144	10.0
J1740+0646	17 40 12	+06 45 56	30.89	18.91	2.3±0.3	6948±5	178±10	218±15	100	9.7
J1741+0255	17 41 06	+02 57 29	27.43	16.98	1.6±0.3	2197±3	73±7	88±10	32	8.6
J1742+0312	17 42 05	+03 12 02	27.78	16.87	2.3±0.5	8535±6	149±11	175±17	123	9.9
J1742+0312	17 42 14	+03 12 06	27.80	16.84	5.8±0.6	6797±5	432±10	469±15	98	10.1
J1742+0724	17 43 01	+07 24 43	31.83	18.57	2.5±0.3	9101±2	56±5	75±7	131	10.0
J1746+0207	17 46 18	+02 06 18	27.27	15.44	4.4±0.4	3021±3	150±6	178±9	44	9.3
J1753+0344	17 52 59	+03 45 11	29.58	14.71	2.0±0.5	1124±10	97±19	172±29	17	8.1

Table C.4 (cont'd)

ALFAZOA	RA (J2000.0)	Dec (J2000.0)	l (°)	b (°)	F_{HI} (Jy km s^{-1})	v_{hel} (km s^{-1})	W_{50} (km s^{-1})	W_{20} (km s^{-1})	D_{LG} (Mpc)	$logM_{HI}$ (M$_\odot$)
J1754+0610	17 54 20	+06 11 52	32.00	15.51	3.2±0.4	2925±3	93±7	131±10	43	9.1
J1754+0251	17 54 36	+02 52 43	28.97	13.95	23.0±0.9	1751±1	169±3	206±4	26	9.6
J1758+0343	17 58 12	+03 42 14	30.14	13.53	3.0±0.6	7856±3	33±6	52±9	113	10.0
J1758+0041	17 58 59	+00 41 08	27.49	11.97	5.2±0.4	3899±3	55±6	144±10	57	9.6
J1759+0616	17 59 29	+06 17 00	32.67	14.40	49.3±1.3	1807±1	249±2	284±4	27	9.9
J1759+0706	17 59 31	+07 07 25	33.45	14.77	5.6±0.3	1904±3	139±7	225±10	28	9.0
J1759+0623	17 59 42	+06 24 00	32.80	14.41	1.3±0.4	1654±6	70±13	101±19	25	8.3
J1801+0657	18 01 53	+06 57 40	33.57	14.17	107.4±1.6	1956±1	317±1	342±2	29	10.3
J1802+0700	18 02 12	+06 59 51	33.64	14.11	24.3±0.5	1962±1	309±2	342±3	29	9.7
J1803+0722	18 03 49	+07 22 33	34.17	13.92	2.3±0.3	1801±4	73±8	117±12	27	8.6
J1808+0459	18 08 18	+04 59 48	32.49	11.87	1.4±0.3	6553±4	35±8	68±12	95	9.5
J1809−0040	18 09 34	–00 40 13	27.51	9.00	2.6±0.5	7150±4	139±9	158±13	103	9.8
J1810+0134	18 10 24	+01 35 03	29.64	9.85	8.2±1.1	1799±3	171±7	196±10	27	9.1
J1810−0104	18 10 46	–01 05 33	27.28	8.53	4.5±0.5	2110±3	143±6	162±8	31	9.0
J1811−0004	18 11 30	–00 04 14	28.28	8.84	2.9±0.5	1690±3	130±6	145±9	25	8.6

Table C.4 (cont'd)

ALFAZOA	RA (J2000.0)	Dec (J2000.0)	l (°)	b (°)	F_{HI} (Jy km s^{-1})	v_{hel} (km s^{-1})	W_{50} (km s^{-1})	W_{20} (km s^{-1})	D_{LG} (Mpc)	$logM_{HI}$ (M$_\odot$)
J1817+0621	18 17 50	+06 22 23	34.83	10.36	4.3±0.5	6048±4	172±7	198±11	88	9.9
J1819+0109	18 19 25	+01 09 59	30.31	7.65	13.1±0.4	2578±1	122±2	151±3	38	9.6
J1823+0015	18 23 26	+00 16 01	29.97	6.35	15.5±0.7	2897±1	140±2	154±3	42	9.8
J1826+0134	18 26 31	+01 34 41	31.49	6.26	5.1±0.5	2755±2	147±5	166±7	41	9.3
J1826+0302	18 26 41	+03 02 57	32.83	6.90	3.4±0.3	2935±3	53±6	111±9	43	9.2
J1828+0243	18 28 33	+02 42 30	32.74	6.32	3.8±0.5	6626±4	110±7	149±11	96	9.9
J1830+0607	18 30 58	+06 07 28	36.08	7.33	5.0±0.4	2883±2	116±5	149±7	43	9.3
J1832+0625	18 32 15	+06 24 36	36.48	7.17	9.7±0.7	2818±2	91±4	119±6	42	9.6
J1833+0333	18 33 23	+03 33 38	34.05	5.64	4.7±0.4	5253±4	213±7	252±11	76	9.8
J1847+0402	18 47 17	+04 02 39	36.06	2.77	3.9±0.4	2753±4	148±9	194±13	41	9.2
J1850+3358	18 50 45 :	+33 58 38 :	63.83 :	14.89 :	···	5230 :	···	···	···	···
J1851+3325	18 51 56	+33 25 22	63.40	14.45	6.2±0.4	2985±1	100±3	116±4	46	9.5
J1852+3350	18 52 31	+33 49 58	63.84	14.50	4.0±0.4	2948±3	184±7	221±10	45	9.3
J1853+3304	18 53 17	+33 04 39	63.19	14.06	5.4±0.5	5125±2	174±4	190±6	76	9.9
J1856+2845	18 56 49	+28 45 09	59.46	11.60	3.8±0.5	6121±5	192±10	232±15	90	9.9

Table C.4 (cont'd)

ALFAZOA	RA (J2000.0)	Dec (J2000.0)	l (°)	b (°)	F_{HI} (Jy km s^{-1})	v_{hel} (km s^{-1})	W_{50} (km s^{-1})	W_{20} (km s^{-1})	D_{LG} (Mpc)	$logM_{HI}$ (M$_\odot$)
J1857+3713	18 57 03	+37 14 31	67.46	14.99	2.9±0.6	6907±7	143±13	178±20	102	9.9
J1859+0013	18 58 59	+00 14 08	34.00	–1.57	2.1±0.4	6166±2	30±4	46±7	90	9.6
J1859+3318	18 59 01	+33 19 08	63.91	13.05	4.5±0.3	4505±2	184±4	207±6	67	9.7
J1900+2847	19 00 40	+28 47 42	59.86	10.85	5.7±0.5	4393±3	268±6	295±9	66	9.8
J1901+0651	19 01 36	+06 51 02	40.19	0.87	24.0±0.8	2936±1	65±2	102±3	44	10.0
J1904+0301	19 04 13	+03 01 50	37.09	–1.46	4.7±0.3	3283±1	76±3	102±4	49	9.4
J1904+0316	19 04 36	+03 16 02	37.34	–1.43	3.4±0.5	3142±5	191±10	225±16	47	9.2
J1904+0316	19 04 41	+03 15 34	37.34	–1.46	2.2±0.4	3079±5	65±9	97±14	46	9.0
J1905+2842	19 05 28	+28 42 37	60.24	9.86	3.7±0.4	7151±5	141±11	211±16	105	10.0
J1906+2858	19 06 36	+28 59 14	60.60	9.76	0.7±0.4	3733±5	50±11	60±16	56	8.7
J1906+0057	19 06 42	+00 56 56	35.52	–2.96	2.2±0.5	6238±9	96±18	159±26	91	9.6
J1906+0734	19 06 44	+07 34 42	41.42	0.07	3.2±0.4	3063±6	177±12	251±18	46	9.2
J1907+2900	19 07 06	+29 00 33	60.67	9.67	20.3±1.1	3904±3	409±6	457±9	59	10.2
J1907−0057	19 07 50	–00 57 06	33.96	–4.08	4.6±0.5	5048±7	151±14	264±21	74	9.8
J1908+0559	19 08 24	+05 59 18	40.19	–1.02	3.7±0.4	4560±3	183±6	204±9	67	9.6

Table C.4 (cont'd)

ALFAZOA	RA (J2000.0)	Dec (J2000.0)	l (°)	b (°)	F_{HI} (Jy km s^{-1})	v_{hel} (km s^{-1})	W_{50} (km s^{-1})	W_{20} (km s^{-1})	D_{LG} (Mpc)	$logM_{HI}$ (M$_\odot$)
J1909+3416	19 09 03	+34 16 55	65.70	11.56	2.1±0.4	6168±5	105±10	130±14	91	9.6
J1910+2857	19 10 03	+28 57 40	60.91	9.07	2.8±0.4	3998±3	105±7	134±10	60	9.4
J1910+0031	19 10 26	+00 31 55	35.58	–3.98	21.4±1.0	1487±1	188±2	211±4	23	9.4
J1910+3339	19 10 31	+33 41 03	65.28	11.03	4.4±0.5	6213±3	216±6	235±9	92	9.9
J1912+0317	19 12 30	+03 17 56	38.28	–3.17	3.5±0.5	8743±4	260±7	276±11	127	10.1
J1913+2836	19 13 28	+28 34 49	60.90	8.23	2.5±0.7	9922±7	107±15	148±22	145	10.1
J1914+2958	19 14 23	+29 58 53	62.26	8.67	5.2±0.5	3970±2	220±5	239±7	60	9.6
J1915+3734	19 16 02	+37 34 06	69.35	11.68	3.0±0.3	5142±6	59±11	162±17	77	9.6
J1917+3325	19 17 15	+33 26 06	65.67	9.66	3.7±0.3	4452±7	134±14	314±21	67	9.6
J1917+0749	19 17 27	+07 49 15	42.86	–2.17	6.5±0.5	3021±2	231±4	249±6	45	9.5
J1917−0101	19 17 38	–01 01 13	35.02	–6.29	3.5±0.6	1796±3	184±6	200±10	27	8.8
J1917+0425	19 17 41	+04 25 57	39.88	–3.79	8.8±0.3	6312±3	373±6	459±9	92	10.2
J1917+3451	19 17 45	+34 51 38	67.02	10.19	1.9±0.3	4384±5	67±10	111±15	66	9.3
J1918+3449	19 18 22	+34 50 16	67.05	10.07	20.8±0.8	4460±3	263±6	352±8	67	10.3
J1920+3050	19 20 30	+30 49 32	63.62	7.88	8.2±0.4	3941±2	188±4	221±6	59	9.8

Table C.4 (cont'd)

ALFAZOA	RA (J2000.0)	Dec (J2000.0)	l (°)	b (°)	F_{HI} (Jy km s^{-1})	v_{hel} (km s^{-1})	W_{50} (km s^{-1})	W_{20} (km s^{-1})	D_{LG} (Mpc)	$logM_{HI}$ (M$_\odot$)
J1920+0016	19 20 32	+00 16 42	36.51	–6.34	4.8±0.4	1270±2	143±4	162±6	20	8.7
J1923+2837	19 23 37	+28 37 03	61.96	6.26	1.6±0.5	6677±6	99±12	117±18	99	9.6
J1923+3337	19 23 54	+33 37 36	66.47	8.51	2.7±0.4	7863±7	163±14	229±22	116	9.9
J1926+0255	19 26 02	+02 56 56	39.53	–6.33	3.1±0.4	6297±4	166±7	191±11	92	9.8
J1926+0200	19 26 52	+02 00 38	38.79	–6.95	8.7±0.4	6352±2	359±4	386±6	93	10.2
J1929+3030	19 29 42	+30 29 38	64.25	5.97	6.4±0.4	8929±1	28±2	46±3	131	10.4
J1930+3546	19 30 36	+35 47 04	69.05	8.27	9.8±0.9	4555±2	166±4	181±7	68	10.0
J1931+3552	19 31 28	+35 53 16	69.22	8.16	5.9±0.5	4425±2	391±5	401±7	67	9.8
J1931+3209	19 31 47	+32 10 57	65.96	6.37	1.3±0.4	4393±5	51±10	68±14	66	9.1
J1932+0702	19 32 33	+07 02 53	43.94	–5.83	2.2±0.5	7232±9	136±19	196±28	105	9.8
J1933+3326	19 33 12	+33 26 29	67.21	6.70	1.2±0.3	2066±6	33±12	70±17	33	8.5
J1933−0038	19 33 17	–00 38 05	37.17	–9.59	8.5±0.6	1421±2	70±4	101±5	22	9.0
J1933+3550	19 33 28	+35 50 08	69.37	7.78	8.1±0.3	4442±2	304±4	345±5	67	9.9
J1933−0032	19 33 51	–01 20 31	36.60	–10.04	5.0±0.5	3496±7	172±14	283±21	52	9.5
J1934+3432	19 34 10	+34 34 46	68.32	7.06	2.2±0.3	4501±5	45±9	136±14	68	9.4

Table C.4 (cont'd)

ALFAZOA	RA (J2000.0)	Dec (J2000.0)	l (°)	b (°)	F_{HI} (Jy km s^{-1})	v_{hel} (km s^{-1})	W_{50} (km s^{-1})	W_{20} (km s^{-1})	D_{LG} (Mpc)	$logM_{HI}$ (M$_\odot$)
J1934+2940	19 34 23	+29 40 33	64.01	4.69	1.3±0.4	3319±7	95±15	125±22	51	8.9
J1935+0639	19 35 31	+06 39 20	43.94	–6.67	3.5±0.4	5930±3	120±6	146±9	87	9.8
J1935+0033	19 35 41	+00 35 10	38.55	–9.56	2.7±0.6	2461±8	153±17	206±25	37	8.9
J1936+3747	19 36 14 :	+37 47 27 :	71.37 :	8.21 :	···	8690 :	···	···	···	···
J1936−0058	19 36 52	–00 58 17	37.29	–10.54	4.9±0.7	6356±5	264±10	292±15	93	10.0
J1937+3035	19 37 43	+30 35 05	65.15	4.49	4.9±0.3	7034±5	229±10	350±16	104	10.1
J1938+0731	19 38 44	+07 31 55	45.10	–6.95	8.0±0.9	3132±4	176±7	207±11	47	9.6
J1940+0040	19 40 25	+00 41 30	39.21	–10.56	2.4±0.4	1286±4	70±8	111±12	20	8.4
J1940+2922	19 40 31	+29 22 27	64.39	3.37	3.2±0.5	7653±4	95±9	133±13	113	10.0
J1941+0151	19 41 20	+01 51 57	40.37	–10.21	2.4±0.5	5887±4	98±9	120±13	86	9.6
J1942−0003	19 42 45	–00 02 35	38.82	–11.42	4.4±0.4	5742±2	146±5	164±7	84	9.9
J1943+0319	19 43 14	+03 19 02	41.90	–9.95	2.1±0.5	1736±5	90±10	117±16	27	8.6
J1943−0111	19 43 23	–01 11 20	37.86	–12.09	4.5±0.6	1419±4	178±8	208±13	22	8.7
J1949+3111	19 49 01	+31 12 24	66.90	2.69	4.3±0.7	5159±4	217±8	237±12	77	9.8
J1949+0330	19 49 14	+03 30 08	42.79	–11.17	3.5±0.3	7362±6	130±12	255±18	107	10.0

Table C.4 (cont'd)

ALFAZOA	RA (J2000.0)	Dec (J2000.0)	l (°)	b (°)	F_{HI} (Jy km s^{-1})	v_{hel} (km s^{-1})	W_{50} (km s^{-1})	W_{20} (km s^{-1})	D_{LG} (Mpc)	$logM_{HI}$ (M$_\odot$)
J1949+0709	19 49 19	+07 09 34	46.05	–9.43	17.2±1.3	3147±3	274±5	296±8	47	10.0
J1950+0008	19 50 34	+00 08 57	39.93	–13.06	2.0±0.4	606±5	102±10	135±15	11	7.7
J1950+0208	19 50 35	+02 08 43	41.73	–12.12	1.7±0.4	5059±6	74±11	106±17	74	9.3
J1951+0418	19 51 14	+04 19 08	43.76	–11.22	4.4±0.6	5948±2	180±5	190±7	87	9.9
J1951+2835	19 51 50 :	+28 35 17 :	64.95 :	0.84 :	···	2300 :	···	···	···	···
J1951+0130	19 51 59	+01 31 15	41.34	–12.72	5.6±0.6	1266±4	89±9	154±13	20	8.7
J1952+0445	19 52 05	+04 46 23	44.27	–11.19	7.4±0.8	5811±3	313±7	334±10	85	10.1
J1952+3437	19 52 32	+34 36 48	70.21	3.79	6.1±0.3	4080±2	207±5	248±7	62	9.7
J1953+3217	19 53 01	+32 17 15	68.26	2.51	2.4±0.3	4493±4	92±7	126±11	68	9.4
J1953+3021	19 53 28	+30 21 33	66.66	1.44	14.3±1.2	4456±3	326±6	353±9	67	10.2
J1954+3037	19 54 04	+30 37 58	66.96	1.47	4.3±0.4	4710±3	146±5	172±8	71	9.7
J1954+0551	19 55 06	+05 53 18	45.64	–11.30	19.1±1.1	3304±2	181±4	212±6	49	10.0
J1955+0552	19 55 18	+05 57 15	45.72	–11.31	6.2±0.4	3309±3	175±6	219±8	50	9.6
J1955+0210	19 55 39	+02 10 33	42.38	–13.22	6.4±0.5	7608±3	161±7	215±10	111	10.3
J1956+2935	19 56 24	+29 35 15	66.32	0.50	9.2±0.3	3476±1	189±2	214±3	53	9.8

Table C.4 (cont'd)

ALFAZOA	RA (J2000.0)	Dec (J2000.0)	l (°)	b (°)	F_{HI} (Jy km s^{-1})	v_{hel} (km s^{-1})	W_{50} (km s^{-1})	W_{20} (km s^{-1})	D_{LG} (Mpc)	$logM_{HI}$ (M$_\odot$)
J1958+0236	19 57 00	+02 43 07	43.03	–13.25	3.9±0.4	7562±3	154±6	176±9	110	10.1
J1957+0553	19 57 18	+05 53 30	45.91	–11.78	29.4±1.0	3245±2	467±4	519±6	49	10.2
J1957−0014	19 57 38	–00 14 11	40.43	–14.80	7.7±0.4	6794±2	217±4	243±6	99	10.3
J1958+0236	19 58 39	+02 36 10	43.13	–13.67	12.9±0.6	7562±1	157±3	178±4	110	10.6
J2000+3632	20 01 16	+36 32 38	72.79	3.27	1.8±0.6	531±8	75±17	110±25	11	7.7
J2002+3400	20 02 15	+34 00 30	70.74	1.76	1.1±0.4	2158±6	88±11	104±17	34	8.5
J2002+0746	20 02 27	+07 46 10	48.23	–11.96	3.9±0.2	5605±1	131±3	146±4	83	9.8
J2003+3121	20 03 35	+31 22 12	68.65	0.12	5.1±0.4	4063±3	225±6	259±10	62	9.7
J2004+0725	20 04 22	+07 24 54	48.16	–12.55	15.3±0.9	5932±2	122±4	159±6	87	10.4
J2006+3504	20 06 38	+35 05 17	72.13	1.57	34.1±0.9	686±1	117±1	138±2	13	9.2
J2008+3052	20 08 28	+30 52 56	68.80	–1.02	1.5±0.5	410±5	61±10	78±15	9	7.5
J2008+3155	20 08 51	+31 56 04	69.73	–0.52	4.0±0.4	4100±4	148±8	201±13	62	9.6
J2008+0630	20 08 56 :	+06 30 52 :	47.94 :	–13.98 :	···	7360 :	···	···	···	···
J2010+2903	20 10 52	+29 03 53	67.56	–2.45	11.0±0.5	3163±1	117±3	155±4	49	9.8
J2012+3247	20 12 33	+32 47 30	70.88	–0.71	16.3±1.1	4247±2	70±3	99±5	64	10.2

Table C.4 (cont'd)

ALFAZOA	RA (J2000.0)	Dec (J2000.0)	l (°)	b (°)	F_{HI} (Jy km s^{-1})	v_{hel} (km s^{-1})	W_{50} (km s^{-1})	W_{20} (km s^{-1})	D_{LG} (Mpc)	$logM_{HI}$ (M$_\odot$)
J2013+2901	20 13 55	+29 01 48	67.90	–3.03	15.8±1.1	4227±4	172±9	268±13	64	10.2
J2015+2929	20 15 54	+29 29 59	68.53	–3.12	7.4±0.6	4240±6	215±12	336±18	64	9.9
J2016+3428	20 16 17	+34 28 17	72.71	–0.42	17.0±0.9	4100±2	204±3	227±5	62	10.2
J2017+3150	20 17 02	+31 49 59	70.60	–2.03	21.3±1.0	1234±2	280±3	301±5	21	9.4
J2020+2949	20 20 55	+29 50 15	69.42	–3.84	7.9±0.4	3161±1	52±2	78±3	49	9.6
J2021+3019	20 21 04	+30 20 15	69.85	–3.58	2.3±0.5	6132±4	110±7	126±11	91	9.7
J2022+3123	20 22 44	+31 23 24	70.93	–3.28	2.9±0.3	1165±6	98±12	197±18	20	8.4
J2029+3120	20 29 50	+31 20 06	71.75	–4.55	16.3±0.7	1041±1	136±2	155±3	19	9.1
J2032+3236	20 32 08	+32 35 54	73.07	–4.20	12.2±1.0	3224±3	66±6	137±10	50	9.9
J2032+3255	20 32 11	+32 56 10	73.35	–4.01	25.2±1.3	4148±3	315±5	358±8	63	10.4
J2033+3234	20 33 20	+32 35 11	73.21	–4.41	3.7±0.3	3245±2	56±5	103±7	50	9.3
J2043+3117	20 43 37	+31 17 42	73.49	–6.93	5.6±0.3	4144±2	152±5	207±7	63	9.7
J2040+3619	20 44 39	+36 23 13	77.66	–3.97	2.9±0.3	7629±5	60±10	196±15	113	9.9
J2045+3030	20 45 21	+30 29 41	73.09	–7.72	6.6±0.3	4214±3	224±6	304±8	64	9.8
J2045+3058	20 45 50	+30 58 29	73.53	–7.50	1.4±0.4	4265±4	100±8	110±12	65	9.1

Table C.4 (cont'd)

ALFAZOA	RA (J2000.0)	Dec (J2000.0)	l (°)	b (°)	F_{HI} (Jy km s^{-1})	v_{hel} (km s^{-1})	W_{50} (km s^{-1})	W_{20} (km s^{-1})	D_{LG} (Mpc)	$logM_{HI}$ (M$_\odot$)
J2048+3737	20 46 56	+37 34 57	78.88	–3.58	3.0±0.6	7941±11	177±22	257±33	117	10.0
J2049+3421	20 49 27	+34 22 05	76.68	–5.99	2.6±0.4	6252±7	103±14	183±21	93	9.7
J2050+2959	20 50 00	+29 59 38	73.31	–8.82	12.2±0.7	731±1	66±3	99±4	14	8.8
J2050+2946	20 50 27	+29 45 49	73.19	–9.03	17.4±0.7	716±1	60±2	86±3	14	8.9
J2054+3714	20 54 23	+37 15 15	79.56	–4.93	1.7±0.5	6954±6	98±12	121±18	103	9.6
J2056+3458	20 56 45	+34 58 47	78.12	–6.76	1.1±0.5	7509±11	75±23	119±34	111	9.5
J2103+2953	21 03 32 :	+29 53 49 :	75.13 :	–11.14 :	···	795 :	···	···	···	···
J2105+3231	21 05 33	+32 32 20	77.45	–9.74	2.5±0.4	3067±3	92±6	109±10	48	9.1
J2106+3250	21 06 16	+32 46 52	77.74	–9.69	4.2±0.8	3768±5	606±10	622±15	58	9.5
J2106+3335	21 06 39	+33 35 11	78.40	–9.22	7.2±0.7	3081±3	142±7	180±10	48	9.6
J2106+3438	21 06 41	+34 39 04	79.21	–8.52	3.3±0.5	10042±3	174±7	190±10	147	10.2
J2115+3324	21 15 33	+33 24 45	79.53	–10.71	2.1±0.6	3907±6	190±13	210±19	60	9.2
J2117+3002	21 17 23	+30 02 40	77.28	–13.29	3.4±0.5	2557±4	339±8	356±12	40	9.1
J2121+2927	21 21 21	+29 27 39	77.44	–14.31	24.8±1.6	4726±2	269±4	301±6	71	10.5
J2122+3224	21 22 43	+32 25 04	79.85	–12.49	2.6±0.5	4649±6	141±13	183±19	70	9.5

Table C.4 (cont'd)

ALFAZOA	RA (J2000.0)	Dec (J2000.0)	l (°)	b (°)	F_{HI} (Jy km s^{-1})	v_{hel} (km s^{-1})	W_{50} (km s^{-1})	W_{20} (km s^{-1})	D_{LG} (Mpc)	$logM_{HI}$ (M$_\odot$)
J2126+3639	21 26 48	+36 40 06	83.54	–10.10	1.6±0.4	4377±4	59±8	77±12	67	9.2
J2128+3149	21 28 48	+31 50 16	80.35	–13.81	4.3±0.4	4572±2	82±4	103±6	69	9.7
J2129+3457	21 29 05	+34 57 15	82.65	–11.65	4.0±0.5	4474±3	163±7	190±10	68	9.6
J2136+3542	21 36 34	+35 41 25	84.29	–12.17	6.0±0.8	4597±6	362±12	400±18	70	9.8
J2137+3217	21 37 25	+32 17 13	82.02	–14.77	4.3±0.5	4286±3	217±6	240±10	65	9.6
J2137+3410	21 37 40	+34 10 07	83.40	–13.44	2.2±0.4	750±3	107±6	117±9	15	8.1
J2138+3550	21 38 17	+35 49 40	84.65	–12.31	3.1±0.6	9052±6	84±11	121±17	133	10.1
J2138+2949	21 38 28	+29 49 39	80.43	–16.70	4.7±0.4	4959±2	181±5	205±7	75	9.8

Table C.5. Catalog of potential counterparts for ALFA ZOA B+C detections.

ALFAZOA	b (°)	A_B (mag)	NED Counterpart	EM Bands	Sep. (′)	Δv (km s^{-1})
J1814+1316	14.2	0.6	UGC1168	V/NIR/FIR/HI	1.6	31
J1816+1346	14.0	0.5	PGC061658	V/NIR/FIR/HI	0.5	21
J1816+1001	12.3	0.7	CGMW 5–02290	V	0.4	...
J1816+1124	12.8	0.6	CGMW 5–02327	V	0.3	...
J1816+1421	14.1	0.6	2MASX J18165563+1423473	NIR	0.9	...
...	...	...	CGMW 5–02377	V	1.0	...
...	...	...	CGMW 5–02401	V	1.6	...
J1817+0959	12.1	0.7	KKR 43	V	0.5	18
J1817+1256	13.3	0.6	PGC 061685	V/NIR	0.6	6
J1817+1247	13.1	0.6	PGC 061696	V/NIR	0.3	...
J1820+1438	13.5	0.8	PGC 061746	V/NIR/HI	0.5	7
J1821+1305	12.4	0.7	CGMW 5–02961	V/NIR	0.4	...
J1822+1517	13.2	0.9	CGMW 5–03082	V	0.2	...
J1822+1542	13.4	0.7	NGC 6627	V/NIR/FIR/HI	0.7	2
J1822+1226	11.9	0.8	UGC 11214	V/NIR/FIR/HI	1.7	7
J1823+1449	12.7	1.0	CGMW 5–03296	V	0.5	...
J1824+1220	11.5	0.8	CGMW 5–03387	V/NIR	0.2	...

Table C.5 (cont'd)

ALFAZOA	b (°)	A_B (mag)	NED Counterpart	EM Bands	Sep. (′)	Δv (km s^{-1})
J1825+1509	12.5	1.3	2MASX J18253632+1509303	NIR	0.5	···
J1827+0928	9.6	0.7	2MASX J18272857+0929332	NIR	0.3	···
J1828+1123	10.2	0.7	2MASX J18284519+1123437	NIR	0.5	···
J1830+1150	9.9	1.1	CGMW 5–04342	V	0.1	···
J1830+0929	8.9	0.9	2MASX J18305065+0928414	NIR	0.7	12
J1833+1035	8.8	1.1	CGMW 5–04913	V/HI	0.7	1
J1836+1133	8.6	1.2	2MASX J18361584+1134149	NIR	0.1	···
J1836+1018	8.0	1.1	2MASX J18362423+1018467	NIR	0.8	192
J1836+1025	8.0	1.1	UGC 11293	V/NIR/FIR/HI	0.1	30
J1837+1224	8.8	1.5	CGMW 5–05772	V	0.5	···
J1837+1959	12.0	0.9	UGC 11297	V/NIR/FIR	0.4	9
J1837+2625	14.6	0.3	NGC 6671	V/NIR/FIR/HI	0.1	1
J1837+1155	8.4	1.2	HIPASS J1837+11	HI	0.3	5
J1837+2204	12.7	0.6	UGC 11302	V/NIR/HI	0.6	2
J1837+2747	15.0	0.5	UGC 11307	V/NIR	0.3	2
J1838+2522	13.9	0.4	NGC 6674	V/NIR/FIR/HI	0.4	17
J1839+2210	12.5	0.6	UGC 11310	V/NIR	0.7	···

Table C.5 (cont'd)

ALFAZOA	b (°)	A_B (mag)	NED Counterpart	EM Bands	Sep. (′)	Δv (km s^{-1})
J1839+1318	8.6	2.4	CGMW 5–06280	V/NIR/HI	1.4	13
J1839+2342	13.0	0.4	CGMW 5–06381	V	0.7	···
J1840+2129	12.0	0.8	UGC 11314	V/NIR	0.3	3
J1840+2441	13.3	0.5	UGC 11316	V/NIR	0.8	1
J1840+2411	13.1	0.5	UGC 11315	V/NIR	0.1	10
J1840+2836	14.8	0.7	PGC 062235	V/NIR	0.3	8
J1840+2341	12.8	0.4	UGC 11320	V/NIR/FIR	1.4	2
J1840+2340	12.8	0.4	UGC 11320	V/NIR/FIR	1.4	2
J1840+2304	12.5	0.5	UGC 11323	V/NIR	0.2	0
J1841+0911	6.4	1.5	CGMW 5–06629	V	0.4	···
J1842+2453	13.0	0.5	PGC 062281	V/NIR/FIR	0.3	33
J1842+1701	9.5	1.4	CGMW 5–06843	V/NIR/HI	0.8	0
J1842+2135	11.5	0.7	CGMW 5–06881	V/NIR	0.6	···
J1843+1501	8.6	2.0	CGMW 5–06865	V/NIR/HI	0.2	5
J1843+2411	12.5	0.4	CGMW 5–06957	V/HI	0.9	3
J1843+2455	12.8	0.5	CGMW 5–06968	V	0.1	···
J1843+2010	10.7	0.9	CGMW 5–07051	V/HI	0.1	29

Table C.5 (cont'd)

ALFAZOA	b (°)	A_B (mag)	NED Counterpart	EM Bands	Sep. (′)	Δv (km s^{-1})
J1844+2409	12.2	0.4	UGC 11344	V/NIR/FIR/HI	0.5	5
J1844+2514	12.7	0.7	UGC 11346	V/NIR	0.4	2
J1844+1618	8.9	1.7	CGMW 5–07141	V	0.1	...
J1844+2147	11.1	0.8	CGMW 5–07250	V/NIR/FIR	0.6	33
J1845+2124	10.9	0.7	CGMW 5–07277	V	0.6	...
J1845+2134	10.9	0.8	CGMW 5–07334	V/NIR	0.3	...
...	...	...	CGMW 5–07316	V	0.7	...
...	...	...	CGMW 5–07326	V	0.5	...
...	...	...	CGMW 5–07327	V/NIR	0.7	...
J1845+2755	13.5	0.7	CGMW 5–07370	V	0.6	...
...	...	...	CGMW 5–07368	V	2.0	...
J1846+2231	11.2	0.9	UGC 11350	V/NIR/FIR/HI	0.2	6
J1846+2716	13.1	0.5	CGMW 5–07512	V	0.5	...
J1846+2302	11.3	0.8	CGMW 5–07537	V/NIR	0.8	...
J1846+1542	8.1	1.2	CGMW 5–07508	V	0.4	...
J1847+1555	8.1	1.2	CGMW 5–07619	V/NIR/FIR	0.3	49
J1847+2546	12.3	0.5	PGC 062397	V/NIR/FIR	0.7	23

Table C.5 (cont'd)

ALFAZOA	b (°)	A_B (mag)	NED Counterpart	EM Bands	Sep. (′)	Δv (km s^{-1})
J1847+2256	11.0	0.8	UGC 11355	V/NIR	0.5	3
J1848+2020	9.9	1.2	CGMW 5–07776	V/NIR	0.4	···
J1848+2309	10.9	0.8	PGC 062446	V/NIR/FIR	1.3	18
J1848+1655	8.2	1.3	CGMW 5–07870	V	0.4	···
J1849+2314	10.7	0.9	UGC 11362	V	0.4	3
J1851+1954	8.9	1.3	CGMW 5–08422	V/NIR	0.9	···
J1851+2634	11.7	0.8	UGC 11370	V/NIR	0.7	6
J1851+2629	11.6	0.8	UGC 11371	V/NIR/FIR	0.4	1
J1852+2255	9.9	1.2	CGMW 5–08614	V	0.1	···
J1853+0951	4.0	3.3	HIZOA J1853+09	HI	0.5	2
J1854+2630	11.2	0.8	2MASX J18540795+2628558	NIR	0.9	···
	···	···	2MASX J18540988+2628418	NIR	1.4	···
J1854+2438	10.4	0.7	UGC 11375	V/NIR	0.7	2
J1856+2513	10.1	0.9	UGC 11379	V/NIR/FIR	0.6	9
J1857+2558	10.2	0.8	CGMW 5–09243	V	0.4	···
J1859+1316	4.3	3.2	CGMW 5–09365	V/NIR/FIR	0.2	···
J1900+2241	8.3	1.7	CGMW 5–09445	V	0.2	···

Table C.5 (cont'd)

ALFAZOA	b (°)	A_B (mag)	NED Counterpart	EM Bands	Sep. (′)	Δv (km s^{-1})
J1900+2847	10.8	0.8	NGC 6740	V/NIR/FIR	0.4	2
J1901+2456	9.0	1.1	CGMW 5–09565	V/NIR	0.2	···
J1901+1944	6.7	2.1	CGMW 5–09560	V/NIR	1.0	···
J1901+2647	9.8	0.9	CGMW 5–09571	V	0.2	···
J1901+2819	10.4	0.9	CGMW 5–09587	V	0.7	···
J1902+2717	9.8	0.8	UGC 11393	V/NIR/FIR	0.8	2
J1903+2736	9.8	0.9	UGC 11394	V/NIR	0.4	6
J1903+2420	8.3	1.5	UGC 11396	V	0.4	3
J1905+2700	9.2	0.8	CGMW 5–09828	V/NIR	0.6	···
J1905+2842	9.9	1.0	CGMW 5–09839	V	0.5	···
J1906+1256	2.6	5.5	2MASX J19061820+1256195	NIR/HI	0.6	15
J1906+2328	7.3	2.1	CGMW 5–09944	V/NIR	0.8	···
J1909+2648	8.2	0.9	CGMW 5–10135	V/NIR	0.5	52
J1910+1933	4.8	3.5	CGMW 5–10190	V/NIR/HI	1.8	21
J1911+2112	5.3	3.5	2MASX J19112756+2112142	NIR	0.1	···
J1913+1656	2.9	8.5	2MASX J19135226+1655279	NIR/HI	0.6	5
J1915+2008	4.1	5.8	2MASX J19150245+2010197	NIR	0.8	···

Table C.5 (cont'd)

ALFAZOA	b (°)	A_B (mag)	NED Counterpart	EM Bands	Sep. (′)	Δv (km s^{-1})
J1915+2254	5.3	3.1	CGMW 5–10486	V/NIR	0.2	···
J1917+0748	2.2	7.0	HIZOA J1917+07	HI	0.3	0
J1925+0815	3.8	3.0	HIZOA J1926+08	HI	0.6	17
J1927+2804	5.3	1.3	CGMW 5–10831	V	0.1	···
J1927+2011	1.5	12.3	HIPASS J1927+20	HI	1.2	5
J1932+0824	5.3	1.4	IRAS 19305+0820	FIR	0.6	16
J1933+1042	4.4	2.0	2MASX J19335171+1042247	NIR/HI	0.1	11
J1937+2317	1.0	12.2	HIPASS J1937+23	HI	1.8	1
J1937+0922	5.9	1.6	HIPASS J1937+09	HI	0.2	2
J1939+0849	6.4	1.4	UGC 11461	V/NIR/FIR	0.4	11
J1939+1406	4.0	2.2	2MASX J19395186+1405177	NIR	1.0	···
J1940+1242	4.9	1.4	2MASX J19405597+1241500	NIR	0.2	···
J1944+0818	7.7	2.0	2MASX J19440465+0819397	NIR	0.1	47
J1949+2410	1.0	11.7	HIPASS J1949+24	HI	1.3	8
J1950+1055	7.8	1.3	2MASX J19503416+1056127	NIR	0.3	···
J1951+2049	3.0	2.8	2MASX J19511597+2050118	NIR	0.0	···
J1956+1238	8.2	0.9	2MASX J19561970+1241000	NIR	1.4	···

Table C.5 (cont'd)

ALFAZOA	b (°)	A_B (mag)	NED Counterpart	EM Bands	Sep. (′)	Δv (km s^{-1})
J2000+2202	4.2	2.5	CGMW 5–11283	V/NIR/FIR	0.8	···
J2000+1129	9.6	0.7	2MASX J20002051+1129335	NIR	1.4	···
J2002+1247	9.4	0.6	2MASX J20023730+1249205	NIR	0.3	···
J2003+1345	9.2	0.6	2MASX J20035234+1343557	NIR	0.9	···
J2004+1244	9.9	0.5	UGC 11512	V/NIR/FIR	0.5	19
J2004+1403	9.2	0.7	UGC 11513	V/FIR/HI	0.3	5
J2009+0838	12.9	0.6	PGC 064171	V/NIR/HI	0.6	10
J2008+0746	13.4	0.5	UGC 11519	V/NIR	0.4	3
J2011+0829	13.1	0.7	2MASX J20115681+0927544	NIR	0.3	···
J2015+1240	12.3	0.7	HIPASS J2015+12	HI	0.8	1
J2017+1614	10.7	0.5	2MASX J20172777+1614250	NIR	0.3	25
J2018+1637	10.8	0.5	2MASX J20184716+1637351	NIR	0.3	7
J2020+0747	15.7	0.6	PGC 064494	V/NIR/HI	0.8	78
J2020+1452	12.0	0.7	2MASX J20202031+1453014	NIR	0.3	···
J2023+0831	16.1	0.4	ADBS J202344+0832	HI	1.3	4
J2023+1223	14.1	0.5	2MASX J20235953+1222340	NIR	0.4	···
J2024+1235	14.1	0.5	PGC 064627	V/NIR/FIR/HI	0.3	6

Table C.5 (cont'd)

ALFAZOA	b (°)	A_B (mag)	NED Counterpart	EM Bands	Sep. (′)	Δv (km s^{-1})
J2024+1225	14.2	0.5	UGC 11552	V/NIR/FIR/HI	0.7	24
	···	···	UGC 11550	V/NIR	2.0	22
J2025+1223	14.3	0.5	UGC 11556	V/NIR	0.2	5
J2027+0806	17.1	0.7	NGC 6917	V/NIR	0.4	5
J2027+1045	15.7	0.5	UGC 11564	V/NIR	0.5	2
J2027+1329	14.3	0.4	PGC 064734	V/NIR/HI	0.6	51
J2028+2222	9.4	1.0	2MASX J20280787+2223249	NIR	0.7	···
	···	···	2MASX J20280413+2222539	NIR	0.7	···
J2028+1044	15.9	0.5	UGC 11568	V/NIR/FIR	0.2	2
J2029+1040	16.1	0.5	UGC 11571	V/NIR/FIR	0.4	29
J2029+2233	9.6	0.9	2MASX J20295803+2232528	NIR	1.2	···
J2030+2011	11.1	0.6	PGC 064840	V/HI	0.4	10
J2030+2017	11.1	0.7	UGC 11582	V/NIR/HI	0.2	2
J2036+2459	9.5	0.6	2MASX J20364431+2500416	NIR	1.5	···
J2045+2811	9.2	1.0	PGC 065330	V/FIR/HI	0.4	3
J2047+2451	11.5	0.7	2MASX J20473131+2453427	NIR	1.1	···
J2047+2048	14.0	0.5	PGC 065389	V/NIR/HI	0.4	10

Table C.5 (cont'd)

ALFAZOA	b (°)	A_B (mag)	NED Counterpart	EM Bands	Sep. (′)	Δv (km s^{-1})
J2050+2538	11.6	0.7	2MASX J20502915+2537370	NIR	0.4	···
J2054+2555	12.1	0.8	2MASX J20542827+2556202	NIR	0.5	···
J2054+2401	13.4	0.7	PGC 065701	V/NIR	0.4	···
J2056+2600	12.4	1.0	2MASX J20562904+2559449	NIR	0.2	···
J2057+2557	12.6	1.0	UGC 11651	V/NIR	0.1	4
J2057+2537	12.9	0.8	UGC 11655	V/NIR	0.3	8
J2105+2423	15.0	0.6	2MASX J21051330+2423362	NIR	0.9	7
J2105+2708	13.3	0.9	ADBS J210538+2709	HI	1.3	39
J1852+1027	4.4	2.7	···	WISE	···	···
J1855+1239	4.8	3.0	···	WISE	···	···
J1903+2213	7.4	2.9	···	WISE	···	···
J1925+2044	2.3	8.1	···	WISE	···	···
J1927+0927	−3.7	4.2	···	WISE	···	···
J1930+1211	−2.9	3.7	···	WISE	···	···
J1932+2248	1.7	10.6	···	WISE	···	···
J1932+1330	−2.8	4.8	···	WISE	···	···
J1933+1336	−2.9	4.6	···	WISE	···	···

Table C.5 (cont'd)

ALFAZOA	b (°)	A_B (mag)	NED Counterpart	EM Bands	Sep. (′)	Δv (km s^{-1})
J1941+2816	2.6	3.6	...	WISE	...	...
J1942+2823	2.5	3.3	...	WISE	...	...
J1943+2219	−0.7	12.6	...	WISE	...	...
J1958+1253	−8.6	0.7	...	WISE	...	...
J2004+2727	−2.1	7.1	...	WISE	...	...
J2007+1243	−10.4	0.6	...	WISE	...	...
J2012+2114	−6.9	1.7	...	WISE	...	...
J2020+2700	−5.3	2.9	...	WISE	...	...
J2044+2215	−12.6	0.4	...	WISE	...	...
J2051+2454	−12.2	0.7	...	WISE	...	...
J2100+2122	−16.1	0.5	...	WISE	...	...
J2106+2531	−14.2	0.6	...	WISE	...	...